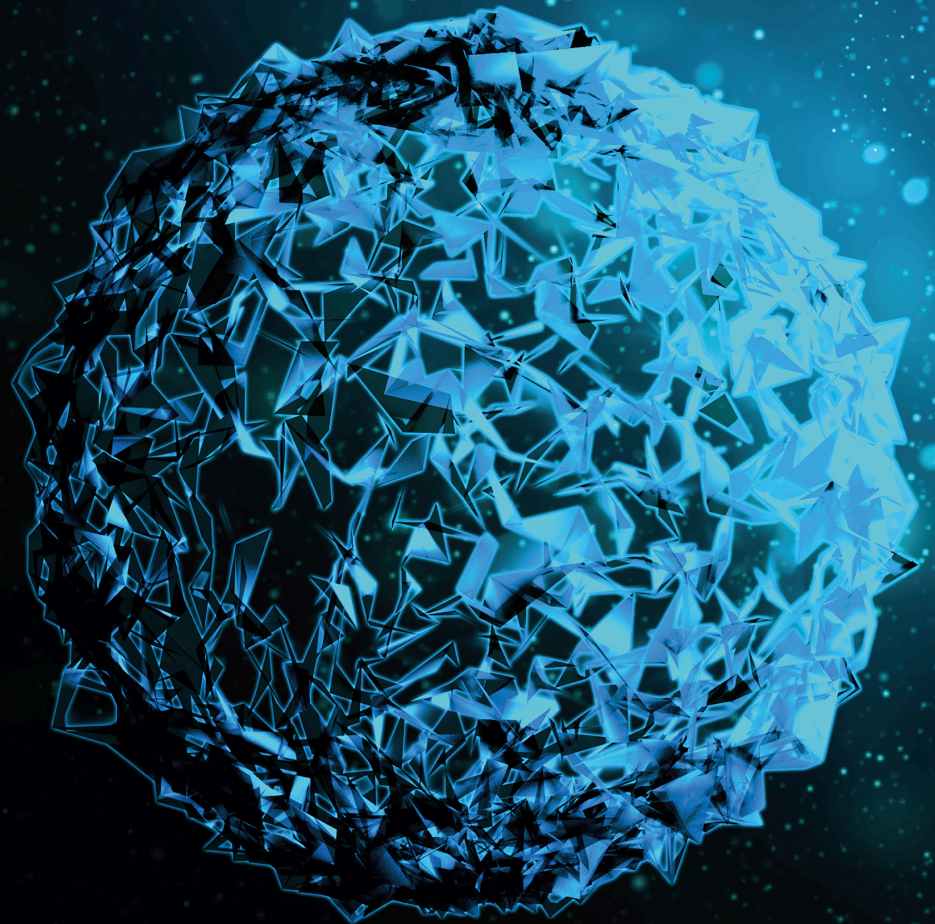


Applications of 3D Printing Technology in Orthopedic Treatment

Lead Guest Editor: Xiaojun Duan

Guest Editors: Ben Wang, Liu Yang, and Anish R. Kadakia





Applications of 3D Printing Technology in Orthopedic Treatment

BioMed Research International

Applications of 3D Printing Technology in Orthopedic Treatment

Lead Guest Editor: Xiaojun Duan

Guest Editors: Ben Wang, Liu Yang, and Anish R.
Kadakia



Copyright © 2021 Hindawi Limited. All rights reserved.

This is a special issue published in "BioMed Research International." All articles are open access articles distributed under the Creative Commons Attribution License, which permits unrestricted use, distribution, and reproduction in any medium, provided the original work is properly cited.

Editorial Board

Y. Ahn, Republic of Korea
Parisa Azimi, Iran
George Babis, Greece
Fabiano Bini, Italy
Elisa Borsani, Italy
Barbara Buffoli, Italy
Feng Cai, China
Frederic CAILOTTO, France
Antonio Capone, Italy
Ming-Chau Chang, Taiwan
Chul Hyun Cho, Republic of Korea
Marcello De Fine, Italy
Lars Donath, Germany
Peter Dr. Varga, Switzerland
Thaqif El Khassawna, Germany
Giuseppe Filardo, Italy
Mattia Fortina, Italy
You-Shui Gao, China
Alberto Grassi, Italy
Zbigniew Gugala, USA
Niels Hammer, New Zealand
Hyuk-Soo Han, Republic of Korea
Philipp Honigmann, Switzerland
Ying-Hui Hua, China
Francesco Inchingolo, Italy
Fang-chun Jin, China
Joby John, United Kingdom
Jean-François Kaux, Belgium
Amal Khoury, Israel
Sae Hoon Kim, Republic of Korea
Naomi Kobayashi, Japan
Panagiotis Korovessis, Greece
Arvind G. Kulkarni, India
Zhu Kun-Peng, China
Yong Seuk Lee, Republic of Korea
Kai-Uwe Lewandrowski, Brazil
Chenshuang Li, USA
Xiaodong Li, USA
Jianfeng Li, China
Dohyung Lim, Republic of Korea
Sheldon Lin, USA
Matthew R. McCann, Canada

Hiroaki Minehara, Japan
Kyeongsoon Park, Republic of Korea
Kun Bo Park, Republic of Korea
Jose A. Parraca, Portugal
Dmitry Popkov, Russia
William B. Rodgers, USA
Thomas S. Roukis, USA
Ajoy Prasad Shetty, India
Kangquan Shou, China
Hae-Ryong Song, Republic of Korea
Martin Stoddart, Switzerland
Zdenek Svoboda, Czech Republic
Mitsuhiro Takeno, Japan
Kentaro Uchida, Japan
Meng-Huang Wu, Taiwan
Radovan Zdero, Canada
Haining Zhang, China
Chunfeng Zhao, USA
Jun Zou, China







Contents

Applications of 3D Printing Technology in Orthopedic Treatment

Xiaojun Duan , Ben Wang, Liu Yang, and Anish R. Kadakia





Editorial (3 pages), Article ID 9892456, Volume 2021 (2021)

Corrigendum to “Application of 3D Printing-Assisted Articulating Spacer in Two-Stage Revision Surgery for Periprosthetic Infection after Total Knee Arthroplasty: A Retrospective Observational Study”

Lingtong Kong , Jiawei Mei , Wufei Ge , Xiansheng Jin, Xiaoxuan Chen , Xianzuo Zhang , and Chen Zhu 

Corrigendum (1 page), Article ID 9792626, Volume 2021 (2021)

Overview of In-Hospital 3D Printing and Practical Applications in Hand Surgery

Marco Keller , Alissa Guebeli , Florian Thieringer , and Philipp Honigmann 

Research Article (14 pages), Article ID 4650245, Volume 2021 (2021)

Application of Mixed Reality Using Optical See-Through Head-Mounted Displays in Transforaminal Percutaneous Endoscopic Lumbar Discectomy

Xiaoyang Liu, Jianmin Sun, Meimei Zheng, and Xingang Cui 







Research Article (8 pages), Article ID 9717184, Volume 2021 (2021)

The Bony Resection Accuracy with Patient-Specific Instruments during Total Knee Arthroplasty: A Retrospective Case Series Study

Liang Yuan , Bin Yang , Xiaohua Wang, Bin Sun, Ke Zhang, Yichen Yan, Jie Liu , and Jie Yao 







Research Article (9 pages), Article ID 8674847, Volume 2021 (2021)

Application of 3D Printing-Assisted Articulating Spacer in Two-Stage Revision Surgery for Periprosthetic Infection after Total Knee Arthroplasty: A Retrospective Observational Study

Lingtong Kong , Jiawei Mei , Wufei Ge , Xiansheng Jin, Xiaoxuan Chen , Xianzuo Zhang , and Chen Zhu 






Research Article (12 pages), Article ID 3948638, Volume 2021 (2021)

In-Hospital 3D Printed Scaphoid Prosthesis Using Medical-Grade Polyetheretherketone (PEEK) Biomaterial

Philipp Honigmann , Neha Sharma , Ralf Schumacher , Jasmine Rueegg , Mathias Haefeli , and Florian Thieringer 



Research Article (7 pages), Article ID 1301028, Volume 2021 (2021)

Endoscopic Treatment of Symptomatic Foot and Ankle Bone Cyst with 3D Printing Application

Changgui Zhang, Jin Cao , Hongli Zhu , Huaquan Fan , Liu Yang , and Xiaojun Duan 

Research Article (10 pages), Article ID 8323658, Volume 2020 (2020)

Three-Dimensional-Printed Guiding Template for Unicompartmental Knee Arthroplasty

Fei Gu, Liangliang Li, Huikang Zhang, Xuxiang Li, Chen Ling, Liming Wang , and Qingqiang Yao 



Research Article (10 pages), Article ID 7019794, Volume 2020 (2020)

In Vivo Reconstruction of the Acetabular Bone Defect by the Individualized Three-Dimensional Printed Porous Augment in a Swine Model

Jun Fu , Yi Xiang , Ming Ni , Xiaojuan Qu , Yonggang Zhou , Libo Hao , Guoqiang Zhang , and Jiying Chen 



Research Article (10 pages), Article ID 4542302, Volume 2020 (2020)

Reconstruction of Bony Defects after Tumor Resection with 3D-Printed Anatomically Conforming Pelvic Prostheses through a Novel Treatment Strategy

Wei Peng , Runlong Zheng, Hongmei Wang, and Xunwu Huang 



Research Article (16 pages), Article ID 8513070, Volume 2020 (2020)

3D Printed Personalized Guide Plate in the Femoral Head Core Decompression

Liangliang Cheng , Xing Qiu, Lei Yang, Chi Xiao, Baoyi Liu, Chukwuemeka Samuel Okoye, and Dewei Zhao 

Research Article (5 pages), Article ID 7250528, Volume 2020 (2020)

3D-Printed Patient-Specific Instrumentation Technique Vs. Conventional Technique in Medial Open Wedge High Tibial Osteotomy: A Prospective Comparative Study

Yunhe Mao , Yang Xiong, Qi Li, Gang Chen, Weili Fu, Xin Tang, Luxi Yang, and Jian Li 



Research Article (10 pages), Article ID 1923172, Volume 2020 (2020)

Influence of the Postcuring Process on Dimensional Accuracy and Seating of 3D-Printed Polymeric Fixed Prostheses

Jaewon Kim and Du-Hyeong Lee 

Research Article (7 pages), Article ID 2150182, Volume 2020 (2020)

Corrigendum to “Prime-Boost Vaccination Using Chemokine-Fused gp120 DNA and HIV Envelope Peptides Activates Both Immediate and Long-Term Memory Cellular Responses in Rhesus Macaques”

Hong Qin, Pramod N. Nehete , Hong He , Bharti Nehete, Stephanie Buchl, Soung-chul Cha, Jagannadha K. Sastry, and Larry W. Kwak




Corrigendum (2 pages), Article ID 5471638, Volume 2020 (2020)

Corrigendum to “Combined Industrial Wastewater Treatment in Anaerobic Bioreactor Post-Treated in Constructed Wetland”

Bibi Saima Zeb , Qaisar Mahmood , Saima Jadoon , Arshid Pervez, Muhammad Irshad , Muhammad Bilal, and Zulfiqar Ahmad Bhatti

Corrigendum (9 pages), Article ID 6102379, Volume 2020 (2020)

Acetabular Bone Defect in Total Hip Arthroplasty for Crowe II or III Developmental Dysplasia of the Hip: A Finite Element Study

Yinqiao Du , Jun Fu, Jingyang Sun, Guoqiang Zhang, Jiying Chen, Ming Ni , and Yonggang Zhou 

Research Article (12 pages), Article ID 4809013, Volume 2020 (2020)

Editorial

Applications of 3D Printing Technology in Orthopedic Treatment

Xiaojun Duan ¹, Ben Wang,² Liu Yang,¹ and Anish R. Kadakia³

¹Center for Joint Surgery, Southwest Hospital, Third Military Medical University (Army Medical University), Chongqing, China

²Georgia Institute of Technology, Atlanta, USA

³Northwestern University, Chicago, USA

Correspondence should be addressed to Xiaojun Duan; duanxiaojun@hotmail.com

Received 28 July 2021; Accepted 28 July 2021; Published 15 August 2021

Copyright © 2021 Xiaojun Duan et al. This is an open access article distributed under the Creative Commons Attribution License, which permits unrestricted use, distribution, and reproduction in any medium, provided the original work is properly cited.

Three-dimensional (3D) printing technology, also known as additive manufacturing (AM) or rapid prototyping (RP), is a special technique which could fabricate 3D models using computer-assisted design (CAD). It was firstly developed by a Japanese doctor forty years ago and initially used in manufacturing and industry [1]. During recent decades, with the development of manufacturing technology and materials science, 3D printing has also been used in some medical fields such as dentistry, maxillofacial surgery, and neurosurgery [2]. Application of 3D printing in orthopedics is also increasingly popular, mainly including preoperative planning, surgical guides, personalized implants, and customized prostheses [3, 4]. Individualized surgical treatment could be easily and accurately formulated under the aid of 3D printing and reduce the operation time and postoperative complications [5–7]. Depending on its unique advantages, 3D printing will lead a surgeon to precision medicine and provide patients with better treatment effects at lower cost [8, 9]. At present, the Chinese government, enterprises, universities, and institutes have invested a lot of resources in related research including printing technology, raw materials, and clinical applications and have made important progress. For example, our center uses 3D printing technology to manufacture implants of porous tantalum for clinical surgical treatment; in this special issue, a great majority of the submissions come from China, which report their latest developments in 3D printing. As the editorial team, we pay attention to some recent progressive research in 3D printing technology for orthopedic treatment. Below is a summary of these accepted articles.

The study by L. Kong et al. reported a set of articular spacer solutions using 3D printing technology in revision surgery for periprosthetic joint infection (PJI) after total knee arthroplasty. They compared the treatment effects between 3D printing spacer and static spacer in a retrospective study and stated that the 3D printing spacer group had less bone loss, less intraoperative blood loss, and greater knee function than the static spacer group. This technique effectively provides a new method to make accurate and personalized spacers in PJI and lower the rates of reinfection and complications.

The paper by Y. Du et al. evaluated the stability of the acetabular cup with different types of bone defects in total hip arthroplasty for developmental dysplasia of the hip (DDH) using the finite element analysis (FEA) model. The authors found that the diameter of the femoral ceramic head had no significant impact on the stability of the acetabular cup. When the uncoverage rates of the cup were less than 24.5%, the stability of the cup was satisfactory even without the use of screws. However, when the uncoverage rates were more than 24.5%, it was necessary to apply screws to improve the primary stabilization of the cup. Although their study is just based on the FEA model instead of clinical application, the results are still beneficial to the subsequent clinical study.

L. Yuan et al. retrospectively analyzed the bony resection accuracy during total knee arthroplasty (TKA) with patient-specific instrumentation (PSI) produced by 3D printing technology. They conducted full-length computed tomography (CT) for every patient and drafted detailed preoperative plans including the bony resection thickness. PSI was manu-

factured based on the CT data and operation plan. Each bone resected in the operation was also measured with CT to reconstruct the three-dimensional radiographs. The bone resection thickness was compared between the preoperative plan and intraoperative data to assess the resection accuracy in different bone sites. The results of this study show that PSI had a generally good accuracy during the femur and tibia bone resection in TKA.

X. Liu et al. evaluated the application of mixed reality (MixR) technology during transforaminal percutaneous endoscopic discectomy (TPED), and optical see-through head-mounted displays (OST-HMDs) were used to assist operation. They compared the difference of clinical effects between conventional TPED and MixR-assisted TPED and found that mixed reality (MixR) technology could significantly reduce the operation time and radiation exposure during the total operation procedure. This technology may be a powerful auxiliary tool for TPED but would increase the eye fatigue because of the application of OST-HMDs.

J. Kim et al. investigated whether the postcuring process could influence the dimensional accuracy and seating of 3D printing dental prostheses. A study stone model was designed and fabricated to verify this hypothesis. Results showed that the postcuring process significantly affected the fit and dimensional precision of 3D printing polymeric prostheses. They suggested that seating on the stone model was a better choice for minimizing the deformity of the dental prosthesis and reducing adverse effects during the postcuring process.

F. Gu et al. designed a three-dimensional printed patient-customized guiding template (3DGT) to increase the efficacy and safety of unicompartmental knee arthroplasty (UKA). Personalized guiding template could provide helpful assistance in several procedures of operation planning, intraoperative positioning, and osteotomy. This study concluded that 3DGT could shorten operation time, reduce surgical trauma, and promote recovery.

P. Honigmann et al. presented the first in-hospital 3D printed scaphoid prosthesis using polyetheretherketone (PEEK) biomaterial via fused filament fabrication (FFF), one of the 3D printing technologies. The surface of this medical grade PEEK prosthesis did not show "FFF stair-stepping" phenomenon, which was usually common in the industrial grade scaphoid prosthesis. The biocompatible and implantable polymers such as PEEK applied in 3D printing could offer great potential in the treatment of complex joint damage in the hospital environment.

M. Keller et al. reviewed the latest practical application of 3D printing in hand surgery and introduced the most common printing techniques and some materials. They provided a useful overview of the 3D printing technology applied in numerous aspects such as surgical guides, personalized implants for bone defects, customized splints, and preoperative plan. The authors hold the opinion that orthopedics, especially hand surgery, will benefit from 3D printing in the near future.

L. Cheng et al. retrospectively investigated the utilization and feasibility of 3D printing technology for core decompression in patients with osteonecrosis of the femoral head (ONFH). The operation process went well and consumed less

time than traditional methods with the aid of personalized guide plates and reduced the usage of intraoperative X-ray fluoroscopy. The results indicated that 3D printing had several advantages of improving efficiency, being more convenient, and accurate positioning.

C. Zhang et al. revealed the efficacy of arthroscopy in treating bone cysts of the foot and ankle combined with 3D printing individualized guides. Better VAS score and AOFAS score and less intraoperative bleeding were displayed in patients with the assistance of 3D printing. It is concluded that 3D printing could significantly help surgeons to fast and smoothly establish a portal in arthroscopic ankle surgery.

J. Fu et al. reconstructed the acetabular bone defect in a swine model to evaluate the bone ingrowth, biomechanics, and matching degree of the 3D printed porous prosthesis. Based on the results, the authors found that the 3D printed porous augments showed great porosity and pore size and had magnificent stiffness and elastic modulus. The anatomical matching extent was excellent, which could enhance the stability of the porous prosthesis. Although this study was conducted in minipigs, it displayed the great potential of 3D printed porous augment in the treatment of clinical severe acetabular bone defects.

Y. Mao et al. compared the clinical effects of 3D printed patient-specific instrumentation (PSI) with conventional surgical techniques in medial open wedge high tibial osteotomy (MOWHTO). The results of this prospective comparative study showed that 3D printed PSI had significantly lower correction errors in terms of mFTA and mMPTA and demanded shorter duration and less radiation exposure. They concluded that 3D printing technique could be recommended as an effective assistant for MOWHTO in the treatment of varus because of its accuracy and effectiveness.

W. Peng et al. reported an entirely anatomically conforming pelvic prosthesis for pelvic reconstruction. Pelvic tumor is a complex disease due to the vascular invasion of tumor issue, and most of the patients suffering from pelvic tumor undergo the surgery of tumor resection and hemipelvic replacement. The authors showed that 3D-printed prosthesis was of value for patients with complex pelvic tumors.

Conflicts of Interest

The editors declare that there are no conflicts of interest regarding the publication of this special issue.

Acknowledgments

We would like to express our great gratitude to Xin Chen from the Center for Joint Surgery of Southwest Hospital for language support and appreciate all authors and editors who contributed to this special issue. We also want to thank the reviewers who made this special issue possible.

*Xiaojun Duan
Ben Wang
Liu Yang
Anish R. Kadakia*

References

- [1] A. Zhakeyev, P. Wang, L. Zhang, W. Shu, H. Wang, and J. Xuan, "Additive manufacturing: unlocking the evolution of energy materials," *Advanced Science*, vol. 4, no. 10, article 1700187, 2017.
- [2] M. Michalski and J. Ross, "The shape of things to come: 3D printing in medicine," *JAMA*, vol. 312, no. 21, pp. 2213-2214, 2014.
- [3] M. Burn, A. Ta, and G. Gogola, "Three-dimensional printing of prosthetic hands for children," *The Journal of Hand Surgery*, vol. 41, no. 5, pp. e103-e109, 2016.
- [4] N. Skelley, M. Smith, R. Ma, and J. L. Cook, "Three-dimensional printing technology in orthopaedics," *The Journal of the American Academy of Orthopaedic Surgeons*, vol. 27, no. 24, pp. 918-925, 2019.
- [5] P. Fadero and M. Shah, "Three dimensional (3D) modelling and surgical planning in trauma and orthopaedics," *The Surgeon*, vol. 12, no. 6, pp. 328-333, 2014.
- [6] M. Citak, L. Kochsiek, T. Gehrke, C. Haasper, E. M. Suero, and H. Mau, "Preliminary results of a 3D-printed acetabular component in the management of extensive defects," *Hip International*, vol. 28, no. 3, pp. 266-271, 2018.
- [7] X. Duan, P. He, H. Fan, C. Zhang, F. Wang, and L. Yang, "Application of 3D-printed personalized guide in arthroscopic ankle arthrodesis," *BioMed Research International*, vol. 2018, Article ID 3531293, 8 pages, 2018.
- [8] S. Lawson, A. Alwakwak, A. Rownaghi, and F. Rezaei, "Gel-print-grow: a new way of 3D printing metal-organic frameworks," *ACS Applied Materials & Interfaces*, vol. 12, no. 50, pp. 56108-56117, 2020.
- [9] X. Duan, H. Fan, F. Wang, P. He, and L. Yang, "Application of 3D-printed customized guides in subtalar joint arthrodesis," *Orthopaedic Surgery*, vol. 11, no. 3, pp. 405-413, 2019.

Corrigendum

Corrigendum to “Application of 3D Printing-Assisted Articulating Spacer in Two-Stage Revision Surgery for Periprosthetic Infection after Total Knee Arthroplasty: A Retrospective Observational Study”

Lingtong Kong ¹, Jiawei Mei ¹, Wufei Ge ¹, Xiansheng Jin,² Xiaoxuan Chen ³,
Xianzuo Zhang ⁴ and Chen Zhu ¹

¹Department of Orthopedics, The Affiliated Provincial Hospital of Anhui Medical University, Hefei 230001, China

²IAT-Chungu Joint Laboratory for Additive Manufacturing Anhui Chungu 3D Printing Institute of Intelligent Equipment and Industrial Technology, Wuhu 241200, China

³College of Chemistry and Chemical Engineering, Xiamen University, Xiamen 361005, China

⁴Department of Orthopedics, The First Affiliated Hospital of USTC, Division of Life Sciences and Medicine, University of Science and Technology of China, Hefei 230022, China

Correspondence should be addressed to Xianzuo Zhang; zhangxianzuo@foxmail.com and Chen Zhu; zhuchena@ustc.edu.cn

Received 24 May 2021; Accepted 24 May 2021; Published 7 June 2021

Copyright © 2021 Lingtong Kong et al. This is an open access article distributed under the Creative Commons Attribution License, which permits unrestricted use, distribution, and reproduction in any medium, provided the original work is properly cited.

In the article titled “Application of 3D Printing-Assisted Articulating Spacer in Two-Stage Revision Surgery for Periprosthetic Infection after Total Knee Arthroplasty: A Retrospective Observational Study” [1], some of the authors were linked to the incorrect affiliations in the affiliation list. The correct author affiliations are now corrected in the author information above.

References

- [1] L. Kong, J. Mei, W. Ge et al., “Application of 3D printing-assisted articulating spacer in two-stage revision surgery for periprosthetic infection after total knee arthroplasty: a retrospective observational study,” *BioMed Research International*, vol. 2021, Article ID 3948638, 12 pages, 2021.

Research Article

Overview of In-Hospital 3D Printing and Practical Applications in Hand Surgery

Marco Keller ^{1,2} **Alissa Guebeli** ^{1,2} **Florian Thieringer** ^{2,3}
and **Philipp Honigmann** ^{1,2,4}

¹Hand Surgery, Department of Orthopaedic Surgery and Traumatology, Kantonsspital Baselland, 4410 Liestal, Switzerland

²Medical Additive Manufacturing Research Group, Department of Biomedical Engineering, University of Basel, 4123 Allschwil, Switzerland

³Department of Oral and Cranio-Maxillofacial Surgery, University Hospital Basel, Basel, Switzerland

⁴Department of Biomedical Engineering and Physics, Amsterdam UMC, University of Amsterdam, Amsterdam, Netherlands

Correspondence should be addressed to Marco Keller; marco.keller@ksbl.ch

Received 23 June 2020; Revised 3 January 2021; Accepted 22 March 2021; Published 27 March 2021

Academic Editor: Xiaojun Duan

Copyright © 2021 Marco Keller et al. This is an open access article distributed under the Creative Commons Attribution License, which permits unrestricted use, distribution, and reproduction in any medium, provided the original work is properly cited.

Three-dimensional (3D) printing is spreading in hand surgery. There is an increasing number of practical applications like the training of junior hand surgeons, patient education, preoperative planning, and 3D printing of customized casts, customized surgical guides, implants, and prostheses. Some high-quality studies highlight the value for surgeons, but there is still a lack of high-level evidence for improved clinical endpoints and hence actual impact on the patient's outcome. This article provides an overview over the latest applications of 3D printing in hand surgery and practical experience of implementing them into daily clinical routine.

1. Introduction

Three-dimensional (3D) printing, also known as Additive Manufacturing (AM), is a manufacturing technology which enables the production of three-dimensional models of a computer-designed template or data from medical imaging technologies by specially designed printers.

In 1981, a Japanese doctor, Hideo Kodama, developed a rapid prototyping technique, using a photosensitive resin that was polymerized by an UV light, creating the first 3D printing technique, an ancestor for SLA (stereolithography). In 1986, the first patent for SLA was submitted by Chuck Hull, and in 1988, two further 3D printing techniques were developed: SLS (“selective laser sintering”, in which powder grains are fused together locally by a laser) and FDM (“fused deposition modelling”, 3D printing with filaments) [1, 2].

In the following years, several additional methods were developed, including Binder Jetting and Polyjet, which are

methods based on the inkjet printing technology, making color printing and combination of different materials possible [3].

3D printing was first used in the automobile, aerospace, and consumer product industries. Along with the radical improvements financed by these industries, new applications have been developed for its use in the medical field. According to the different aspects of every medical subspecialty, the implementation of 3D printing occurred with different pace and intensity. The applications of 3D printing in hand surgery are, compared to other subspecialties like for example craniomaxillofacial surgery, currently limited. In orthopaedic surgery, especially hand surgery, 3D printing enables the production of complex anatomical forms from data such as Computertomography (CT) images.

Current fields of application are the training of young hand surgeons, patient education, preoperative planning and fabrication of customized rehabilitation devices, customized surgical guiding tools, implants, and prostheses [4, 5].

An overview over the development and current implementations of 3D printing in each field is given in the subsequent paragraphs.

2. Printing Techniques and Materials

The entire 3D printing process consists of the following steps:

- (1) *Data Acquisition.* Acquisition of a 3D model of a medical image (CT, MRI, others) in DICOM format (Digital Imaging and Communications in Medicine)
- (2) *Image Processing.* Segmentation of the anatomy and transfer of DICOM into STL (stereolithography) format using a suitable software tool
- (3) *3D Slicing/Printing.* Slicing the STL model into several 2D slices and printing the 3D model by layering the slices on top of each other using a suitable printing technique
- (4) *Postprocessing.* Depending on the printing technique, the printed 3D model needs to be finalized by removing excess material, increasing the mechanical strength, removing the support structures, and improving the object's appearance

In the following table, the most common printing techniques and their characteristics are listed (Table 1).

Advantages of SLA printing are the accurate surface, and the relatively cheap price, weaknesses are the time-consuming removal of excess material and the limited size of the printed objects.

The SLS printing method allows the use of many different materials, including metals and does not rely on supporting structures. Furthermore, up to 100% density can be achieved. However, its surface is porous, the production time is longer due to the heating process, and the price for metal printing can be very high.

The strengths of FDM printing are the low price, fast production, and the possibility to print low density and, thus, light objects. On the other hand, this method relies on supporting structures needed to attach the printed object to the printing platform, which results in more time consumed for postprocessing to remove these supports.

The great advantages of the binder and material jetting techniques are the possibility to print different colors and materials in one object. BJ, unlike Polyjet, does not need any supporting structures, but the printed objects are less force resistant [3–5].

Of the mentioned printing methods, FDM is the most common today. The relatively simple mechanism and affordable materials make it the most accessible printing process for nonprofessionals.

3. Practical Applications in Hand Surgery

3.1. Training. The beneficial effect of 3D-printed models within orthopaedic education is well described. Some high-quality studies were able to highlight this effect especially with the involvement of bones with complex anatomical

structures like the pelvis or the spine [6–9]. In the field of hand surgery, only very few articles on 3D printing technology in the education of junior surgeons have been published so far. Two reports from the same study group presented a synthetic wrist procedural simulator (Wristsim®, Biomedex™, Paris, France) based on 3D printing technology. They were able to highlight its potential use in training of volar plating in distal radius fractures and distal radius shortening osteotomy but also recognized its inferiority to cadaver specimen training [10, 11].

Despite the potential benefits, surgical training with models based on 3D printing technology has not found its way into hand surgery daily routine or even the curriculum of hand surgery specialisation yet. From our experience, we see the following reasons: only few clinics have the infrastructure and resources to provide every trainee with enough 3D-printed models and implants to ensure a good learning curve. Another reason is the complexity of the functional units: an isolated model of the distal radius might be useful to practice plating osteosynthesis or osteotomies. But due to the complex biomechanical units of the wrist and hand, hardly any other bone of the hand can be separated from its adjacent structures and still serve the purpose of a useful model to practice. The intercarpal relations are very complex and building an adequate model takes more effort than in the pelvis or the spine (Figure 1).

3.2. Patient Education. Comprehension of the injury is a cornerstone for a healthy patient-doctor-relationship. An adequate grasp of the extent of a patient's own lesion will help setting realistic expectations and increase the adherence to the proposed treatment. A tangible 1 : 1 model of, e.g., a fracture can facilitate the achievement of this goal. In a clinical trial on distal radius fractures, Chen et al. were able to show that not only were patients more likely to understand their condition and the operative plan, but the satisfaction and usefulness of the 3D prototype was even higher among patients than among surgeons themselves. This effect was measured with questionnaires and compared to the routine approach (patient education without the use of 3D-printed models) [12].

We find patient education with 3D-printed models especially useful in settings where patients suffered a complex, intra-articular fracture and need to understand how grave the damage to the joint is. In these cases, the printed model can simultaneously be used for preoperative planning.

3.3. Preoperative Planning. Numerous studies were published on the advantages of preoperative planning using 3D-printed models, and some were even able to highlight measurable improvements like shorter operation time, less intraoperative blood loss, and faster time to bony union [13, 14]. Preoperative planning can be roughly divided into visualizing and training with the help of three-dimensional models of a fracture or a soft tissue defect and the preoperative conduction of the actual surgery on a three-dimensional model including modifying (prebending or assembling) implants, which then are sterilized and used in the actual surgery resulting in shorter operation time.

TABLE 1: Overview of different 3D printing techniques and their characteristics (SLA: stereolithography; SLS: selective laser sintering; DMLS: direct metal laser sintering; FDM: Fused deposition modelling; UV: Ultra-violet [3–5]).

| Type of printing | Build material | Material distribution | Binding technique | Color printing | Material combination | Postprocessing | | Increase strength | Remove support | Material costs (US\$ per kg, nonprofessional use) |
|--|---|-----------------------|-------------------------|----------------|----------------------|----------------|-----|-------------------|----------------|---|
| | | | | | | Remove excess | | | | |
| Photopolymerization (SLA) | Photopolymer (resin) | Vat | Light (laser) | No | No | Yes | Yes | Yes | Yes | 50 |
| Directed energy deposition (SLS, DMLS) | Powder | Bed | Heat (laser or welding) | No | No | Yes | No | No | No | 45-75 (nonmetal) 350-550 (metal) |
| Material extrusion (FDM) | Filaments of plastic, food, paste, etc. | Extrusion | Heat (most often) | No | No | No | No | No | Yes | 20-70 |
| Binder jetting (BJ) | Powder | Bed | Jet adhesive | Yes | Yes | Yes | Yes | Yes | No | 300-1000 |
| Material jetting (Polyjet) | Photopolymer (resin) | Jet | Light (UV) | Yes | Yes | No | No | No | Yes | 300-1000 |



FIGURE 1: 1 : 1 model based on 3D-Computertomography (CT) data of the carpal bones printed on an FDM-printer. This model allows analysis of intracarpal relationships und surgical training.

In hand surgery research, the use of 3D-printed models has mainly been focussed on preoperative planning in patients with distal radius fractures or scaphoid pathologies. Bizzotto et al. reported that the preoperative planning (especially the placement of the fixation plate and screw orientation) with the use of 3D-printed models of distal radius fractures leads to substantial improvement in comprehension of the fracture. This effect was measured with a questionnaire to obtain feedback of the surgeon and was particularly observed in intra-articular fractures (with gaps or step of ≥ 2 mm or with a multifragmentary fracture pattern) [15].

With the conduction of a randomized controlled trial (RCT), Kong et al. were able to show that the use of a 3D-printed 1 : 1 model of a forearm with a distal radius fracture resulted in reduced operation time, intraoperative bleeding, and times of intraoperative fluoroscopy [16]. The exact same three beneficial effects could be shown in another RCT on “die-punch”-radius fractures [12].

Due to the complex three-dimensional shape of the scaphoid, the reduction and fixation of scaphoid fractures can be challenging. Jew et al. reported a series of four cases where preoperative planning with a 3D-printed model of the fracture facilitated the choice of approach, implant, and size of the cannulated screw [17]. Sometimes, despite adequate reduction and fixation, a scaphoid nonunion can occur. In recalcitrant scaphoid nonunions, the use of a vascularized osseous or osteocartilaginous graft from the medial femoral condyle (MFC) has proven to be a safe and reliable treatment option [18]. Some authors reported a method of

proximal pole replacement with a vascularized osteocartilaginous MFC graft using a 3D-printed model of the graft based on CT-data from the contralateral uninjured hand. With this method, the harvesting and shaping of the graft can be conducted accurately and efficiently according to the authors [19, 20].

In our institution, the planning of operations with 3D printing technology is mainly used for ORIF (open reduction with internal fixation) of dislocated intra-articular fractures of the radius or metacarpal fractures where the placement of single screws can be crucial (Figure 2). The models are printed with an FDM-printer based on 3D-CT images with high accuracy. A comparison of the dimensional accuracy of an isosymmetric-shaped test body printed with different technologies showed that FDM produces the highest precision (0.05 ± 0.005 mm) whereas SLS (0.11 ± 0.016 mm) and binder jetting (0.14 ± 0.02 mm) show a slightly lower but still satisfactory accuracy for surgical use [21]. A 1 : 1 model allows a more accurate assessment of the size and dislocation of key fragments than a sole analysis of CT-scans (Figure 3). The additional tactile and visual feedback provides valuable information on bony step-offs and gaps. However, this effect must not be overrated since much more factors than only fracture size and dislocation need to be taken into account. The relevance of single fragments varies according to attached ligaments, and the surgeon needs to be aware in which areas the reduction and fixation needs to be perfect (e.g., dorsal ulnar and volar ulnar corner in distal radius fractures) and in which areas minor gaps can be tolerated. This information cannot be provided by a 3D-printed fracture model. Furthermore, we do not see a major benefit of conducting the actual procedures on 3D-printed models and then sterilizing the implants, because most of the currently used implants in hand surgery fit very well and rarely need any bending or adaption which could be done prior to save time. This stands in contrast to other surgical subspecialties like for example craniomaxillofacial surgery where a retrospective survey showed that precontouring plates based on 3D-printed orbital models leads to a significant reduction of surgery time compared to intraoperative free-hand bending (57.3 ± 23.4 min vs. 99.8 ± 28.9 min, $p = 0.001$) in surgical repair of isolated orbital floor fractures [22]. With some experience, the choice of implant in hand surgery is mostly straightforward. So without having conducted an actual study on this distinct topic, we confirm the findings of Bizzotto et al. who reported no change in surgical decisions when 3D-printed models were used for the planning of ORIF in distal radius fractures [15]. There is also still a lack of studies that correlate presurgical planning using 3D-printed models with clinical endpoints to exhibit possible advantages for the patient compared to conventional planning.

3.4. Customized Braces/Splints. One of the most established applications of 3D printing technology in hand surgery is the fabrication of casts and splints. However, still no major widespread in hand surgery daily routine has taken place. Currently, most implementations of this technology happen within the framework of case series or feasibility studies. In our opinion, this is due to the following reasons: up to now,

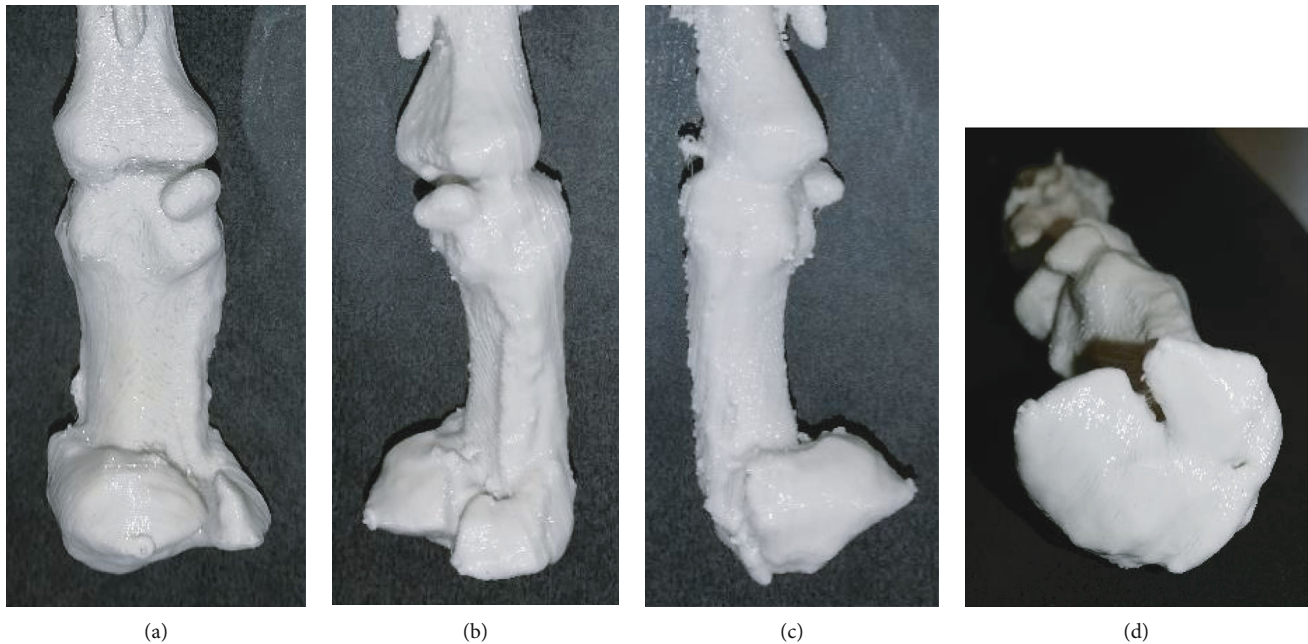


FIGURE 2: (a–d) 3D-printed 1 : 1 model of a displaced, multifragmentary, intra-articular fracture of the proximal part of the first metacarpal bone. The model was used to educate the patient about possible surgical treatment options and for preoperative planning.

the use of digital design software is challenging and time-consuming; the printing process is lengthy and error-prone and hospitals without the possibility of in-house-printing rely on external suppliers which is costly. All in all, this effort mostly exceeds the effort of having a conventional plaster cast or splint built by far. A successful implementation of 3D-printed orthotics in daily routine requires the following premises: an intuitive and purpose-oriented designing software, a stable and fast printing process which is available around the clock, little required postprocessing but easy adaption if necessary, an efficient in-hospital workflow with collaboration of doctors and hand therapists and redundancy of skilled users at any level of the workflow, in case a person is unavailable (e.g., in the OR).

Most of the published papers on 3D-printed upper extremity orthotics focus on the composition of materials, the printing process, and feasibility. Up to date, no high-quality clinical trial was able to demonstrate the noninferiority or even superiority concerning wearing comfort or clinical outcome compared to conventional plaster casts and splints. Several *in vitro* [23, 24] and *in vivo* studies [25–29] highlight the safety and effectiveness of customized 3D-printed forearm casts. These trials indicate a good patient satisfaction due to light, breathable and waterproof splints. In another case series, Nam et al. highlighted the feasibility of 3D-printed finger splints for posthand burn patients [30].

Our research group has implemented the use of 3D-printed hand and wrist rehabilitation devices in daily routine. Furthermore, we initiated the (up to our knowledge) first prospective randomized clinical trial assessing the relevance, feasibility, safety, and patient comfort of 3D-printed forearm casts compared to conventional plaster casts in the nonoperative treatment of distal radius fractures. The patients are scanned in the outpatient clinic with a handheld device.

The data of the 3D-scan are processed and sliced using a software (“Spentys© Point-of-Care Solution” [Spentys SA/NV, Brussels, BE]) from a software company specializing in medical orthoses and immobilization devices. The forearm casts (“Polycast©” [Spentys SA/NV, Brussels, BE]) are then printed overnight and in-hospital using a 3D-printer with FDM-technology and Polypropylene (PP) filament (Figure 4). The postprocessing of the cast including the application of Velcro fasteners is carried out by the investigators before putting them on the patients. The control group is treated with conventional plaster casts for immobilization by a professional plasterer. During follow-up visits in our out-patient clinic, the patient’s comfort is assessed at multiple times using two questionnaires specialized for this purpose. Additionally, several other clinical and radiological endpoints are measured. The first patient feedbacks show a good acceptance and patient comfort in the group with 3D-printed casts with a relatively low price of approximately 6 US\$ per cast. To reduce printing and postprocessing time substantially, we recently started to additionally use a DLP-(Digital Light Processing) printer which results in a price of approximately 20 US\$ per cast.

3.5. Surgical Guides. 3D-printed surgical guides are mostly used for internal fixation of fractures or corrective osteotomy of malunions. These customized guides are usually either prebent/fitted on 3D-printed templates of the malunion and later sterilized [31] or 3D-printed themselves based on a digital model of the malunited bone [32]. The aim is to facilitate the osteotomy based on a preoperatively planned ideal osteotomy location and angle. The desired result is usually based on the contralateral healthy side.

Patient-specific surgical cutting guides have been described for malunions of the distal radius [33–35], for malunions of the diaphyseal area of both forearm bones (with

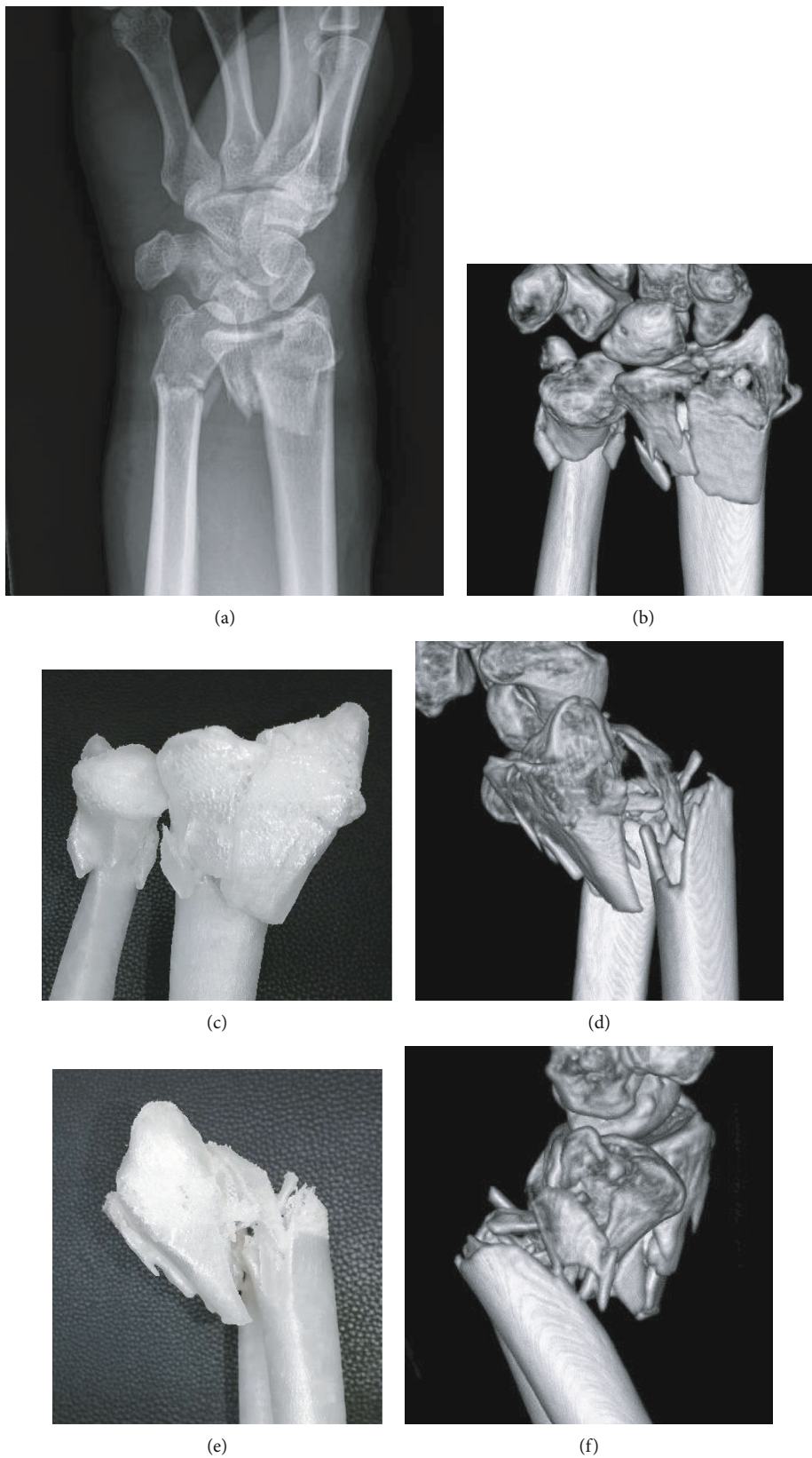


FIGURE 3: Continued.

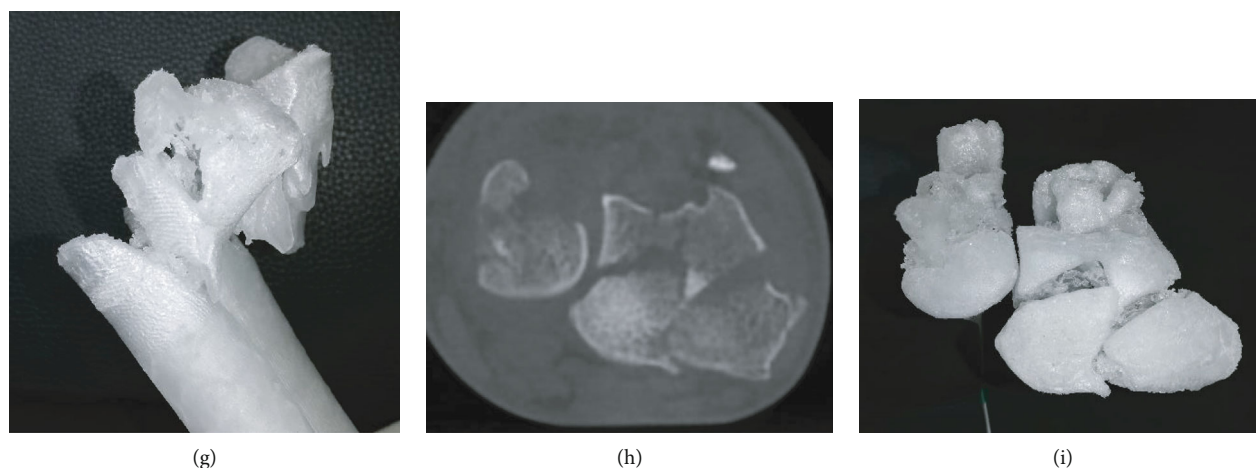


FIGURE 3: (a) Dorsopalmar radiographic view of a displaced, multifragmentary, intra-articular fracture of the distal radius, and ulna of a 45-year-old female. (b, c) Coronal view of the 3D-CT reconstruction and the equivalent view on the 3D-printed Polypropylene-model. (d, e) Sagittal view (radial aspect) of the 3D-CT reconstruction and the equivalent view on the 3D-printed Polypropylene-model. (f, g) Sagittal view (ulnar aspect) of the 3D-CT reconstruction and the equivalent view on the 3D-printed Polypropylene-model. (h, i) Axial CT-projection and the equivalent view on the 3D-printed Polypropylene-model allowing an overview on the intra-articular key fragments of the distal radius fracture.

custom-made fixation plates) [32], and for malunions of the scaphoid [36]. The senior author of this article presented a method using an acrylate Kirschner wire guide in combination with an acrylate wedge template for distal radius malunions which allow to harvest a precisely suitable iliac crest bone graft [37]. In a retrospective assessment of the early clinical outcome, 3D-planned and guided single-cut osteotomies of the forearm proved to be an accurate and reliable method [38].

Customized 3D-printed guides have also been used for osteosynthesis of scaphoid fractures. Yin et al. presented a method using a 3D-printed glove-like patient-specific guiding template to allow 1-shot percutaneous fixation [39]. De Wolf et al. presented another 3D-printed targeting device for scaphoid fractures and were able to show on cadavers that it provides similar accuracy while significantly reducing intraoperative radiation exposure and procedure time [40].

Most of these studies have a descriptive character and lack a control group. A systematic review on three-dimensional virtual planning of corrective osteotomies of distal radius malunions identified the following issues: no clinical study comparing the results of 3D-planning techniques with conventional planning methods could be identified. While the authors highlighted the benefit of 3D-planning, most studies used conventional two-dimensional (2D) radiographs to assess the radiological result of the procedures. This might lead to underestimation of residual deformities. Furthermore, a great heterogeneity of different radius malunions was seen. The authors concluded that no full comprehension of the added value of 3D-planning in distal radius malunion corrective osteotomy can be achieved without randomized controlled trials [41].

3.6. Personalized Implants/Solutions for Bone Defects. Besides orthopaedic aids like personalized splints, the trend for customization has also gained widespread use in the production

of surgical implants. 3D printing technology is well established in the field of plastic and reconstructive surgery, where it is used to fabricate individualized synthetic and biologic implants, regenerative scaffolds, and cell-specific tissues and organs [42]. In craniofacial surgery, the use of patient-specific implants made from polymethylmethacrylate (PMMA) has proven to be cost-effective and applicable in daily clinical practice [43]. Yet again in hand surgery, up to now, there is only a hand full of case reports and feasibility studies on this topic. The printed implants are mostly based on scans of the contralateral healthy side.

In 2017, Kim et al. compared a 3D-printed volar locking distal radius plate fabricated by laser sintering of titanium alloy powder with two conventional volar locking plates. Biomechanical testing showed that the 3D-printed plate had a significantly higher strength than conventional plates, yet the implant was not customized to the bone [44].

Other authors reported a 3D-printed (titanium) replacement of a finger proximal phalanx after recurrence of a giant cell tumor [45] or the replacement of the distal radius with customized, uncemented 3D-printed prostheses (Metal-PE (polyethylene)-combination with hydroxyapatite coating) in 11 patients with giant cell tumors [46]. Both report satisfactory functional outcomes with short-term oncologic salvage. Our own study group was able to replace parts of the proximal phalanx in a patient with a defect-lesion of the index finger after a chainsaw accident with a patient-specific implant. Since an “off the shelf” implant was not a favourable option due to insufficient bone stock a patient-specific 3D-printed partial joint replacement made of titanium was used. The shaft was designed with a porous surface to allow osteointegration (Figure 5). The patient’s range of motion in the proximal interphalangeal joint improved from preoperative 20° to postoperative 60°.

Carpal bones are complex in their anatomy and are at risk for fracture nonunion or avascular necrosis. Surgical

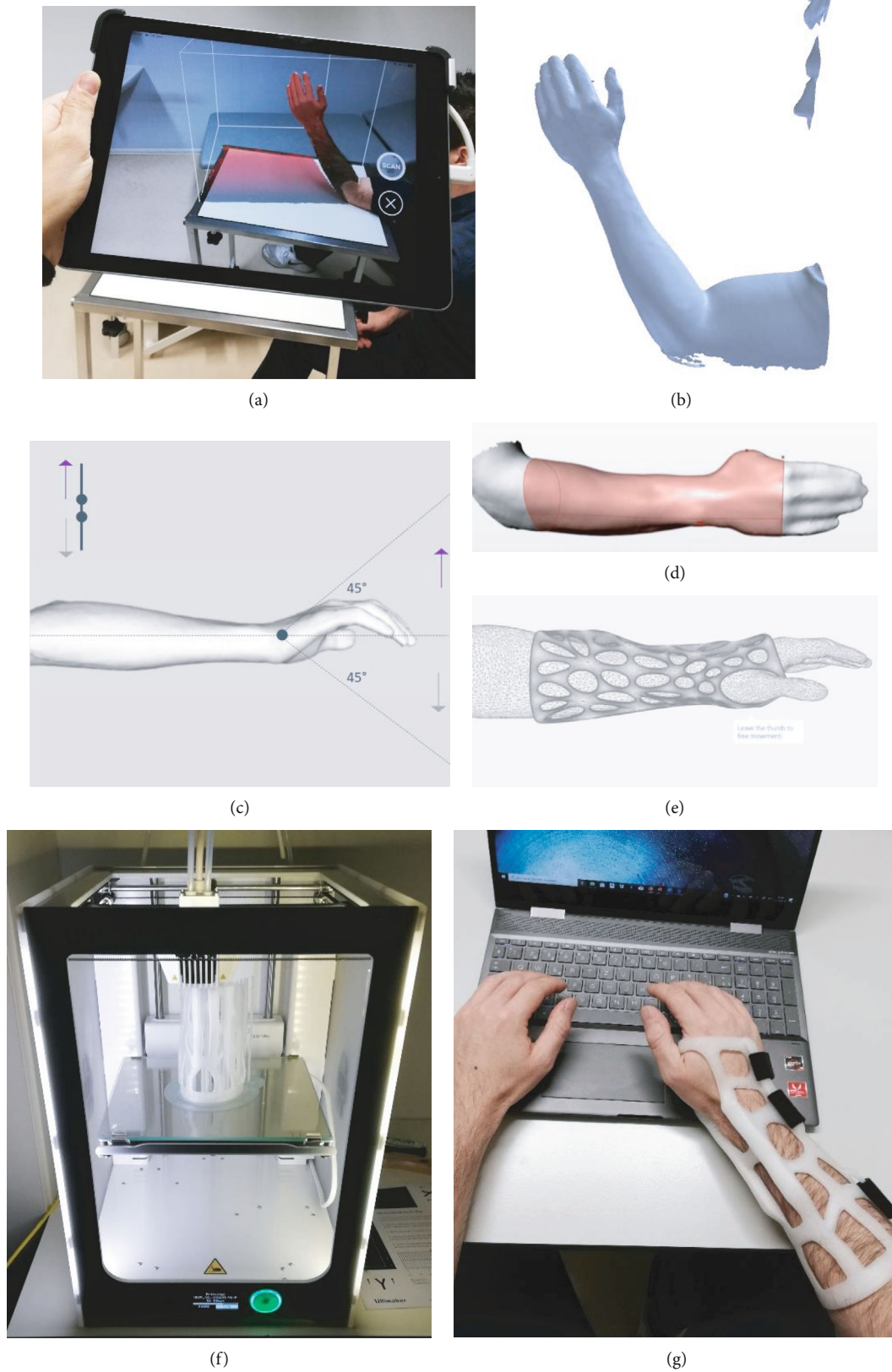


FIGURE 4: (a, b) 3D-scanning of the injured forearm using a tablet with an optical sensor (“Spentys© Point-of-Care Solution”, Spentys SA/NV, Brussel, BE). (c) Virtual adjustment of the wrist position if necessary (d, e) Designing of the forearm cast (“Polycast©” [Spentys SA/NV, Brussels, BE]) and generating an STL-file. (f) In-hospital, overnight printing using an FDM-printer with Polypropylene- (PP-) filament. (g) Fitted customized forearm-cast with ventilation openings and Velcro-Fasteners.



(a)



(b)



(c)

FIGURE 5: Continued.



(d)

FIGURE 5: (a, b) Patient-specific 3D-printed partial joint replacement made of titanium (Xilloc Medical B.V., Sittard-Geleen, ND). (c) The shaft was designed with porous surface to enable osteointegration. (d) Lateral radiographic view of the finger after implantation of the patient-specific implant fitting precisely to the bone defect.

treatment with nonvascularized or vascularized bone grafts is challenging. A prosthetic replacement of those bones could offer an appealing alternative. Xie et al. reported a case of patient-specific replacement of a collapsed lunate in stage IIIc Kienböck's disease. The implantation of a customized 3D-printed polyethylene spacer led to a nearly full range of motion and good pain relief 12 months after surgery [47]. The senior author of this article developed and showed the feasibility of a scaphoid prosthesis 3D-printed of titanium and ceramic and suggested 3D-printed Polyetheretherketon (PEEK) for further use [48, 49].

3.7. Personalized Prosthesis for Amputations. (Partial) hand amputations are a unique entity and more common in developing countries. Providing patients with proper prosthetic replacement is often problematic in these areas. The feasibility of using 3D printing technology to fabricate hand prostheses was shown in several reports [50, 51]. Some authors laid their focus on providing children in developing countries and those with limited access to healthcare providers with reasonable prosthetic hand replacements [52]. Some of the designs were published online as open source files (Figure 6). Alturkistani et al. presented a 3D-printed prosthesis design with manufacturing costs of approximately 20 USD. Functional assessment showed that the prosthesis improved the patient's manual handling capabilities, especially regarding grasp stability [53].

4. Practical Issues

The eventual goal of implementing 3D printing technology in daily hospital routine is to enable mass production of cus-

tomized splints, fracture models, and surgical guides. The workflow should be so efficient that it saves resources compared to conventional techniques. Until now, this goal is difficult to achieve in an in-hospital setting. According to our experience, problems can occur at every step of the process.

Even with intuitive and easy-to-use applications, the use of 3D printing technology requires extensive training for new users. Depending on the used printing technology, safety issues with flammable or potential harmful components need to be addressed. The workspace needs to be equipped with sufficient room, ventilation, stable temperature, and air humidity. Surface scanning devices need to be accessible and charged at any time. Frequently used printers need regular maintenance. Printers with repeated malfunctions need replacement. Software malfunctions or unexpected software updates can lead to delay which is particularly unfavourable if it leads to waiting time for a patient. Patients will show little acceptance for a new technology if it means more waiting time or additional hospital visits. The designing and slicing of 3D-models can either be done by the healthcare professional her/himself or an outside partner (e.g., an industrial partner specialized in 3D printing software). We recommend an interdisciplinary workflow where every medical and non-medical specialist plays out his strength: the course of action is initiated by the surgeon with the request for a particular application, a radiologist should be responsible for acquisition and formatting of image data, a medical engineer should oversee the 3D-design process and printing and an occupational therapist should handle the fitting and postprocessing. With third parties involved, there are issues concerning data protection (location of the server storing patient data),

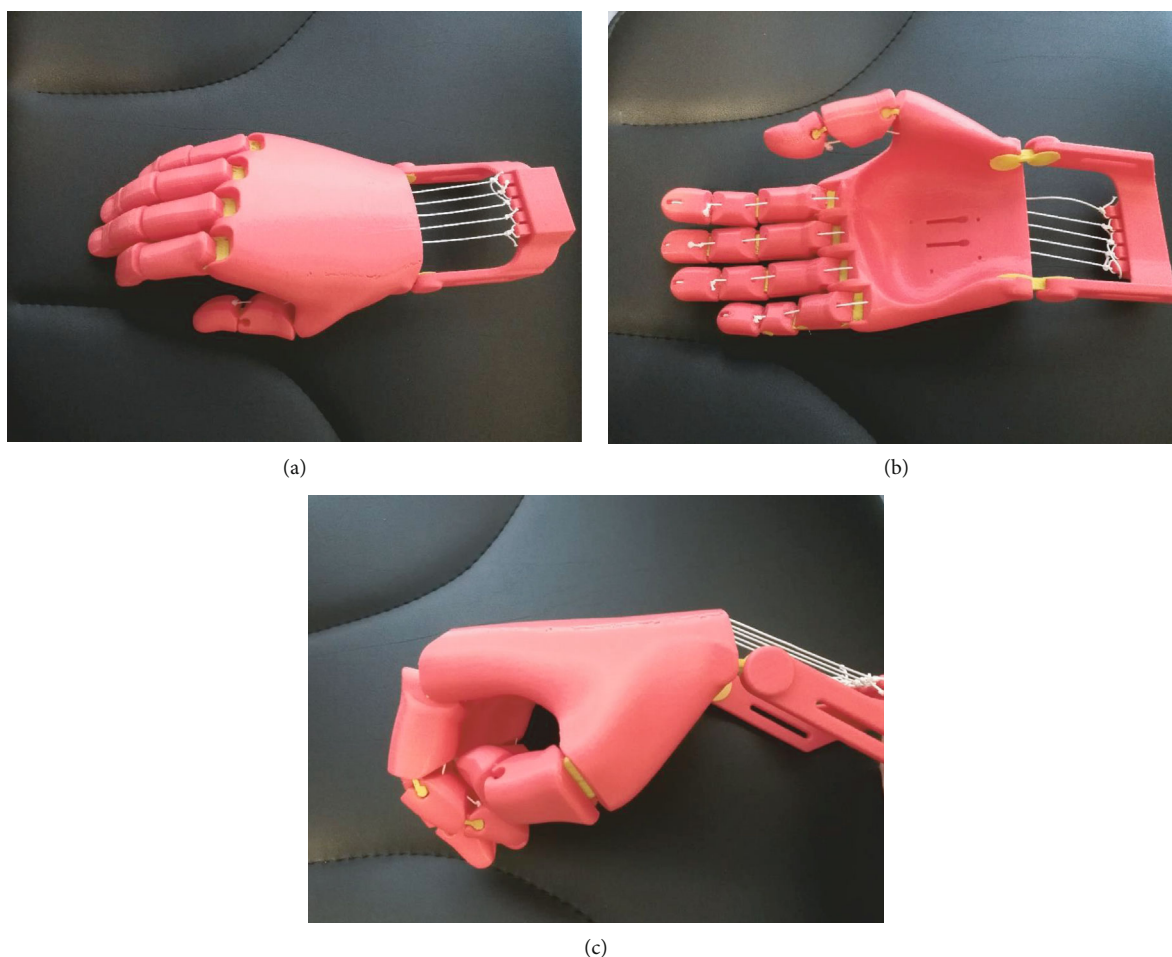


FIGURE 6: (a–c) “Flexy Hand 2”, a 3D-printed open source hand prosthesis (<http://enablingthefuture.org/upper-limb-prosthetics/the-flexy-hand/>).

financial relationship, and workflow efficiency (the fewer institutions involved the faster the process) that have to be settled.

Prior to the commercialization of a drug or medical device in the United States, FDA-clearance is required. To be referred as “FDA-Approved,” the manufacturer needs to prove substantial equivalence to a predicate device. This means that the performance and intended use of the new device is similar to a previously cleared device. To demonstrate effectiveness, often clinical data are needed which can be a considerable hurdle for manufacturers. In 2017, the FDA published the guidance document “Technical Considerations for Additive Manufactured Medical Devices” which provides information for manufacturers when working on a 3D-printed medical device regarding regulatory and quality assurance control [54, 55]. In Europe, the certification of medical devices needs to follow the European Union Medical Device Regulation (Council Regulation 2017/745 of 5 April 2017 concerning medical devices) which applies in all countries of the European union [56]. Additionally, these supranational regulations also local regulations (e.g., Non-EU countries in Europe) need to be taken into account. We recommend not only the certification of the actual 3D-printed products but also certification of the manufacturing process

through a third party. This will facilitate the expansion of applications and scaling of the project once effectiveness has been proven [57].

Postprocessing of splints or 3D-models requires specialized tools and can be very time-consuming. It needs to be planned carefully so it does not prolong the patient’s outpatient clinic visit. Furthermore, it is important to plan a sufficient interval until the next visit of the patient to allow an additional printing attempt in case of failure of the first print. With FDM being the most common technology, this can mean an additional day.

3D-scans of tissue depict a snapshot at one certain moment of time. Increasing or decreasing soft tissue swelling, secondary dislocation of bones or other changes needs to be taken into account using customized splints (e.g., using PP that can be heated and adapted) or surgical guides based on skin or bone surface.

Another relevant potential problem is patient malcompliance. Since 3D-printed splints are mostly removable, there is an increased risk that the patient removes the splint deliberately during the immobilization period. This occurs less frequently using traditional circular plaster casts.

All of the abovementioned issues cause a significant amount of personnel and financial expenses which can

initially be overwhelming compared to using conventional technologies. In our opinion, the efficiency can be maximized by conducting as many substeps as possible in-hospital, even if it requires substantial financial investments in the beginning. The workflow should be tested extensively and used on patients only when its stability is proved to guarantee good treatment quality.

5. Conclusion

Although the history of 3D printing technology is nearly 40 years old, its use is not yet well established in hand surgery compared to other medical subspecialties like craniomaxillofacial surgery or dentistry. Only in the last few years, interest among hand surgeons and the 3D printing industry has risen and intensive research has been initiated. Possible reasons for this delay are the following: in the eyes of the industry, hand surgery was not known to be a lucrative business investment. Hand surgeons relied on conventional proven products in their daily routine and did not see a significant potential benefit of the 3D printing technology for their work. With the general interest focussing more and more on patient-specific or personalized treatment, 3D printing became increasingly interesting for hand surgeons.

However, research on its use in hand surgery is still scarce. Up to now, complicated digital design software, lengthy and error-prone printing processes and expensive hardware were factors that inhibited a major widespread of 3D printing in daily routine. The idea that one person should be able to perform all substeps of the process, which require profound skills in different areas, might be another reason. For a successful implementation of 3D printing in daily routine, we therefore recommend the involvement of different medical and nonmedical specialists throughout the process. With today's complexity of digital design software programs, we found it to be most efficient to outsource the digital designing to closely collaborating medical engineers. At least with applications, where no complete automation is possible yet. In order to increase efficiency, postprocessing of printed objects can be handled by hand therapists, who often have more expertise in this area compared to hand surgeons.

The technical foundations for future applications such as bioprinting (replacement of tissue defects), in-hospital, or even in-OR implant-printing on demand are mostly known today. But due to missing clinical proof of effectiveness, governmental regulations, and too expensive and elaborate printing processes and materials their implementation in daily hand surgery routine is currently far from realistic. By simplifying workflows and reducing production costs, we believe that in the near future 3D printing technology can add a significant value to hand surgery.

Data Availability

Readers can access any data underlying the findings of this research article by contacting the authors.

Conflicts of Interest

The senior author has an honorary-based consultant function at the company Medartis AG, Basel, Switzerland. Our research group is supported by the company Spentys© (Spentys SA/NV, Brussels, BE) with printing materials and technical support.

References

- [1] H. Kodama, "A scheme for three-dimensional display by automatic fabrication of three-dimensional model," *IEICE Transactions on Electronics*, vol. J64-C, pp. 237–241, 1981.
- [2] C. Hull, "Apparatus for production of three-dimensional objects by stereolithography," 1986, US Patent 638905.
- [3] V. Matter-Parrat and P. Liverneaux, "3D printing in hand surgery," *Hand Surgery and Rehabilitation*, vol. 38, no. 6, pp. 338–347, 2019.
- [4] S. Negi, S. Dhiman, and R. Kumar Sharma, "Basics and applications of rapid prototyping medical models," *Rapid Prototyping Journal*, vol. 20, no. 3, pp. 256–267, 2014.
- [5] M. Javaid and A. Haleem, "Additive manufacturing applications in orthopaedics: a review," *Journal of Clinical Orthopaedics and Trauma*, vol. 9, no. 3, pp. 202–206, 2018.
- [6] B. Langridge, S. Momin, B. Coumbe, E. Woin, M. Griffin, and P. Butler, "Systematic review of the use of 3-dimensional printing in surgical teaching and assessment," *Journal of Surgical Education*, vol. 75, no. 1, pp. 209–221, 2018.
- [7] Y. AbouHashem, M. Dayal, S. Savanah, and G. Štrkalj, "The application of 3D printing in anatomy education," *Medical Education Online*, vol. 20, no. 1, article 29847, 2015.
- [8] Z. Huang, W. Song, Y. Zhang et al., "Three-dimensional printing model improves morphological understanding in acetabular fracture learning: a multicenter, randomized, controlled study," *PLoS One*, vol. 13, no. 1, article e0191328, 2018.
- [9] A. Wu, K. Wang, J. Wang et al., "The addition of 3D printed models to enhance the teaching and learning of bone spatial anatomy and fractures for undergraduate students: a randomized controlled study," *Annals of Translational Medicine*, vol. 6, no. 20, p. 403, 2018.
- [10] P. Lazarus, E. Pire, C. Sapa et al., "Design and evaluation of a new synthetic wrist procedural simulator (Wristsim[®]) for training of distal radius fracture fixation by volar plating," *Hand Surgery and Rehabilitation*, vol. 36, no. 4, pp. 275–280, 2017.
- [11] I. Naroura, J. J. Hidalgo Diaz, F. Xavier et al., "Teaching of distal radius shortening osteotomy: three-dimensional procedural simulator versus bone procedural simulator," *The Journal of Hand Surgery, European Volume*, vol. 43, no. 9, pp. 961–966, 2018.
- [12] C. Chen, L. Cai, C. Zhang, J. Wang, X. Guo, and Y. Zhou, "Treatment of die-punch fractures with 3D printing technology," *Journal of Investigative Surgery*, vol. 31, no. 5, pp. 385–392, 2017.
- [13] P. S. Corona, M. Vicente, K. Tetsworth, and V. Glatt, "Preliminary results using patient-specific 3d printed models to improve preoperative planning for correction of post-traumatic tibial deformities with circular frames," *Injury*, vol. 49, Suppl 2, pp. S51–S59, 2018.
- [14] L. Xie, C. Chen, Y. Zhang, W. Zhong, H. Chen, and L. Cai, "Three-dimensional printing assisted ORIF versus

- conventional ORIF for Tibial plateau fractures: a systematic review and meta-analysis," *International Journal of Surgery*, vol. 57, pp. 35–44, 2018.
- [15] N. Bizzotto, I. Tami, A. Tami et al., "3D printed models of distal radius fractures," *Injury*, vol. 47, no. 4, pp. 976–978, 2016.
- [16] L. Kong, G. Yang, J. Yu et al., "Surgical treatment of intra-articular distal radius fractures with the assistance of three-dimensional printing technique," *Medicine*, vol. 99, no. 8, article e19259, 2020.
- [17] N. Jew, J. D. Lipman, and M. G. Carlson, "The use of three-dimensional printing for complex scaphoid fractures," *The Journal of Hand Surgery*, vol. 44, no. 2, pp. 165.e1–165.e6, 2019.
- [18] M. Keller, T. Kastenberger, A. F. Anoar et al., "Clinical and radiological results of the vascularized medial femoral condyle graft for scaphoid non-union," *Archives of Orthopaedic and Trauma Surgery*, vol. 140, no. 6, pp. 835–842, 2020.
- [19] M. T. Houdek, J. M. Matsumoto, J. M. Morris, A. T. Bishop, and A. Y. Shin, "Technique for 3-dimensional (3D) modeling of osteoarticular medial femoral condyle vascularized grafting to replace the proximal pole of unsalvageable scaphoid non-unions," *Techniques in Hand & Upper Extremity Surgery*, vol. 20, no. 3, pp. 117–124, 2016.
- [20] E. M. Taylor and M. L. Iorio, "Surgeon-based 3D printing for microvascular bone flaps," *Journal of Reconstructive Microsurgery*, vol. 33, no. 6, pp. 441–445, 2017.
- [21] B. Msallem, N. Sharma, S. Cao, F. S. Halbeisen, H. F. Zeilhofer, and F. M. Thieringer, "Evaluation of the dimensional accuracy of 3D-printed anatomical mandibular models using FFF, SLA, SLS, MJ, and BJ printing technology," *Journal of Clinical Medicine*, vol. 9, no. 3, p. 817, 2020.
- [22] G. R. Sigron, N. Rüedi, F. Chammartin et al., "Three-dimensional analysis of isolated orbital floor fractures pre- and post-reconstruction with standard titanium meshes and "hybrid" patient-specific implants," *Journal of Clinical Medicine*, vol. 9, no. 5, article E1579, p. 1579, 2020.
- [23] P. Hoogervorst, R. Knox, K. Tanaka et al., "A biomechanical comparison of fiberglass casts and 3-dimensional-printed, open-latticed, ventilated casts," *Hand*, vol. 15, no. 6, pp. 842–849, 2020.
- [24] A. Cazon, S. Kelly, A. M. Paterson, R. J. Bibb, and R. I. Campbell, "Analysis and comparison of wrist splint designs using the finite element method: multi-material three-dimensional printing compared to typical existing practice with thermoplastics," *Proceedings of the Institution of Mechanical Engineers. Part H*, vol. 231, no. 9, pp. 881–897, 2017.
- [25] Y. J. Chen, H. Lin, X. Zhang, W. Huang, L. Shi, and D. Wang, "Application of 3D-printed and patient-specific cast for the treatment of distal radius fractures: Initial Experience," *3D Printing in Medicine*, vol. 3, no. 1, p. 11, 2017.
- [26] J. Graham, M. Wang, K. Frizzell, C. Watkins, P. Beredjikian, and M. Rivlin, "Conventional vs 3-dimensional printed cast wear comfort," *Hand*, vol. 15, no. 3, pp. 388–392, 2020.
- [27] H. Lin, L. Shi, and D. Wang, "A Rapid and intelligent designing technique for patient-specific and 3D-printed orthopedic cast," *3D Printing in Medicine*, vol. 2, no. 1, 2016.
- [28] J. Li and H. Tanaka, "Rapid customization system for 3D-printed splint using programmable modeling technique - a practical approach," *3D Printing in Medicine*, vol. 4, no. 1, p. 5, 2018.
- [29] C. Kienzle and M. Schäfer, *Integration of additive manufacturing processes (3D Printing) in orthopaedic technology fitting routine*, Verlag Orthopädie-Technik, Dortmund, 2018.
- [30] H. S. Nam, C. H. Seo, S. Y. Joo, D. H. Kim, and D. S. Park, "The application of three-dimensional printed finger splints for post hand burn patients: a case series investigation," *Annals of Rehabilitation Medicine*, vol. 42, no. 4, pp. 634–638, 2018.
- [31] Y. Hamada, H. Gotani, K. Sasaki, Y. Tanaka, H. Egawa, and T. Kanchanathepsak, "Corrective osteotomy of malunited diaphyseal fractures of the forearm simplified using 3-dimensional CT data: proposal of our simple strategy through case presentation," *Hand*, vol. 12, no. 5, pp. NP95–NP98, 2017.
- [32] A. M. Byrne, B. Impelmans, V. Bertrand, A. van Haver, and F. Verstreken, "Corrective osteotomy for malunited diaphyseal forearm fractures using preoperative 3-dimensional planning and patient-specific surgical guides and implants," *The Journal of Hand Surgery*, vol. 42, no. 10, pp. 836.e1–836.e12, 2017.
- [33] A. Schweizer, P. Fürnstahl, and L. Nagy, "Three-dimensional correction of distal radius intra-articular malunions using patient-specific drill guides," *The Journal of Hand Surgery*, vol. 38, no. 12, pp. 2339–2347, 2013.
- [34] M. Kunz, B. Ma, J. F. Rudan, R. E. Ellis, and D. R. Pichora, "Image-guided distal radius osteotomy using patient-specific instrument guides," *The Journal of Hand Surgery*, vol. 38, no. 8, pp. 1618–1624, 2013.
- [35] S. Roner, F. Carrillo, L. Vlachopoulos, A. Schweizer, L. Nagy, and P. Fürnstahl, "Improving accuracy of opening-wedge osteotomies of distal radius using a patient-specific ramp-guide technique," *BMC Musculoskeletal Disorders*, vol. 19, no. 1, p. 374, 2018.
- [36] A. Schweizer, F. Mauler, L. Vlachopoulos, L. Nagy, and P. Fürnstahl, "Computer-assisted 3-dimensional reconstructions of scaphoid fractures and nonunions with and without the use of patient-specific guides: early clinical outcomes and postoperative assessments of reconstruction accuracy," *The Journal of Hand Surgery*, vol. 41, no. 1, pp. 59–69, 2016.
- [37] P. Honigmann, F. Thieringer, R. Steiger, M. Haefeli, R. Schumacher, and J. A. Henning, "A Simple 3-Dimensional Printed Aid for a Corrective Palmar Opening Wedge Osteotomy of the Distal Radius," *The Journal of Hand Surgery*, vol. 41, no. 3, pp. 464–469, 2016.
- [38] S. Roner, L. Vlachopoulos, L. Nagy, A. Schweizer, and P. Fürnstahl, "Accuracy and early clinical outcome of 3-dimensional planned and guided single-cut osteotomies of malunited forearm bones," *The Journal of Hand Surgery*, vol. 42, no. 12, pp. 1031.e1–1031.e8, 2017.
- [39] H. Yin, J. Xu, and W. Xu, "3-Dimensional Printing-Assisted Percutaneous Fixation for Acute Scaphoid Fracture: 1-Shot Procedure," *The Journal of Hand Surgery*, vol. 42, no. 4, pp. 301.e1–301.e5, 2017.
- [40] M. C. DeWolf, A. Hartov, T. A. Fortney, and L. G. Warhold, "Three-dimensional printed targeting device for scaphoid fracture fixation," *Hand*, 2020.
- [41] R. J. O. de Muinck Keizer, K. M. Lechner, M. A. M. Mulders, N. W. L. Schep, D. Eygendaal, and J. C. Goslings, "Three-dimensional virtual planning of corrective osteotomies of distal radius malunions: a systematic review and meta-analysis," *Strategies in Trauma and Limb Reconstruction*, vol. 12, no. 2, pp. 77–89, 2017.
- [42] A. J. Bauermeister, A. Zuriarrain, and M. I. Newman, "Three-dimensional printing in plastic and reconstructive surgery: a

- systematic review,” *Annals of Plastic Surgery*, vol. 77, no. 5, pp. 569–576, 2016.
- [43] D. Chamo, B. Msallem, N. Sharma, S. Aghlmandi, C. Kunz, and F. M. Thieringer, “Accuracy assessment of molded, patient-specific polymethylmethacrylate craniofacial implants compared to their 3D printed originals,” *Journal of Clinical Medicine*, vol. 9, no. 3, p. 832, 2020.
- [44] S. J. Kim, Y. H. Jo, W. S. Choi et al., “Biomechanical properties of 3-dimensional printed volar locking distal radius plate: comparison with conventional volar locking plate,” *The Journal of Hand Surgery*, vol. 42, no. 9, pp. 747.e1–747.e6, 2017.
- [45] G. Beltrami, “Custom 3D-printed finger proximal phalanx as salvage of limb function after aggressive recurrence of giant cell tumour,” *BMJ Case Reports*, no. article bcr2018226007, 2018.
- [46] M. Lu, L. Min, C. Xiao et al., “Uncemented three-dimensional-printed prosthetic replacement for giant cell tumor of distal radius: a new design of prosthesis and surgical techniques,” *Cancer Management and Research*, vol. Volume 10, pp. 265–277, 2018.
- [47] M. M. Xie, K. L. Tang, and C. S. Yuan, “3D printing lunate prosthesis for stage IIIc Kienböck’s disease: a case report,” *Archives of Orthopaedic and Trauma Surgery*, vol. 138, no. 4, pp. 447–451, 2018.
- [48] P. Honigmann, N. Sharma, B. Okolo, U. Popp, B. Msallem, and F. M. Thieringer, “Patient-specific surgical implants made of 3D printed PEEK: material, technology, and scope of surgical application,” *BioMed Research International*, vol. 2018, Article ID 4520636, 8 pages, 2018.
- [49] P. Honigmann, R. Schumacher, R. Marek, F. Büttner, F. Thieringer, and M. Haefeli, “A three-dimensional printed patient-specific scaphoid replacement: a cadaveric study,” *The Journal of Hand Surgery, European Volume*, vol. 43, no. 4, pp. 407–412, 2018.
- [50] M. B. Burn, A. Ta, and G. R. Gogola, “Three-dimensional printing of prosthetic hands for children,” *The Journal of Hand Surgery*, vol. 41, no. 5, pp. e103–e109, 2016.
- [51] M. Yoshikawa, R. Sato, T. Higashihara, T. Ogasawara, and N. Kawashima, “Rehand: realistic electric prosthetic hand created with a 3D printer,” in *Conference Proceedings: Annual International Conference of the IEEE Engineering in Medicine and Biology Society*, pp. 2470–2473, Milan, Italy, Aug 2015.
- [52] J. Zuniga, D. Katsavelis, J. Peck et al., “Cyborg beast: a low-cost 3d-printed prosthetic hand for children with upper-limb differences,” *BMC Research Notes*, vol. 8, no. 1, p. 10, 2015.
- [53] R. Alturkistani, K. A. S. Devasahayam et al., “Affordable passive 3D-printed prosthesis for persons with partial hand amputation,” *Prosthetics and Orthotics International*, vol. 44, no. 2, pp. 92–98, 2020.
- [54] J. D’Alessio and A. Christensen, “Chapter 7-3D printing for commercial orthopedic applications: advances and challenges,” in *3D Printing in Orthopaedic Surgery*, pp. 65–83, Elsevier B.V., 2019.
- [55] FDA, *Technical Considerations for Additive Manufactured Medical Devices, Guidance for Industry and FDA Staff* <https://www.fda.gov/downloads/MedicalDevices/DeviceRegulationandGuidance/GuidanceDocuments/UCM499809.pdf>.
- [56] European Union Medical Device Regulation (Council Regulation 2017/745 of 5 April 2017 concerning medical devices), <https://eur-lex.europa.eu/legal-content/EN/TXT/?uri=CELEX:32017R0745>.
- [57] J. Graham and J. Peck, “Chapter 17 FDA Regulation of Polyaryletheretherketone Implants,” in *PEEK Biomaterials Handbook*, pp. 431–445, William Andrew Publishing, 2019.

Research Article

Application of Mixed Reality Using Optical See-Through Head-Mounted Displays in Transforaminal Percutaneous Endoscopic Lumbar Discectomy

Xiaoyang Liu,¹ Jianmin Sun,¹ Meimei Zheng,² and Xingang Cui¹

¹Department of Spine, Shandong Provincial Hospital Affiliated to Shandong First Medical University, Shandong Provincial Hospital Affiliated to Shandong University, Jinan, China

²Department of Neurology, The First Affiliated Hospital of Shandong First Medical University, Jinan, China

Correspondence should be addressed to Xingang Cui; spine2014@163.com

Received 9 July 2020; Revised 17 January 2021; Accepted 30 January 2021; Published 16 February 2021

Academic Editor: Hyuk-Soo Han

Copyright © 2021 Xiaoyang Liu et al. This is an open access article distributed under the Creative Commons Attribution License, which permits unrestricted use, distribution, and reproduction in any medium, provided the original work is properly cited.

Purpose. Mixed reality (MixR) technology merges the real and virtual worlds to produce new environments and visualizations; it is being tested for numerous minimally invasive surgical procedures. This study is aimed at evaluating the use of MixR technology using optical see-through head-mounted displays (OST-HMDs) during transforaminal percutaneous endoscopic discectomy (TPED). **Methods.** Forty-four patients treated with MixR-assisted TPED through OST-HMDs were compared with matched patients treated with conventional TPED ($n = 43$). In the MixR-assisted TPED group, MixR technology was used to navigate the four procedures of marking, needle insertion, foraminoplasty, and positioning of the working sheath. The clinical outcomes were evaluated based on the numerical rating scale (NRS) scores and Oswestry Disability Index (ODI) on preoperative and postoperative day 1 and at the last follow-up examination. The procedural times, radiation exposure, and eye fatigue were also recorded. All patients were followed up for at least 6 months. **Results.** The NRS scores and ODI were significantly improved in both groups at the last follow-up visit compared with the preoperative values ($P < 0.05$); these values were not statistically different between the groups. The operation time and radiation exposure during marking, needle insertion, and total procedure significantly decreased in the MixR-assisted TPED group compared to those in the conventional TPED group ($P < 0.05$). Unfortunately, the incidence of eye fatigue increased owing to the use of OST-HMDs in the MixR-assisted TPED group. **Conclusion.** This study shows the utility of MixR technology for image guidance in conventional TPED. Radiation exposure is decreased, and this technology serves as a valuable tool during the TPED procedure; however, the assistance of conventional fluoroscopy is still required.

1. Introduction

Transforaminal percutaneous endoscopic discectomy (TPED) is a typical minimally invasive discectomy procedure. Precise puncture and cannulation are significant steps in TPED, and the achievement of precise puncture and cannulation depends on the surgeon's experience and fluoroscopic guidance [1]. Thus, the surgical process of TPED is reported to have a steep learning curve and involves radiation exposure [2]. Increased radiation exposure may be associated with potential radiation-induced adverse events [3]. Therefore, it is impor-

tant to reduce the radiation dose of practitioners to minimize the risk of potential radiation-induced complications.

Virtual reality has proven to be feasible in TPED. It enables precise surgical planning and improves intraoperative procedures; therefore, it has the potential for application in clinical practice [4]. Mixed reality (MixR) technology is the merging of real and virtual worlds to create new environments and visualizations where the physical and digital objects coexist and interact in real time [5, 6]. Optical see-through head-mounted displays (OST-HMDs) with high resolution and high contrast capabilities offer real-time MixR

visualization of radiographic images that can be projected over the interventional site without hampering direct control of procedural manipulations [7]. MixR devices have been tested in image-guided minimally invasive surgical procedures [6, 7]. It is speculated that MixR technology may improve the surgical experience, shorten the operating time, and decrease the adverse effects of TPED. Unfortunately, MixR through OST-HMDs has not been introduced in TPED. Herein, we attempt to introduce and determine the utility of MixR navigation during the conventional TPED procedure.

2. Material and Methods

2.1. Patients. This comparative study was approved by the ethics committee of a university hospital and was conducted in accordance with the guidelines of the Declaration of Helsinki. Written informed consent was obtained from each participant. From June 2018 to July 2019, 44 patients with lumbar disc herniation, who had failed to respond to conservative treatment for more than 6 weeks, were treated with MixR-assisted TPED. Another 43 patients were selected from a clinical database between February 2018 and June 2019, according to their demographic characteristics and disease-related features to ensure comparability between the two groups; these patients were treated with conventional TPED. The inclusion criteria were as follows: (1) radicular leg pain due to lumbar disc herniation confirmed through magnetic resonance imaging and (2) TPED at a single level. The exclusion criteria were as follows: (1) segmental instability, (2) lumbar spinal stenosis, (3) calcified disc herniation, (4) recurrent lumbar disc herniation, (5) painless weakness, and (6) TPED at multiple levels. All patients were followed up for at least 6 months, with an average of 12 months.

2.2. 3D Virtual Model Reconstruction and Working Plan. The patient with the diagnosis of lumbar disc herniation confirmed using magnetic resonance imaging was positioned in the prone position on a hard sponge cushion for the lumbar computed tomography (CT) examination preoperatively (Figure 1(a)). While referring to the anteroposterior radiograph, six steel balls with a diameter of 2.5 mm were attached to the skin, close to the surface projections of the S1 and L2 spinous processes, both posterior superior iliac spines, and both transverse tips of the fourth lumbar vertebra (Figure 1(b)). The CT images were acquired using a 64-row CT scanner (Siemens Healthineers, Erlangen, Germany) set at 120 kVp or 140 kVp with an adaptive tube load of 200–300 mAs, depending on the patients' weight and size. After the CT examination, all markers were labeled on the skin and then removed. The original DICOM data were input into Mimics software version 20.0 (Interactive Medical Image Control System, Materialise, Leuven, Belgium) and reconstructed into the 3D virtual model. The soft tissues, vertebrae, discs, nerves, and markers were extracted and colored using the threshold, mask, region growth, and other embedded tools. The puncture target was determined from the preoperative radiographic evaluations. If foraminoplasty was required,

the superior articular process of the inferior lumbar vertebra was considered the puncture target. Otherwise, the ruptured disc served as the puncture target. The models of the needle and working sheath were created and placed on the preoperative model (Figures 1(c)–1(f)).

2.3. Building a MixR Environment. The Microsoft HoloLens using a Windows Holographic platform under the native Windows 10 operating system was connected to a local area wireless network [8]. The integrated 3D virtual model was loaded into the Scene Editing System (Midivi, Changzhou, China, <https://www.midivi.cn>). All elements were defined by different colors and transparencies, aimed at optimal visualization. The final 3D model was then exported and loaded into the MixR system (Midivi, Changzhou, China, <https://www.midivi.cn>) on a computer for processing and uploading into the local network. The OST-HMD (HoloLens 2, Microsoft Corporation, State of Washington, USA) loaded the data and displayed the 3D virtual model. The operators could simultaneously visualize the 3D model, working plan, and procedural site in a MixR environment.

2.4. MixR-Assisted TPED Technique. The patient was positioned in the prone position on a radiolucent table. During the surgery, the 3D model was preliminarily integrated into the corresponding patient's body according to the external markers (Figures 2(a) and 2(b)). Standard anteroposterior and lateral views obtained with X-ray fluoroscopy were used to identify the superficial positions of the anatomical structures, and the precision of matching between the virtual model and the patient was assessed. The middle of the superior endplate and the superior facet process of the inferior vertebra were the most valuable anatomical landmarks (Figures 2(c) and 2(d)). If an unacceptable misalignment (≥ 5 mm) was present, the registration procedure was further optimized by incorporating the external and internal anatomical landmarks till an acceptable misalignment (< 5 mm) was achieved [9]. Referring to the precisely matched virtual model in the MixR environment, the spinal level, midline, skin entry point, and puncture direction were marked on the skin. Needle insertion, foraminoplasty, and positioning of the working sheath were performed according to the preoperative plan under the guidance of MixR technology (Figure 3). The final positions of the spinal needle and working sheath were confirmed with fluoroscopy (Figure 4). Once the proper positioning of the working sheath was confirmed, endoscopic discectomy was performed after removing the OST-HMD.

2.5. Assessment of the Clinical Outcomes. For each patient, the demographic and disease-related data was collected from the medical records, including age, sex, body mass index (BMI), type of disc herniation, and surgical level; these data were also used to enroll patients into the matched conventional TPED group. The clinical outcomes were evaluated using the MacNab standard (excellent, good, fair, or poor) at the last follow-up examination [10]. A numerical rating scale (NRS) was used to assess the severity of leg or back pain preoperatively, on postoperative day 1, and at the last follow-up

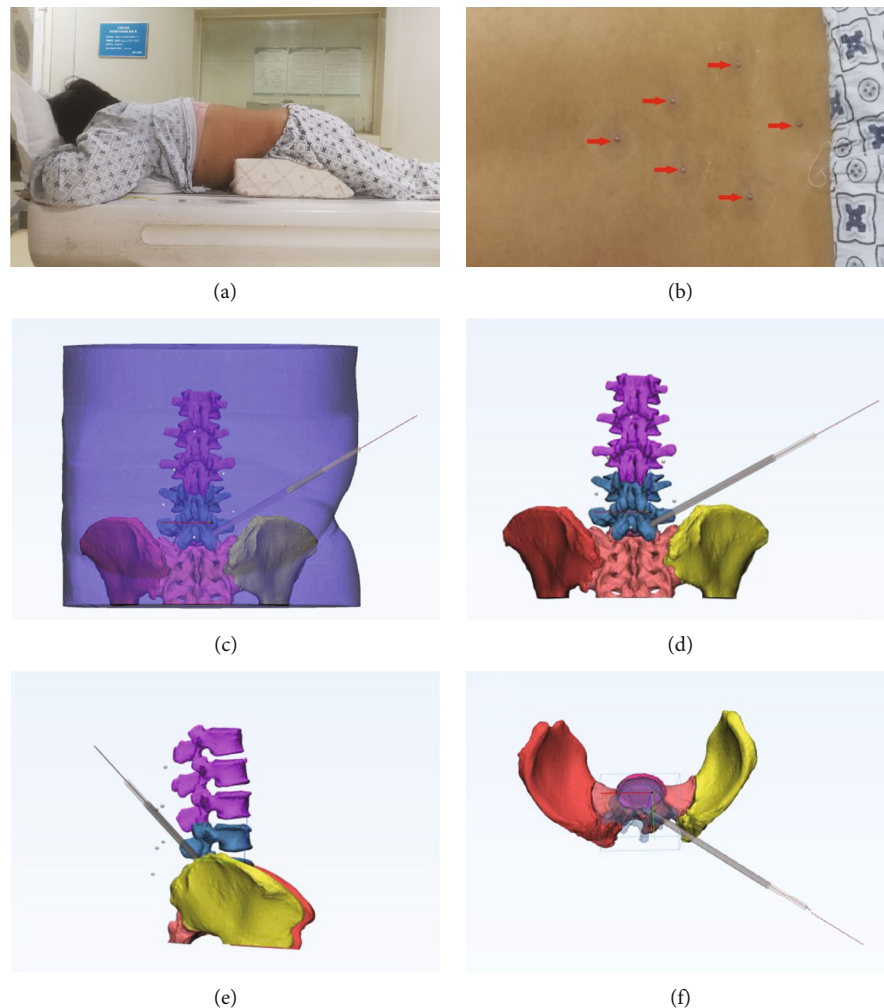


FIGURE 1: Computed tomography (CT) examination and reconstruction of the three-dimensional (3D) model. (a) Flexion position during lumbar CT examination in which the patient was positioned in the prone position on a hard sponge cushion. (b) External landmarks (red arrows) attached to the skin around the surgical segment during the CT examination; these landmarks were used for preliminary matching. (c–f) 3D model reconstructed from the CT data.

examination [11]. Furthermore, the Oswestry Disability Index (ODI) was used to evaluate the disability status [12]. The minimally important clinical difference (MICD) was defined as 3 for the NRS and 10% for the ODI. Exposure duration, from positioning to final fluoroscopy, and procedural duration, from the time of administration of local anesthesia to the end of the operation, were recorded and compared between the two groups.

2.6. Radiation Dose Measurement and Data Collection. The same surgeon performed all the procedures using a G-arm fluoroscope (Whale Healthcare, Beijing, China). The fluoroscopy time, tube voltage (TV), tube current (TC), and radiation dose for the anteroposterior and lateral views were directly read on G-arm fluoroscopy. The exposure duration was recorded in minutes.

2.7. Eye Fatigue Test. The operators completed the eye fatigue test before and after each operation. The eye fatigue test measured subjective fatigue from 0 to 7 points for tired eyes, sore

or aching eyes, irritated eyes, dry eyes, eyestrain, hot or burning eyes, blurred vision, difficulty in focusing, and visual discomfort [13]. In addition, headache, dizziness, nausea, and decreased concentration were evaluated.

2.8. Statistical Analysis. Statistical analysis was performed using SPSS for Windows, version 20.0 (IBM Corp., Armonk, NY, USA). The continuous variables are expressed as the mean \pm standard deviation (SD). For all patients, the NRS and ODI scores were compared preoperatively and postoperatively using paired *t*-tests. The two groups were compared using *t*-tests. $P < 0.05$ was considered statistically significant.

3. Results

3.1. General Information. There was no significant difference between the two groups with respect to the baseline parameters, including age, sex, BMI, and types and levels of disc herniation. The detailed information is listed in Table 1. Surgery was successfully completed for all patients, without dural

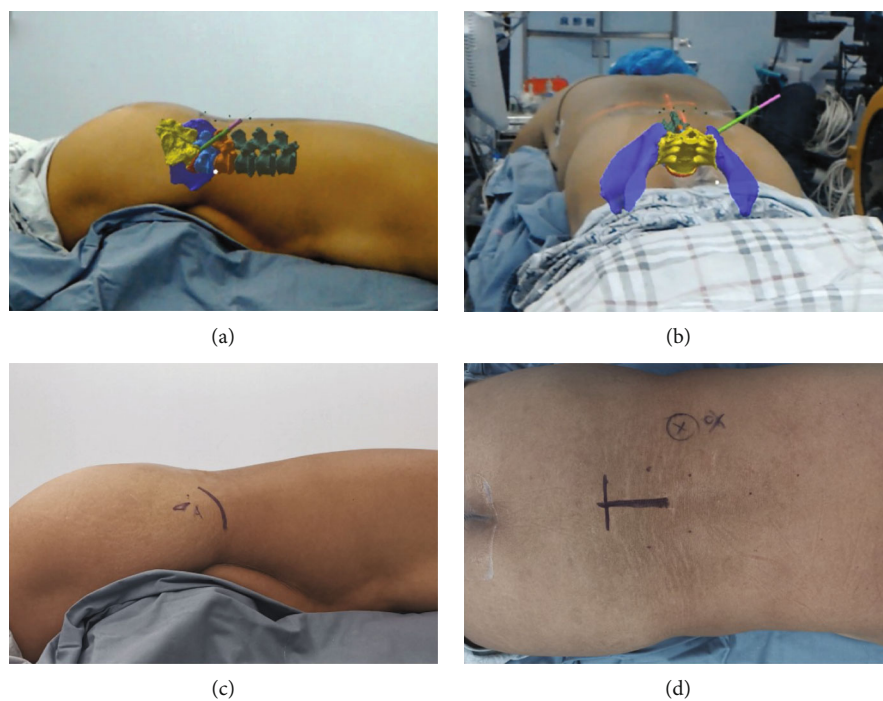


FIGURE 2: Integration of the three-dimensional (3D) model in the patient's body according to the external markers and internal anatomical landmarks. (a, b) The 3D model is matched with the patient's body from different directions. (c, d) Specific internal anatomical landmarks, such as the superior facet process of dorsal vertebra and the middle of the superior endplate, are identified by fluoroscopy and are used for matching with the 3D model.

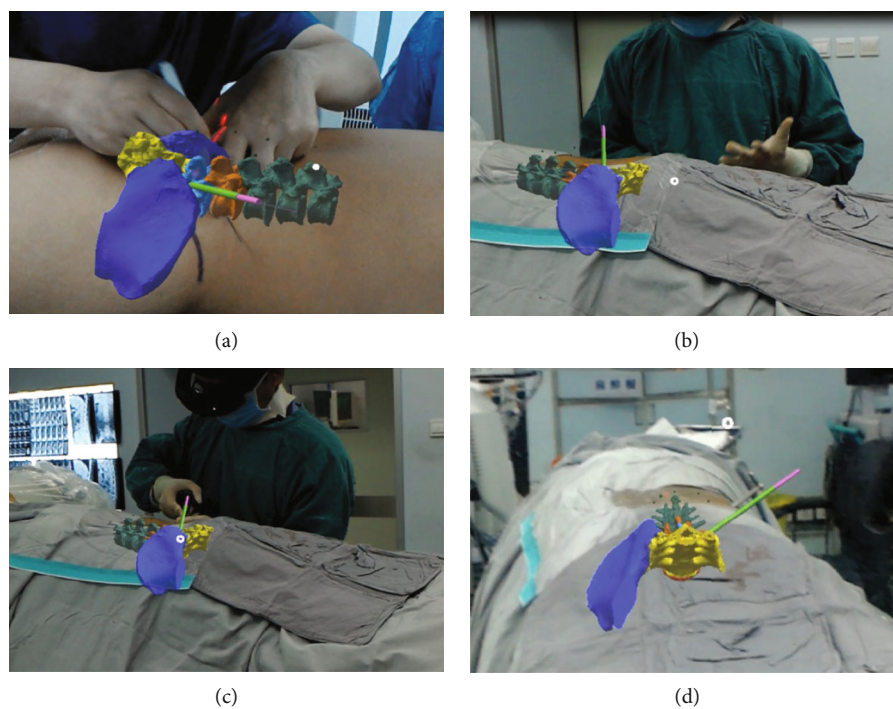


FIGURE 3: Four steps of the surgical procedure assisted with mixed reality technology: (a) marking; (b) needle insertion; (c) foraminoplasty; (d) positioning of the working sheath.

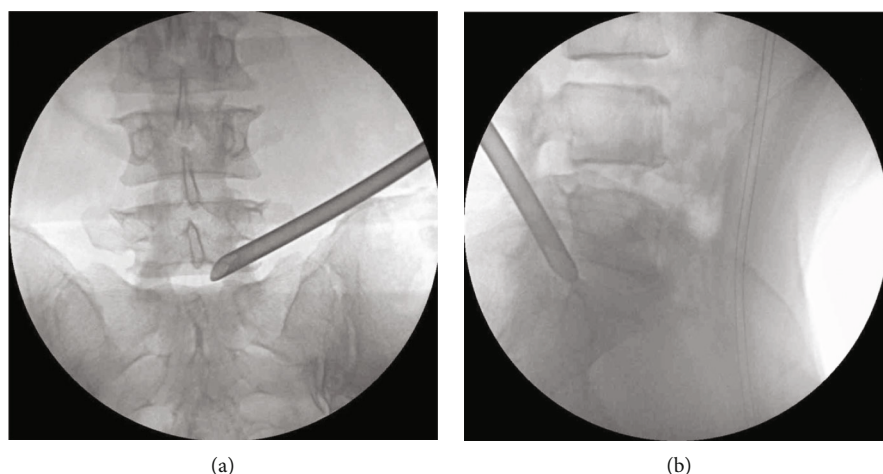


FIGURE 4: Final position of the working sheath confirmed with fluoroscopy: (a) anteroposterior radiograph; (b) lateral radiography.

TABLE 1: Demographic and disease-related data of enrolled patients.

| Group | MixR-assisted TPED group | Conventional TPED group | <i>P</i> |
|--------------------------|--------------------------|-------------------------|----------|
| <i>N</i> | 44 | 43 | |
| Male | 24 | 24 | 0.91 |
| Female | 20 | 19 | |
| Age (years) | 41.21 (17-64) | 38.93 (19-62) | 0.45 |
| BMI (kg/m ²) | 24.27 | 24.19 | 0.86 |
| Disc herniation type | | | |
| Central | 16 | 14 | |
| Paracentral | 20 | 20 | 0.98 |
| Foraminal | 7 | 8 | |
| Far-lateral | 1 | 1 | |
| Surgical level | | | |
| L3/4 | 4 | 1 | |
| L4/5 | 19 | 18 | 0.37 |
| L5/S1 | 21 | 24 | |

TPED: transforaminal percutaneous endoscopic discectomy; MixR: mixed reality; BMI: body mass index.

rupture, nerve root injury, infection, poor healing of the incision, or serious allergy.

The clinical outcomes are listed in Table 2. Thirty-eight patients in the MixR-assisted TPED group and thirty-six cases in the conventional TPED group achieved excellent outcomes. Fair or poor outcomes were not observed at the last follow-up examination. There was no significant difference between the two groups with respect to the NRS score for leg or back pain, which significantly improved at 1 day postoperatively ($P < 0.05$) and at the last follow-up examination ($P < 0.05$), compared with the preoperative values. Significant improvement was observed in the ODI at the last follow-up visit compared with the preoperative value ($P < 0.05$). The NRS score and ODI did not differ significantly between the two groups at the last follow-up examination. All patients in both groups presented with greater

TABLE 2: Clinical outcomes of the two groups.

| | MixR-assisted TPED group | Conventional TPED group | <i>P</i> |
|-----------------------|--------------------------|-------------------------|----------|
| Preoperative NRS | | | |
| Back pain | 3.57 ± 1.11 | 3.74 ± 1.07 | 0.45 |
| Leg pain | 6.57 ± 1.02 | 6.72 ± 0.91 | 0.46 |
| Preoperative ODI (%) | 63.02 ± 9.32 | 62.02 ± 8.22 | 0.60 |
| Postoperative NRS | | | |
| Back pain | 1.43 ± 0.90 | 1.60 ± 1.00 | 0.40 |
| Leg pain | 1.45 ± 0.98 | 1.70 ± 1.23 | 0.31 |
| Postoperative ODI (%) | 10.93 ± 5.02 | 9.56 ± 3.35 | 0.14 |
| Improved NRS | | | |
| Back pain | 2.14 ± 1.25 | 2.14 ± 1.44 | 0.99 |
| Leg pain | 5.11 ± 1.15 | 5.02 ± 1.52 | 0.75 |
| Improved ODI (%) | 52.09 ± 10.60 | 52.47 ± 9.52 | 0.86 |
| Operation time (min) | 103 ± 18 | 116 ± 29 | 0.01 |

TPED: transforaminal percutaneous endoscopic discectomy; MixR: mixed reality; NRS-LP: numerical rating scale for leg pain; NRS-BP: numerical rating scale for back pain; ODI: Oswestry Disability Index.

improvement in the NRS score and ODI than in the MICD at the last follow-up visit compared with the preoperative values. The mean operation time in the MixR-assisted TPED and conventional TPED groups was 103 and 116 minutes, respectively ($P = 0.01$).

3.2. Fluoroscopic Data and Radiation Exposure. There was no significant difference in the mean TV and TC between the two groups. The durations of marking and needle insertion were shorter in the MixR-assisted TPED group than in the conventional TPED group (1.80 min vs. 2.75 min, $t = 4.64$, $P < 0.001$ and 5.39 min vs. 7.88 min, $t = 3.58$, $P = 0.001$, respectively). Similarly, with MixR assistance, the number of puncture attempts and radiation doses in the procedures of marking (3.93 vs. 6.88, $t = 7.62$, $P < 0.001$ and 3.01 mGy vs. 5.17 mGy, $t = 7.38$, $P < 0.001$, respectively) and needle

TABLE 3: Radiation exposure outcomes of the two groups.

| | MixR-assisted TPED group | Conventional TPED group | <i>P</i> |
|---------------------------|-----------------------------|----------------------------|----------|
| Marking | | | |
| Puncture attempts | 3.93 ± 1.88 | 6.88 ± 1.72 | <0.001 |
| Duration (min) | 1.80 ± 0.67 | 2.75 ± 1.20 | <0.001 |
| Dose (mGy) | 3.01 ± 1.36 | 5.17 ± 1.36 | <0.001 |
| Needle insertion | | | |
| Puncture attempts | 3.41 ± 1.91 | 6.33 ± 3.18 | <0.001 |
| Duration (min) | 5.39 ± 2.17 | 7.88 ± 4.10 | 0.001 |
| Dose (mGy) | 2.73 ± 1.71 | 4.72 ± 2.33 | <0.001 |
| Foraminoplasty | | | |
| Puncture attempts | 6.09 ± 4.52 | 6.74 ± 6.81 | 0.60 |
| Duration (min) | 7.28 ± 5.42 | 7.95 ± 7.50 | 0.63 |
| Dose (mGy) | 4.80 ± 3.71 | 5.05 ± 5.07 | 0.80 |
| Positioning sheath | | | |
| Puncture attempts | 3.81 ± 1.42 | 4.77 ± 3.02 | 0.06 |
| Duration (min) | 4.01 ± 2.30 | 5.28 ± 3.73 | 0.06 |
| Dose (mGy) | 3.04 ± 1.38 | 3.68 ± 2.63 | 0.16 |
| Total | | | |
| Puncture attempts | 17.25 ± 4.28 | 24.72 ± 8.87 | <0.001 |
| Duration (min) | 18.48 ± 6.38 | 23.87 ± 9.64 | 0.003 |
| Dose (mGy) | 13.59 ± 4.56 | 18.62 ± 7.07 | <0.001 |

TPED: transforaminal percutaneous endoscopic discectomy; MixR: mixed reality.

insertion (3.41 vs. 6.33, $t = 5.21$, $P < 0.001$ and 2.73 mGy vs. 4.72 mGy, $t = 4.56$, $P < 0.001$) was significantly decreased. No significant differences were found with respect to the number of puncture attempts, duration, and radiation doses in the procedures of foraminoplasty and positioning of the working sheath between the two groups. With MixR assistance, the total radiation dose in the TPED procedure (13.59 mGy vs. 18.62 mGy, $t = 3.96$, $P < 0.001$) significantly decreased. The total number of puncture attempts and duration were obviously lower in the MixR-assisted TPED group than in the conventional TPED group (17.25 vs. 24.72, $t = 5.01$, $P < 0.001$ and 18.48 min vs. 23.87 min, $t = 3.08$, $P = 0.003$, respectively). The detailed information is displayed in Table 3.

3.3. Eye Fatigue Test. In the MixR-assisted TPED group, the eye fatigue scores were, in descending order, as follows: visual discomfort (2.7), headache (2.7), and blurred vision (2.6). In the conventional group, the main complaint regarding eye fatigue was decreased concentration (0.91). A few complaints were noted for other discomforts. We noted no significant

differences in decreased concentration between the conventional TPED group and the MixR-assisted TPED group ($P = 0.46$).

4. Discussion

Recently, many guided techniques and strategies aimed at decreasing the radiation dose have been introduced [14]. MixR technology has been introduced in percutaneous kyphoplasty for the treatment of osteoporotic vertebral compression fractures. This suggests that MixR technology is practical and advantageous in percutaneous spinal operations. Thus, we introduced MixR technology in TPED with the aim of shortening the operating time and decreasing the radiation dose.

Using OST-HMDs, the operators can directly visualize the anatomical structure and virtual protruded disc. In our study, the operators made the needle coincide with that in the preoperative planned model; thus, the needle could reach the target quickly and accurately. Our results revealed that MixR assistance reduced the radiation dose and shortened the exposure duration during the procedures of marking and needle insertion. The number of puncture attempts and radiation dose were significantly reduced in the MixR-assisted TPED procedure compared to those in the conventional TPED procedure.

Foraminoplasty is strongly recommended in TPED for enlarging the intervertebral foramen near the facet joint, especially for complicated cases [15, 16]. During foraminoplasty, the target points need to be accurately reached through fluoroscopy. To reach the ideal target, fluoroscopy was routinely performed to identify the position of the reamer and the working sheath. Thus, the radiation dose and duration were not significantly reduced in the procedures of foraminoplasty and positioning of the working sheath in the MixR-assisted TPED group. Although the radiation dose is reduced and operating time is shortened with MixR technology [17], this technology still needs the assistance of conventional fluoroscopy. We also found greater displacement between superficial markers and anatomical structures in obese patients with a BMI greater than 30 kg/m². It is necessary to ensure that the position of the patient during the CT scan is consistent with that assumed in the operation. Still, obese patients may experience more puncture attempts and radiation than others.

The incorporation of MixR technology in conventional fluoroscopy transformed the complicated surgical task into a simplified line alignment between the planned trajectory and working tools in multiple views, which helped surgeons reach the target site in a shorter time [18]. To easily and precisely match the 3D model with the anatomical spine, markers were extracted from the reconstructed 3D model. During the procedure of matching, the operators should endeavor to match multiple markers. After primary matching, standardized anteroposterior and lateral views were used to position the superficial projection of the anatomical structures, aiming the superficial projection at the 3D model from multiple perspectives aided in increasing the accuracy of the 3D model. We noted that the middle of

the superior endplate and the superior facet process of the inferior vertebra were the ideal anatomical landmarks. Moreover, the operators should intermittently match the holographic model with the anatomical structures and superficial markers from multiple directions during the surgical procedure. We also found that the 3D holographic model reconstructed from flexion CT images provided greater accuracy and practicality in the TPED procedure than that obtained from conventional supine CT images. Flexion CT examination was considered the necessary component of the preoperative evaluation in patients who were diagnosed using magnetic resonance images. Thus, an additional CT scan was not required when MixR technology was used.

There are several potential advantages of MixR-assisted TPED. First, the 3D model and the procedural site are constantly present in the operator's field of view. The operators do not need to move their field of view away from the procedural site to obtain image guidance information. In addition, the change from the procedural site to the virtual model can be easily achieved by slightly raising the head. The transition from a classic clinical set-up to an OST-HMD display requires less adaptation than that required in other visualization models [19].

The introduction of MixR into TPED is aimed at not only decreasing the radiation dose and operation time but also reducing the operation difficulty and shortening the learning curve of residents [4]. In addition, we found great significance in MixR assistance in both the preoperative plan and the guidance of surgical procedures. Meanwhile, medical consumable material is not needed in MixR-assisted operations. Thus, the use of MixR technology cannot increase the expenses of patients and the government. Therefore, MixR technology has good cost-effectiveness in clinical practice and operations.

There are several limitations. The procedural time and radiation dose during working sheath placement may differ among patients with disc herniation at L5/S1 or L4/L5 [4]. Unfortunately, we cannot perform subgroup analysis according to the different levels because of the small sample size. Moreover, users may experience discomfort and eye fatigue when using the HoloLens for durations longer than half an hour. In addition, at the current early stage of development of this technology, only a few software programs of use are available to the surgeons. Both MixR system (Midivi) and StarAtlas 3.0 (Visual3D, Beijing, China) present the ability to manipulate and visualize holograms [20]. As the popularity of MixR technology increases, we expect that more surgically useful software will be developed [21].

5. Conclusions

This preliminary study shows the utility of MixR technology for image guidance in conventional TPED. The radiation exposure significantly decreased with MixR visualization guidance, and this technology serves as a valuable tool during the TPED procedure; however, the assistance of conventional fluoroscopy is still required.

Data Availability

The data used to support the findings of this study are included within the article.

Conflicts of Interest

The authors declare that they have no conflicts of interest.

Acknowledgments

The study was supported by funding from the Key Research and Development Program of Shandong Province (2018GSF118074).

References

- [1] R. Wu, X. Liao, and H. Xia, "Radiation exposure to the surgeon during ultrasound-assisted transforaminal percutaneous endoscopic lumbar discectomy: a prospective study," *World Neurosurgery*, vol. 101, pp. 658–665.e1, 2017.
- [2] G. Fan, C. Feng, W. Xie et al., "Isocentric navigation for the training of percutaneous endoscopic transforaminal discectomy: a feasibility study," *BioMed Research International*, vol. 2018, Article ID 6740942, 8 pages, 2018.
- [3] M. W. Mariscalco, T. Yamashita, M. P. Steinmetz, A. A. Krishnaney, I. H. Lieberman, and T. E. Mroz, "Radiation exposure to the surgeon during open lumbar microdiscectomy and minimally invasive microdiscectomy: a prospective, controlled trial," *Spine (Phila Pa 1976)*, vol. 36, no. 3, pp. 255–260, 2011.
- [4] Z. Zhou, S. Hu, Y. Z. Zhao et al., "Feasibility of virtual reality combined with isocentric navigation in transforaminal percutaneous endoscopic discectomy: a cadaver study," *Orthopaedic Surgery*, vol. 11, no. 3, pp. 493–499, 2019.
- [5] T. M. Peters and C. A. Linte, "Image-guided interventions and computer-integrated therapy: quo vadis?," *Medical Image Analysis*, vol. 33, pp. 56–63, 2016.
- [6] G. Ameri, J. S. H. Baxter, D. Bainbridge, T. M. Peters, and E. C. S. Chen, "Mixed reality ultrasound guidance system: a case study in system development and a cautionary tale," *International Journal of Computer Assisted Radiology and Surgery*, vol. 13, no. 4, pp. 495–505, 2018.
- [7] G. Deib, A. Johnson, M. Unberath et al., "Image guided percutaneous spine procedures using an optical see-through head mounted display: proof of concept and rationale," *Journal of NeuroInterventional Surgery*, vol. 10, no. 12, pp. 1187–1191, 2018.
- [8] M. G. Hanna, I. Ahmed, J. Nine, S. Prajapati, and L. Pantanowitz, "Augmented reality technology using Microsoft HoloLens in anatomic pathology," *Archives of Pathology & Laboratory Medicine*, vol. 142, no. 5, pp. 638–644, 2018.
- [9] Y. Zhao, X. Bo, C. Wang et al., "Guided punctures with ultrasound volume navigation in percutaneous transforaminal endoscopic discectomy: a technical note," *World Neurosurgery*, vol. 119, pp. 77–84, 2018.
- [10] I. Macnab, "Negative disc exploration. An analysis of the causes of nerve-root involvement in sixty-eight patients," *The Journal of Bone & Joint Surgery*, vol. 53, no. 5, pp. 891–903, 1971.
- [11] J. S. Dixon and H. A. Bird, "Reproducibility along a 10 cm vertical visual analogue scale," *Annals of the Rheumatic Diseases*, vol. 40, no. 1, pp. 87–89, 1981.

- [12] J. C. Fairbank, J. Couper, J. B. Davies, and J. P. O'Brien, "The Oswestry low back pain disability questionnaire," *Physiotherapy*, vol. 66, no. 8, pp. 271–273, 1980.
- [13] C. H. Kim, S. Y. Ryu, J. Y. Yoon et al., "See-through type 3D head-mounted display-based surgical microscope system for microsurgery: a feasibility study," *JMIR mHealth and uHealth*, vol. 7, no. 3, article e11251, 2019.
- [14] P. Stefan, S. Habert, A. Winkler et al., "A radiation-free mixed-reality training environment and assessment concept for C-arm-based surgery," *International Journal of Computer Assisted Radiology and Surgery*, vol. 13, no. 9, pp. 1335–1344, 2018.
- [15] K. C. Choi, J. S. Kim, D. C. Lee, and C. K. Park, "Percutaneous endoscopic lumbar discectomy: minimally invasive technique for multiple episodes of lumbar disc herniation," *BMC Musculoskeletal Disorders*, vol. 18, no. 1, p. 329, 2017.
- [16] M. T. N. Knight, I. Jago, C. Norris, L. Midwinter, and C. Boynes, "Transforaminal endoscopic lumbar decompression & foraminoplasty: a 10 year prospective survivability outcome study of the treatment of foraminal stenosis and failed back surgery," *International Journal of Spine Surgery*, vol. 8, 2014.
- [17] M. Fischer, B. Fuerst, S. C. Lee et al., "Preclinical usability study of multiple augmented reality concepts for K-wire placement," *International Journal of Computer Assisted Radiology and Surgery*, vol. 11, no. 6, pp. 1007–1014, 2016.
- [18] S. C. Lee, B. Fuerst, K. Tateno et al., "Multi-modal imaging, model-based tracking, and mixed reality visualisation for orthopaedic surgery," *Healthcare Technology Letters*, vol. 4, no. 5, pp. 168–173, 2017.
- [19] L. Qian, A. Barthel, A. Johnson et al., "Comparison of optical see-through head-mounted displays for surgical interventions with object-anchored 2D-display," *International Journal of Computer Assisted Radiology and Surgery*, vol. 12, no. 6, pp. 901–910, 2017.
- [20] P. Wei, Q. Yao, Y. Xu, H. Zhang, Y. Gu, and L. Wang, "Percutaneous kyphoplasty assisted with/without mixed reality technology in treatment of OVCF with IVC: a prospective study," *Journal of Orthopaedic Surgery and Research*, vol. 14, no. 1, p. 255, 2019.
- [21] O. M. Tepper, H. L. Rudy, A. Lefkowitz et al., "Mixed reality with HoloLens: where virtual reality meets augmented reality in the operating room," *Plastic and Reconstructive Surgery*, vol. 140, no. 5, pp. 1066–1070, 2017.

Research Article

The Bony Resection Accuracy with Patient-Specific Instruments during Total Knee Arthroplasty: A Retrospective Case Series Study

Liang Yuan ¹, Bin Yang ¹, Xiaohua Wang,¹ Bin Sun,¹ Ke Zhang,¹ Yichen Yan,² Jie Liu ³ and Jie Yao ²

¹Department of Orthopedics, Peking University International Hospital, Beijing 102206, China

²Key Laboratory for Biomechanics and Mechanobiology of Ministry of Education, School of Biological Science and

Medical Engineering, Beijing Advanced Innovation Centre for Biomedical Engineering, Beihang University, Beijing 100191, China

³Department of Vascular and Endovascular Surgery, Chinese PLA General Hospital, Beijing 100853, China

Correspondence should be addressed to Jie Liu; liujie3514@163.com and Jie Yao; astromilk@163.com

Received 4 August 2020; Revised 23 December 2020; Accepted 27 January 2021; Published 16 February 2021

Academic Editor: Liu Yang

Copyright © 2021 Liang Yuan et al. This is an open access article distributed under the Creative Commons Attribution License, which permits unrestricted use, distribution, and reproduction in any medium, provided the original work is properly cited.

Purpose. Bony resection is the primary step during total knee arthroplasty. The accuracy of bony resection was highly addressed because it was deemed to have a good relationship with mechanical line. Patient-specific instruments (PSI) were invented to copy the bony resection references from the preoperative surgical plan during a total knee arthroplasty (TKA); however, the accuracy still remains controversial. This study was aimed at finding out the accuracy of the bony resection during PSI-assisted TKA. **Methods.** Forty-two PSI-assisted TKAs (based on full-length leg CT images) were analyzed retrospectively. Resected bones of every patient were given a CT scan, and three-dimensional radiographs were reconstructed. The thickness of each bony resection was measured with the three-dimensional radiographs and recorded. The saw blade thickness (1.27 mm) was added to the measurements, and the results represented intraoperative bone resection thickness. A comparison between intraoperative bone resection thickness and preoperatively planned thickness was conducted. The differences were calculated, and the outliers were defined as >3 mm. **Results.** The distal femoral condyle had the most accurate bone cuts with the smallest difference (median, 1.0 mm at the distal medial femoral condyle and 0.8 mm at the distal lateral femoral condyle) and the least outliers (none at the distal medial femoral condyle and 1 (2.4%) at the distal lateral femoral condyle). The tibial plateau came in second (median difference, 0.8 mm at the medial tibial plateau and 1.4 mm at the lateral tibial plateau; outliers, none at the medial tibial plateau and 1 (2.6%) at the lateral tibial plateau). Regardless of whether the threshold was set to >2 mm (14 (17.9%) at the tibial plateau vs. 12 (14.6%) at the distal femoral condyle, $p > 0.05$) or >3 mm (1 (1.3%) at the tibial plateau vs. 1 (1.2%) at the distal femoral condyle, $p > 0.05$), the accuracy of tibial plateau osteotomy was similar to that of the distal femoral condyle. Osteotomy accuracy at the posterior femoral condyle and the anterior femoral condyle were the worst. Outliers were up to 6 (15.0%) at the posterior medial femoral condyle, 5 (12.2%) at the posterior lateral femoral condyle, and 6 (15.8%) at the anterior femoral condyle. The percentages of overcut and undercut tended to 50% in most parts except the lateral tibial plateau. At the lateral tibial plateau, the undercut percentage was twice that of the overcut. **Conclusion.** The tibial plateau and the distal femoral condyle share a similar accuracy of osteotomy with PSI. PSI have a generally good accuracy during the femur and tibia bone resection in TKA. PSI could be a kind of user-friendly tool which can simplify TKA with good accuracy. **Level of Evidence.** This is a Level IV case series with no comparison group.

1. Introduction

Total knee arthroplasty (TKA) has been a reliable option with excellent long-term results for patients suffering from

advanced knee osteoarthritis and other severe knee diseases [1–4]. One of the keys to a good TKA is the reconstruction of the lower extremity mechanical axis. To achieve this purpose, precise bony resection and accurate prosthesis

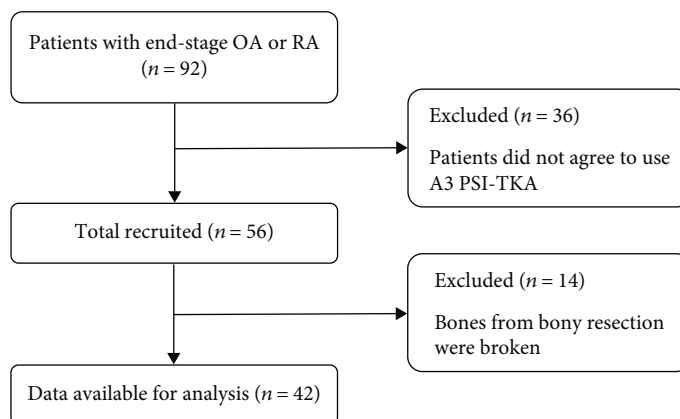


FIGURE 1: Study flowchart.

TABLE 1: Baseline characteristics of participants.

| Characteristics | All patients (n = 42) |
|---|-----------------------|
| Sex | |
| Male, n (%) | 4 (9.5%) |
| Female, n (%) | 38 (90.5%) |
| Age (years, mean \pm SD) | 69.1 \pm 6.7 |
| Height (meter, mean \pm SD) | 1.6 \pm 0.1 |
| Weight (kg, mean \pm SD) | 66.7 \pm 10.2 |
| BMI (mean \pm SD) | 26.4 \pm 3.4 |
| Extension (degree, median, Q1-Q3) | 8.0 (3.0-15.0) |
| Flexion (degree, mean \pm SD) | 113.0 \pm 15.3 |
| HKA (degree, mean \pm SD) | 169.9 \pm 5.5 |
| Alignment angle (degree, median, Q1-Q3) | 9.0 (6.2-12.8) |
| Side | |
| Left, n (%) | 22 (52.4%) |
| Right, n (%) | 20 (47.6%) |
| Diagnosis | |
| OA, n (%) | 39 (92.9%) |
| RA, n (%) | 3 (7.1%) |
| Alignment | |
| Varus, n (%) | 42 (100.0%) |
| Valgus, n (%) | 0 |

Abbreviations: BMI=body mass index; HKA=hip-knee-ankle angle; OA=osteoarthritis; RA=rheumatoid arthritis.

implanting are necessary. Implanting each prosthesis component as accurately as possible has always been an essential principle in TKA, and implant malalignment is considered a common cause of failure [5, 6]. To improve the accuracy of prosthesis implantation and facilitate the surgery, patient-specific instruments (PSI) were introduced to TKA [7].

PSI are usually made based on the patient's computer tomography (CT) or magnetic resonance imaging (MRI) data [8–10], which can be directly used to guide patient-specific osteotomy during TKA. Three-dimensional (3D) models of the patient's anatomy are derived and developed from CT/MRI data, and then a simulated surgery is performed on the model

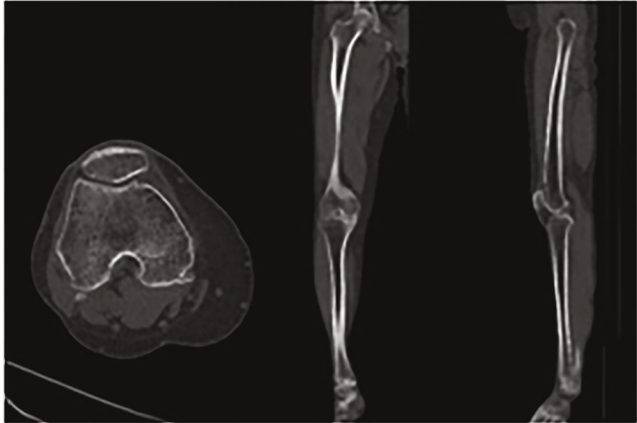
with some software. During this process, the parameters required for osteotomy of the knee joint would be accurately calculated. PSI are produced by 3D-printing technology according to these parameters. PSI became a favorable bridge between pre-operative planning and the final TKA surgery, which allowed the surgeon to copy the surgical plan to a specific patient. Thus, its accuracy has been one of the main concerns of PSI.

3D-printed PSI have been used in TKA for more than 15 years; however, its accuracy reported by the literature was not satisfactory [11–16]. As for these results, there can be many kinds of interpretations. Delpont and Vander Sloten put forward several vital points worth pondering in the letter to the Journal of Arthroplasty [17]. Inherent to this technology was that patients were treated with personalized surgical plans. PSI played a role in transferring the preoperative plans to the patients' anatomy during TKA. The intended output of PSI-assisted TKA is a postoperative result which is identical to the preoperative plan. Many researchers compared X-ray-based postoperative results with the CT/MRI-based preoperative plan regardless of the consensus amongst clinicians that a postoperative X-ray image could not qualify as an accurate measurement tool [17]. In this way, the error caused by the measurement tool might have put the blame on PSI. Therefore, we should be cautious with those results based on an X-ray study. Just as Delpont and Vander Sloten concluded [17], an accurate measurement tool should be used, and the postoperative result should be compared to the actual preoperative plan.

Some researchers smartly came up with a way to study PSI accuracy without using X-ray measurement. In these studies, the amount of bony resection was measured and compared with planned osteotomy [18–22]. However, the results of these studies were covered with controversy. A study with meta-analysis has also reported controversial results [8]. The present study is focused on this issue by evaluating the efficacy of PSI in copying the bony resection reference value from the surgical plan. We assume that PSI has good accuracy in bone resection during TKA.

2. Materials and Methods

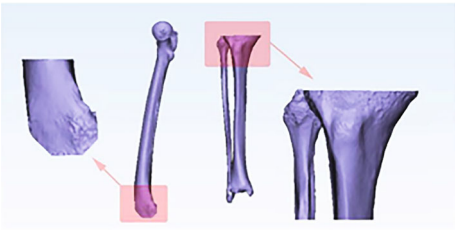
2.1. Study Population. A retrospective review of all the PSI-assisted TKAs from January 2019 to June 2020 was



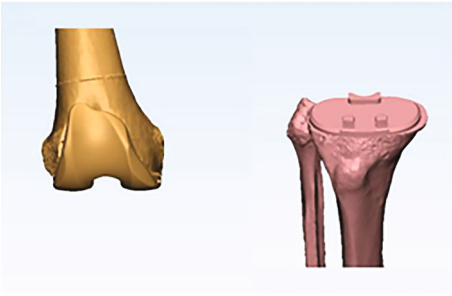
(a)



(b)



(c)



(d)

FIGURE 2: Continued.

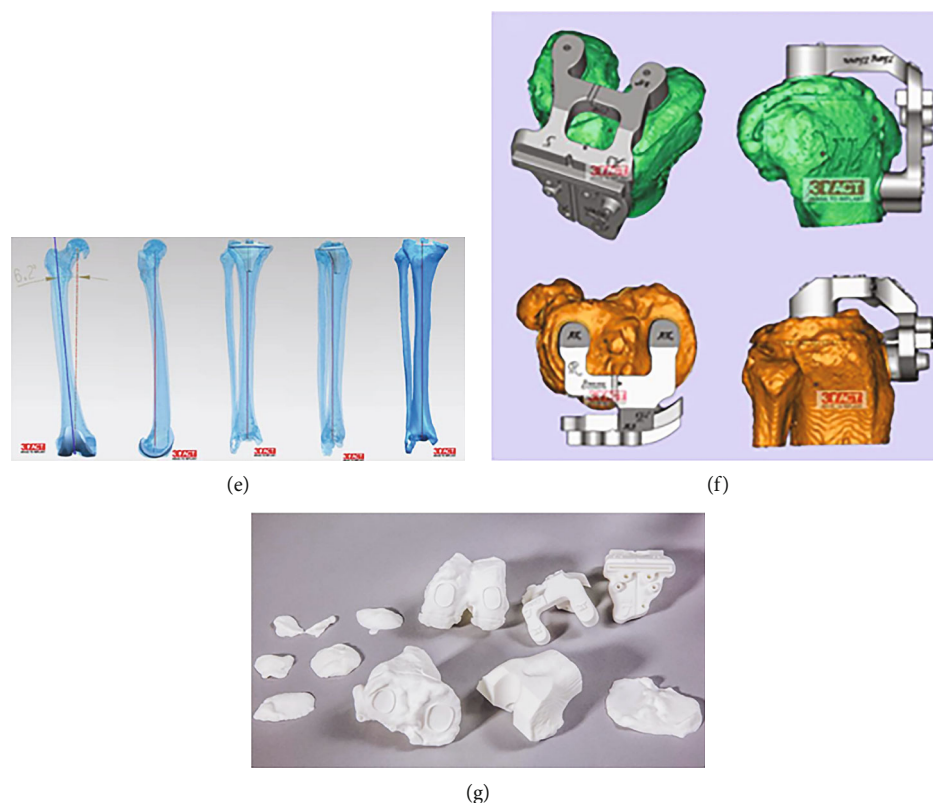


FIGURE 2: Standard workflow of the preoperation protocol. (a) Full-leg CT scans. (b) Three-dimensional digital reconstructions of the femur and the tibia by UG/NX 10.0 (Siemens PLM Software Ltd., Germany). (c) Simulated bone cutting. (d) Assembling components of the prosthesis and matching them with the bones. (e) Measuring the femur and the tibia, and checking the joint alignment. (f) Designing the PSI according to the virtual surgery. (g) Printing the PSI.

conducted. Inclusion criteria were patients suffering end-stage osteoarthritis or rheumatoid arthritis of the knee without operational contraindications and patients who agreed to use A3 prosthesis (AK Medical, Beijing, China). However, both the candidates whose bones from bony resection could not be obtained integrally during TKA and those who were added extra bone cuts after PSI-assisted bony resection were excluded (Figure 1). We have retrospectively collected data on 42 patients. The cohort consisted of 38 (90.5%) women and 4 (9.5%) men. Mean age was 69.1 years (range: 54-81 years), and mean body mass index (BMI) was 26.4 kg/m² (range: 19.2-35.6 kg/m²). All the 42 cases were varus knees. More detailed information is shown in Table 1. The data are anonymous, and the requirement for informed consent was therefore waived. The study protocol was approved by the ethics committee of Peking University International Hospital (YJ2017-020 and 2019-030BMR). All operations were performed in accordance with relevant guidelines and regulations.

2.2. Preoperative Planning and PSI Production. All patients received an A3 posterior-stabilized prosthesis (AK Medical, Beijing, China). Informed consent of receiving TKA by PSI was acquired before the operation for all patients. A computed tomography scan from the pelvis to the foot should be done as soon as a patient decided to accept TKA. After-

ward, a full preoperation plan was drafted according to the data from the CT scans, which was followed by a set of three-dimensional- (3D-) printed PSI (Figure 2(g)). From the CT data to the PSI, a constant group consisting of one surgeon and two mechanical engineers would finish a preoperation protocol following a standard workflow (Figure 2). A full preoperation protocol would provide the surgeon with all the critical references needed during a TKA operation, including the bony resection thickness, rotation alignment, frontal alignment, sagittal alignment, and prosthesis sizes. Before an operation, the paper version of the preoperative plan would be printed and hung on the wall in the operation room. During the surgery, the actual situation should be checked. If the PSI could not match the bones, they would be abandoned, and the conventional instruments would be used instead.

2.3. Surgical Procedure. A medial parapatellar approach was adopted in all TKA surgeries. After appropriate soft tissue release, joint exposure, and scraping of the articular cartilage, PSI components were fixed on the bone surface correctly, and bone cuts were conducted subsequently (Figure 3). Femoral cuts were followed by tibial cuts. The distal femoral condyle and tibial plateau osteotomies were assisted by PSI, while the posterior femoral condyle and anterior femoral condyle osteotomies were performed with conventional jigs. All the

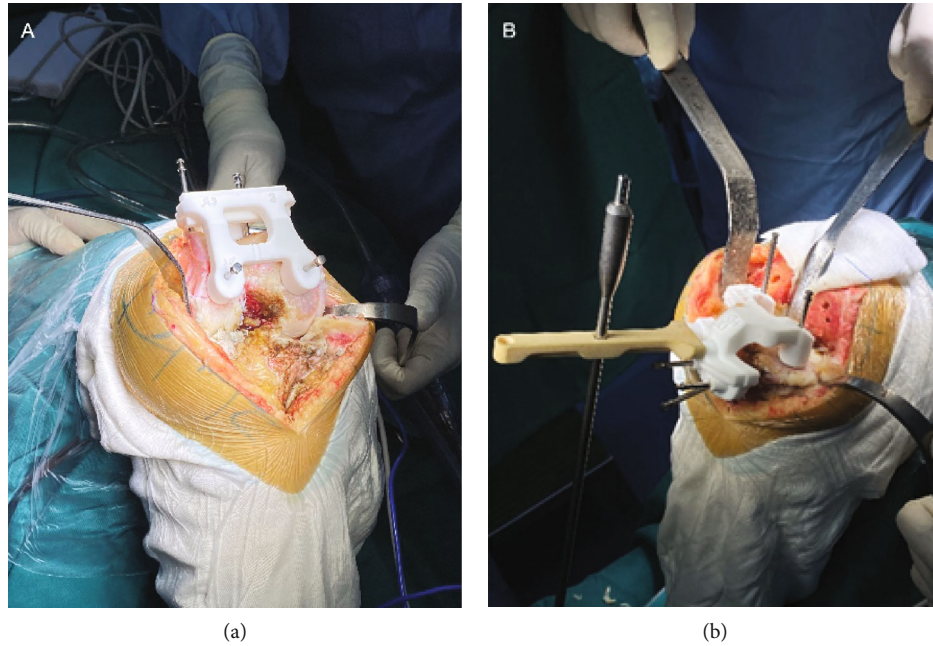


FIGURE 3: PSI-assisted femur (a) and tibia (b) cutting. PSI were fixed correctly on the bones before cutting.

bony resections were operated with a 1.27 mm thick saw blade. All the operations were performed by the same group of senior doctors.

2.4. Bony Resection Measurement. Bone fragments including the distal medial femoral condyle (DMFC), the distal lateral femoral condyle (DLFC), the posterior medial femoral condyle (PMFC), the posterior lateral femoral condyle (PLFC), the anterior femoral condyle (AFC), the medial tibial plateau (MTP), and the lateral tibial plateau (LTP) were collected after the completion of femoral and tibial bony resection. The surgeon would manually compare the bone fragments with the printed models one by one (Figure 4). In the following steps, CT scans were used for the bone fragments to obtain the radiological images. CT data were imported to Mimics® 19.0 (Materialise NV, Belgium), and three-dimensional images were reconstructed. Bony resection amount was calculated by 3-matic® software (version 11.0, Materialise NV, Belgium) based on 3D images imported from Mimics® (Figures 5 and 6). All the measurements were done by a doctor (Liang Yuan) blind to the preoperative surgical plans. The difference of osteotomy was obtained by subtracting the planned osteotomy amount from the actual osteotomy amount. Negative numbers indicate inadequate osteotomy (undercut), while positive numbers mean excessive osteotomy (overcut). The magnitude of the difference is measured in absolute value.

2.5. Statistical Analysis. Categorical variables were presented as frequencies and percentages. Continuous variables were summarised as either means and standard deviations or medians with interquartile ranges. To find out potential patterns of error, the proportion of outliers was compared between femoral and tibial cuts, and a Chi-square test was performed. All analyses were performed with the statistical



FIGURE 4: Actual cut bones (the bloody color) and 3D-printed planned cut references (the white color).

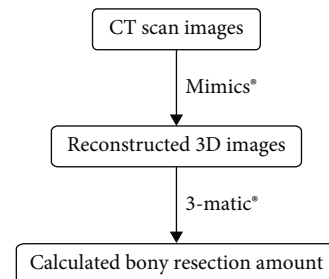


FIGURE 5: Workflow of the bony resection measurement.

software packages R (<http://www.R-project.org>, The R Foundation) and EmpowerStats (<http://www.empowerstats.com>, X&Y Solutions, Inc., Boston, MA).

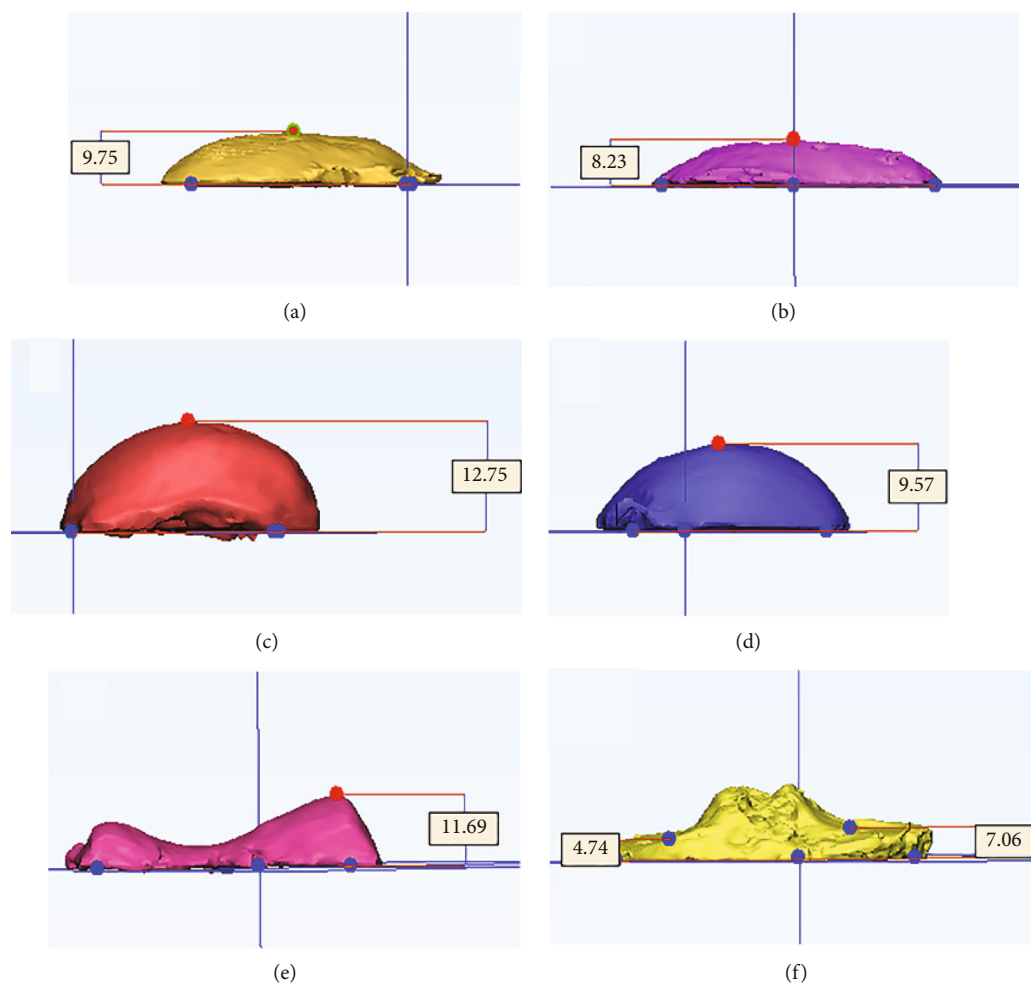


FIGURE 6: Measurement of the bony resection by 3-matic®. (a) Distal medial femoral condyle. (b) Distal lateral femoral condyle. (c) Posterior medial femoral condyle. (d) Posterior lateral femoral condyle. (e) Anterior femoral condyle. (f) Tibial plateau.

TABLE 2: Differences between actual bone cuts and surgical plan at each location^a.

| Anatomical location | Median, Q1-Q3 (mm) | ≤1.0mm, <i>n</i> (%) | 1.1-2.0 mm, <i>n</i> (%) | 2.1-3.0mm <i>n</i> (%) | Outliers, ^b <i>n</i> (%) | Undercut <i>n</i> (%) | Overcut, <i>n</i> (%) |
|---------------------|--------------------|----------------------|--------------------------|------------------------|-------------------------------------|-----------------------|-----------------------|
| DMFC | 1.0 (0.4-1.5) | 20 (48.8%) | 14 (34.1%) | 7 (17.1%) | 0 | 17 (41.5%) | 24 (58.5%) |
| DLFC | 0.8 (0.4-1.0) | 28 (68.3%) | 8 (19.5%) | 4 (9.8%) | 1 (2.4%) | 23 (56.1%) | 18 (43.9%) |
| PMFC | 1.0 (0.5-1.9) | 21 (52.5%) | 11 (27.5%) | 2 (5.0%) | 6 (15.0%) | 19 (47.5%) | 21 (52.5%) |
| PLFC | 1.0 (0.6-1.7) | 21 (51.2%) | 12 (29.3%) | 3 (7.3%) | 5 (12.2%) | 21 (51.2%) | 20 (48.8%) |
| AFC | 1.6 (0.5-2.6) | 13 (34.2%) | 9 (23.7%) | 10 (26.3%) | 6 (15.8%) | 19 (50.0%) | 19 (50.0%) |
| MTP | 0.8 (0.3-1.6) | 22 (56.4%) | 12 (30.8%) | 5 (12.8%) | 0 | 21 (53.8%) | 18 (46.2%) |
| LTP | 1.4 (0.6-1.9) | 18 (46.2%) | 12 (30.8%) | 8 (20.5%) | 1 (2.6%) | 26 (66.7%) | 13 (33.3%) |

^aAll the numbers in the table were calculated by absolute value except the undercut and overcut columns. ^bThe outliers were defined as >3mm. Abbreviations: DMFC=distal medial femoral condyle; DLFC=distal lateral femoral condyle; PMFC=posterior medial femoral condyle; PLFC=posterior lateral femoral condyle; AFC=anterior femoral condyle; MTP=medial tibial plateau; LTP=lateral tibial plateau.

3. Results

3.1. Characteristics of the Subjects. A total of 56 patients were included in the study, and 14 cases were excluded because of incomplete bone fragments. Forty-two cases were eventually included in the data analysis. Table 1 shows the basic characteristics of the subjects. The majority of the cases were female

patients (38 (90.5%)) with knee osteoarthritis (39 (92.9%)), and their ages were relatively old (69.1 ± 6.7 years). All cases had mild to moderate genu varus deformity (median angle: 9.0 degrees).

3.2. The Differences between Actual and Planned Osteotomies. Differences in osteotomy at different anatomical sites were

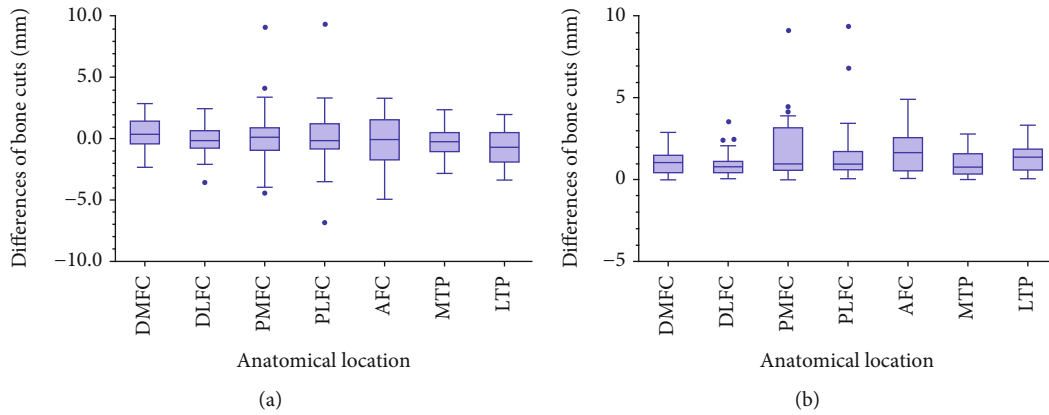


FIGURE 7: Differences in osteotomy at each anatomical site. (a) The difference of osteotomy was calculated by subtracting the planned osteotomy amount from the actual osteotomy amount. Negative numbers indicate inadequate osteotomy (undercut), while positive numbers mean excessive osteotomy (overcut). (b) The magnitude of the difference is measured in absolute value. Abbreviations: DMFC=distal medial femoral condyle; DLFC=distal lateral femoral condyle; PMFC=posterior medial femoral condyle; PLFC=posterior lateral femoral condyle; AFC=anterior femoral condyle; MTP=medial tibial plateau; LTP=lateral tibial plateau.

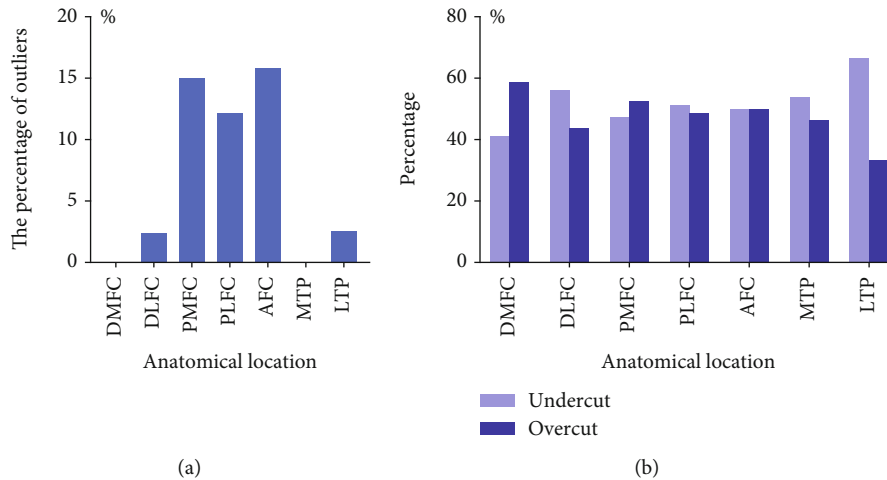


FIGURE 8: The percentages of outliers (a), and the percentages of undercut and overcut (b) at each anatomical location.

presented in Table 2 and in Figures 7 and 8. The distal femoral condyle had the most accurate bone cuts with the smallest differences (median: 1.0 mm at DMFC and 0.8 mm at DLFC) and the least outliers (none at DMFC and 1 (2.4%) at DLFC). The tibial plateau came in second (median difference: 0.8 mm at MTP and 1.4 mm at LTP; outliers: none at MTP and 1 (2.6%) at LTP). To further compare the distal femur and tibial plateau, DMFC and DLFC and MTP and LTP were summed. Regardless of whether the threshold was set to >2mm (14 (17.9%) at the tibial plateau vs. 12 (14.6%) at the distal femoral condyle, $p > 0.05$) or >3 mm (1 (1.3%) at the tibial plateau vs. 1 (1.2%) at the distal femoral condyle, $p > 0.05$), the accuracy of tibial plateau osteotomy was similar to that of the distal femoral condyle. Osteotomy accuracy at the posterior femoral condyle and the anterior femoral condyle was the worst. Outliers were up to 6 (15.0%) at PMFC, 5 (12.2%) at PLFC, and 6 (15.8%) at AFC. The percentages of overcut and undercut tended to be 50% in most parts except LTP. At LTP, the undercut percentage was twice that of overcut.

4. Discussion

This case series study mainly describes the accuracy of PSI in replicating preoperatively programmed osteotomy with the usage of the CT-based measuring method. With the assistance of PSI, the distal femoral condyle and tibial plateau osteotomies showed small differences with the preoperative plan. This implied that PSI might have good accuracy in bone cuts during TKA.

To our best knowledge, this is the first study to use CT data to measure the bony resection amount. Previous similar studies used the vernier caliper [18, 21, 22]. It is well known that PSI are patient-specific cutting guides based on CT or MRI images, and that preoperatively planned bone cuttings are also measured from CT or MRI data [10, 16, 23]. We assume that the error of the micrometer measurement may be greater than that of the CT or MRI data. In this study, both the preoperative and postoperative measurements were based on CT data. In theory, measurements with the same method can result in much smaller errors. In addition, the

measurement based on CT data can effectively avoid the influence of the cartilage layer. Clinical experience tells us that more or less cartilage remained on the surface of the bones. When a vernier caliper was used, the measured value must have included the cartilage layer thickness, which would bias the research results.

Several previous studies have explored the accuracy of PSI-assisted osteotomy [19, 21, 22, 24–26]. All of them reported high accuracy of distal femoral condyle osteotomy. Zambianchi et al. [24] found that the proportion of differences within ± 2 mm between intraoperative measured bony resections and planned bone cuts occurred in more than 90% of the cohort for distal femoral resections. Nankivell et al. [21] and Kievit et al. [26] reported even better accuracy, which showed that average resection errors were less than 1 mm both medially and laterally for the distal femur. However, the accuracy of the tibial plateau osteotomy did not seem to be so good. The percentage of osteotomy error within ± 2 mm on the proximal lateral tibia was less than 70%, according to Okada et al. [25]. Levy et al. [22] also reported a similar result, which showed that the tibial cuts had the lowest proportion of acceptable cuts (68.9%). In this study, we got different results. Regardless of whether the threshold was set to >2 mm (14 (17.9%) at the tibial plateau vs. 12 (14.6%) at the distal femoral condyle, $p > 0.05$) or >3 mm (1 (1.3%) at the tibial plateau vs. 1 (1.2%) at the distal femoral condyle, $p > 0.05$), the accuracy of tibial plateau osteotomy was similar to that of the distal femoral condyle.

In this study, we found that osteotomy tended to be undercut at LTP. Generally, the percentages of overcut and undercut were close to 50% in most parts except LTP. At LTP, the undercut percentage was twice that of overcut (Figure 8(b)). This may be attributed to the anatomical characteristics of the tibial plateau. The medial side of the tibial plateau was concave, and the lateral side was convex, and as a consequence, the attachment point of the PSI on the outside was easier to shift. This phenomenon was indeed observed during the surgery. In addition, there was another possible reason. This cohort entirely consisted of varus knees, which were characterized by more wear of the medial cartilage [27]. Therefore, a thicker cartilage layer remained on the lateral side. If the lateral cartilage was not removed cleanly before the PSI attached, it would easily lead to less osteotomy. This finding reminds us to pay special attention to the pitfalls of PSI-assisted TKA caused by the difference between the medial and lateral sides of the tibial plateau during the operation.

Besides, there was another interesting finding in this study. Compared with the distal femoral condyle and tibial plateau, there were much more outliers at PMFC (6 (15.0%)), PLFC (5 (12.2%)), and AFC (6 (15.8%)). This implies that the accuracy of osteotomy of the posterior femoral condyle and anterior femoral condyle was much worse. Coincidentally, the posterior femoral condyle osteotomy and the anterior femoral condyle osteotomy were performed with traditional metal jigs rather than the 3D-printed PSI. This suggested that PSI accuracy might be better than traditional tools. Nevertheless, this still needs to be confirmed by a later study that we are going to conduct next.

This study also has several limitations. Firstly, the majority of the cases in this study were female patients. Secondly, all cases were genu varus. Therefore, the data in this study cannot describe whether valgus knees have similar results. We assume that valgus knees are likely to have different results, and one previous study also suggested this [22]. Moreover, given that this was a descriptive study with no controls, it was not able to determine whether PSI would be superior to conventional tools in bone cuttings, although some of the results suggested that possibility. In the end, we should be very cautious in interpreting the results of this article. The purpose of this study was to describe the accuracy of the bony resection with PSI in transferring the preoperative plan to TKA surgery. The concept of PSI accuracy cannot be easily extended to problems related to lower limb alignment. Numerous factors may affect the lower limb alignment even if a precise osteotomy is performed.

5. Conclusion

The tibial plateau and distal femoral condyle share a similar accuracy of osteotomy with PSI. PSI have a generally good accuracy during the femur and tibia bone resection in TKA. PSI could be a kind of user-friendly tool which can simplify TKA with good accuracy.

Data Availability

The data supporting the results are available from the corresponding authors upon request.

Conflicts of Interest

All of the authors declare that they have no conflicts of interest.

Authors' Contributions

Liang Yuan and Bin Yang contributed equally to this work.

Acknowledgments

We gratefully thank Dr. Zheng Wu for valuable discussion and useful comments regarding the manuscript. This study was supported by the Peking University International Hospital Research Funds (YN2016QN08 and YN2019ZD05), the National Natural Science Foundation of China (NSFC) (11502014), and the Young Elite Scientist Sponsorship Program by CAST (YESS20150048).

References

- [1] D. Diduch, J. Insall, W. Scott, G. Scuderi, and D. Font-Rodriguez, "Total knee replacement in young, active patients. Long-term follow-up and functional outcome*," *The Journal of Bone & Joint Surgery*, vol. 79, no. 4, pp. 575–582, 1997.
- [2] W. J. Long, C. D. Bryce, C. S. Hollenbeak, R. W. Benner, and W. N. Scott, "Total knee replacement in young, active patients: long-term follow-up and functional outcome: a concise follow-

- up of a previous report," *The Journal of Bone and Joint Surgery-American Volume*, vol. 96, pp. e151–e151, 2014.
- [3] Y. Ishii, H. Noguchi, J. Sato, T. Sakurai, and S. Toyabe, "Comparison of long-term clinical outcomes after bilateral mobile-bearing total knee arthroplasties using PCL-retaining and PCL-substituting implants in the same patients," *Knee Surgery, Sports Traumatology, Arthroscopy*, vol. 25, no. 12, pp. 3711–3717, 2017.
 - [4] J. T. Evans, R. W. Walker, J. P. Evans, A. W. Blom, A. Sayers, and M. R. Whitehouse, "How long does a knee replacement last? A systematic review and meta-analysis of case series and national registry reports with more than 15 years of follow-up," *Lancet*, vol. 393, no. 10172, pp. 655–663, 2019.
 - [5] P. F. Sharkey, W. J. Hozack, R. H. Rothman, S. Shastri, and S. M. Jacoby, "Why are total knee arthroplasties failing today?," *Clinical Orthopaedics and Related Research*, vol. 404, pp. 7–13, 2002.
 - [6] P. F. Sharkey, P. M. Lichstein, C. Shen, A. T. Tokarski, and J. Parvizi, "Why are total knee arthroplasties failing today—has anything changed after 10 years?," *The Journal of Arthroplasty*, vol. 29, no. 9, pp. 1774–1778, 2014.
 - [7] R. M. Nunley, B. S. Ellison, E. L. Ruh et al., "Are patient-specific cutting blocks cost-effective for total knee arthroplasty?," *Clinical Orthopaedics and Related Research*, vol. 470, pp. 889–894, 2012.
 - [8] E. Thienpont, P. Schwab, and P. Fennema, "Efficacy of patient-specific instruments in total knee arthroplasty," *The Journal of Bone and Joint Surgery*, vol. 99, no. 6, pp. 521–530, 2017.
 - [9] Z. Li, Z. Yang, W. Liao et al., "Fewer femoral rotational outliers produced with CT- than with MRI-based patient-specific instrumentation in total knee arthroplasty," *Knee Surgery, Sports Traumatology, Arthroscopy*, vol. 28, no. 9, pp. 2930–2941, 2020.
 - [10] V. V. G. An, B. S. Sivakumar, K. Phan, Y. D. Levy, and W. J. M. Bruce, "Accuracy of MRI-based vs. CT-based patient-specific instrumentation in total knee arthroplasty: a meta-analysis," *Journal of Orthopaedic Science*, vol. 22, no. 1, pp. 116–120, 2017.
 - [11] P. B. Voleti, M. J. Hamula, K. D. Baldwin, and G. Lee, "Current data do not support routine use of patient-specific instrumentation in total knee arthroplasty," *The Journal of Arthroplasty*, vol. 29, no. 9, pp. 1709–1712, 2014.
 - [12] R. Russell, T. Brown, M. Huo, and R. Jones, "Patient-specific instrumentation does not improve alignment in total knee arthroplasty," *The Journal of Knee Surgery*, vol. 27, no. 6, pp. 501–504, 2014.
 - [13] E. Cavaignac, R. Pailhé, G. Laumond et al., "Evaluation of the accuracy of patient-specific cutting blocks for total knee arthroplasty: a meta-analysis," *International Orthopaedics*, vol. 39, no. 8, pp. 1541–1552, 2015.
 - [14] H. J. T. A. Huijbregts, R. J. K. Khan, E. Sorensen, D. P. Fick, and S. Haebich, "Patient-specific instrumentation does not improve radiographic alignment or clinical outcomes after total knee arthroplasty," *Acta Orthopaedica*, vol. 87, no. 4, pp. 386–394, 2016.
 - [15] B. Sharareh and R. Schwarzkopf, "Review article: patient-specific versus standard instrumentation for total knee arthroplasty," *Journal of Orthopaedic Surgery*, vol. 23, no. 1, pp. 100–106, 2015.
 - [16] E. Thienpont, P. E. Schwab, and P. Fennema, "A systematic review and meta-analysis of patient-specific instrumentation for improving alignment of the components in total knee replacement," *The Bone & Joint Journal*, vol. 96-B, no. 8, pp. 1052–1061, 2014.
 - [17] H. P. Delpont and S. J. Vander, "Evaluation of patient specific instruments. To measure is to know!," *The Journal of Arthroplasty*, vol. 30, no. 4, pp. 720–721, 2015.
 - [18] C. H. Yeo, A. Jariwala, N. Pourgiezis, and A. Pillai, "Assessing the accuracy of bone resection by cutting blocks in patient-specific total knee replacements," *ISRN Orthopedics*, vol. 2012, 4 pages, 2012.
 - [19] G. C. Wernecke, S. Taylor, P. Wernecke, S. J. MacDessi, and D. B. Chen, "Resection accuracy of patient-specific cutting guides in total knee replacement," *ANZ Journal of Surgery*, vol. 87, no. 11, pp. 921–924, 2017.
 - [20] I. Nizam and A. V. Batra, "Accuracy of bone resection in total knee arthroplasty using CT assisted-3D printed patient specific cutting guides," *SICOT-J*, vol. 4, p. 29, 2018.
 - [21] M. Nankivell, G. West, and N. Pourgiezis, "Operative efficiency and accuracy of patient-specific cutting guides in total knee replacement," *ANZ Journal of Surgery*, vol. 85, no. 6, pp. 452–455, 2015.
 - [22] Y. D. Levy, V. V. G. An, C. J. W. Shean, F. R. Groen, P. M. Walker, and W. J. M. Bruce, "The accuracy of bony resection from patient-specific guides during total knee arthroplasty," *Knee Surgery, Sports Traumatology, Arthroscopy*, vol. 25, no. 6, pp. 1678–1685, 2017.
 - [23] X. Wu, B. Xiang, M. G. M. Schotanus, Z. Liu, Y. Chen, and W. Huang, "CT- versus MRI-based patient-specific instrumentation for total knee arthroplasty: a systematic review and meta-analysis," *The Surgeon*, vol. 15, no. 6, pp. 336–348, 2017.
 - [24] F. Zambianchi, A. Colombelli, V. Digennaro et al., "Assessment of patient-specific instrumentation precision through bone resection measurements," *Knee Surgery, Sports Traumatology, Arthroscopy*, vol. 25, pp. 2841–2848, 2015.
 - [25] Y. Okada, A. Teramoto, T. Suzuki, Y. Kii, K. Watanabe, and T. Yamashita, "Preoperative corrections are required for planning of patient-specific instrumentation in total knee arthroplasty," *The Knee*, vol. 24, no. 6, pp. 1492–1497, 2017.
 - [26] A. J. Kievit, J. G. G. Dobbe, G. J. Streekstra, L. Blankevoort, and M. U. Schafroth, "Predicted osteotomy planes are accurate when using patient-specific instrumentation for total knee arthroplasty in cadavers: a descriptive analysis," *Knee Surgery, Sports Traumatology, Arthroscopy*, vol. 26, no. 6, pp. 1751–1758, 2018.
 - [27] M. K. Harman, G. D. Markovich, S. A. Banks, and W. A. Hodge, "Wear patterns on tibial plateaus from varus and valgus osteoarthritic knees," *Clinical Orthopaedics and Related Research*, pp. 149–158, 1998.

Research Article

Application of 3D Printing-Assisted Articulating Spacer in Two-Stage Revision Surgery for Periprosthetic Infection after Total Knee Arthroplasty: A Retrospective Observational Study

Lingtong Kong ^{1,2}, Jiawei Mei ^{1,2}, Wufei Ge ^{1,2}, Xiansheng Jin,³ Xiaoxuan Chen ⁴,
Xianzuo Zhang ² and Chen Zhu ²

¹Department of Orthopedics, The Affiliated Provincial Hospital of Anhui Medical University, Hefei 230001, China

²Department of Orthopedics, The First Affiliated Hospital of USTC, Division of Life Sciences and Medicine, University of Science and Technology of China, Hefei 230022, China

³IAT-Chungu Joint Laboratory for Additive Manufacturing Anhui Chungu 3D Printing Institute of Intelligent Equipment and Industrial Technology, Wuhu 241200, China

⁴College of Chemistry and Chemical Engineering, Xiamen University, Xiamen 361005, China

Correspondence should be addressed to Xianzuo Zhang; zhangxianzuo@foxmail.com and Chen Zhu; zhuchena@ustc.edu.cn

Received 4 August 2020; Revised 24 November 2020; Accepted 27 January 2021; Published 8 February 2021

Academic Editor: Liu Yang

Copyright © 2021 Lingtong Kong et al. This is an open access article distributed under the Creative Commons Attribution License, which permits unrestricted use, distribution, and reproduction in any medium, provided the original work is properly cited.

Background. Bone cement spacers are widely used in two-stage revision surgeries for periprosthetic joint infection (PJI) after total knee arthroplasty. Current spacer design results in insufficient release of drugs; therefore, current spacers have low efficacy. In this study, we explored a set of alternative articular spacer using 3D printing technology. This novel spacer will increase effectiveness of revision surgery for PJI. **Methods.** The spacer was designed using CAD software and constructed on site using 3D-printed silicone mold during debridement surgery. We carried out a retrospective study among patients undergoing treatment using traditional static and new articular spacers. Infection control rate, bone loss, difficulty of revision surgery, knee joint range of motion, function evaluation, and subjective satisfaction of the patients in the two groups were compared. **Results.** Forty-two patients undergoing knee revision surgery between Jan 2014 and Nov 2019 were included in this study. Twenty-two patients were treated with static antibiotic cement spacers, whereas the other twenty patients were with treated with 3D printing-assisted antibiotic loaded articulating spacers. Patients in the articular group showed significantly lower bone loss on the femur site and tibial site compared with patients in the static group. In addition, patients in the articular group showed significantly less operation time, intraoperative blood loss, and improved knee function and patient overall satisfaction compared with patients in the static group. **Conclusions.** The 3D printing-assisted articular spacer provides satisfactory range of motion during the interim period, prevents bone loss, facilitates second-stage reimplantation and postoperative rehabilitation, and results in low reinfection and complication rates.

1. Introduction

Total knee arthroplasty (TKA) is an effective method for treatment of end-stage knee disorders, including osteoarthritis, traumatic arthritis, and inflammatory arthritis [1, 2]. Approximately, 400,000 TKA procedures are performed in the United States yearly [3]. However, TKA surgery is associated with periprosthetic joint infection (PJI). Primary TKA is associated with approximately 0.5%-2.0% PJI incidence,

whereas total knee revision (TKR) surgeries are associated with approximately 15%-20% PJI incidence [4-6].

Although new approaches for treatment of PJIs such as debridement and implant retention (DAIR) and one-stage revision have been proposed, two-stage revision strategy remains the gold standard treatment for chronic PJI after TKA [7-9]. Previous studies report that the infection control rate after treatment using two-stage revision strategy is approximately 80%-90% [9, 10]. The patient undergoes at

least two surgeries in the two-stage revision procedure. The first surgery is carried out to remove original prosthesis, debride the knee joint, and insert an antibiotic cement spacer to control infection. The spacer can be replaced with a revision prosthesis after inflammation elimination and infection control.

Different temporary spacers are used in clinical practice. In the temporary spacers, the surgeon first fills the joint cavity with unshaped bone cement which is solidified during surgery. The filling allows the knee to be fixed in a functional position without leaving dead space thus minimizes infection [11]. Articular spacer is used to avoid joint stiffness [12]. Hsu et al. reports a bone cement spacer mold that simplifies and standardizes the spacer fabrication process [13]. In addition, alternative approaches such as use of partial original prosthesis [14], metal spacers [15], and various commercially available products available for clinical application have been reported [16, 17].

Cement spacers are mainly prepared on table during surgery. Currently, there is no consensus on an optimal spacer. Spacer choices mainly depend on preference of the surgeon, balance between hand manufactural convenience, size matching, and functional performance. Most temporary bone cement spacers lack mechanical considerations unlike mature artificial joint prostheses; therefore, they are not conducive for knee functions. This may be an overlook in intraoperative manufactural instructions. Predesigned molds for spacer casting are short in size and models and unable to adapt to severe conditions such as bone defects and ligament insufficiency during revision surgery.

Recent advances in technology have resulted in development of 3D printing technology. Recently, applications of 3D printing technology in orthopaedics have steadily increased. 3D printing enables rapid prototyping based on customs of individual patient, thus improving anatomic matching and mechanical stability. In this study, we designed a complete set of solutions based on rapid prototyping and 3D printing. Further, we used the 3D-assisted solutions to construct antibiotic-loaded bone cement spacer holders for use in two-stage knee revision of PJI. We hypothesized that this 3D printing-assisted solution will facilitate knee revision surgery and provide better clinical effects. We then compared the preliminary outcomes after using 3D-assisted antibiotic-loaded spacers TKR in this study with outcomes of static bone cement spacers obtained in previous studies.

2. Materials and Methods

2.1. Design and Preparation of the Articular Spacer. A prototype of the bone cement spacer (Figure 1) was designed using CAD software (OpenSCAD v2013.01, <http://www.openscad.org/>). The spacer consisted of a femoral component and a tibial component imitating the geometry of a permanent artificial knee joint. Femoral condyles were shaped on both sides to effectively reduce pressure on the soft tissue. The anterior condyle was thin to reduce anterior patellar pressure and avoid anterior patellofemoral pain. The diseased carriage was extended, deepened, and lengthened, to help the patella enter the carriage movement early. Therefore, it reduces the

risk of adverse reactions such as dislocation and ringing after surgery. Tibial side of the AP/ML ratio was designed with reference to anatomical characteristics of the Asian race to provide better platform coverage. Thickness of the tibial platform component was adjustable according to the platform bone deficit, and the tibial platform was tilted 5° posteriorly to provide effective anterior stability. The tibial column was elevated to provide effective posterior stability. Further, the tibial platform sliding interface was designed with a deep disc, sacrificing some range of motion for a joint stability, reducing ligament wear during absenteeism. The platform column was designed to match the intercondylar fossa, allowing for restriction of the occupying apparatus, thus providing lateral stability.

The production process of 3D printing-assisted articulating spacer was as follows. First, CT images of the contralateral knee of the patient were obtained and calculated to confirm the size of the spacer and for designing the casting mold accurately (silicone mold, mold A). The corresponding CAD model was selected from the digital library and resized based on actual needs, and the file was exported in STL format. An entire set of nylon molds (mold B) was then manufactured using a nylon fused deposition modelling (FDM) printer. The silicone solution and curing agent were mixed in a 1:1 mass ratio, stirred under vacuum (100 pa) to remove air bubbles. The solution was poured into the prepared nylon mold (mold B) for casting. The workable time of silica gel is about 20 minutes (at 25°C room temperature); therefore, silica gel should be injected into the nylon mold immediately after removing air bubbles. Stirring of the solution in vacuum should be repeated to remove bubbles if necessary. The silicone was cured in a constant temperature heating oven at 60°C for about 8 hours (increasing the temperature could reduce curing time; however, high temperatures accelerate aging of the silicone). The silicone mold (mold A) was then sterilized by conventional autoclaving (140°C, 60 min) and used in surgery.

Bone cement spacer was prepared on site during surgery. PMMA solution and fluoroscopically photographic crosslink catalyst powder (AGC Style Company Biomet Orthopaedics Inc., Warsaw, USA) were thoroughly mixed, injected, and pressed into the silicone molds with special tools. The composite was placed at room temperature for 8-10 minutes to obtain the complete bone cement spacer. Spacer installation was done during surgery.

2.2. Clinical Data Acquirement. A retrospective study was conducted after obtaining approval from IRB. The experimental design of this study is shown in Figure 2. We performed a chart review using the medical record system. Patients receiving total knee revision surgeries between Jan 2014 and Nov 2019 were included in this study. The inclusion criteria were (1) patients clinically or pathogenically diagnosed with PJI after TKA, (2) patients who underwent 2-stage procedures involving use of an interim antibiotic bone cement spacer, and (3) patients treated with hand-made static spacer or 3D printing assistant articular spacer. The exclusion criteria included (1) patients who received other surgical treatments before (e.g., DAIR and

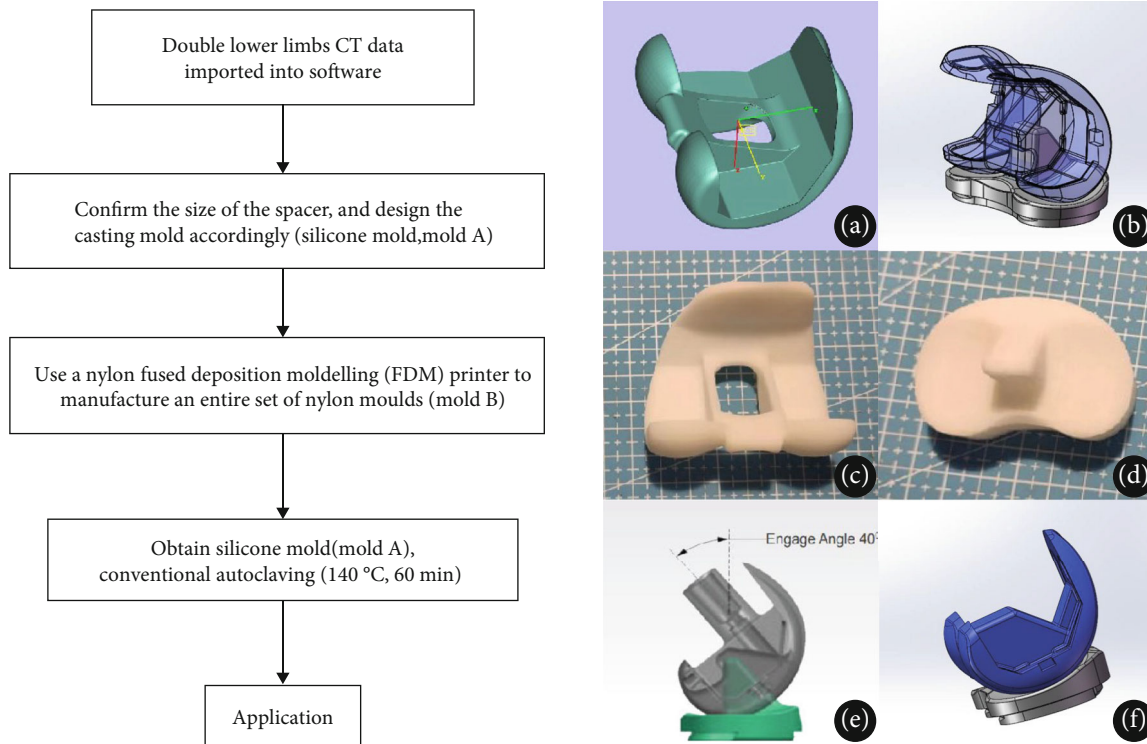


FIGURE 1: The production process and design of 3D printing assisted articulating spacer. (a) The spacer imitates the geometry of a permanent artificial knee joint, and the anterior condyle is thinned to reduce anterior patellar pressure. (b) The diseased carriage is extended, deepened, and lengthened, enabling the patella to enter the carriage movement early. Therefore, patients are less likely to have adverse reactions such as dislocation and ringing after surgery. (c, d) Femoral component and tibial component of the 3D printing-assisted articulating spacer. (e) The tibial column is elevated to provide effective posterior stability. (f) The tibial platform sliding interface is designed with a deep disc, allowing a range of motion for joint stability.

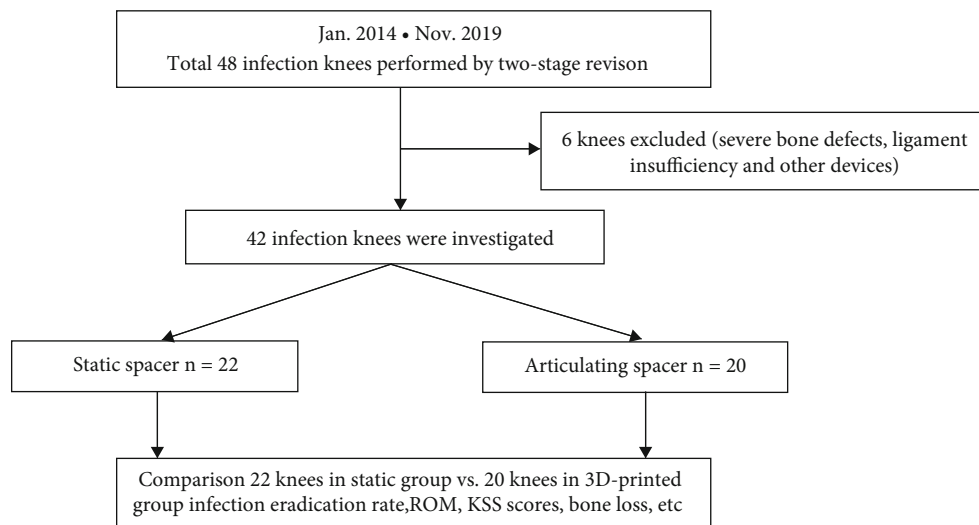


FIGURE 2: Flow chart on the design of this retrospective observational study.

amputation), (2) patients with severe bone defects (>30 mm) and ligament insufficiency before revision surgery, (3) patients who used other devices as interim spacers (e.g., femoral component in hip prosthesis) before the surgery, and (4) patients who failed to complete a 6-month follow-up. Diagnosis of PJI was carried out according to recommendations

by International Consensus Meeting on Peri-prosthetic Joint Infection (ICMPJI) in 2013 [18]. Two reviewers independently screened and decided on inclusion of cases. A third senior doctor made the final decision in case of disagreement.

Patient baseline characteristics, including age, gender, primary disease comorbidities, and pathogenic microorganisms

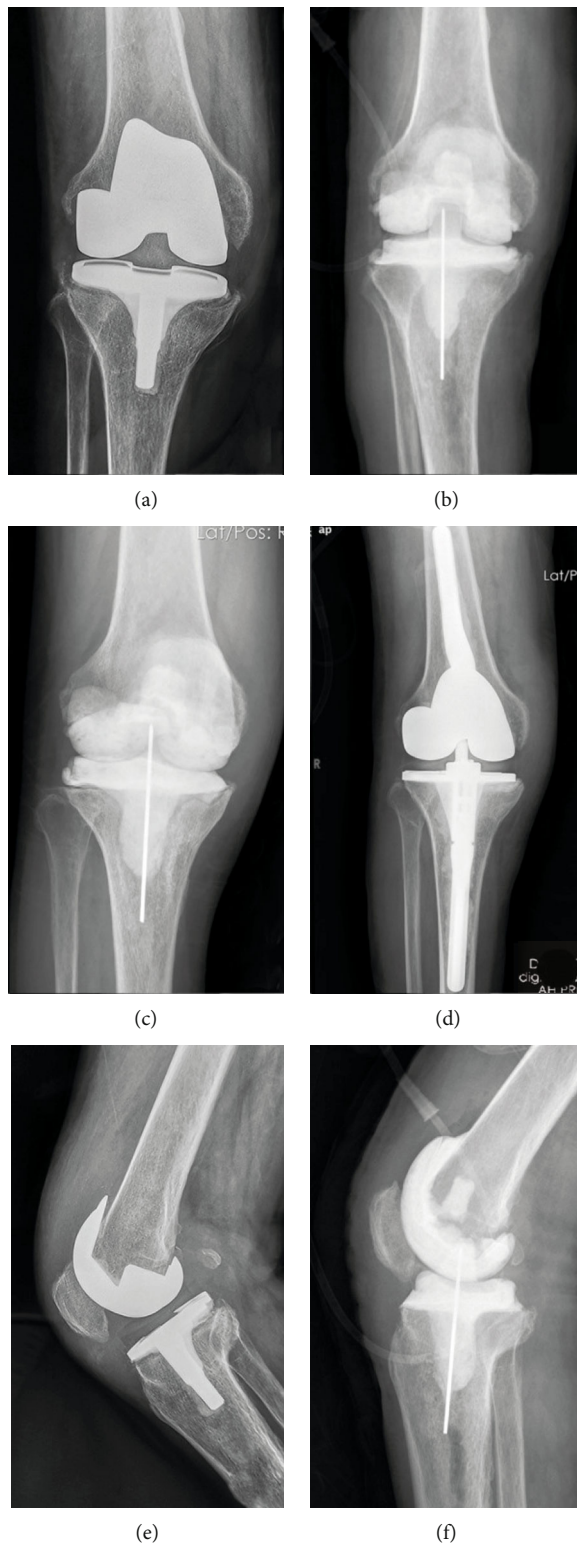


FIGURE 3: Continued.

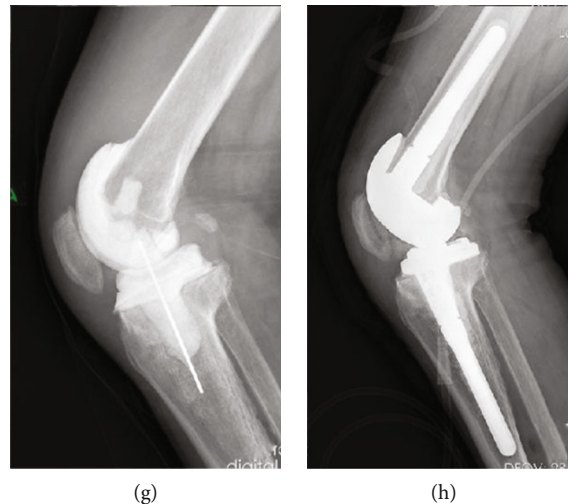


FIGURE 3: (a, e) X-ray films of periprosthetic joint infections. (b, f) X-ray films immediately after insertion of 3D printing-assisted articulating spacer. (c, g) Eight weeks later, X-ray films showed no obvious bone loss. (d, h) X-ray films immediately after the second-stage revision.

were retrieved from the admission assessment form in the medical records. Interval time between two operations, reinfection rates, required tibial tubercle osteotomy in revision surgery, and operation time in second-stage surgery was obtained by searching linked medical records using the unified health record management system. Radiologic images before and after surgery and images obtained from follow-ups were acquired from the hospital picture archiving and communication system (PACS). Bone loss was defined as the distance between original joint line and current remained bone substance. Bone loss was observed and calculated on anteroposterior and lateral X-ray image. Range of motion was measured before discharge from the hospital. Knee flexion deformity exceeding 20° or joint range of motion less than 45° was considered a serious joint mobility disorder. The KSS score system was used to evaluate the patient knee function [19]. The Danish Health and Medicine Authority questionnaire was used for satisfactory evaluation [20]. An overall satisfactory score above 7 showed that the patient was satisfied with the treatment process. Data for questionnaires were obtained during clinical follow-ups or through telephone calls.

2.3. Hospitalization Management. All patients were hospitalized in general wards or infectious units in our joint centre. Preoperative evaluation, blood tests, and pathogen detection were performed after admission. Surgical treatments were divided into two stages. In the first stage, original infection-related prosthesis and bone cement were removed and cultured. Antibiotic loaded bone cement was used as the controlled release system, either through static or articular approach. Patients were given intravenous or oral drugs against infections after debridement surgery until infectious indicators, and bacterial culture was all negative. Patients were then admitted for revision surgery; otherwise, another debridement was performed. Patients received standard rehabilitation schedules between two surgeries and after the final revision.

2.4. Surgical Techniques. Debridement and revision surgeries were performed using original incision. Original prosthesis and bone cements were removed in the 1st stage debridement. Iterative irrigation was performed using 1% iodophor solution, 3% hydrogen peroxide solution, and normal saline after thorough debridement. Antibiotic bone cement was formulated, plasticized, and installed into the cavity of the joint. The antibiotic was prescribed following preoperative pathogen culture and drug-sensitivity test. A broad-spectrum coverage of antibiotic scheme was used for clinically confirmed PJI with negative culture [21]. A mixed formulation containing 1 g vancomycin, 0.8 g meropenem, 0.4 g fluconazole, and 0.3 g isoniazid in every 40 g Heraeus bone cement was used. A silicone tube was placed in the joint cavity for continuous drainage until an effusion less than 50 ml per day was achieved. Static spacer was used to fill the joint cavity between the femur and tibia. 3D printing assistant articular spacer was casted on table using sterile silicone molds as described before. Tibial and femoral component was installed separately using additional adhesive cement. Details on patients who received articular spacer are shown in Figures 3 and 4.

A 2nd revision surgery was performed after the infection was completely controlled. The bone cement spacer was replaced with revision joint replacement prostheses. Proper knee alignment adjustment and soft tissue balancing were performed during the surgery. Cavernous and inclusive bone defects were filled with bone cement, and no-inclusive or structural bone defects were repaired using renovation pads. Tibial tuberosity osteotomy (TTO) was performed for stiff knees.

2.5. Statistical Analysis. Statistical analysis was performed using SPSS, version 20.0 (SPSS Inc., Chicago, Illinois). Normally distributed data were presented as mean \pm standard deviation (SD), whereas non-normally distributed data were presented as median \pm interquartile range (IQR). The paired *t*-test was used to compare changes in postoperative range of motion in each group. The unpaired *t*-test was used to



FIGURE 4: (a) Periprosthetic infection after TKA, abscess is about to break. (e) Installation of 3D printing-assisted articulating spacer. (b, f) The knee joint is straightened and knee flexion is about 85° after spacer insertion. (c, g) Eight weeks later, the knee flexion is about 90° . (d, h) Flexion and straightening function of the knee joint was good after the second stage revision.

compare the KSS score, bone loss, second-stage operation time, and intraoperative blood loss between the two groups. The χ^2 test was used to compare differences in the number of osteotomies, patellar tendon contracture, and reinfection between the two groups.

3. Results

3.1. Patient Characteristics. A total of 48 PJI cases of patients who received two-stage revision surgery after a comprehensive review of medical records between Jan 2014 and Nov 2019 were included in this study. Six knees were excluded as they showed severe bone defects, ligament insufficiency,

and other devices that had been used before. A total of 42 patients with infected knees were included in this study. Out of the 42 cases, 22 patients were treated with static antibiotic cement spacers, whereas the other 20 patients were treated using 3D printing-assisted articulating spacers.

The average age of patients in the static group was 67.2 ± 10.1 years. The mean follow-up period of the static group was 43 months (ranging 30-61 months). The average age of patients in the 3D-printed articulating group was 65.5 ± 11.4 years. The mean follow-up period for the 3D-printed articulating group was 18 months (ranging 8-28 months). The primary conditions for the 42 infected knees were osteoarthritis in 30 knees, rheumatoid arthritis

TABLE 1: Patient baseline data and data during follow-up time.

| | Gender (F/M) | Age (years) | Follow-up time (months) |
|------------------|-----------------|----------------|----------------------------|
| Static group | 7/15 | 67.2 ± 10.1 | 43 (30~61) |
| 3D-printed group | 8/12 | 65.5 ± 11.4 | 18 (8 ~ 28) |

TABLE 2: Pathogen spectrum.

| Organism | Spacer type | |
|----------------------------|--------------|----------------------------|
| | Static group | 3D-printed articular group |
| MSSA | 9 | 7 |
| Staphylococcus epidermidis | 4 | 5 |
| MRSA | 2 | 1 |
| Pseudomonas aeruginosa | 2 | 1 |
| Streptococcus | 1 | 2 |
| Aspergillus species | 0 | 1 |
| Other | 2 | 1 |
| No growth | 2 | 2 |
| Total | 22 | 20 |

MSSA: methicillin susceptible *staphylococcus aureus*; MRSA: methicillin-resistant *staphylococcus aureus*.

in 11 knees, and ankylosing spondylitis in 1 knee. Details on baseline characteristics are summarized in Table 1.

Infection in most of the subjects was completely controlled after single debridement, whereas two patients (one using static spacer and the other using articular spacer) required secondary debridement and change of spacer. All patients recovered after the treatment cycle.

3.2. Pathogen Spectrum. Joint fluid culture showed different sources of bacterial infection. The most common pathogens observed in the cultures were methicillin susceptible *Staphylococcus aureus*, which was found in 16 knees, and *Staphylococcus epidermidis* in 9 knees. A total of 4 knees showed a negative culture. High-throughput sequencing was used to detect the presence of pathogenic bacteria in some cases. Details on pathogen spectrum are shown in Table 2.

3.3. Bone Loss. Bone loss was measured using anterior-posterior and lateral X-ray radiographs as shown in Figure 5. Bone defect over 5 mm under joint line was considered as significant bone loss. Among the 42 knees, all 22 with static spacers had significant bone loss, whereas only 4 patients in the articulating group showed bone loss. The mean femoral bone loss in the static group was 9.6 mm (range, 5-20 mm), whereas tibial bone loss in this group was 5.5 mm (range, 0-10 mm). In the 3D-printed articulating group, the mean femur bone loss was 1.7 mm (range, 0-10 mm), whereas mean tibial bone loss was 1 mm (range, 0-5 mm). Bone loss in the articulating group was significantly lower compared with bone loss in the static group (Table 3).

3.4. Second-Stage Revision. All patients received secondary revision surgery. The average operation time for the static group was significantly higher compared with the average operation time for the articulating group. In addition, the average intraoperative blood loss level of the static group was significantly higher compared with the average blood loss in the articulating group. The average operation time for the static group was 119 minutes (range, 75-150 minutes), whereas the average intraoperative blood loss was 439 ml (range, 250-650 ml). The average operative time of the articulating group was 98 minutes (range, 65-135 minutes), whereas the average intraoperative bleeding level was 358 ml (range, 150-600 ml). Four knees in the static group were administered with TTO due to stiff knee, whereas in the articular group, patients did not require additional TTO.

3.5. Knee Function. The mean ROM of the knee joint was not significantly different between the two groups. A total of 5 patients received static spacer and severe knee movement limitation before operation. In addition, 4 patients received articular spacer. The number of patients who received static spacer and number of patients who received articular spacer was not significantly different. During the interim period, ROM of patients in the static group was almost 0 (0-8°), whereas the average ROM of articular group reached 88° (80°-100°). The average ROM of the static group after the second-stage revision was significantly different from the ROM of the articular group ($p < 0.05$). After the second-stage revision, average ROM in the static group was 80° (70°~110°), whereas the average ROM in the articular group was 94° (80°~115°). After a month and six months after surgery, and at the last follow-up, the joint range of motion in the articular group was significantly higher compared with the joint range of motion of the static group (Figure 6).

The KSS score of patients in the static group was not significantly different from KSS score of patients in the articular group during admission. KSS clinical score, functional score, and total score of patients in the articular group during the interim period were significantly higher compared with the scores in the static group ($p < 0.05$). Notably, KSS clinical score, functional score, and total score of patients in the static group during the interim period were 60 ± 6.3 , 38 ± 3.3 , and 98 ± 8.7 , respectively, whereas the scores for the articular group were 75 ± 11.5 , 42 ± 3.6 , and 117 ± 14.4 . Further, the KSS score after the final revision surgery in the articular was significantly higher compared with the KSS score of the articular group after the final revision surgery. The KSS score of the static group after the final revision surgery was 73 ± 5.8 , 42 ± 4.6 , and 115 ± 9.9 , whereas the KSS score for the articular group after the final revision surgery was 82 ± 3.9 , 49 ± 5.0 , and 131 ± 8.9 . Moreover, the articular group showed higher functional evaluation scores compared with functional evaluation scores for the static group at 1 month, 6 months, and during last follow-up. (Table 3).

3.6. Patient Satisfaction. Fifty-nine % (13/22) of patients in the fixation group reported overall satisfaction during the interim period, whereas in the joint group, ninety-five %

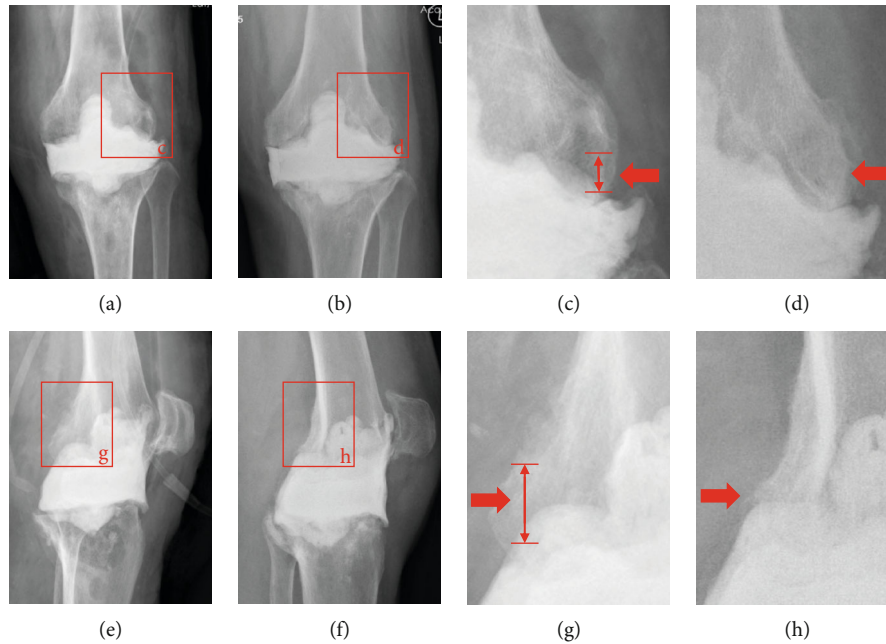


FIGURE 5: (a, e) X-ray films immediately after static spacer insertion. (b, f) Nine weeks later, X-ray films showed bone loss. The upward displacement of the spacer relative to the original joint line is the bone loss of the femur, and the downward displacement of the spacer relative to the joint line is the bone loss of the tibia. (c) and (d) show the amount of bone loss in the distal femur on the anteroposterior X-ray films. (g) and (h) show the amount of bone loss in the distal femur on lateral X-ray films.

(19/20) of patients reported overall satisfaction. The number of patients satisfied with overall treatment in the articular group was significantly higher compared with the number of satisfied patients in the static group ($p < 0.05$). After the final revision surgery, fifty-five % (12/22) of patients in the static group were satisfied with overall treatment, whereas 90% (18/20) of patients in the articular group were satisfied with overall treatment (Table 3).

4. Discussion

In this study, we designed a new articular spacer for two-staged PJI revision using 3D printing technology. Results from the retrospective study show that this new device reduces technical complexity of PJI surgery, improves surgical outcomes, and enhances quality of life of patients.

The recent studies have explored approaches to improve the design and formulation of bone cement spacer [22–24]. Currently, there are no reports on the clinical advantage of using static spacer over articular spacer [25, 26]. Previous studies reported that joint bracing helps in preventing active infections; therefore, treatment of infected arthritis or even PJI should be adequately braced [27]. These findings led to the development and wide use of fixed joint. In addition, a variety of joint spacers are used in clinical practice to simulate the physiological function of the knee to achieve better quality of life. However, due to limitations in industrial advances, production and design of articulated spacers for PJI treatment are poor. Previous studies do not report advantages of articulated spacers over conventional spacers. In this study, we designed a novel articulated spacer using 3D printing technology which improved the quality of the product,

functionality, and strength. In addition, the spacer can be customized to match the size of the bones of the patient. Furthermore, the findings of this study reveals that the novel articular spacer is more effective compared with the gold standard approach.

The infection cure rate of the novel articular spacer developed in this study was not significantly different compared with the cure rate of the fixed spacer. In addition to effective surgical debridement and rational antibiotic formulations, the design of the new spacer improved overall infection resistance compared with the fixed spacer. The morphology of the articulated prosthesis is designed to effectively fit and reduce the dead space in the joint (Figure 1). The cement spacer has a thicker carriage compared with the thin carriage design of metal prostheses; therefore, it improves overall strength and reduces volume of the suprapatellar pouch thus reducing joint effusion. The amount of antibiotic bone cement used in the preparation and installation of each articular spacer in this study was 50-60 g, which is above the 40 g used in the fixed spacer. Asians have a generally smaller body size; therefore, increase in dosage increases overall local antibiotic dosage for the fixed formula concentration. Moreover, the surface area of articular spacer is larger compared with that of static spacer of the same volume, facilitating effective release of antibiotics.

The spectrum of pathogens cultured in this study was similar to that reported in previous study, with high levels of *Staphylococcus aureus* observed [28, 29]. Improving the culture positivity rate of pathogenic bacteria and identifying causative bacteria are important in improving PJI treatment [30]. In the present study, culture-negative cases were observed, and a broad-spectrum antibiotic formulation was

TABLE 3: Comparison of outcomes between the static group and 3D-printed group.

| | Static group (<i>n</i> = 22) | 3D-printed articular group (<i>n</i> = 20) | <i>p</i> value |
|----------------------------------|-------------------------------|---|----------------|
| Interval time (wk) | 13.1 (8-24) | 12.8 (9-22) | 0.75 |
| Interim reinfection rate | 1/22 | 1/20 | 0.95 |
| Bone loss | 22/22 | 4/20 | 0.00 |
| Femoral bone loss(mm) | 9.6 (5 ~ 20) | 1.7 (0 ~ 10) | 0.00 |
| Tibial bone loss(mm) | 5.5 (0 ~ 10) | 1 (0 ~ 5) | 0.00 |
| TTO surgery | 4/22 | 0/20 | 0.04 |
| Second-stage operation time(min) | 119 (75~150) | 98 (65~135) | 0.00 |
| Operation bleeding volume | 439 (250~650) | 358 (150~600) | 0.02 |
| Preoperative KSS | | | |
| Clinical score | 42 ± 5.7 | 40 ± 6.2 | 0.28 |
| Function score | 29 ± 5.7 | 28 ± 5.4 | 0.51 |
| Total score | 71 ± 10.5 | 68 ± 11 | 0.35 |
| Interim KSS | | | |
| Clinical score | 60 ± 6.3 | 75 ± 11.5 | 0.00 |
| Function score | 38 ± 3.3 | 42 ± 3.6 | 0.00 |
| Total score | 98 ± 8.7 | 117 ± 14.4 | 0.00 |
| Postoperative KSS | | | |
| Clinical score | 73 ± 5.8 | 82 ± 3.9 | 0.00 |
| Function score | 42 ± 4.6 | 49 ± 5.0 | 0.00 |
| Total score | 115 ± 9.9 | 131 ± 8.9 | 0.00 |
| Mean ROM (degree) | | | |
| Preoperative ROM | 71 (30~110) | 73 (23~105) | 0.74 |
| Interim ROM | 1 (0 ~ 8) | 88 (80~100) | 0.00 |
| Postoperation ROM | 80 (70~110) | 94 (80~115) | 0.00 |
| Serious joint mobility disorder | 5/22 | 4/20 | 0.83 |
| Reinfection rate | 1/22 | 1/20 | 0.95 |
| Satisfaction rate | 12/22 | 18/20 | 0.01 |

TTO: tibial tuberosity osteotomy; KSS: knee society score; ROM: range of motion.

used for controlled release. These antibiotics are predominantly time-dependent, and some antibiotics have significant postantibiotic effects (e.g., vancomycin, meropenem, and fluconazole) [31, 32]. Rational administration of antibiotics is carried out to ensure prolonged dosage at minimum inhibitory concentrations. Previous study reports that amphotericin B is effective and is not easily affected by resistance in control of fungi and can be added to formulation of controlled release systems. However, amphotericin B is a concentration-dependent drug; therefore, it is more effective when administered as a single high concentration dose.

X-ray analysis carried out in the interim period showed that patients using static spacer had more pronounced bone defects compared with patients using the articular spacer. Severe bone defects observed in the static spacer group may have been caused by limited knee motion and subsequent stress masking the contact area. Bone defects in the static group were mainly noninclusive defects occurring mainly on the tibial plateau side and the distal femur. Bone defects increase the cost of treatment and limit effectiveness of secondary surgical reconstruction.

The new articular spacer also provided favorable conditions for 2nd-stage revision. An articulated spacer-equipped limb maintained mobility and was less likely to develop stiff knee during the exclusion period. Therefore, surgical exposure, spacer removal, clean-up, and soft tissue balancing during the revision surgery are easier in articular spacers compared with static spacers. Patients using the new articular spacer showed less operative time and intraoperative bleeding for phase II revisions. In addition, none of the patients fitted with the articular spacer required a TTO osteotomy, which is technically difficult, time consuming, and is associated with poor prognosis. Previous studies reported that articulating spacer performs better compared with static spacer [33–35].

Previous studies report that the function scores of static spacer are not significantly different from function scores of articular spacer [13, 36, 37]. However, these findings do not report subjective feelings of patients. Use of a static spacer and fixing the knee in an extended position lead to loss of self-care abilities, such as wearing pants and using the toilet as the interim period takes more than two months. The

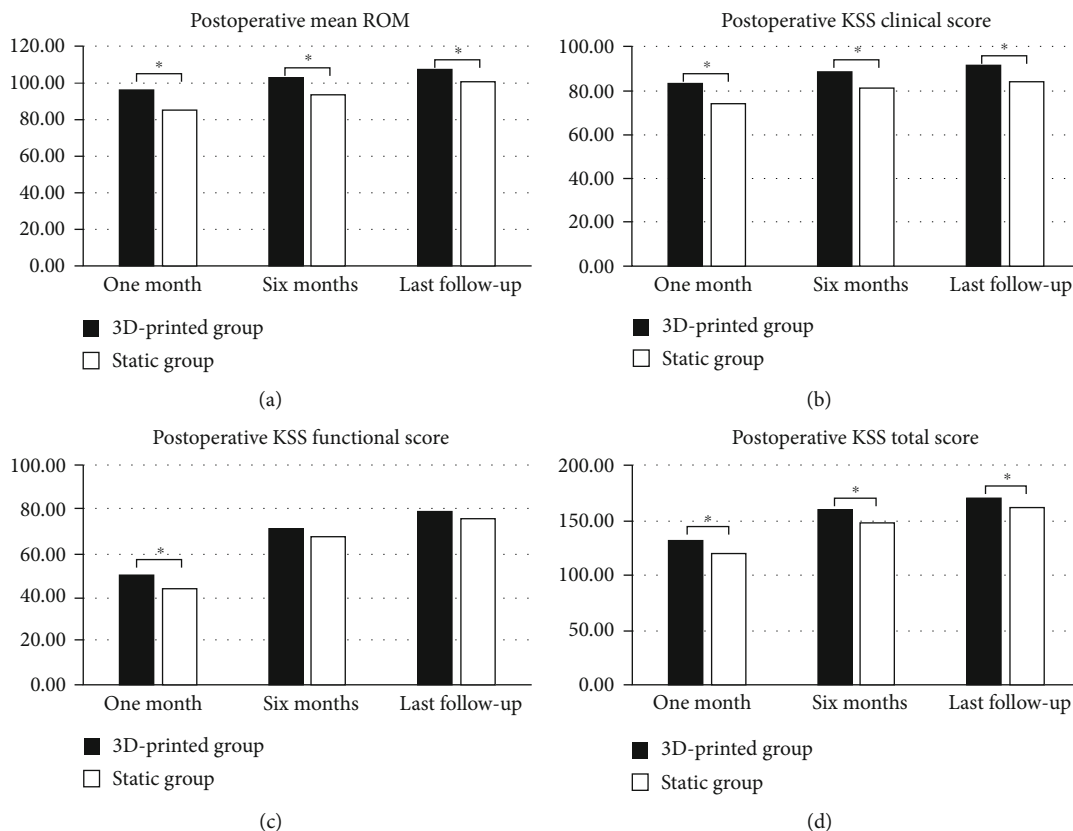


FIGURE 6: (a) Postoperative mean ROM, (b) Postoperative KSS clinical score, (c) postoperative KSS function score, and (d) postoperative KSS total score ($*p < 0.05$).

overall satisfaction of patients using 3D printing-assisted articular spacers was higher compared with that of the control group. High overall satisfaction of patients can be attributed to higher early postoperative function scores and better joint function during the interim period.

Spacers designed in advance before surgery have a smoother friction interface, a more stable mechanical structure, and a better interim period joint function compared with hand-made bone cement spacers (static or articular spacers). However, spacers designed before surgery are few in the market. The model size of the mold of available commercial spacer types is limited. Traditional methods of manufacturing spacer molds are complicated and expensive, and it is difficult to customize products for a single patient. Use of 3D printing increases efficiency of spacer production and reduces the cost of production.

However, use of this technique has potential risks. There is no clinical evidence using in vivo studies to support long-term use of bone cement cast spacers. Long-term wear of the friction interface of PMMA material may loosen the articular spacer and cause instability of the joints. In addition, presence of worn particles is in the human body. In this study, the longest interim period was 4 months, and no visible particles or osteolysis symptoms were found at the 2nd revision. Secondly, use of self-made surgical tools should follow local medical laws and regulations, or approval from relevant authorities (such as FDA). Further-

more, this study had some limitations. Firstly, this is a retrospective study, and clinicians were not blinded to the type of spacer used when collecting data. Secondly, a low number of patients were recruited to the study. In addition, the length of follow-up time of the two groups was different. This is an unavoidable defect in a retrospective study comparing a new technique to a conventional one, but study shows knee functions seldomly change around 12 months after TKA surgery, and we assume that the functional outcomes are comparable at the time point we selected. These limitations may lead to potential bias in our results. Prospective randomized controlled trials with a larger number of cases and longer follow-up periods should be carried out to confirm effectiveness of articular spacers in PJI treatment.

5. Conclusion

This study reports preliminary findings of using 3D-printed articulating antibiotic cement spacer. The findings provide a new method for production of effective and personalized spacers. Articular spacer provides satisfactory range of motion during the interim period, prevents bone loss, facilitates second-stage reimplantation and postoperative rehabilitation, and results in low reinfection and complication rates. This technique could be considered to in a 2-stage revision surgery.

Data Availability

The data used to support the findings of this study are available from the corresponding author upon request.

Ethical Approval

This study was approved by the ethics committee of the First Affiliated Hospital of USTC. An optout of the informed consent, information disclosure, and a negative opportunity is guaranteed in the Ethical approval.

Consent

All the patients included in this study gave informed consent for the article to be published.

Conflicts of Interest

Authors declare that they have no conflicts of interest.

Authors' Contributions

XZ conceived and designed the study. LK collected the data and performed the statistical analysis. LK, JM, and WG wrote the manuscript. XJ and XC provided the 3D printing technique support. CZ provided funding and administrative support. All authors read and approved the final manuscript. Lingtong Kong, Jiawei Mei, and Wufei Ge contributed equally to this work.

Acknowledgments

This study was supported by the National Natural Science Foundation of China (Grant No. 81871788), the Project for Science and Technology leader of Anhui Province (Grant No. 2018H177), Scientific Research Fund of Anhui Education (Grant No. 2017jyxm1097), Anhui Provincial Postdoctoral Science Foundation (Grant No. 2019B302), the Fundamental Research Funds for the Central Universities (WK9110000173) and Key Research and Development Plan of Anhui Province (Grant No. 912278014064).







References

- [1] A. J. Price, A. Alvand, A. Troelsen et al., "Knee replacement," *Lancet*, vol. 392, no. 10158, pp. 1672–1682, 2018.
- [2] A. J. Carr, O. Robertsson, S. Graves et al., "Knee replacement," *Lancet*, vol. 379, no. 9823, pp. 1331–1340, 2012.
- [3] M. Varacallo, T. D. Luo, and N. A. Johanson, *Total knee arthroplasty (TKA) techniques*, StatPearls, Treasure Island (FL), 2020.
- [4] B. H. Kapadia, R. A. Berg, J. A. Daley, J. Fritz, A. Bhave, and M. A. Mont, "Periprosthetic joint infection," *Lancet*, vol. 387, no. 10016, pp. 386–394, 2016.
- [5] A. R. Cochran, K. L. Ong, E. Lau, M. A. Mont, and A. L. Malkani, "Risk of reinfection after treatment of infected Total knee Arthroplasty," *The Journal of Arthroplasty*, vol. 31, no. 9, pp. 156–161, 2016.
- [6] H. Dale, A. M. Fenstad, G. Hallan et al., "Increasing risk of prosthetic joint infection after total hip arthroplasty," *Acta Orthopaedica*, vol. 83, no. 5, pp. 449–458, 2012.
- [7] N. S. Nagra, T. W. Hamilton, S. Ganatra, D. W. Murray, and H. Pandit, "One-stage versus two-stage exchange arthroplasty for infected total knee arthroplasty: a systematic review," *Knee Surgery, Sports Traumatology, Arthroscopy*, vol. 24, no. 10, pp. 3106–3114, 2016.
- [8] A. Siddiqi, N. E. George, P. B. White et al., "Articulating spacers as a modified one-stage revision total knee arthroplasty: a preliminary analysis," *Surgical Technology International*, vol. 32, pp. 239–248, 2018.
- [9] J. Lu, J. Han, C. Zhang, Y. Yang, and Z. Yao, "Infection after total knee arthroplasty and its gold standard surgical treatment: spacers used in two-stage revision arthroplasty," *Intractable & rare diseases research*, vol. 6, no. 4, pp. 256–261, 2017.
- [10] D. R. Osmon, E. F. Berbari, A. R. Berendt et al., "Diagnosis and management of prosthetic joint infection: clinical practice guidelines by the Infectious Diseases Society of America," *Clinical Infectious Diseases*, vol. 56, no. 1, pp. e1–e25, 2013.
- [11] A. D. Hanssen and M. J. Spanghel, "Practical applications of antibiotic-loaded bone cement for treatment of infected joint replacements," *Clinical Orthopaedics and Related Research*, vol. 427, pp. 79–85, 2004.
- [12] A. A. Hofmann, K. R. Kane, T. K. Tkach, R. L. Plaster, and M. P. Camargo, "Treatment of infected total knee arthroplasty using an articulating spacer," *Clinical Orthopaedics & Related Research*, vol. 321, pp. 45–54, 1995.
- [13] Y. C. Hsu, H. C. Cheng, T. P. Ng, and K. Y. Chiu, "Antibiotic-loaded cement articulating spacer for 2-stage reimplantation in infected total knee arthroplasty: a simple and economic method," *The Journal of Arthroplasty*, vol. 22, no. 7, pp. 1060–1066, 2007.
- [14] E. Jämsen, P. Sheng, P. Halonen et al., "Spacer prostheses in two-stage revision of infected knee arthroplasty," *International Orthopaedics*, vol. 30, no. 4, pp. 257–261, 2006.
- [15] M. Gathen, J. Schmolders, M. D. Wimmer et al., "Modular arthrodesis system TITAN (KAM-TITAN) after failed revision total knee arthroplasty: operative technique and clinical experience," *Operative Orthopädie und Traumatologie*, vol. 32, no. 1, pp. 58–72, 2020.
- [16] A. A. Shaikh, C. W. Ha, Y. G. Park, and Y. B. Park, "Two-stage approach to primary TKA in infected arthritic knees using intraoperatively molded articulating cement spacers," *Clinical Orthopaedics and Related Research*, vol. 472, no. 7, pp. 2201–2207, 2014.
- [17] L. C. Warth, C. J. Hadley, and E. L. Grossman, "Two-stage treatment for Total knee Arthroplasty infection utilizing an articulating prefabricated antibiotic spacer," *The Journal of Arthroplasty*, vol. 35, no. 3, pp. S57–S62, 2020.
- [18] H. J. Cooper and C. J. Della Valle, "The two-stage standard in revision total hip replacement," *The bone & joint journal*, vol. 95-B, 11 Supplement A, pp. 84–87, 2013.
- [19] W. Lopez-Aqueres, B. Kemp, M. Plopper, F. R. Staples, and K. Brummel-Smith, "Health needs of the Hispanic elderly," *Journal of the American Geriatrics Society*, vol. 32, no. 3, pp. 191–198, 1984.
- [20] H. Husted, H. C. Hansen, G. Holm et al., "Accelerated versus conventional hospital stay in total hip and knee arthroplasty III: patient satisfaction," *Ugeskrift for Laeger*, vol. 168, no. 22, pp. 2148–2151, 2006.

- [21] J. Wang, Q. Wang, H. Shen, and X. Zhang, "Comparable outcome of culture-negative and culture-positive periprosthetic hip joint infection for patients undergoing two-stage revision," *International Orthopaedics*, vol. 42, no. 3, pp. 469–477, 2018.
- [22] M. Villanueva, A. Ríos, J. Pereiro, F. Chana, and H. Fahandez-Saddi, "Hand-made articulating spacers for infected total knee arthroplasty: a technical note," *Acta Orthopaedica*, vol. 77, no. 2, pp. 329–332, 2006.
- [23] Y. P. Su, O. K. Lee, W. M. Chen, and T. H. Chen, "A facile technique to make articulating spacers for infected total knee arthroplasty," *Journal of the Chinese Medical Association*, vol. 72, no. 3, pp. 138–145, 2009.
- [24] S. M. Sporer, "Spacer design options and consideration for periprosthetic joint infection," *The Journal of Arthroplasty*, vol. 35, no. 3, pp. S31–S34, 2020.
- [25] P. B. Voleti, K. D. Baldwin, and G. C. Lee, "Use of static or articulating spacers for infection following total knee arthroplasty: a systematic literature review," *The Journal of Bone and Joint Surgery. American Volume*, vol. 95, no. 17, pp. 1594–1599, 2013.
- [26] M. Citak, M. Citak, and D. Kendoff, "Dynamic versus static cement spacer in periprosthetic knee infection: a meta-analysis," *Orthopade*, vol. 44, no. 8, pp. 599–606, 2015.
- [27] R. M. Meek, D. Dunlop, D. S. Garbuz, R. McGraw, N. V. Greidanus, and B. A. Masri, "Patient satisfaction and functional status after aseptic versus septic revision total knee arthroplasty using the PROSTALAC articulating spacer," *The Journal of Arthroplasty*, vol. 19, no. 7, pp. 874–879, 2004.
- [28] D. Zajonz, L. Wuthe, A. C. Rodloff et al., "Infektionen von Hüft- und Knieendoprothesen," *Chirurg*, vol. 87, no. 4, pp. 332–339, 2016.
- [29] T. Rosteius, O. Jansen, T. Fehmer et al., "Evaluating the microbial pattern of periprosthetic joint infections of the hip and knee," *Journal of Medical Microbiology*, vol. 67, no. 11, pp. 1608–1613, 2018.
- [30] J. H. J. van Erp, A. C. Heineken, R. J. A. van Wensen et al., "Optimization of the empirical antibiotic choice during the treatment of acute prosthetic joint infections: a retrospective analysis of 91 patients," *Acta Orthopaedica*, vol. 90, no. 5, pp. 455–459, 2019.
- [31] V. Post, P. Wahl, R. G. Richards, and T. F. Moriarty, "Vancomycin displays time-dependent eradication of mature *Staphylococcus aureus* biofilms," *Journal of Orthopaedic Research*, vol. 35, no. 2, pp. 381–388, 2017.
- [32] D. J. Tennent, S. M. Shiels, C. J. Sanchez Jr. et al., "Time-dependent effectiveness of locally applied Vancomycin powder in a contaminated traumatic orthopaedic wound model," *Journal of Orthopaedic Trauma*, vol. 30, no. 10, pp. 531–537, 2016.
- [33] E. C. Bowman and A. L. Malkani, "Point/Counterpoint: Static vs Articulating Spacers—Static Spacers for Resection Arthroplasty of the Knee," *The Journal of Arthroplasty*, vol. 35, no. 3, pp. S35–S39, 2020.
- [34] P. M. Preobrazhensky, S. A. Bozhkova, A. V. Kazemirsky, R. M. Tikhilov, T. A. Kulaba, and N. N. Kornilov, "Functional outcome of two-stage reimplantation in patients with periprosthetic joint infection after primary total knee arthroplasty," *International Orthopaedics*, vol. 43, no. 11, pp. 2503–2509, 2019.
- [35] C. R. Nahhas, P. N. Chalmers, J. Parvizi et al., "A randomized trial of static and articulating spacers for the treatment of infection following total knee arthroplasty," *The Journal of Bone and Joint Surgery. American Volume*, vol. 102, no. 9, pp. 778–787, 2020.
- [36] H. Ding, J. Yao, W. Chang, and F. Liu, "Comparison of the efficacy of static versus articular spacers in two-stage revision surgery for the treatment of infection following total knee arthroplasty: a meta-analysis," *Journal of Orthopaedic Surgery and Research*, vol. 12, no. 1, 2017.
- [37] M. G. Freeman, T. K. Fehring, S. M. Odum, K. Fehring, W. L. Griffin, and J. B. Mason, "Functional advantage of articulating versus static spacers in 2-stage revision for total knee arthroplasty infection," *The Journal of Arthroplasty*, vol. 22, no. 8, pp. 1116–1121, 2007.

Research Article

In-Hospital 3D Printed Scaphoid Prosthesis Using Medical-Grade Polyetheretherketone (PEEK) Biomaterial

Philipp Honigmann ^{1,2,3}, Neha Sharma ^{2,4}, Ralf Schumacher ⁵, Jasmine Rueegg ⁵,
Mathias Haefeli ^{3,6} and Florian Thieringer ^{2,4}

¹Hand Surgery, Cantonal Hospital Baselland, Rheinstrasse 26, 4410 Liestal, Switzerland

²Medical Additive Manufacturing Research Group, Department of Biomedical Engineering, University of Basel, Gewerbestrasse 16, 4123 Allschwil, Switzerland

³Amsterdam UMC, University of Amsterdam, Department of Biomedical Engineering and Physics, Amsterdam Movement Sciences, Meibergdreef 9, Amsterdam, Netherlands

⁴Department of Oral and Cranio-Maxillofacial Surgery, University Hospital Basel, Spitalstrasse 21, 4031 Basel, Switzerland

⁵Medartis AG, Hochbergerstrasse 60 E, 4057 Basel, Switzerland

⁶Hand Surgery, Cantonal Hospital of Grisons, Loenstrasse 170, 7000 Chur, Switzerland

Correspondence should be addressed to Philipp Honigmann; philipp.honigmann@ksbl.ch

Received 9 June 2020; Revised 3 November 2020; Accepted 26 December 2020; Published 12 January 2021

Academic Editor: Liu Yang

Copyright © 2021 Philipp Honigmann et al. This is an open access article distributed under the Creative Commons Attribution License, which permits unrestricted use, distribution, and reproduction in any medium, provided the original work is properly cited.

Recently, three-dimensional (3D) printing has become increasingly popular in the medical sector for the production of anatomical biomodels, surgical guides, and prosthetics. With the availability of low-cost desktop 3D printers and affordable materials, the in-house or point-of-care manufacturing of biomodels and Class II medical devices has gained considerable attention in personalized medicine. Another projected development in medical 3D printing for personalized treatment is the in-house production of patient-specific implants (PSIs) for partial and total bone replacements made of medical-grade material such as polyetheretherketone (PEEK). We present the first in-hospital 3D printed scaphoid prosthesis using medical-grade PEEK with fused filament fabrication (FFF) 3D printing technology.

1. Introduction

Additive manufacturing, also known as three-dimensional (3D) printing, is a growing trend in the medical field. Even though 3D printing technology is over 30 years old. This aspect is distinctly evident with an exponential increase in the number of publications on 3D printing in the medical specialties, especially in the orthopedic field [1, 2].

Medical 3D printing has entirely transformed the current era of personalized medicine with its state-of-art usefulness and applications. With the utilization of consumer-level desktop 3D printers in hospitals, 3D printing offers several medical and clinical applications including, but not limited to, anatomical, pathological fracture, and tumor biomodels,

customized surgical tools, and prosthetic aids [3–8]. This technology can build a 3D object by creating complex, customized anatomical and medical structures as defined in a computer-aided design (CAD) digital file. In a basic technical setup, the two-dimensional (2D) Digital Imaging and Communications in Medicine (DICOM) medical imaging datasets are converted into 3D data, which are transferred to a 3D printer. An illustration of an in-house 3D printed biomodel for a distal intra-articular radius fracture case, fabricated via a fused filament fabrication (FFF) 3D printing technology using cone-beam computed tomography (CBCT) DICOM dataset, is shown in Figure 1 [9].

While the fabrication of biomodels is easily conceivable at the point-of-care, the production of Class II medical devices



FIGURE 1: In-house printed fracture model using an FFF consumer-level desktop 3D printer (MakerBot Replicator+, MakerBot Brooklyn, New York City, New York, USA).

such as surgical guides that come in contact with the patient's blood was usually outsourced to external sources. These medical devices need to be printed with certified biocompatible materials requiring expensive professional certified 3D printers, which were not affordable to many hospitals, and therefore, these products were often printed externally by certified companies [2]. However, recently with the availability of in-house 3D printing setups and affordable desktop 3D printers, the fabrication of surgical guides has slowly shifted from external service providers to the hands of the clinicians. Another projected development in medical 3D printing for personalized treatment is the in-house fabrication of patient-specific implants (PSIs) such as osteosynthesis plates and prosthesis.

With a significant change from the old mass-production system of medical implants to the PSI production system, 3D printing has attained an essential place in the medical implant manufacturing industry. In consideration of the evolving technological trends in personalized medicine, we investigated the printing feasibility of medical-grade polyetheretherketone (PEEK) biomaterial, especially for the production of PSIs in a hospital environment. Our preliminary results were promising, which contributed towards the progression of an FFF PEEK 3D printer solely designed for medical PEEK applications [10]. Later in 2018, Honigmann et al. presented the first cadaveric results of a patented 3D printed titanium patient-specific scaphoid prosthesis [11]. This patient-specific prosthesis was designed for cases of nonreconstructable scaphoids because of nonunion or trauma.

More recently, the use of polymer as an alternative to metallic biomaterials is being explored. PEEK meets the perfect criteria for the orthopedic field as a printable material for PSIs [12]. It is a lightweight, biocompatible, nontoxic, and noninflammable biomaterial exhibiting excellent mechanical strength [13]. The osteoconductive properties of PEEK support the bone integration process [14]. Moreover, PEEK is radiolucent in X-ray imaging with no relevant artifacts, providing computed tomography (CT) and magnetic resonance imaging (MRI) compatibility. These inherent advantageous characteristics of PEEK, along with the capability to print medical-grade PEEK in a certified 3D printer, make this

material an attractive option suitable for 3D printed PSIs at the hospital or point-of-care manufacturing [10]. Therefore, in this article, we present the preliminary results on the first in-house 3D printed scaphoid prosthesis made of medical-grade PEEK fabricated via material extrusion (FFF) 3D printing.

2. Materials and Methods

2.1. Computer-Aided Design Modeling of the Scaphoid Prosthesis. The anatomical department provided a Thiel conserved wrist with no degenerative changes or posttraumatic changes. A multislice CT scan (Biograph mCT Flow™, Siemens Medical Solutions USA Inc., Malvern, USA) was used to acquire the DICOM dataset. The DICOM files were processed in a medically certified image processing software (Mimics®, Materialise, Leuven, Belgium) to generate a 3D volumetric reconstruction model of the scaphoid. The native surface of the generated 3D model was smoothed, and mesh repairing procedures such as fixing holes were executed in a CAD software (3DS Geomagic Freeform®, Rock Hill, USA) (Figure 2). Finally, a curved channel was designed inside the scaphoid 3D model in accordance with the patented design (Figure 3) [15, 16]. The CAD file of the designed prosthesis is finally converted and saved in a standard tessellation language (STL) file format.

2.2. FFF PEEK 3D Printer. The FFF 3D printer used for fabrication of scaphoid prosthesis was an Apium M220, a third-generation desktop printer explicitly designed for PEEK medical additive manufacturing (Apium Additive Technologies GmbH, Karlsruhe, Germany) (Figure 4). It is intended to produce PSIs in a hospital environment according to the biocompatibility standard ISO 10993 [17]. The printer incorporates an advanced temperature management system, which controls the temperature during the printing process in a layer-by-layer fabrication manner. In addition, to prevent contamination, a constant influx of hot airflow is integrated into the printer which filters the atmosphere around the 3D printed part during the fabrication process. The technical specifications of the PEEK FFF 3D printer are listed in Table 1.

2.3. PEEK Filament. Due to the physical properties of PEEK biomaterial, FFF 3D printing is a challenge, and it usually requires an iterative process to print the test samples [13, 18]. Therefore, from an economic perspective, the printing feasibility of PEEK scaphoid prosthesis was initially conducted with an industrial-grade 1.75 mm PEEK filament (Apium 4000 natural, Apium Additive Technologies GmbH, Karlsruhe, Germany). Once established, a medical-grade 1.75 mm diameter PEEK filament developed from Vestakeep® i4 G resin (Evonik Vestakeep®i4 G resin, Evonik Industries AG, Essen, Germany) was used for the fabrication of scaphoid prosthesis. This filament is an implant-grade material that meets the ASTM F2026-17 guidelines—Standard specification for Polyetheretherketone (PEEK) Polymers for Surgical Implant Applications [19, 20]. It is a natural-colored, high-viscosity, and high-performance PEEK

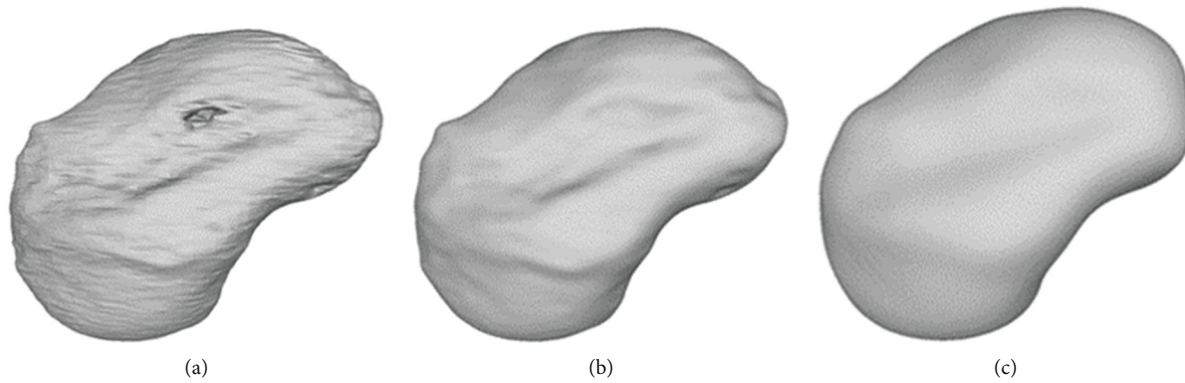


FIGURE 2: Surface smoothing of the scaphoid prosthesis: (a) native; (b) filled holes; (c) final smoothed surface.

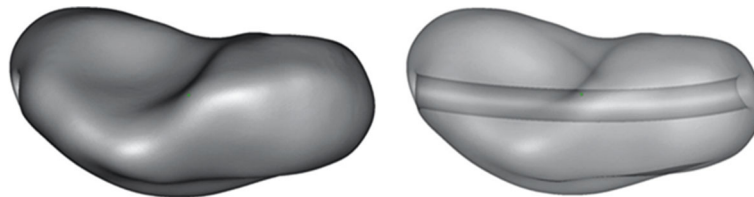


FIGURE 3: Design of the curved channel in the scaphoid prosthesis.

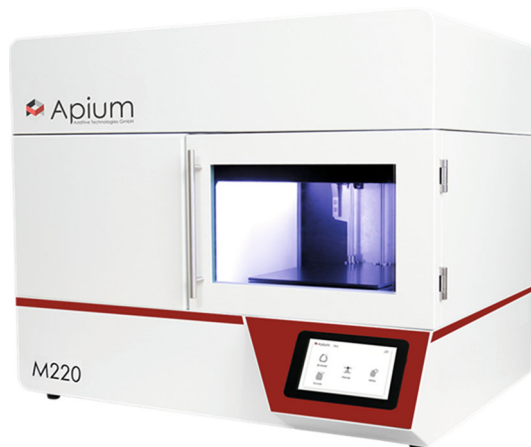


FIGURE 4: FFF PEEK 3D printer (Apium Additive Technologies GmbH, Karlsruhe, Germany).

polymer widely used for long-term implantable medical devices. The material is supplied either directly as a filament on a spool or as cylindrical pellets, which is used for extrusion (FFF) processing technologies to manufacture the PEEK filament. The medical-grade PEEK filament has a density of 1.30 g/cm^3 , a melting temperature of $\sim 340^\circ\text{C}$, and a glass transition temperature of $\sim 135\text{-}155^\circ\text{C}$. Besides, the material is very tolerant to gamma radiation, stable against hydrolysis, and suitable for autoclave sterilization process.

2.4. FFF PEEK 3D Printing Process Parameters. The STL file of the scaphoid prosthesis was imported into a commercially available slicing software (Simplify 3D version 4.0, Cincinnati, USA). To prevent collapse and ensure optimal printing, temporary support structures were generated underneath the prosthesis in this software (Figure 5(a)).

TABLE 1: Technical specifications of the FFF PEEK 3D printer.

| Parameter | Technical specifications |
|-------------------------------|---|
| Number of extruders | 1 |
| Nozzle diameter (mm) | 0.4 |
| Filament diameter (mm) | 1.75 |
| Print volume | 132 mm × 132 mm × 120 mm |
| Temperature management system | Full metal hot end with heating up to 540°C Controlled airflow temperature up to 200°C |
| Print bed material | 316L stainless steel |
| Machine operation software | Apium control software |
| Slicing software compatible | Simplify 3D |

Finally, the STL file was digitally sliced with the respective printing parameters to generate a g-code file (Figure 5(b)), which was later on sent to the 3D printer software for printing. The printing parameters used for the light-colored industrial PEEK (Apium PEEK 4000, Apium Additive Technologies GmbH, Karlsruhe, Germany) were similar to the darker medical-grade PEEK filament (Evonik Vestakeep®i4 G resin, Evonik Industries AG, Essen, Germany). The printing parameters selected for the fabrication process are listed in Table 2. To increase the adhesion between the scaphoid prosthesis and the print bed, automatic raft generation functionality integrated into the printer's software was used.

3. Results

The total printing time for each scaphoid prosthesis was 1 hour and 52 minutes. After printing, the support structures were manually removed, and the scuff marks were trimmed

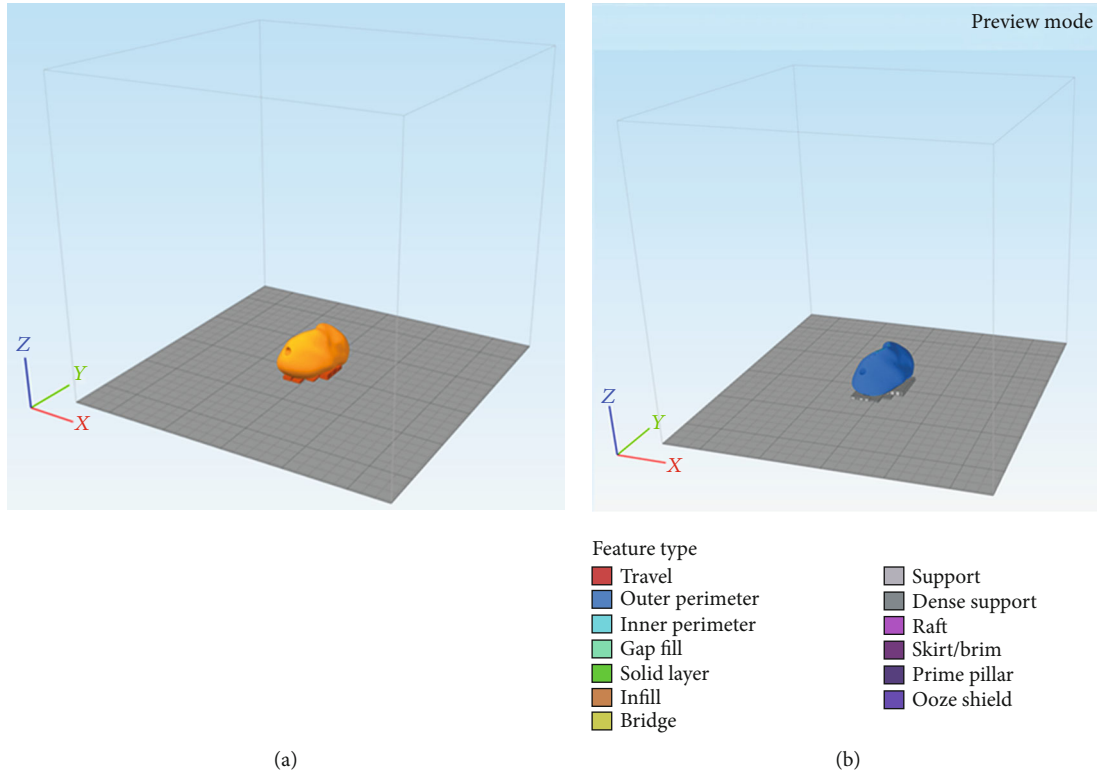


FIGURE 5: Orientation of the scaphoid prosthesis on the 3D printer's build platform in the 3D slicing software: (a) addition of support structures; (b) g-code generation with selected printing parameters.

TABLE 2: Printing parameters selected for FFF 3D printed PEEK scaphoid prosthesis.

| | |
|--------------------------------|-------------|
| <i>Extruder</i> | |
| Nozzle diameter (mm) | 0.4 |
| <i>Temperature</i> | |
| Extruder temperature (°C) | 485 |
| Airflow temperature (°C) | 170 |
| <i>Layer</i> | |
| 1st layer height (mm) | 0.1 |
| Top solid layers | 4 |
| Bottom solid layer | 4 |
| Outline/perimeter shells | 2 |
| <i>Infill</i> | |
| Internal fill pattern | Rectilinear |
| External fill pattern | Rectilinear |
| Interior fill percentage | 80% |
| Raster angle | 45/-45 |
| <i>Support</i> | |
| Support infill percentage | 40% |
| Support pillar resolution (mm) | 4 |
| <i>Speed (mm/min)</i> | |
| Printing speed | 1500 |

off from the prosthesis. The prints of the prosthesis shown in Figure 6 were not further postprocessed. The scaphoid prosthesis on the left (light-colored) was printed with industrial-grade PEEK filament (Apium 4000), while the prosthesis on the right was printed in medical-grade implantable PEEK biomaterial (Evonik Vestakeep®i4 G resin). No black speck formation or discoloration (improper crystallization) was detected in the test parts. Unlike the industrial-grade 3D printed PEEK scaphoid prosthesis, the surface of the medical-grade PEEK printed version did not display the classical “FFF stair-stepping” phenomenon. Moreover, the articular surfaces and the edges at the channel opening had a smoother finish, which is mandatory to articulate with the cartilage and guide the tendon graft in a frictionless manner.

4. Discussion

We report on the first results of a medical-grade 3D printed patient-specific scaphoid prosthesis fabricated at the point-of-care manufacturing. In recent years, material extrusion-based 3D printing of PEEK has achieved a considerable amount of attention for in-house production. The precision of FFF 3D printers has considerably improved and is almost equal to industrial 3D printing technologies for polymers [21]. With the development and availability of medical-grade PEEK filament, it is possible to use FFF 3D printing technology for the production of patient-specific Class III implants for various surgical applications [10]. FFF PEEK 3D printing has certain advantages over other subtractive manufacturing processes, such as milling or injection

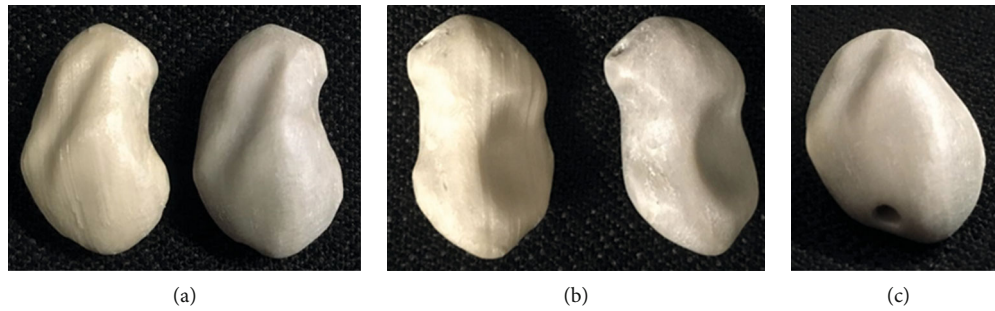


FIGURE 6: FFF 3D printed scaphoid prosthesis made of industrial-grade (light-colored) and medical-grade (dark-colored) PEEK: (a) radial aspect; (b) ulnar aspect; (c) proximal pole with exit orifice of the channel.

molding. In a milling process, the amount of waste generation is considerably high. Moreover, the fabrication of complex structures such as the curved channel in the patented scaphoid prosthesis is not possible. The injection molding technique requires less material; however, the technology is more suitable for mass production, and its use in patient-specific or customized implant production is limited [10].

The three major standard organizations that drive the advancement and innovation in medical devices are the ASTM International, the International Standards Organization (ISO), and the Association for the Advancement of Medical Instrumentation (AAMI). These organizations develop consensus technical standards for a wide range of materials, including PEEK [19]. Besides, the Food and Drug Administration (FDA) has recognized some standards for PEEK medical products. It states that by conforming to the abovementioned technical standards, the manufacturer is exempt from the fundamental material property submission reports [20]. In point-of-care manufacturing, maintaining high efficacy and manufacturing quality of the printed parts are of paramount importance and one of the fundamental tasks in compliance with these regulations. Therefore, specific operational and regulatory standards should be established to assess whether the intended 3D printed part conforms to its clinical use. Furthermore, standard organization-based certification for quality management protocols (ISO 13485) including a risk-based approach (ISO 14971) for the whole process, including data conversion, modeling, 3D printing and all post-processes should be integrated into a hospital environment.

PEEK is suitable for orthopedic implants, which are in direct contact with the bone. It is considered as an alternative material in total hip arthroplasty, to avoid metal-metal debris and to minimize the risk of particle-induced aseptic implant loosening [22, 23]. In hand and wrist surgery, PEEK-related complications, such as foreign body synovitis, can occur in a total wrist arthroplasty because of the shearing forces on the implant [24]. Our task as a research lab was to demonstrate and illustrate the possibility of FFF PEEK 3D printing in a hospital environment. The study results show a smoother integration and faster production potential for in-house PEEK PSI manufacturing. Furthermore, as FFF 3D printed parts are anisotropic, appropriate orientation of the scaphoid prosthesis on the 3D printer's build platform concerning its clinical use should be considered. As adhesion is

made layer by layer, the printed part will be less weak if the force is applied 90° to the layer and much stronger if the forces are applied along the layer direction, whereas if the center of rotation of the scapholunate axis is oriented perpendicular to the printed layers, the forces of transmission will be in the axial direction. Therefore, we chose the specific orientation of the scaphoid prosthesis for 3D printing [25]. The suspension of the prosthesis is maintained through a fiber-wire augmented tendon graft, which is passed through the curved channel. A rough surface inside the channel could lead to a better connection between the tendon and the PEEK surface. The well-known osseointegration abilities of PEEK into the bone might also contribute to the adhesion between the tendon and the PEEK surface [23, 26–28].

The in-hospital production of PEEK itself by FFF 3D printing is technically demanding and requires a lot of experience especially in the field of FFF 3D printing technology. The printer needs meticulous inspections and maintenance to secure a stable, reliable, and reproducible printing environment to perfectly maintain the print parameters listed in Table 2 during the printing process. If not maintained appropriately, formation of irregularities, color changes, and delamination can potentially develop in the printed parts, which suggest uncontrollable thermodynamically driven changes during the printing process.

Finally, with this proof of concept, further studies regarding the biomechanical properties of the postprocessed patented PEEK scaphoid prosthesis to evaluate the joint cartilage and the channel-tendon graft interface are required. Investigations on the wear properties of PEEK bearing combinations in total knee arthroplasties have shown a cross-shear dependency of PEEK when articulating on hard surfaces such as metal. Therefore, we have the impression that the joint cartilage-PEEK interface depends on the smoothness of the surface of the implant, like in pyrocarbon or titanium implants for carpal bone replacement [29–31]. These types of cartilage damage due to the surface characteristics are underinvestigated and require further evaluation.

5. Conclusions

This proof of concept showed the possibility for the additive manufacturing of biocompatible and implantable polymers such as PEEK, in our case, a complex geometry with many joint surfaces in the hospital environment.

Data Availability

Availability of the digital STL and g-code files is restricted due to the ownership of the patent by Medartis AG. Requests for a patient-specific scaphoid replacement should be made to the abovementioned company. More data on the material and the printer can be found at <https://apiumtec.com>.

Conflicts of Interest

PH, MH, and FT are consultants at Medartis AG, Basel, Switzerland. The company owns the patent of the patient-specific scaphoid prosthesis.

Authors' Contributions

Philipp Honigmann and Neha Sharma contributed equally to this work.

Acknowledgments

The development of the prosthesis was supported by the Deutsche Arthro-Hilfe e.V [P341-A544-Hintermann/EP2-honi1-hand-en-III-2017-17].

References

- [1] S. Weidert, S. Andress, E. Suero et al., "3D printing in orthopedic and trauma surgery education and training: possibilities and fields of application," *Unfallchirurg*, vol. 122, no. 6, pp. 444–451, 2019.
- [2] K. C. Wong, "3D-printed patient-specific applications in orthopedics," *Orthopedic Research and Reviews*, vol. 8, pp. 57–66, 2016.
- [3] N. Bizzotto, I. Tami, A. Tami et al., "3D printed models of distal radius fractures," *Injury*, vol. 47, no. 4, pp. 976–978, 2016.
- [4] A. A. Giannopoulos, L. Chepelev, A. Sheikh et al., "3D printed ventricular septal defect patch: a primer for the 2015 Radiological Society of North America (RSNA) hands-on course in 3D printing," *3D Printing in Medicine*, vol. 1, no. 1, pp. 1–20, 2015.
- [5] M. D. Tam, S. D. Laycock, D. Bell, and A. Chojnowski, "3-D printout of a DICOM file to aid surgical planning in a 6 year old patient with a large scapular osteochondroma complicating congenital diaphyseal aclasia," *Journal of Radiology Case Reports*, vol. 6, no. 1, pp. 31–37, 2012.
- [6] M. Guvendiren, *3D Bioprinting in Medicine*, Springer, 2019.
- [7] J. Zuniga, D. Katsavelis, J. Peck et al., "Cyborg beast: a low-cost 3D-printed prosthetic hand for children with upper-limb differences," *BMC Research Notes*, vol. 8, no. 1, pp. 1–10, 2015.
- [8] J. M. Zuniga, J. L. Peck, R. Srivastava et al., "Functional changes through the usage of 3D-printed transitional prostheses in children," *Disability and Rehabilitation Assistive Technology*, vol. 14, no. 1, pp. 68–74, 2019.
- [9] A. Pallaver and P. Honigmann, "The role of cone-beam computed tomography (CBCT) scan for detection and follow-up of traumatic wrist pathologies," *The Journal of Hand Surgery*, vol. 44, no. 12, pp. 1081–1087, 2019.
- [10] P. Honigmann, N. Sharma, B. Okolo, U. Popp, B. Msallem, and F. M. Thieringer, "Patient-specific surgical implants made of 3D printed PEEK: material, technology, and scope of surgical application," *BioMed Research International*, vol. 2018, no. 8, Article ID 4520636, p. 8, 2018.
- [11] P. Honigmann, R. Schumacher, R. Marek, F. Büttner, F. Thieringer, and M. Haefeli, "A three-dimensional printed patient-specific scaphoid replacement: a cadaveric study," *Journal of Hand Surgery*, vol. 79, 2018.
- [12] A. Padolino, G. Porcellini, B. Guollo et al., "Comparison of CFR-PEEK and conventional titanium locking plates for proximal humeral fractures: a retrospective controlled study of patient outcomes," *Musculoskeletal Surgery*, vol. 102, Supplement 1, pp. 49–56, 2018.
- [13] M. Vaezi and S. Yang, "Extrusion-based additive manufacturing of PEEK for biomedical applications," *Virtual and Physical Prototyping*, vol. 10, no. 3, pp. 123–135, 2015.
- [14] P. Johansson, R. Jimbo, Y. Naito, P. Kjellin, F. Currie, and A. Wennerberg, "Polyether ether ketone implants achieve increased bone fusion when coated with nano-sized hydroxyapatite: a histomorphometric study in rabbit bone," *International Journal of Nanomedicine*, vol. 11, pp. 1435–1442, 2016.
- [15] P. Honigmann, F. Thieringer, R. Schumacher, and M. Haefeli, *US020170143501A120170525*, pp. 1–23, 2017.
- [16] P. Honigmann, F. Thieringer, R. Schumacher, and M. Haefeli, "Scaphoid prosthesis-European Patent Office - EP 3170477 A1 scaphoid prosthesis-European Patent Office-EP 3170477 A1," pp. 1–27, 2017.
- [17] M. Garcia-Leiner, O. Ghita, R. McKay, and S. K. P. Biomaterials, "Additive manufacturing of polyaryletherketones," in *PEEK Biomaterials Handbook*, pp. 89–103, Elsevier, 2019.
- [18] J. W. Stansbury and M. J. Idacavage, "3D printing with polymers: challenges among expanding options and opportunities," *Dental Materials: Official Publication of the Academy of Dental Materials*, vol. 32, no. 1, pp. 54–64, 2016.
- [19] ASTM International, *F2026-17, Standard Specification for Polyetheretherketone (PEEK) Polymers for Surgical Implant Applications*, ASTM International, West Conshohocken, PA, 2010.
- [20] J. Graham and J. Peck, "FDA regulation of PEEK implants," in *PEEK Biomaterials Handbook*, pp. 431–445, William Andrew Publishing, 2019.
- [21] B. Msallem, N. Sharma, S. Cao, F. S. Halbeisen, H.-F. Zeilhofer, and F. M. Thieringer, "Evaluation of the dimensional accuracy of 3D-printed anatomical mandibular models using FFF, SLA, SLS, MJ, and BJ printing technology," *Journal of Clinical Medicine*, vol. 9, no. 3, p. 817, 2020.
- [22] S. M. Kurtz, *Chapter 2- Synthesis and Processing of PEEK for Surgical Implants*, Elsevier Inc., 2019.
- [23] M. Jarman-Smith, M. Brady, S. M. Kurtz, N. M. Cordaro, W. R. Walsh, and E. Ouellette, *Chapter 13- Porosity in PEEK*, Elsevier Inc., 2019.
- [24] T. Karjalainen, K. Pamilo, and A. Reito, "Implant failure after Motec Wrist Joint Prosthesis due to failure of ball and socket-type articulation-two patients with adverse reaction to metal debris and polyether ether ketone," *The Journal of Hand Surgery*, vol. 43, no. 11, pp. 1044.e1–1044.e4, 2018.
- [25] M. G. A. de Roo, M. Muurling, J. G. G. Dobbe, M. E. Brinkhorst, G. J. Streekstra, and S. D. Strackee, "A four-dimensional-CT study of in vivo scapholunate rotation axes: possible implications for scapholunate ligament reconstruction," *Journal of Hand Surgery (European Volume)*, vol. 44, no. 5, pp. 479–487, 2019.

- [26] J. W. Brantigan, P. C. McAfee, B. W. Cunningham, H. Wang, and C. M. Orbegoso, "Interbody lumbar fusion using a carbon fiber cage implant versus allograft bone," *Spine*, vol. 19, no. 13, pp. 1436–1443, 1994.
- [27] A. H. C. Poulsson, D. Eglin, S. Zeiter et al., "Osseointegration of machined, injection moulded and oxygen plasma modified PEEK implants in a sheep model," *Biomaterials*, vol. 35, no. 12, pp. 3717–3728, 2014.
- [28] R. D. Carpenter, B. S. Klosterhoff, F. B. Torstrick et al., "Effect of porous orthopaedic implant material and structure on load sharing with simulated bone ingrowth: a finite element analysis comparing titanium and PEEK," *Journal of the Mechanical Behavior of Biomedical Materials*, vol. 80, pp. 68–76, 2018.
- [29] O. Spingardi and M. I. Rossello, "The total scaphoid titanium arthroplasty: a 15-year experience," *Hand*, vol. 6, no. 2, pp. 179–184, 2011.
- [30] M. Henry, "Outcomes assessment of lunare replacement arthroplasty with intrinsic carpal ligament reconstruction in Kienböck's disease," *The Hand*, vol. 9, no. 3, pp. 364–369, 2014.
- [31] P. Bellemère, "Pyrocarbon implants for the hand and wrist," *Hand Surgery & Rehabilitation*, vol. 37, no. 3, pp. 129–154, 2018.

Research Article

Endoscopic Treatment of Symptomatic Foot and Ankle Bone Cyst with 3D Printing Application

Changgui Zhang, Jin Cao , Hongli Zhu , Huaquan Fan , Liu Yang ,
and Xiaojun Duan 

Center for Joint Surgery, Southwest Hospital, Third Military Medical University (Army Medical University),
Chongqing 400038, China

Correspondence should be addressed to Xiaojun Duan; duanxiaojun@hotmail.com

Received 1 July 2020; Revised 12 November 2020; Accepted 14 December 2020; Published 28 December 2020

Academic Editor: Filippo Piccinini

Copyright © 2020 Changgui Zhang et al. This is an open access article distributed under the Creative Commons Attribution License, which permits unrestricted use, distribution, and reproduction in any medium, provided the original work is properly cited.

Objective. To study the efficacy of arthroscopy for treating symptomatic bone cysts of the foot and ankle through the follow-up of patients and to further explore the application value of 3D printing technology in this treatment. **Methods.** Twenty-one patients with symptomatic bone cysts in the foot and ankle who underwent arthroscopic surgery in our Center from March 2010 to December 2018 were enrolled, including 11 in the experimental group and 10 in the control group. For the control group, C-arm fluoroscopy was used intraoperatively to confirm the positioning of the cysts; for the experimental group, a 3D model of the lesion tissue and the 3D-printed individualized guides were prepared to assist the positioning of the cysts. Debridement of the lesion tissues was conducted under an arthroscope. Regular follow-ups were conducted. The time of establishing arthroscopic approaches and the times of intraoperative fluoroscopy between the two groups were compared. Significance was determined as $P < 0.05$. **Results.** The postoperative pathology of the patients confirmed the diagnosis. No significant perioperative complications were observed in either group, and no recurrence of bone cysts was seen at the last follow-up. The VAS scores and AOFAS scores of the two groups at the last follow-up were significantly improved compared with the preoperative data, but there was no statistical difference between the two groups. All surgeries were performed by the same senior surgeon. The time taken to establish the arthroscopic approaches between the two groups was statistically significant ($P < 0.001$), and the times of intraoperative fluoroscopy required to establish the approach were also statistically significant ($P < 0.001$). The intraoperative bleeding between the two groups was statistically significant ($P < 0.01$). There was 1 case in each group whose postoperative CT showed insufficient bone grafting, but no increase in cavity volume was observed during the follow-up. **Conclusion.** With the assistance of the 3D printing technology for treating symptomatic bone cysts of the ankle and foot, the surgeon can design the operation preoperatively and perform the rehearsal, which would make it easier to establish the arthroscopic approach, better understand the anatomy, and make the operation smoother. This trial is registered with <http://www.clinicaltrials.gov> NCT03152916.

1. Introduction

Bone cysts of the extremities are tumor-like lesions, which mainly occur in the femoral neck, the proximal femur, and the proximal humerus, while those occurring in the foot and ankle are relatively rare. For example, the incidence of talar bone cysts accounts for 0.003% of the bone tumor, and they are commonly diagnosed as simple bone cysts,

aneurysmal bone cysts, intraosseous ganglion, etc. [1–8]. The etiology and mechanism of bone cysts have not been fully elucidated. Some studies have suggested that talar bone cysts were related to the subchondral bone fissures and the increased pressure of fluid in the subchondral bone. Fluid pressure and osteocyte apoptosis might lead to the growth of cysts via mechanically regulated bone adaptation [9]. Bone cysts generally have no obvious

symptoms. Most of its patients seek treatment due to pathological fractures that lead to pain, swelling, and dysfunction. They can be diagnosed by radiographic examination. However, in the clinic, some patients have bone cysts that demonstrate progressive development in a short period of time, and bone destruction is gradually aggravated. If not treated in time, these symptomatic bone cysts can easily lead to pathological fractures. Recent literature has also shown that the destruction of subchondral bone is also an important cause of cartilage damage, and its development can be followed by osteoarthritis [10, 11]. Thus, patients with poor conservative treatment results should consider surgery.

Arthroscopy has the advantages of smaller trauma and clearer vision under the arthroscope, which make it suitable for intra-articular surgery. Besides, the incision is good-looking, and the postoperative joint function recovery is fast. Hence, arthroscopy develops rapidly in recent years and is well received by patients. It has been widely used in foot and ankle surgeries, such as talar osteochondral injury, bony impingement syndrome, ankle joint arthrodesis, ankle joint tuberculosis, and even some benign tumors of the ankle joint [12, 13]. With the continuous advancement of endoscopic techniques, endoscopic treatment of bone cysts has also been reported in some literature recently [1, 4–8, 14, 15]. However, the literature on endoscopic treatment of ankle bone cysts is still very rare, and the validity of this new technology remains controversial. Three-dimensional (3D) printing technology is a hot new technology in orthopedics [16–22], which is especially suitable for individualized precision treatment. We have utilized the 3D printing technology in fields such as ankle joint arthrodesis and subtalar joint arthrodesis and have obtained significant results [17, 18]. In this study, we followed the patients with symptomatic bone cysts of the foot and ankle that were treated with arthroscopic technique in recent years to estimate its application value and to further explore the specific application value of the 3D printing technology, providing a basis for its future promotion.

2. Materials and Methods

2.1. Participants. Patients with symptomatic bone cysts in the foot and ankle and who received surgical treatment in our Center from March 2010 to December 2018 were followed. Indications for surgery are the following: (1) after 6 months of conservative treatment, there were still symptoms of bone cysts; (2) 3D computed tomography (CT) examination indicated that the bone destruction volume $> 1 \text{ cm}^3$. Case inclusion criteria are the following: (1) patients who received arthroscopic treatment for symptomatic bone cysts of the ankle and foot, (2) complete preoperative imaging data, and (3) bone cysts of similar size (1 cm^3 - 3 cm^3). Exclusion criteria are the following: (1) history of previous foot and ankle surgery; (2) history of ankle fracture; (3) ankle joint deformity, abnormal alignment of the lower extremity; (4) severe osteoarthritis of the ankle or subtalar joint; (5) pathological findings suggesting malignant bone tumors; (6) recurrence of bone cysts after previous treatment; and (7) history of mental illness. Twenty-one patients were followed. All cases were unilateral. (See Table 1 for details.)

TABLE 1: Patient data.

| | Experimental group ($n = 11$) | Control group ($n = 10$) | P |
|------------------------------------|---------------------------------|----------------------------|-------|
| Sex (n) | | | |
| Female | 3 | 7 | 0.086 |
| Male | 8 | 3 | |
| Age (yr) | 39.5 ± 5.8 | 45.0 ± 5.2 | 0.485 |
| Location of cyst | | | |
| Talus | 6 | 5 | 0.484 |
| Distal tibia | 3 | 4 | |
| Calcaneus | 1 | 2 | |
| Preoperative symptom duration (mo) | 21.0 ± 6.1 | 34.7 ± 13.1 | 0.340 |
| Pain (n) | 11 | 10 | NA |

Abbreviations: NA: not applicable.

All patients were informed before surgery that there was a risk of recurrence of bone cysts due to incomplete removal of the lesions by arthroscopic techniques. In addition, if the articular cartilage showed obvious damage, the second-stage treatment of cartilage would be required. All surgeries in this study were performed by the same senior surgeon. The study was approved by the hospital's ethics committee, and all patients signed the informed consent form and agreed to be enrolled in the study.

2.2. Preoperative Individualized Application of the 3D Printing Technology. A 1:1 proportional model of the lesion and individualized surgical guide were prepared for the experimental group. The 3D CT thin-layer scan (Siemens, Germany) of the ankle bone cyst was routinely performed, and the CT scan slice thickness was 1 mm. The Digital Imaging and Communications in Medicine (DICM) data was extracted and imported into the Model Intestinal Microflora in Computer Simulation (MIMICS) software to reconstruct the 3D data of the bone cyst and its surrounding tissues. The MIMICS-reconstructed data was imported into the 3D design software SIEMENS NX (Siemens PLM Software, Germany) to design the guide system for arthroscopy. The individualized guides were designed according to the anatomical landmarks to perfectly match with the bone surface, and the center of the guide contained guide holes for the Kirschner wire to drill (Figure 1). The data of the designed guides were converted into STL format and imported into a 3D printer (Model: UP BOX, Tiertime, China) for printing. Polylactic acid (Tiertime, China) was used as a raw material to prepare the individualized guides (Figure 1), and lesion models were prepared. When preparing the lesion models, different colors could be used to distinguish the lesion from the surrounding healthy tissues, which was beneficial to improving surgical planning. The individualized guides were sealed and sterilized with ethylene oxide for intraoperative use.

2.3. Operative Techniques. Nerve block anesthesia or epidural anesthesia were conducted for all patients. Thigh tourniquets were applied after successful anesthesia. Appropriate

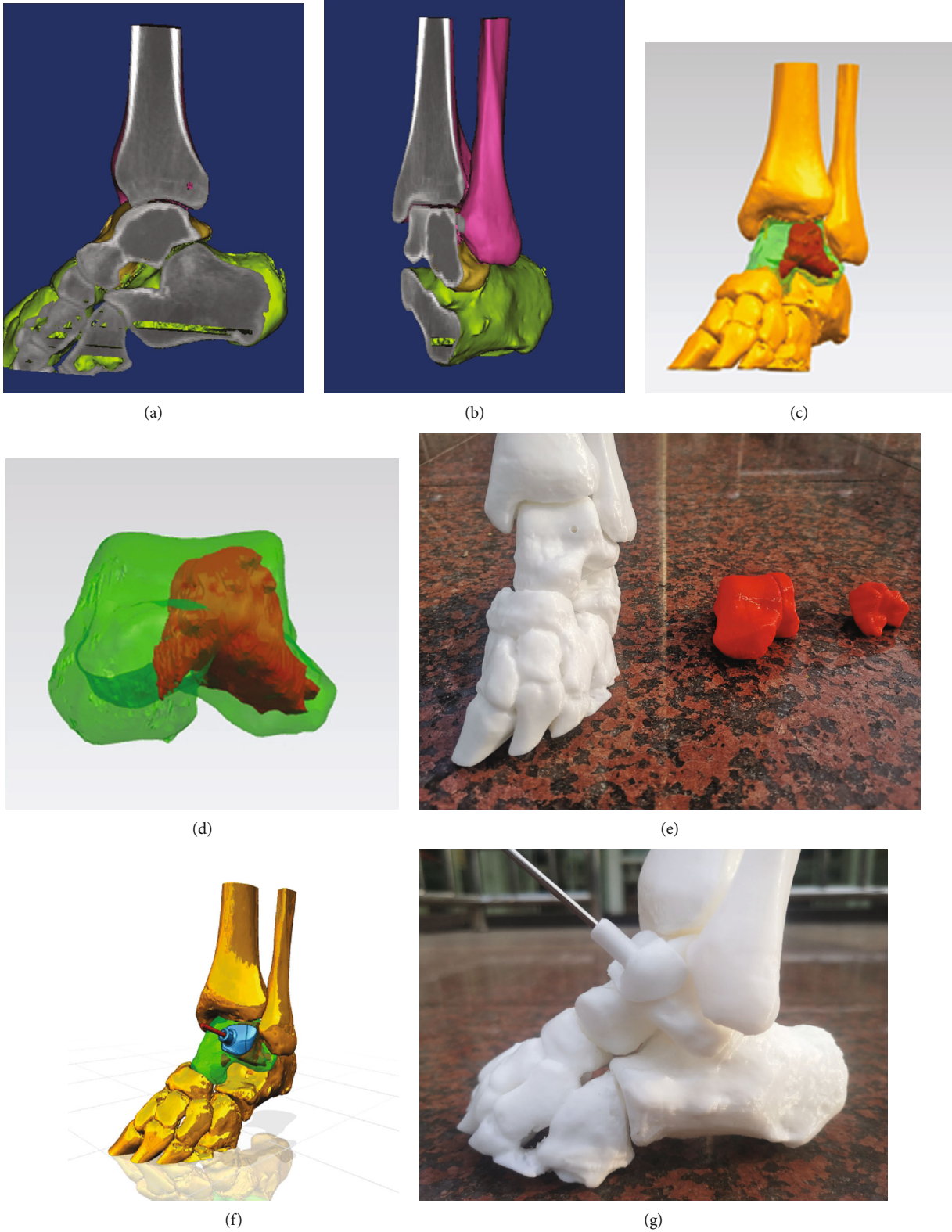


FIGURE 1: Continued.

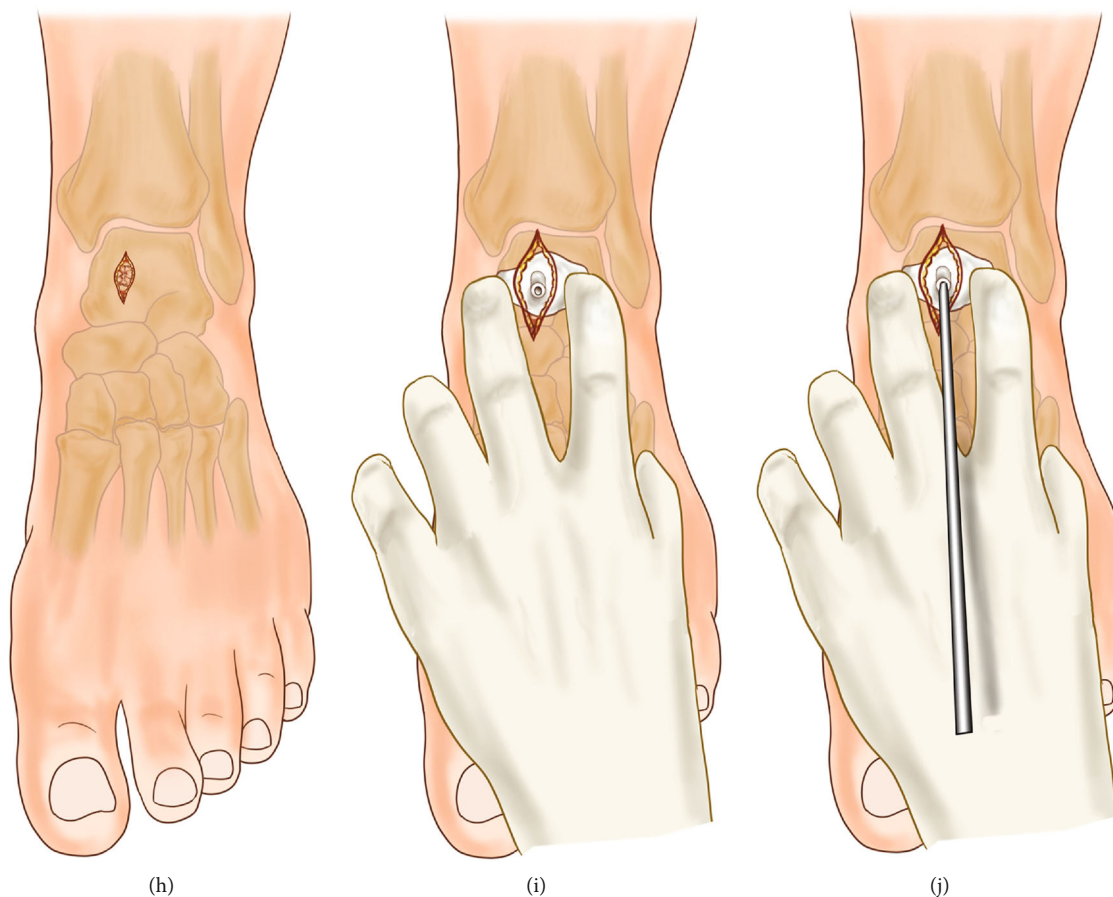


FIGURE 1: Preoperative preparation of 3D-printed lesion models and individualized guide system. (a, b) Talar lesions established based on the 3D CT images before surgery; (c, d) the software was used to distinguish lesions from healthy tissues; (e) 3D-printed lesion model that could be used for surgical planning and rehearsal; (f, g) design and preparation of individualized guides to assist in determining the position of the Kirschner wire. (h) The location of the lesion was entered through the incision, and the bony structure was confirmed; (i) the anatomical position was determined through the bony structure, and the cyst position was located with the guide; (j) the guide was used to assist the accurate positioning of the Kirschner wire.

position was chosen according to the location of the bone cyst. If it was a distal tibial bone cyst, the patient could use the routine supine position; if it was a calcaneal bone cyst, the lateral position should be used. In cases with the talar bone cyst, the supine position was usually selected. In order to facilitate the operation, the hip on the affected side was moderately elevated to maintain the neutral position of the lower limbs. After routine sterilization and draping, the tourniquet pressure was set to 300 mmHg.

The talar bone cyst was taken as an example to elucidate the surgical procedures. After accurate positioning, 10-20 mL saline was injected into the ankle joint cavity; the anteromedial and anterolateral ankle approaches were routinely established, and the 30-degree arthroscopy (Smith & Nephew) was placed into the joint cavity through these approaches. Careful exploration of the joint cavity was conducted to observe whether there was synovial hyperplasia or corresponding articular cartilage injury; lesions would be treated if detected. After the exploration and debridement, the traction device of the ankle joint was removed, and the medial or lateral incision was moderately enlarged by about 3 cm. The tendon tis-

sue was pulled outward for the drill of the Kirschner wire to drill. Care should be taken not to damage the nerves, blood vessels, ligaments, etc., in this process. For the control group, the surgeon did not use the 3D-printed guide and drilled the Kirschner wire relying on C-arm fluoroscopy. For the experimental group, besides previous experience, the surgeon was assisted by the 3D-printed lesion model and guide for the accurate positioning and drilling of the 2.0 mm Kirschner wire. Attention should be paid to the drilling of the Kirschner wire to avoid the articular cartilage. Then, C-arm fluoroscopy was applied to confirm whether the Kirschner wire had entered the lesion and whether its position met with the preoperative planning; otherwise, it needed to be redrilled. A 4.5 mm drill was drilled into the intraosseous lesion along the Kirschner wire to establish the arthroscopic approach. During this process, there might be a sudden sense of falling out, and at the same time, the fluid of the cyst was often seen. These would confirm the entrance into the cyst. When the cystic fluid was not obvious, a 2.7 mm arthroscope could be used to enter the cavity for probing and adjusting the direction of operation. If the operation under the arthroscope

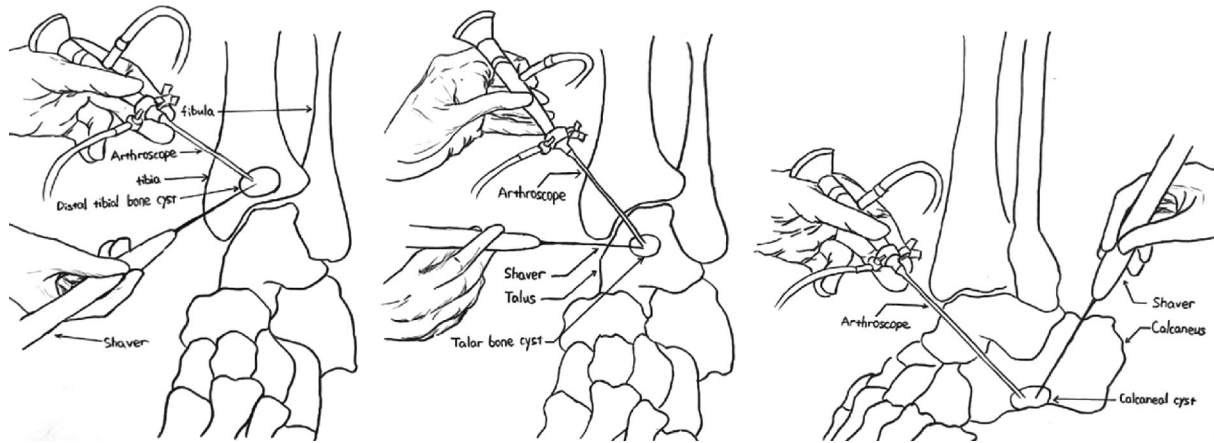


FIGURE 2: Arthroscopically assisted treatment of bone cysts via different approaches.

was difficult, the diameter of the approach could be moderately enlarged. The bone lesions were explored (Figure 2). The tissue morphology of the cyst wall and the nature of the cyst fluid under an arthroscope were observed, and the pathological examination of the lesion tissue was conducted. The cyst wall was scraped with a curette repeatedly to ensure the complete removal of the lesion tissue. A burr was used to drill the sclerotic rim of the wall. Arthrocare radiofrequency ablation of the cystic wall was performed to prevent recurrence of the cystic wall lesions. The cyst wall was drilled using a 1.2 mm Kirschner wire for the infiltration of bone marrow to promote bony union. Finally, the bone defect was impacted tightly with autologous cancellous bone harvested from the iliac crest, allograft cancellous bone, or bone cement. C-arm fluoroscopy was applied to confirm the complete debridement of the cyst and satisfactory filling of the bone defect. A drain was placed into the joint after irrigation. The portals were closed with interrupted sutures. The plaster cast was used to fix the ankle joint to the functional position.

For bone cysts in different locations, we used different methods. If the bone cyst was in the talus, we chose the anterior approach for arthroscopic removal; if it was in the tibia, we performed arthroscopic removal on the anterior part of the tibia; if it was in the calcaneus, removal was conducted on the anterior part of the calcaneus. (Drawn by Changgui Zhang.)

After the anesthetic effect wore off, the patients should start toe activity and perform functional exercises under instruction. The drainage tube was removed 24 hours postoperatively, and the antibiotics were intravenously infused for 48 hours. The suture was removed 2 weeks postoperatively, and partial weight-bearing walking was started from 4 weeks on. Perioperative complications were recorded. Regular follow-ups and corresponding imaging examinations were performed.

2.4. Indicators. The time of surgery was recorded, including the time taken to establish the arthroscopic approach and the times of C-arm fluoroscopy used during the period. The time of establishing arthroscopic approaches was the time from the beginning of the arthroscopic approach establish-

ment to the finish. For the times of C-arm fluoroscopy, it was defined as the times of fluoroscopy applied from the beginning of surgery to its finish. The intraoperative blood loss was recorded. Preoperative and postoperative VAS scores and AOFAS scores were recorded [23, 24]. All patients were followed at 1 month, half a year, and one year after operation; the results of radiographic examinations before and after operation were compared. If the postoperative radiographs were insufficient to confirm the condition, CT examination would be required. At the last follow-up, an ankle joint 3D CT reconstruction was performed to confirm the union of the bone cyst and whether there was a cyst recurrence.

2.5. Statistical Analysis. The measuring index was statistically analyzed by SPSS 22.0 using the mean \pm standard deviation, and the indexes of the experimental group and the control group were compared before and after the operation. If the data conformed to the normal distribution, the *t*-test would be used; if not, the rank sum test would be used. The enumeration data was processed by the chi-squared test. $P < 0.05$ was considered statistically significant.

3. Results

All 21 patients were followed for 40 ± 22 (12-72) months. The final pathological types were 15 cases of simple bone cyst, 5 cases of aneurysmal bone cyst, and 1 case of intraosseous ganglion. No patients had perioperative complications such as infection, neurovascular injury, lower extremity venous thrombosis, or poor wound healing. The VAS score and AOFAS score at the last follow-up of the two groups were significantly improved compared with preoperative ones, but there was no statistical difference between the two groups (Table 2). There was a statistically significant difference in the time taken to establish an arthroscopic approach between the two groups during surgery ($P < 0.001$), and the intraoperative fluoroscopy times required to establish the approach was statistically significant ($P < 0.001$). The intraoperative bleeding between the two groups was statistically significant ($P < 0.01$). At the last follow-up, the radiographs

TABLE 2: The two groups' comparative follow-up study.

| Groups | Experimental group | Control group | <i>t</i> -test |
|--|--------------------|---------------|------------------|
| Cases (<i>n</i>) | 11 | 10 | |
| Preoperative AOFAS scores (pt) | 59.5 ± 2.1 | 61.2 ± 2.4 | <i>P</i> = 0.587 |
| AOFAS scores at the last follow-up (pt) | 94.7 ± 0.7 | 92.5 ± 1.3 | <i>P</i> = 0.135 |
| Preoperative VAS scores (pt) | 7.2 ± 0.3 | 6.9 ± 0.3 | <i>P</i> = 0.522 |
| VAS scores at the last follow-up (pt) | 0.4 ± 0.2 | 0.5 ± 0.2 | <i>P</i> = 0.614 |
| Time of establishing surgical approach (seconds) | 204.5 ± 6.5 | 318.1 ± 7.4 | <i>P</i> = 0.000 |
| Intraoperative fluoroscopy times | 2.2 ± 0.1 | 3.7 ± 0.2 | <i>P</i> = 0.000 |
| Intraoperative blood loss | 14.5 ± 1.1 | 30.5 ± 5.8 | <i>P</i> = 0.009 |

Abbreviations: AOFAS: American Orthopaedic Foot and Ankle Society; VAS: visual analog scale.

and 3D CT reconstruction of the two groups confirmed the union of the bone cyst with no recurrence (Figure 3). However, there was 1 case in each group whose postoperative radiograph showed insufficient bone grafting at the first follow-up, and the following CT confirmed the insufficiency. However, no obvious increase in the defect area was observed via CT at the last follow-up, and the patient did not complain of pain and discomfort, so no special treatment was performed.

4. Discussion

Bone cysts are common in the clinic, but they are rarely seen in the foot and ankle. The etiology and mechanism of bone cysts have not been fully elucidated. There may be a unique mechanism for the formation of bone cysts in the ankle joint. Reilingh et al. studied 66 cases of fresh talar specimens and suggested that talar bone cysts were associated with the subchondral bone fissures and the increased fluid pressure; talar bone cysts were closely related to the cartilage injuries [9]. Due to persistent destruction, the bone cyst at the joint site is prone to lead to pathological fracture or cause osteoarthritis secondary to the cartilage defect [10, 11]. Therefore, surgical treatment should be considered for bone cysts in joints where symptoms persist. Since the local pain and joint function limitation in patients with bone cysts in the foot and ankle are often not particularly serious, if there are major surgical trauma or postoperative complications, the patient satisfaction rate will be greatly reduced. Therefore, surgeons have been exploring better minimally invasive techniques. In the treatment of talar bone cysts, traditional surgery generally involves osteotomy in order to clearly show the lesions [25, 26], but such surgery is more traumatic with prolonged postoperative recovery and may even lead to postoperative ankle joint function limitation. In recent years, with the improvement of arthroscopic equipment and the increasing skill of the technique, reports on arthroscopic treatment of the bone cysts in the foot and ankle have been published [3–5, 7, 11, 15, 27]. For example, Otsuka et al. debrided the calcaneal aneurysmal bone cyst with arthroscopy and achieved good results [3]. Ogut et al. reported treatment of posterior arthroscopy for the

talar bone cyst and showed satisfactory outcomes at the short-term follow-up point [7]. This technique is especially suitable for bone cysts combined with other structural abnormalities at the posterior malleolus, such as tenosynovitis of flexor pollicis longus, symptomatic triquetral bone, and villonodular synovitis. Zhu et al. reported an anterior arthroscopic treatment for 7 cases of talar bone cysts, which also achieved satisfactory results in the short term [5]. In this study, the number of cases has been increased to 21; as for the location of cysts, in addition to the talus, distal tibia and calcaneus were also included. The short-term efficacy of arthroscopic treatment was quite satisfactory. This technique could avoid medial malleolar osteotomy and articular cartilage damage. It has the advantages of relatively safe, less traumatic, and quicker recovery. An arthroscope can be used to more intuitively observe the shape of the lesion; pathological examination of the tissue obtained during surgery can be used to further confirm the diagnosis [28–30]. Of course, there are also deficiencies in the application of this technique, such as a learning curve for surgeons, insufficient lesion scraping, and bone grafting.

Establishing an ideal arthroscopic approach is a critical step in achieving good surgical results. An ideal approach should meet the following requirements: (1) avoiding damage to important structures and close to the lesion tissue for easy operation and (2) providing clear vision to facilitate complete removal of the lesion. In the past, the surgeon relied on local anatomy and previous experience to drill the Kirschner wire for preliminary positioning. Then, C-arm fluoroscopy was used to confirm whether the position of the Kirschner wire was appropriate. In practice, this may cause repeated fluoroscopy for adjusting the position of the Kirschner wire, which would prolong the operation time and increases the intraoperative radiation. In recent years, 3D printing technology has been gaining popularity in orthopedics and has brought new hopes to solve the above problem. We first perform 3D reconstruction and analysis of the lesion, design the 3D-printed guide, and then utilize the 3D printing technology to print out the lesion models to comprehensively evaluate the lesions, observe the relationship between the lesions and the adjacent tissues, design a more scientific surgical plan and perform preoperative surgical

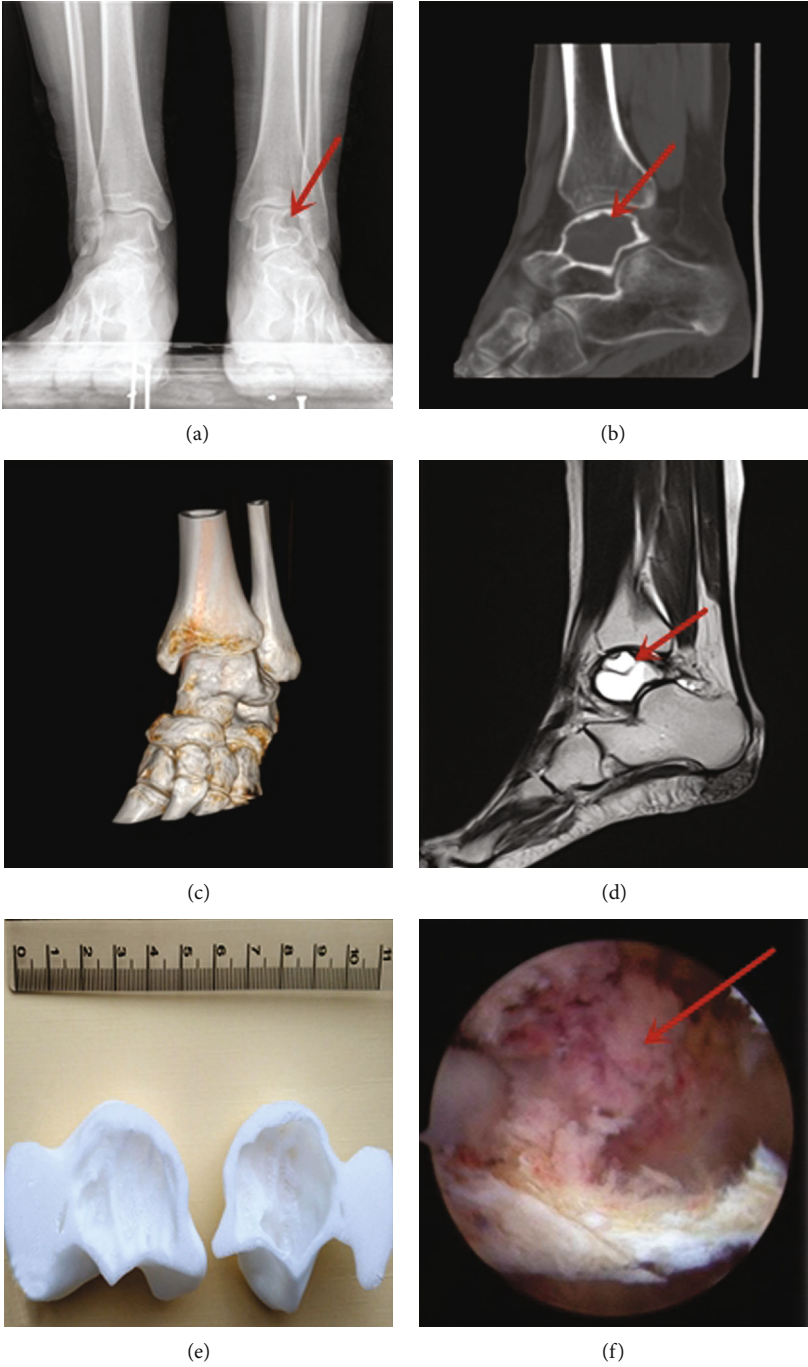


FIGURE 3: Continued.

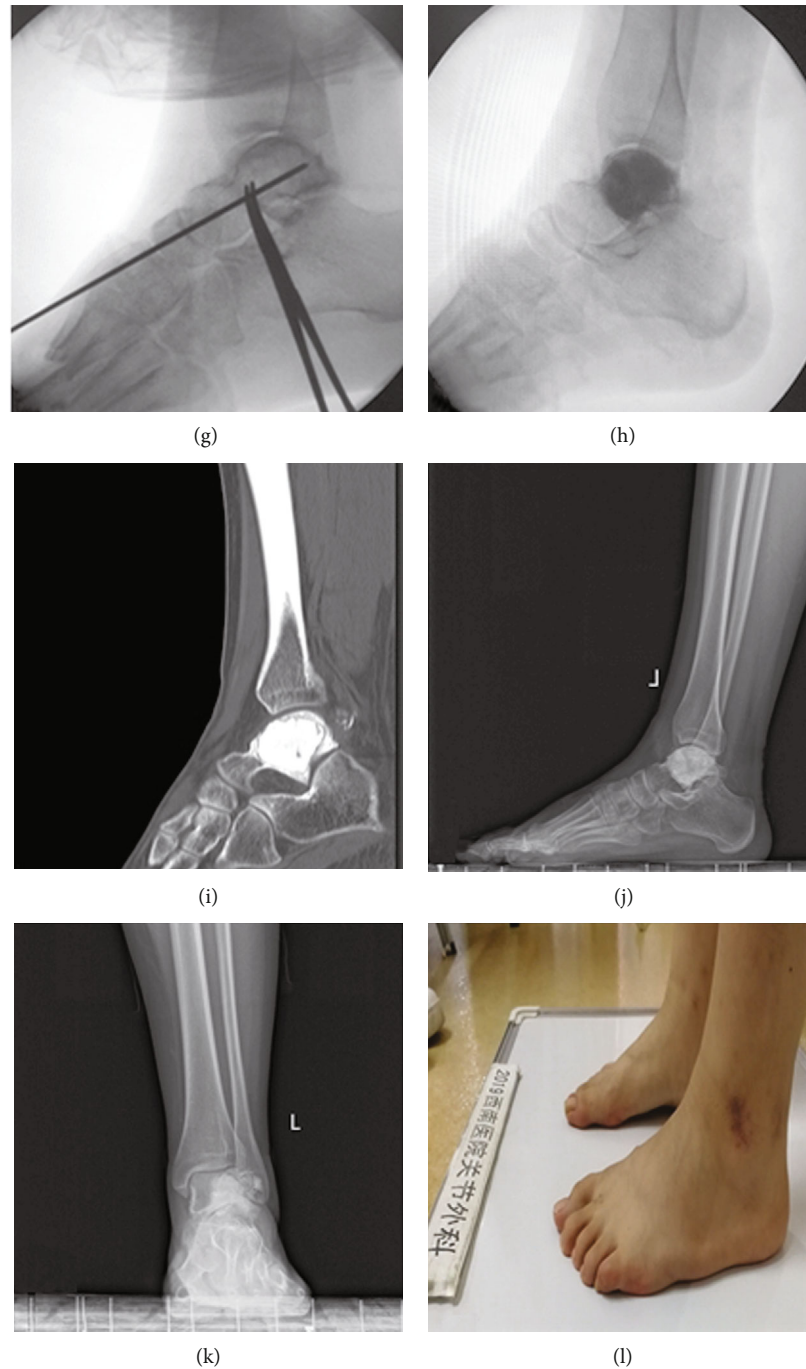


FIGURE 3: Typical case 1 in the experimental group. Female, 15 years old, admitted to the hospital because of left ankle pain for 1 year. Preoperative diagnosis: pathological fracture secondary to the left talar bone cyst. (a–d) Postoperative examinations; the arrows indicated the location of the bone cyst. (e) 3D-printed lesion model; (f) arthroscopic observation of cyst lesion, and the red arrow showed the bone cyst; (g) the Kirschner wire was drilled through the anterior arthroscopic approach with the assistance of individualized guides, and C-arm fluoroscopy was used to confirm that the Kirschner wire had accurately entered the talar cyst site; (h) fluoroscopy was used to confirm the optimal filling of the bone cement; (i) no recurrence of bone cysts was seen in the 3D CT reconstruction after 18 months; (j, k) no recurrence of bone cysts was seen in the radiographs at the last follow-up after 18 months; (l) the left ankle symptoms were relieved at the last follow-up, and the AOFAS score was 94 points.

rehearsals to help reduce the damage of the nerves and blood vessels, shorten the operation time, reduce intraoperative bleeding, and achieve better surgical results. It has been proved to be a safe and reliable new technology, which is

especially suitable for individualized surgical treatment of difficult cases. Besides, the lesion model is particularly useful for communication between surgeons and patients, so that the patients can understand the disease and surgical

content more clearly, which is helpful for increasing the patient satisfaction rate [31–36]. We used polylactic acid polymer materials for the 3D printing model and positioning guide plate, and the cost of materials was about RMB 300 yuan. We hope that with the development of technology, we can further reduce the time and cost. Bone graft after lesion debridement is a controversial topic. Some scholars advocated that bone graft should not be performed [2]. In our opinion, allogeneic bone graft is preferred. The bone strength of the defect area would not be affected after union. Meanwhile, it can also avoid the trauma and prolonged surgery time of the autograft [8].

5. Conclusions

Compared with conventional arthroscopy, the application of 3D printing technology in treating the bone cyst of the foot and ankle can help the surgeon design a preoperative plan and perform rehearsals in advance. It makes it easier for an inexperienced surgeon to understand the anatomical structure and facilitate a faster establishment of the arthroscopic portal. There are still limitations to this study. The follow-up period is relatively short with only 12 months, and the long-term efficacy of the patient has not been followed. In addition, due to the small number of cases of bone cysts in the foot and ankle, as well as the different locations of bone cysts in each group, the number of patients included in this study is also quite small. Thus, it is difficult to analyze the influence of different bone grafting methods or explore the perioperative complications. Future multicenter case-control studies need to be conducted to overcome these deficiencies.

Data Availability

The corresponding author Xiaojun Duan can make data available upon request, email: duanxiaojun@hotmail.com.

Ethical Approval

All procedures performed in studies involving human participants were in accordance with the ethical standards of the institutional and/or national research committee and with the 1964 Helsinki declaration and its later amendments or comparable ethical standards.

Consent

Informed consent was obtained from all individual participants included in the study.

Disclosure

The study design is a case-control study. The level of evidence is III.

Conflicts of Interest

The authors declare that they have no conflicts of interest regarding the publication of this article.

Acknowledgments

The authors thank Xin Chen from the Center for Joint Surgery, Southwest Hospital, Third Military Medical University, for the language support for this article. The study was funded by the China Ministry of Science and Technology National Key Research and Development Project (Grant No. 2016YFB1101404) and Key Research Project of Southwest Hospital (Grant No. SWH2017JSZD-05).

References

- [1] S. O. El, E. S. M. Abou, and A. N. Nasef, "Arthroscopic intralesional curettage for large benign talar dome cysts," *SICOT J*, vol. 1, p. 32, 2015.
- [2] E. Shears, K. Dehne, H. Murata et al., "Healing of ungrafted bone defects of the talus after benign tumour removal," *Foot and Ankle Surgery*, vol. 14, no. 3, pp. 161–165, 2008.
- [3] T. Otsuka, M. Kobayashi, M. Yonezawa, F. Kamiyama, Y. Matsushita, and N. Matsui, "Treatment of chondroblastoma of the calcaneus with a secondary aneurysmal bone cyst using endoscopic curettage without bone grafting," *Arthroscopy: The Journal of Arthroscopic & Related Surgery*, vol. 18, no. 4, pp. 430–435, 2002.
- [4] E. J. Dawe, C. P. Jukes, N. Gougoulias, and A. Wee, "Successful arthroscopic decompression and synthetic grafting of a posterior talar cyst: a case report," *Foot and Ankle Surgery*, vol. 20, no. 2, pp. e35–e36, 2014.
- [5] X. Zhu, L. Yang, and X. Duan, "Arthroscopically assisted anterior treatment of symptomatic large talar bone cyst," *The Journal of Foot and Ankle Surgery*, vol. 58, no. 1, pp. 151–155, 2019.
- [6] X. J. Duan and L. Yang, "Removal of osteoblastoma of the talar neck using standard anterior ankle arthroscopy: a case report," *International Journal of Surgery Case Reports*, vol. 23, pp. 52–55, 2016.
- [7] T. Ogut, A. Seker, and F. Ustunkan, "Endoscopic treatment of posteriorly localized talar cysts," *Knee Surgery, Sports Traumatology, Arthroscopy*, vol. 19, no. 8, pp. 1394–1398, 2011.
- [8] N. Chinzei, N. Kanzaki, T. Fujishiro et al., "Arthroscopic debridement of a talar cyst and bone grafting with the osteochondral autograft transfer system," *Journal of the American Podiatric Medical Association*, vol. 107, no. 6, pp. 541–547, 2017.
- [9] M. L. Reilingh, L. Blankevoort, I. C. van Eekeren, and C. N. van Dijk, "Morphological analysis of subchondral talar cysts on microCT," *Knee Surgery, Sports Traumatology, Arthroscopy*, vol. 21, no. 6, pp. 1409–1417, 2013.
- [10] Y. Ao, Z. Li, Q. You, C. Zhang, L. Yang, and X. Duan, "The use of particulated juvenile allograft cartilage for the repair of porcine articular cartilage defects," *The American Journal of Sports Medicine*, vol. 47, no. 10, pp. 2308–2315, 2019.
- [11] H. T. Adkisson, J. A. Martin, R. L. Amendola et al., "The potential of human allogeneic juvenile chondrocytes for restoration of articular cartilage," *The American Journal of Sports Medicine*, vol. 38, no. 7, pp. 1324–1333, 2010.
- [12] X. Duan and L. Yang, "Arthroscopic management for early-stage tuberculosis of the ankle," *Journal of Orthopaedic Surgery and Research*, vol. 14, no. 1, p. 25, 2019.
- [13] X. Duan, L. Yang, and L. Yin, "Arthroscopic arthrodesis for ankle arthritis without bone graft," *Journal of Orthopaedic Surgery and Research*, vol. 11, no. 1, p. 154, 2016.

- [14] M. E. Abdel-Wanis, H. Tsuchiya, K. Uehara, and K. Tomita, "Minimal curettage, multiple drilling, and continuous decompression through a cannulated screw for treatment of calcaneal simple bone cysts in children," *Journal of Pediatric Orthopedics*, vol. 22, no. 4, pp. 540–543, 2002.
- [15] T. H. Lui, "Arthroscopic curettage and bone grafting of bone cysts of the talar body," *Arthroscopy Techniques*, vol. 6, no. 1, pp. e7–e13, 2017.
- [16] X. Ren, L. Yang, and X. J. Duan, "Three-dimensional printing in the surgical treatment of osteoid osteoma of the calcaneus: a case report," *Journal of International Medical Research*, vol. 45, no. 1, pp. 372–380, 2017.
- [17] X. Duan, P. He, H. Fan, C. Zhang, F. Wang, and L. Yang, "Application of 3D-printed personalized guide in arthroscopic ankle arthrodesis," *BioMed Research International*, vol. 2018, Article ID 3531293, 8 pages, 2018.
- [18] X. J. Duan, H. Q. Fan, F. Y. Wang, P. He, and L. Yang, "Application of 3D-printed customized guides in subtalar joint arthrodesis," *Orthopaedic Surgery*, vol. 11, no. 3, pp. 405–413, 2019.
- [19] P. Zheng, P. Xu, Q. Yao, K. Tang, and Y. Lou, "3D-printed navigation template in proximal femoral osteotomy for older children with developmental dysplasia of the hip," *Scientific Reports*, vol. 7, no. 1, p. 44993, 2017.
- [20] T. Schepers and D. Misselyn, "3D printing calcaneal fractures: continuously improving our care by making a complex problem tangible," *Journal of Investigative Surgery*, vol. 31, no. 6, pp. 568–569, 2018.
- [21] H. Cai, "Application of 3D printing in orthopedics: status quo and opportunities in China," *The Annals of Translational Medicine*, vol. 3, Suppl 1, p. S12, 2015.
- [22] K. J. Chung, B. Huang, C. H. Choi, Y. W. Park, and H. N. Kim, "Utility of 3D printing for complex distal tibial fractures and malleolar avulsion fractures: technical tip," *Foot & Ankle International*, vol. 36, no. 12, pp. 1504–1510, 2015.
- [23] H. B. Kitaoka, I. J. Alexander, R. S. Adelaar, J. A. Nunley, M. S. Myerson, and M. Sanders, "Clinical rating systems for the ankle-hindfoot, midfoot, hallux, and lesser toes," *Foot & Ankle International*, vol. 15, no. 7, pp. 349–353, 1994.
- [24] T. Ibrahim, A. Beiri, M. Azzabi, A. J. Best, G. J. Taylor, and D. K. Menon, "Reliability and validity of the subjective component of the American Orthopaedic Foot and Ankle Society clinical rating scales," *The Journal of Foot and Ankle Surgery*, vol. 46, no. 2, pp. 65–74, 2007.
- [25] T. Y. Emre, T. Ege, H. T. Cift, D. T. Demircioglu, B. Seyhan, and M. Uzun, "Open mosaicplasty in osteochondral lesions of the talus: a prospective study," *The Journal of Foot and Ankle Surgery*, vol. 51, no. 5, pp. 556–560, 2012.
- [26] A. W. Ross, C. D. Murawski, E. J. Fraser et al., "Autologous osteochondral transplantation for osteochondral lesions of the talus: does previous bone marrow stimulation negatively affect clinical outcome?," *Arthroscopy*, vol. 32, no. 7, pp. 1377–1383, 2016.
- [27] O. Cebesoy, "Intraosseous ganglion of the talus treated with the talonavicular joint approach without exposing the ankle joint," *Journal of the American Podiatric Medical Association*, vol. 97, no. 5, pp. 424–427, 2007.
- [28] T. Otsuka, M. Kobayashi, I. Sekiya et al., "A new treatment of aneurysmal bone cyst by endoscopic curettage without bone grafting," *Arthroscopy: The Journal of Arthroscopic & Related Surgery*, vol. 17, no. 7, pp. 1–10, 2001.
- [29] J. F. Dietz, S. M. Kachar, and D. J. Nagle, "Endoscopically assisted excision of digital enchondroma," *Arthroscopy: The Journal of Arthroscopic & Related Surgery*, vol. 23, no. 6, pp. 671–678, 2007.
- [30] J. Y. Jeon, H. W. Chung, J. W. Kwon, S. H. Hong, G. Y. Lee, and K. N. Ryu, "Imaging findings of various talus bone tumors—clinico-radiologic features of talus bone tumors," *Clinical Imaging*, vol. 40, no. 4, pp. 666–677, 2016.
- [31] P. E. Scholten, M. C. Altena, R. Krips, and C. N. van Dijk, "Treatment of a large intraosseous talar ganglion by means of hindfoot endoscopy," *Arthroscopy: The Journal of Arthroscopic & Related Surgery*, vol. 19, no. 1, pp. 96–100, 2003.
- [32] H. He, H. Xu, H. Lu, Y. Dang, W. Huang, and Q. Zhang, "A misdiagnosed case of osteoid osteoma of the talus: a case report and literature review," *BMC Musculoskeletal Disorders*, vol. 18, no. 1, p. 35, 2017.
- [33] S. Tuzuner and A. T. Aydin, "Arthroscopic removal of an osteoid osteoma at the talar neck," *Arthroscopy: The Journal of Arthroscopic & Related Surgery*, vol. 14, no. 4, pp. 405–409, 1998.
- [34] S. W. Snow, M. Sobel, E. F. DiCarlo, F. M. Thompson, and J. T. Deland, "Chronic ankle pain caused by osteoid osteoma of the neck of the talus," *Foot & Ankle International*, vol. 18, no. 2, pp. 98–101, 1997.
- [35] B. Maurel, T. Le Corroller, G. Bierry, X. Buy, P. Host, and A. Gangi, "Treatment of symptomatic para-articular intraosseous cysts by percutaneous injection of bone cement," *Skeletal Radiology*, vol. 42, no. 1, pp. 43–48, 2013.
- [36] K. Zhang, Y. Gao, H. Dai, S. Zhang, G. Li, and B. Yu, "Chondroblastoma of the talus: a case report and literature review," *The Journal of Foot and Ankle Surgery*, vol. 51, no. 2, pp. 262–265, 2012.

Research Article

Three-Dimensional-Printed Guiding Template for Unicompartmental Knee Arthroplasty

Fei Gu,^{1,2,3} Liangliang Li,^{2,4} Huikang Zhang,^{2,5} Xuxiang Li,^{1,2} Chen Ling,^{1,2} Liming Wang^①,^{1,2} and Qingqiang Yao^①,^{1,2}

¹Department of Orthopaedics, Nanjing First Hospital, Nanjing Medical University, No. 68, Changle Rd, Qinhuai District, Nanjing 210006, China

²Institute of Digital Medicine, Nanjing Medical University, No. 68, Changle Rd, Qinhuai District, Nanjing 210006, China

³The Second People's Hospital of Lianyungang, No. 41, Hailian East Rd, Haizhou District, Lianyungang 222000, China

⁴Department of Orthopedics, The Affiliated Jiangning Hospital with Nanjing Medical University, Nanjing 211100, China

⁵Nanjing Clinical Nuclear Medicine Center, Nanjing First Hospital, Nanjing Medical University, No. 68, Changle Rd, Qinhuai District, Nanjing 210006, China

Correspondence should be addressed to Liming Wang; limingwangnj@163.com and Qingqiang Yao; yaoqingqiang@gmail.com

Received 4 August 2020; Accepted 4 December 2020; Published 19 December 2020

Academic Editor: Anish R. Kadakia

Copyright © 2020 Fei Gu et al. This is an open access article distributed under the Creative Commons Attribution License, which permits unrestricted use, distribution, and reproduction in any medium, provided the original work is properly cited.

Background. For unicompartmental knee arthroplasty (UKA), accurate alignment of the limb is crucial. This study is aimed at investigating the efficacy and safety of a three-dimensional printed patient-customized guiding template (3DGT) for UKA. **Methods.** A total of 22 patients receiving UKA were randomly divided into the 3DGT-UKA group ($n = 11$) and traditional UKA group (T-UKA group; $n = 11$). In the 3DGT-UKA group, the line and angle of osteotomy were decided on a 3D image of the limb reconstructed from imaging data; a guiding template was then designed and printed out. The patients in the T-UKA group underwent conventional UKA. Prosthesis size, operation time, postoperative drainage, hip-knee angle (HKA), pain, and Hospital for Special Surgery (HSS) scores were recorded at day 1, week 1, month 1, and month 3 after surgery. **Results.** There was no significant difference in the size of prostheses between the preoperatively designed and actually used in the 3DGT-UKA group ($p > 0.05$). HKA was comparable in 3DGT-UKA and T-UKA patients. Operation time was shorter (53.6 ± 6.4 minutes vs. 75.8 ± 7.1 minutes) and wound drainage was less (93.2 ± 3.9 mL vs. 85.2 ± 3.0 mL) in 3DGT-UKA than in T-UKA ($p < 0.05$). Hospital stay was shorter in the 3DGT-UKA group. The 3DGT-UKA group had a lower VAS score on day 1, week 1, and month 1 and a higher HSS score on week 1 and month 1 after surgery. No varus/valgus deformity or prosthesis loosening was observed in either group at the final follow-up. **Conclusion.** The 3D-printed patient-customized guiding template may help decrease operation time, decrease blood loss, and improve short-term clinical outcomes in patients undergoing UKA surgery.

1. Introduction

The prevalence of osteoarthritis (OA) of the knee has increased rapidly with the aging of the population, and it has become a major cause of pain and disability. For medial compartment knee osteoarthritis (MOA), unicompartmental knee arthroplasty (UKA) has several advantages over total knee arthroplasty (TKA), including the preservation of

almost all functions of the knee joint, lower postoperative complications rate, and quicker postoperative functional recovery. However, for successful UKA, accurate alignment of the limb is crucial; even a minimal shift may decrease the lifespan of the prosthesis and lead to a need for revision surgery [1, 2]. Currently, the balance of soft tissues, the selection of prosthesis size, the angle of osteotomy, and related lower limb alignment are mainly decided by visual assessment of

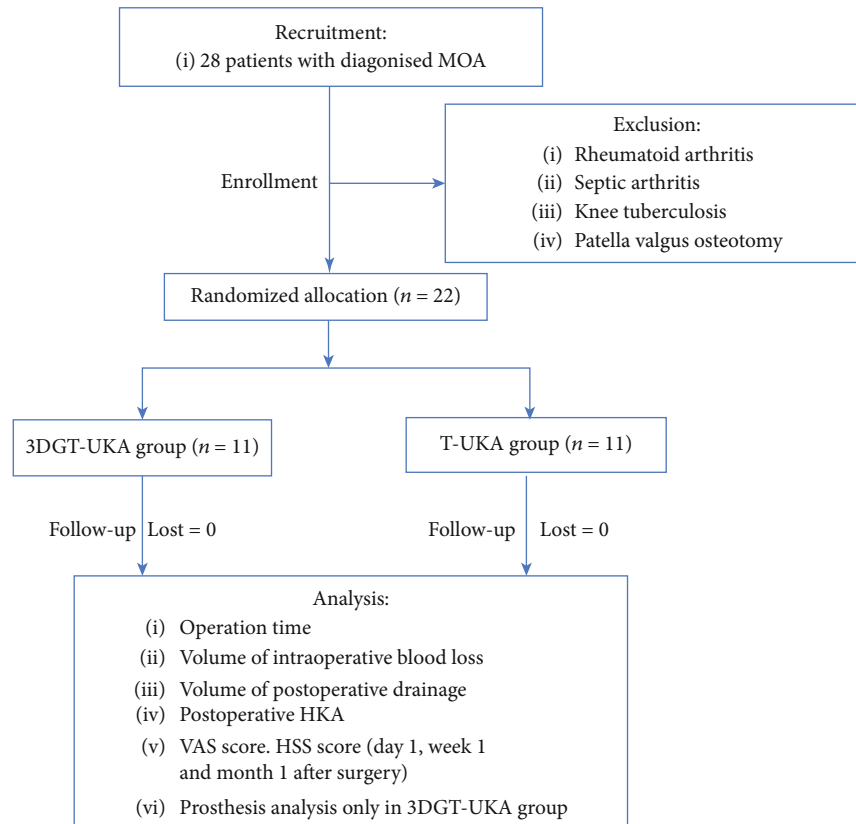


FIGURE 1: Consort diagram.

the surgeon. Therefore, the experience of the surgeon is one of the key factors for the reasonable performance of UKA. However, individual variations between patients and the lack of familiarity of the surgeon with the medical apparatuses might influence the final surgical effect [3].

In recent years, there has been much research on the use of three-dimensional (3D) digital image design and 3D-printing technology to build personalized guiding templates for knee surgery. A 3D-printed individualized guiding template based on CT-MRI fusion data could greatly improve the accuracy of estimation of the angle, the amount of osteotomy, the sizes of the tibial platform, and the femoral condyle prosthesis [4–7]. The aim of this randomized clinical trial was to investigate the efficacy and safety of the use of 3D-printed individual patient-customized guiding templates for assisting UKA.

2. Materials and Methods

2.1. Patients. This randomized clinical trial was performed at the Department of Orthopedics, Nanjing First Hospital, affiliated to Nanjing Medical University. MOA patients requiring UKA surgery during the period of January 2017 to December 2017 were enrolled in this study. Patients were eligible for inclusion if they had (1) a diagnosis of MOA confirmed by X-ray and MRI, (2) intact anterior cruciate ligament, and (3) knee varus deformity that could be corrected manually. Patients with a history of rheumatoid arthritis, septic arthritis, knee tuberculosis, and patella valgus osteotomy

were excluded. A total of 22 patients who met these criteria were enrolled and randomly assigned to receive either 3D-printed patient-customized guiding template-assisted UKA (3DGT-UKA group) or traditional UKA (T-UKA group) (Figure 1).

This study was approved by the Ethics Committee of Nanjing Hospital affiliated to Nanjing Medical University. All patients gave written informed consent for participation in the study.

2.2. Preoperative Preparation. Preoperatively, all patients underwent electrocardiography, routine blood examination, and vascular ultrasonography of the lower limb. Patients with comorbidities received appropriate specialist consultations to rule out contraindications to surgery.

2.3. Design and Production of 3D-Printed Personalized Guiding Template for UKA Osteotomy. Patients in the 3DGT-UKA group first underwent a double-source 64-slice spiral CT (Siemens Sensation, Germany) full-length scan of the lower limbs and MRI scans of the knee joints. The data were imported into a workstation. CT data were processed using the Mimics 17.0 software (Materialise Ltd., Leuven, Belgium) to reconstruct a 3D model of the full length of the lower limbs. The MRI data were processed to obtain a 3D model of the knee joint. The two models were then merged to obtain a 3D model of the lower limbs with the cartilage lining of the knee joints also displayed. The angle between the hip and knee (HKA) and the mechanical axis of the femur

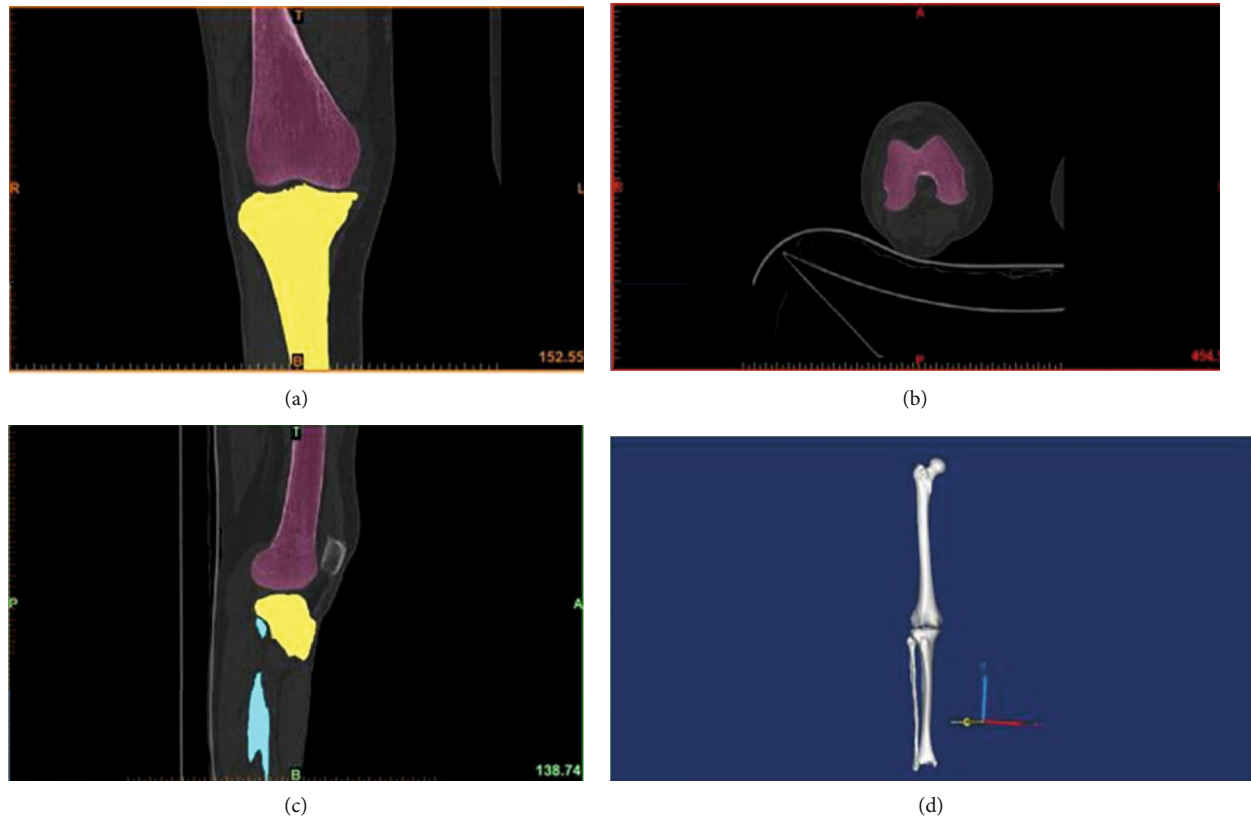


FIGURE 2: (a) Front view CT image of the knee joint. (b) Top view CT image of the knee joint. (c) Side view CT image of the knee joint. (d) Reconstructed three-dimensional model of a lower limb in full length.

and the tibia were measured using a computer-aided design (CAD) software (Medivi, Changzhou, China). The angle and amount of osteotomy were accurately calculated on the reconstructed 3D model, and the posterior oblique angle and amount of osteotomy necessary at the tibial plateau were determined. Finally, a 3D-printed customized guiding template was created for each patient. The template was sterilized with plasma before use (Figures 2 and 3).

2.4. Surgical Methods. The 3rd generation Oxford prostheses for UKA were used for all patients. All surgeries were performed by the same surgical team. Surgery was performed under general anesthesia. Patients in the 3DGT-UKA group were in the supine position, and a tourniquet was placed at the base of the affected limb. The hip was flexed 30° and mildly abducted, with the calf hanging naturally down. Free movement of the knee joint for at least 135° was ensured. With the knee flexed at 90° , a 6-cm incision was made on the medial side of the knee joint, extending from the distal end of the joint line at the medial edge of the tibia up to the medial edge of the femoral muscle. The distal femoral fat pad was removed to expose the distal femur and the superior tibia. The femoral condyle, intercondylar fossa, tibial plateau epiphysis, and the soft tissue attached to the anterior side of the platform were removed. Then, the tibial 3D-printed patient-customized guiding template was carefully and closely applied on the anterior aspect of the tibial plateau, and with its guidance holes were drilled into the proximal

end of the tibia. The positioning nails were inserted, and the 3D-printed patient-customized guiding template was removed. Next, the manufacturer-made matching osteotomy template (Zimmer Ltd., USA) was then positioned, and osteotomy of the tibial plateau was carried out. After the osteotomy, the dimensions of the cut tibial plateau and prosthesis were measured. The distal femur and intercondylar fossa were then exposed. The distal femoral 3D-printed guiding template was placed in position, and the drilling was carried out. The distal femoral template was removed, and the manufacturer-made posterior condylar template (Zimmer Ltd., USA) was placed for posterior condylar osteotomy. The bone bung was inserted into the distal femur for grinding. Finally, a single condylar prosthesis of the appropriate preoperatively determined size was then installed (Figure 4).

In the T-UKA group, the conventional single condylar replacement method was used. Tibial osteotomy aimed at making a downward 7° of posterior tilt in the tibial plateau. The thickness of the tibial osteotomy was 2-3 mm less than the depth of the deepest part of the tibial wear. Osteotomy of the medial femoral condyle was performed by intramedullary positioning. After drilling the anterior angle of the anterior intercondylar fossa, the rods for intramedullary positioning were inserted. The femoral drill guide was placed, ensuring that the handle was parallel with the long axis of the tibia. The kneading surface was close to each other, and the relevant angle was adjusted. The positioning holes (diameter of 4 mm and 6 mm) were drilled and according to the

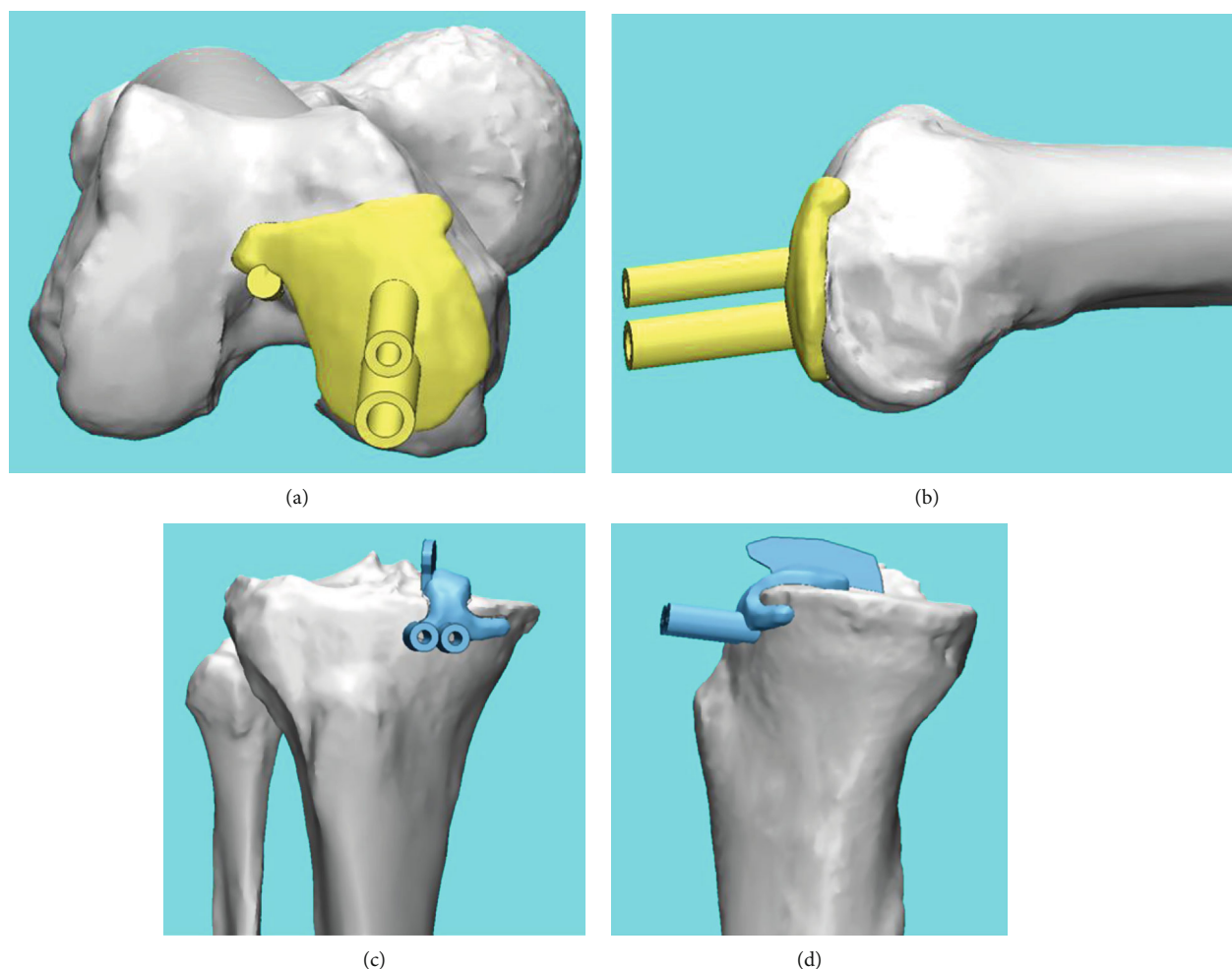


FIGURE 3: (a) Front view of the femoral 3D-printed guiding template. (b) Side view of the femoral 3D-printed guiding template. (c) Front view of the tibial 3D-printed guiding template. (d) Side view of the tibial 3D-printed guiding template.

position of them; the posterior femoral condyle was cut and ground. Prostheses of appropriate sizes were then installed into the tibia and femur.

Drainage tubes were placed in both groups after surgery [8–10]. All patients routinely received antibiotics and analgesics, as well as low-molecular-weight heparin as an anticoagulant therapy. Passive exercises were started 24 hours after surgery. The drainage tube was removed 48 hours after surgery. Patients were encouraged to walk with the help of a walking assistance device and to perform stretching and contracting exercise of quadriceps. A full-length radiograph of the affected lower limb and a positive lateral radiograph of the knee joint were examined at 2 days postoperation, and the HKA deviation was obtained (Figure 5). Sutures were removed 2 weeks after surgery. The VAS scores on day 1, week 1, month 1, and month 3 after surgery, and the Hospital for Special Surgery (HSS) scores on week 1, month 1, and month 3 after surgery, were recorded.

2.5. Postoperative Evaluation. An outpatient follow-up for three months was conducted to evaluate the recovery of the

patients. And all patients involved in this study completed the postoperative follow-up. The sizes of the preoperatively designed theoretical prosthesis and that of the actual prosthesis used during the operation in the 3DGT-UKA group were compared. The operation time, intraoperative blood loss, postoperative drainage, and postoperative HKA were compared between the two groups. VAS score on day 1, week 1, month 1, and month 3 after surgery and HSS score on week 1, month 1, and month 3 were also compared between the two groups. Because the operation time of patients in both groups was within the set time (90 minutes) of a lower extremity tourniquet, the volume of postoperative drainage was recorded and calculated as the volume of blood loss in the current study.

2.6. Statistical Analysis. Statistical analysis was performed using the SPSS 22.0 statistical software (IBM Corp., Armonk, NY, USA). The rank-sum test was performed for ranked data in the two groups. The *t*-test was used for the analysis measurement data and the chi-squared test for enumeration data. Statistical significance was at $p \leq 0.05$.

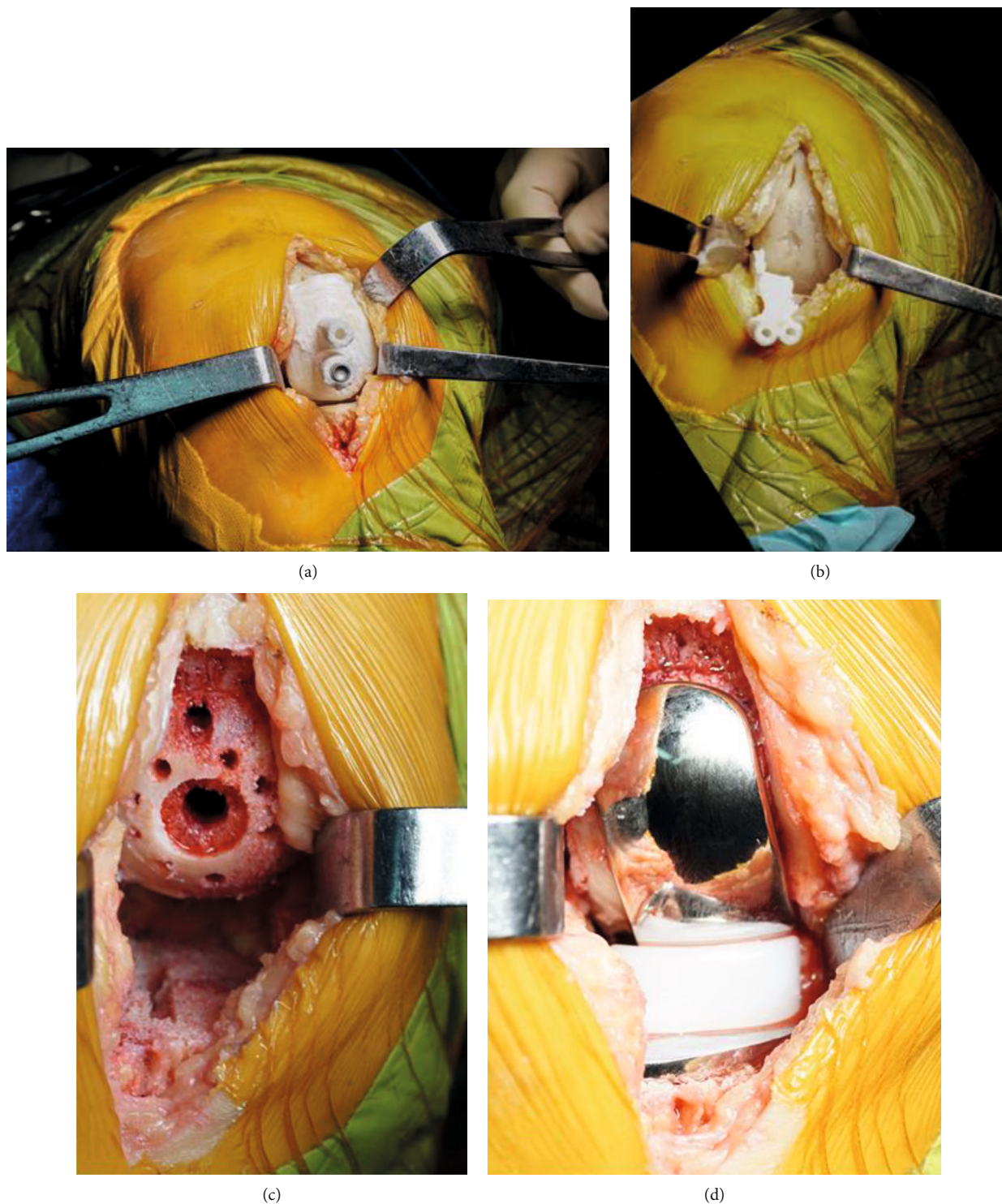


FIGURE 4: (a) Intraoperative placement of the femoral condyle 3D-printed guiding template. (b) Intraoperative placement of the tibial plateau 3D-printed guiding template. (c) Images of the femoral and tibial osteotomy. (d) Images of the installed prosthesis.

3. Results

A total of 22 patients (8 males, 14 females) with mean age 60.8 ± 4.8 years (age range, 52-67 years) were enrolled and randomized to receive either 3DGT-UKA ($n = 11$) or T-

UKA ($n = 11$). The gender ratio, mean age, mean height, pre-operative HSS score, and prevalence of comorbidities were comparable in the two groups (Table 1). In the 3DGT-UKA group, no significant difference was seen between the sizes of actual prosthesis used and preoperative theoretical prosthesis

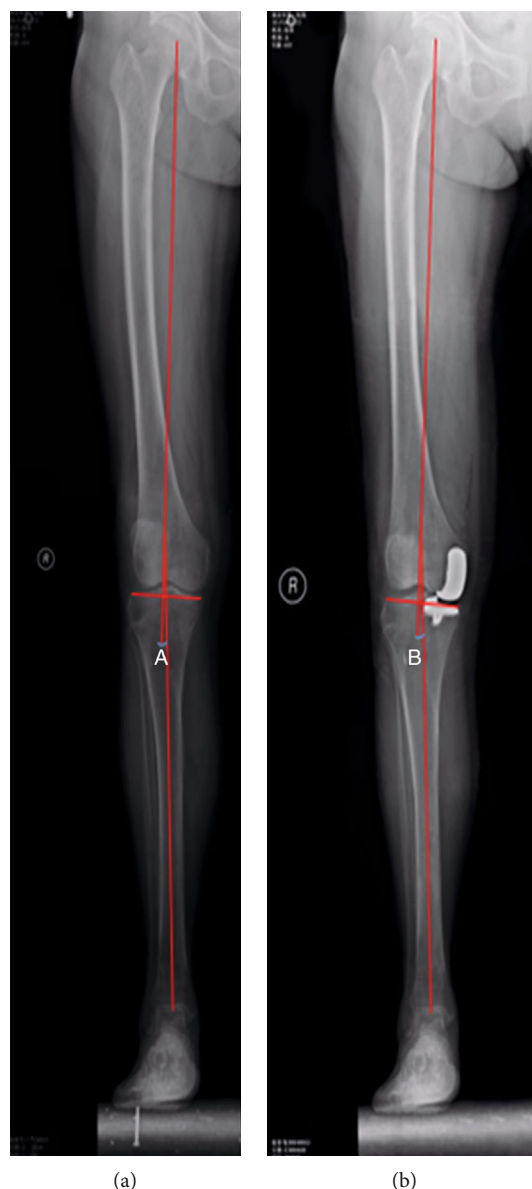


FIGURE 5: (a) Preoperative lower limb line (angle between the hip and knee (A) = 3.5°). (b) Postoperative lower limb line (angle between the hip and knee (B) = 2.4°).

model ($p > 0.05$; Table 2). There was no significant difference between the two groups in postoperative HKA deviation ($p > 0.05$; Table 3). Operation time was significantly shorter in the 3DGT-UKA group than in the T-UKA group (53.6 ± 6.4 minutes vs. 75.8 ± 7.1 minutes; $p < 0.05$). The volume of postoperative drainage was significantly lower in the 3DGT-UKA group than in the T-UKA group (67.5 ± 3.9 mL vs. 93.2 ± 3.0 mL; $p < 0.05$). The mean hospitalization time was longer in the T-UKA group than in the 3DGT-UKA group. The VAS scores on day 1, week 1, and month 1 after surgery were significantly lower in the 3DGT-UKA group than in the T-UKA group ($p < 0.05$). And the HSS scores on week 1 and month 1 after surgery were higher in the 3DGT-UKA group than in the T-UKA group ($p < 0.05$). The HSS scores on month 3 after surgery were comparable between the two groups ($p > 0.05$; Tables 4 and 5).

4. Discussion

In theory, for OA of the knee with only medial compartment lesions, UKA may be a reasonable candidate by the preservation of the anterior-posterior cruciate ligaments. This means that most functions of the knee joint may be retained after UKA surgery. Previous studies proved that UKA showed significant advantages in symptom relief, knee function recovery, and postoperative complications, compared to TKA [8–11]. However, the long-term studies showed that the survival of prostheses in UKA was significantly lower than TKA, which may be caused by the inadequate surgical exposure due to the small incision used in UKA, large errors in intraoperative extracorporeal positioning of the lower extremity force line, and intramedullary positioning of the femoral condyle [12]. It has

TABLE 1: Demographic and clinical characteristics of patients in the 3DGT-UKA group and T-UKA group.

| Group | Number | Gender | | Age (yr, mean ± SD) | Height (cm, mean ± SD) | Difference of knee joints | | Pre-operative HSS score (mean ± SD) | Alignment of lower limb, ° (mean ± SD) | Hypertension, n (%) | Diabetes, n (%) |
|-----------------------------|--------|--------|--------|------------------------|---------------------------|------------------------------|-------|---|--|------------------------|--------------------|
| | | Male | Female | | | Left | Right | | | | |
| 3DGT-UKA | 11 | 3 | 8 | 60.00 ± 4.31 | 159.55 ± 7.94 | 6 | 5 | 77.82 ± 2.44 | 7.23 ± 0.96 | 4 (36%) | 2 (18%) |
| T-UKA | 11 | 5 | 6 | 61.64 ± 5.33 | 161.64 ± 6.44 | 5 | 6 | 76.92 ± 2.47 | 7.19 ± 0.90 | 3 (27%) | 2 (18%) |
| <i>t</i> value ¹ | | | | -0.791 | -0.678 | | | 0.868 | 0.092 | | |
| <i>p</i> value ² | | | 0.659 | 0.438 | 0.505 | 1.000 | 1.000 | 0.395 | 0.928 | 1.000 | 1.000 |

¹The *t* test was used for the comparison of age, height, preoperative HSS score, and alignment of preoperative lower limb. ²Fisher's exact test was used for comparison of gender ratio and surgery.

TABLE 2: Actual and theoretical values of surgical prosthesis models in the 3DGT-UKA group.

| | 3DGT-UKA femoral prosthesis model | | 3DGT-UKA tibial prosthesis model | | | |
|---------------------------|-----------------------------------|-------|----------------------------------|-------|-------|-------|
| | M | S | C | B | A | AA |
| Theoretical value | 1 | 10 | 0 | 4 | 5 | 2 |
| Actual value | 2 | 9 | 1 | 4 | 4 | 2 |
| Test statistics | 0.29 | 0.03 | 0.96 | 0 | 0.08 | 0 |
| t value/ χ^2 value | 0.588 | 0.867 | 0.328 | 1.000 | 0.779 | 1.000 |
| p value | >0.05 | >0.05 | >0.05 | >0.05 | >0.05 | >0.05 |

M, S, C, B, A, and AA represent the prosthesis model of the femoral and tibial.

TABLE 3: Comparison of HKA deviation in the 3DGT-UKA group and T-UKA group.

| Group | Number | HKA deviation | | |
|----------------------|--------|-----------------|--------------------------------|-----------------|
| | | > $\pm 2^\circ$ | $\pm 1^\circ$ to $\pm 2^\circ$ | < $\pm 1^\circ$ |
| 3DGT-UKA | 11 | 3 | 5 | 3 |
| T-UKA | 11 | 4 | 4 | 3 |
| Z value ¹ | | | -0.28 | |
| p value | | | 0.78 | |

¹Mann-Whitney U test.

been confirmed that a slight error in the alignment of the lower limb line and a lower extremity varus increases the need for future revision surgery in patients receiving UKA. Meanwhile, postoperative valgus can significantly increase lateral compartment stress and lead to accelerated cartilage degeneration in the lateral compartment of the knee joint [13]. Therefore, in UKA patients, detailed preoperative planning and precise positioning of the intraoperative prosthesis is crucial.

Routine analysis of radiography, CT, and MRI images of the knee joint is difficult to accurately obtain the 3D structure of the lower extremities, and it is also difficult to quantitatively show the cartilage wear of the medial compartment. It looks like the measurement error cannot be avoided during the operation because the positioning of the tibial plateau in T-UKA patients depends on the extramedullary positioning rods, which is subjective. Furthermore, deviations in the intramedullary positioning of the distal femoral condyle and any other errors in the direction of the positioning rod may lead to impingement or unsatisfactory meniscus trajectory, as well as prolonged operation time, increased blood loss, and the risk of intraoperative fat embolism. Ma et al. studied the positional differences of unicompartmental prostheses caused by the deviation of the intramedullary positioning entrance points in the femurs of 20 corpses and concluded that the intramedullary positioning rods could not accurately indicate the actual anatomical axis of the femur, which usually leads to a deviation with 3.2° of deflection and 2.5° of valgus [14]. Baldini et al. found that 10%-20% of patients who received T-UKA had a significant deviation of the femoral force line on the prosthetic side from the normal [15]. Therefore, we felt that a 3D-printed individualized

guiding template based on quantitative anatomical data and accurate preoperative CAD measurement results would be helpful in the selection of the appropriate osteotomy angle and amount. In addition, there is no need for opening of the femoral bone marrow during femoral osteotomy with 3DGT-UKA, which helps reduce the surgical exposure time, postoperative blood loss, and amount of intraoperative instrumentation.

A 3D-printed guiding template based on CT data alone is difficult to achieve good intraoperative fitting of the guiding template due to it does not take into consideration the cartilage tissue influence, which has been shown to be responsible for the decrease in the accuracy of the 3D-printed guiding template [16]. Therefore, in this present study, the CT and MRI data were merged to reconstruct the 3D anatomy of the knee joint, which allowed accurate calculation of the lower limb force line, angle, and osteotomy amount. This method can help us design an accurate 3D-printed patient-customized guiding template during UKA surgery. Due to the refined and minimally invasive design of the third-generation Oxford knee prosthesis for UKA, the flexible meniscus pad also reduces the risk of impingement and rotation of the prosthesis. Therefore, the design of the 3D-printed guiding template in this study was based on the third-generation Oxford UKA tool kit. We found there was no significant statistical difference in dimensions between the preoperatively designed theoretical prosthesis and the actual prosthesis used in the 3DGT-UKA group. There was also no significant difference in HKA between the 3DGT-UKA and T-UKA groups, indicating the accuracy of the 3DGT-UKA surgery [17, 18].

Compared to the 3DGT-UKA group, which prosthesis selection is based on accurate preoperative measurements of the reconstructed 3D knee joint, leading to less errors and rapid surgery completion [19, 20], the T-UKA group select the prosthesis model based on preoperative radiographic measurements, which is subjective and may cause large errors. Therefore, repeated measurements are necessary during surgery to select the appropriate size. In addition, the 3D-printed guiding template easily and accurately locates the surgical osteotomy tool without slotting, which also contributes to the decrease in operation time and postoperative drainage volume. Also, we found the 3D-printed guiding template can help to reduce surgical trauma during UKA surgery and the duration of

TABLE 4: Comparison of surgical parameters and outcomes between the 3DGT-UKA group and the T-UKA group.

| Group | Number | Operation time (min, mean \pm SD) | Volume of postoperative drainage in 48 hours (mL, mean \pm SD) | Postoperative HKA ($^{\circ}$, mean \pm SD) |
|----------------|--------|-------------------------------------|--|---|
| 3DGT-UKA | 11 | 75.82 \pm 6.91 | 85.18 \pm 2.96 | 1.74 \pm 0.78 |
| T-UKA | 11 | 67.64 \pm 6.41 | 67.55 \pm 3.86 | 1.81 \pm 0.67 |
| <i>t</i> value | | 2.879 | 12.031 | -0.205 |
| <i>p</i> value | | 0.009 | 0.000 | 0.840 |

TABLE 5: Comparison of postoperative VAS score and HSS score between the 3DGT-UKA group and the T-UKA group.

| Group | Postoperative VAS score (mean \pm SD) | | | | Postoperative HSS score (mean \pm SD) | | |
|----------------|---|-----------------|-----------------|-----------------|---|------------------|------------------|
| | Day 1 | Week 1 | Month 1 | Month 3 | Week 1 | Month 1 | Month 3 |
| 3DGT-UKA | 4.64 \pm 0.92 | 2.00 \pm 0.77 | 0.82 \pm 0.60 | 0.46 \pm 0.52 | 80.09 \pm 5.87 | 95.18 \pm 1.40 | 96.46 \pm 1.44 |
| T-UKA | 7.64 \pm 0.92 | 5.70 \pm 0.90 | 2.46 \pm 0.82 | 0.27 \pm 0.47 | 70.10 \pm 5.87 | 93.73 \pm 1.27 | 96.46 \pm 1.21 |
| <i>t</i> value | 7.611 | 10.381 | 5.331 | 0.861 | 3.993 | 2.549 | 0.000 |
| <i>p</i> value | <0.001 | <0.001 | <0.001 | 0.146 | 0.001 | 0.019 | 0.482 |

tourniquet application, which is probably related to the lower VAS score on day 1 and week 1 and higher HSS score on week 1 and month 1 after surgery in the 3DGT-UKA group.

There are also some disadvantages with 3DGT-UKA. On the one hand, patients undergoing 3DGT-UKA need preoperative full-length CT and MRI scans, which increase medical costs and extra radiation exposure. On the other hand, specialized knowledge and special hardware and software are necessary for designing and printing an accurate 3D guiding template. All of these would increase the patient's economic burden. As for this study, we should also emphasize that it has some limitations. First, since the three-dimensional-printed guiding template for UKA is a new technique and the exclusion criteria are very strict, there was not much sample number. Second, we only collected the data of short-term outcomes; maybe we should focus on the midterm and long-term follow-up between these two groups in the further study.

To summarize, the 3D-printed guiding template can provide useful assistance for preoperative planning, intraoperative positioning, and osteotomy during UKA. It shortens the operation time, minimizes surgical trauma, and achieves better short-term clinical outcomes. In addition, the long-term follow-up outcomes need further research.

Abbreviations

| | |
|--------|---|
| UKA: | Unicompartmental knee arthroplasty |
| 3DGT: | Three-dimensional printed patient-customized guiding template |
| T-UKA: | Traditional UKA |
| HKA: | Hip-knee angle |
| HSS: | Hospital for Special Surgery |
| OA: | Osteoarthritis |
| MOA: | Medial compartment knee osteoarthritis |
| TKA: | Total knee arthroplasty |
| 3D: | Three-dimensional |
| CAD: | Computer-aided design. |

Data Availability

The data supporting the findings is available in this manuscript, but we do not wish to share the data before it is published, because it is involved in the privacy of the patients, including age, sex, and the image of the radiology and intraoperative.

Ethical Approval

Ethical approval of the three-dimensional-printed guiding template for unicompartmental knee arthroplasty was given by the medical ethics committee of the Ethical Committee of Nanjing First Hospital with the following reference number: KY20160122-14. All of the participants agree to take part in this study; we have gained the informed consent for publication of the data from the participants.

Consent

All of the authors give permission to publish this manuscript.

Conflicts of Interest

The authors declare that they have no conflicts of interest.

Authors' Contributions

All authors were fully involved in the study and preparation of the manuscript. Dr. Fei Gu, Dr. Liangliang Li, and Hui-kang Zhang were mainly responsible for the collection of CT data of the patients and the 3D printing of the guide templates. Dr. Xuxiang Li and Dr. Chen Ling were mainly responsible for patient recruitment. Dr. Liming Wang, Dr. Qingqiang Yao, Dr. Fei Gu, and Dr. Liangliang Li performed the operation. Dr. Liming Wang and Dr. Qingqiang Yao were mainly responsible for designing the study and wrote the paper. Dr. Fei Gu and Dr. Liangliang Li contributed equally to this work.

Acknowledgments

Thanks are due to Miss Xu and Miss Peng for their help during the collection of the patients' CT data. This study was supported by the National Key Research and Development Program of China (2018YFC1105204), National Natural Science Foundation of China (81601612, 81771985), and Key Research Program of Science & Technology Support Program of Jiangsu Province (BE 2015613, BE 2016763).

References

- [1] N. P. Kort, J. J. van Raay, J. Cheung, C. Jolink, and R. Deutman, "Analysis of Oxford medial unicompartmental knee replacement using the minimally invasive technique in patients aged 60 and above: an independent prospective series," *Knee Surgery, Sports Traumatology, Arthroscopy*, vol. 15, no. 11, pp. 1331–1334, 2007.
- [2] F. Voss, M. B. Sheinkop, J. O. Galante, R. M. Barden, and A. G. Rosenberg, "Miller-Galante unicompartmental knee arthroplasty at 2- to 5-year follow-up evaluations," *The Journal of Arthroplasty*, vol. 10, no. 6, pp. 764–771, 1995.
- [3] M. Chowdhry, R. S. Khakha, M. Norris, A. Kheiran, and S. K. Chauhan, "Improved survival of computer-assisted unicompartmental knee arthroplasty: 252 cases with a minimum follow-up of 5 years," *The Journal of Arthroplasty*, vol. 32, no. 4, pp. 1132–1136, 2017.
- [4] A. Manzotti, P. Cerveri, C. Pullen, and N. Confalonieri, "Computer-assisted unicompartmental knee arthroplasty using dedicated software versus a conventional technique," *International Orthopaedics*, vol. 38, no. 2, pp. 457–463, 2014.
- [5] R. Pailhé, J. Cognault, J. Massfelder et al., "Comparative study of computer-assisted total knee arthroplasty after opening wedge osteotomy versus after unicompartmental arthroplasty," *The bone & joint journal*, vol. 98, no. 12, pp. 1620–1624, 2017.
- [6] D. K. Bae and S. J. Song, "Computer assisted navigation in knee arthroplasty," *Clinics in Orthopedic Surgery*, vol. 3, no. 4, pp. 259–267, 2011.
- [7] D. Saragaglia, J. Massfelder, R. Refaie et al., "Computer-assisted total knee replacement after medial opening wedge high tibial osteotomy: medium-term results in a series of ninety cases," *International Orthopaedics*, vol. 40, no. 1, pp. 35–40, 2017.
- [8] P. Hernigou and G. Deschamps, "Alignment influences wear in the knee after medial unicompartmental arthroplasty," *Clinical Orthopaedics and Related Research*, vol. 423, pp. 161–165, 2004.
- [9] P. Hernigou and G. Deschamps, "Posterior slope of the tibial implant and the outcome of unicompartmental knee arthroplasty," *The Journal of Bone and Joint Surgery. American Volume*, vol. 86, no. 3, pp. 506–511, 2004.
- [10] N. P. Kort, J. J. van Raay, and B. J. Thomassen, "Alignment of the femoral component in a mobile-bearing unicompartmental knee arthroplasty: a study in 10 cadaver femora," *The Knee*, vol. 14, no. 4, pp. 280–283, 2007.
- [11] T. Walker, T. Gotterbarm, T. Bruckner, C. Merle, and M. R. Streit, "Total versus unicompartmental knee replacement for isolated lateral osteoarthritis: a matched-pairs study," *International Orthopaedics*, vol. 38, no. 11, pp. 2259–2264, 2014.
- [12] B. Bordini, S. Stea, S. Falcioni, C. Ancarani, and A. Toni, "Unicompartmental knee arthroplasty," *The Knee*, vol. 21, no. 6, pp. 1275–1279, 2014.
- [13] O. R. Kwon, K. T. Kang, J. Son, D. S. Suh, C. Baek, and Y. G. Koh, "Importance of joint line preservation in unicompartmental knee arthroplasty: finite element analysis," *Journal of Orthopaedic Research*, vol. 35, no. 2, pp. 347–352, 2017.
- [14] B. Ma, W. Long, J. F. Rudan, and R. E. Ellis, "Three-dimensional analysis of alignment error in using femoral intramedullary guides in unicompartmental knee arthroplasty," *The Journal of arthroplasty*, vol. 21, no. 2, pp. 271–278, 2006.
- [15] A. Baldini and P. Adravanti, "Less invasive TKA," *Clinical Orthopaedics and Related Research*, vol. 466, no. 11, pp. 2694–2700, 2008.
- [16] V. De Santis, A. Burrofato, R. D'Apolito et al., "Evaluation of accuracy of bone cuts and implant positioning in total knee arthroplasty using patient specific instrumentation," *Journal of Biological Regulators & Homeostatic Agents*, vol. 31, 4 suppl 1, pp. 51–60, 2017.
- [17] J. Y. Jenny and C. Boeri, "Accuracy of implantation of a unicompartmental total knee arthroplasty with 2 different instrumentations," *The Journal of Arthroplasty*, vol. 17, no. 8, pp. 1016–1020, 2002.
- [18] G. Keene, D. Simpson, and Y. Kalairajah, "Limb alignment in computer-assisted minimally-invasive unicompartmental knee replacement," *Journal of Bone and Joint Surgery. British Volume (London)*, vol. 88, pp. 44–48, 2006.
- [19] R. A. Berger, R. M. Meneghini, J. J. Jacobs et al., "Results of unicompartmental knee arthroplasty at a follow-up of ten-years follow-up," *Journal of Bone and Joint Surgery*, vol. 87, pp. 999–1006, 2005.
- [20] J. Newman, R. V. Pydisetty, and C. Ackroyd, "Unicompartmental or total knee replacement: the 15-year results of a prospective randomised controlled trial," *Journal of Bone and Joint Surgery. British Volume (London)*, vol. 91, pp. 52–57, 2009.

Research Article

In Vivo Reconstruction of the Acetabular Bone Defect by the Individualized Three-Dimensional Printed Porous Augment in a Swine Model

Jun Fu ¹, Yi Xiang ², Ming Ni ¹, Xiaojuan Qu ³, Yonggang Zhou ¹, Libo Hao ¹, Guoqiang Zhang ¹ and Jiying Chen ¹

¹Department of Orthopaedics, The First Medical Centre, Chinese PLA General Hospital, Beijing 100853, China

²Department of Orthopaedics, The Logistics Support Forces of Chinese PLA 985 Hospital, Taiyuan, Shanxi 030001, China

³Otolaryngological Department, The Logistics Support Forces of Chinese PLA 985 Hospital, Taiyuan, Shanxi 030001, China

Correspondence should be addressed to Guoqiang Zhang; gqzhang301@163.com and Jiying Chen; jiyingschen_301@163.com

Received 23 June 2020; Revised 14 October 2020; Accepted 17 November 2020; Published 1 December 2020

Academic Editor: Anish R. Kadakia

Copyright © 2020 Jun Fu et al. This is an open access article distributed under the Creative Commons Attribution License, which permits unrestricted use, distribution, and reproduction in any medium, provided the original work is properly cited.

Background and Purpose. This study established an animal model of the acetabular bone defect in swine and evaluated the bone ingrowth, biomechanics, and matching degree of the individualized three-dimensional (3D) printed porous augment. **Methods.** As an acetabular bone defect model created in Bama miniswine, an augment individually fabricated by 3D print technique with Ti6Al4V powders was implanted to repair the defect. Nine swine were divided into three groups, including the immediate biomechanics group, 12-week biomechanics group, and 12-week histological group. The inner structural parameters of the 3D printed porous augment were measured by scanning electron microscopy (SEM), including porosity, pore size, and trabecular diameter. The matching degree between the postoperative augment and the designed augment was assessed by CT scanning and 3D reconstruction. In addition, biomechanical properties, such as stiffness, compressive strength, and the elastic modulus of the 3D printed porous augment, were measured by means of a mechanical testing machine. Moreover, bone ingrowth and implant osseointegration were histomorphometrically assessed. **Results.** In terms of the inner structural parameters of the 3D printed porous augment, the porosity was $55.48 \pm 0.61\%$, pore size $319.23 \pm 25.05 \mu\text{m}$, and trabecular diameter $240.10 \pm 23.50 \mu\text{m}$. Biomechanically, the stiffness was $21464.60 \pm 1091.69 \text{ N/mm}$, compressive strength $231.10 \pm 11.77 \text{ MPa}$, and elastic modulus $5.35 \pm 0.23 \text{ GPa}$, respectively. Furthermore, the matching extent between the postoperative augment and the designed one was up to $91.40 \pm 2.83\%$. Besides, the maximal shear strength of the 3D printed augment was $929.46 \pm 295.99 \text{ N}$ immediately after implantation, whereas the strength was $1521.93 \pm 98.38 \text{ N}$ 12 weeks after surgery ($p = 0.0302$). The bone mineral apposition rate (μm per day) 12 weeks post operation was $3.77 \pm 0.93 \mu\text{m/d}$. The percentage bone volume of new bone was $22.30 \pm 4.51\%$ 12 weeks after surgery. **Conclusion.** The 3D printed porous Ti6Al4V augment designed in this study was well biocompatible with bone tissue, possessed proper biomechanical features, and was anatomically well matched with the defect bone. Therefore, the 3D printed porous Ti6Al4V augment possesses great potential as an alternative for individualized treatment of severe acetabular bone defects.

1. Introduction

Total hip arthroplasty (THA) represents one of the most successful surgeries in the 20th century and has been employed for releasing pain, correcting the deformity, and improving the function of the hip joint [1, 2]. The management of severe acetabular bone defects in primary or revision THA remains

a challenge for surgeons, and the ideal defect reconstruction is a critical factor for a successful THA [3]. Traditionally, major acetabular defects in primary and revision THA have been reconstructed by impaction bone grafting (IBG), metal augments, and cup/cage constructs [2]. Recently, given the improved biocompatibility and biomechanical properties of the trabecular metal (TM), TM augments and cups are most

commonly used and have achieved good clinical midterm outcomes in patients. Since TM augments are mass-produced with a unitary shape, they tend to anatomically mismatch with acetabular bone defects, and reaming the residual bone stock of acetabular defects is required in most cases [4–6]. Therefore, individualized augments are needed in these cases to better reconstruct the acetabular bone defects.

Titanium and titanium alloy are widely used to fabricate orthopaedic prostheses and instruments for their good biocompatibility, high strength, and low corrosion rates [7]. Multiple studies have been conducted to optimize the microstructure of the Ti6Al4V alloy, and porous Ti6Al4V alloy implants mechanically compatible with the cancellous bone have been developed [8, 9]. Studies showed that the pore size between 200 μm and 500 μm and a porosity of 50–75% were optimal for bone ingrowth and osteointegration [10, 11]. Further studies examined their biocompatibility and biomechanical features of the alloy *in vitro*, *in vivo*, and in clinical patients [12–14].

With the rapid development of the 3D printing technology, the 3D printed medical models, with an advantage of personalized treatment, are being extensively used in orthopaedic prostheses [15, 16]. Although a case report described the clinical application of the 3D printed augments in the repair of the acetabular defect [15], implant-bone integration has not been well assessed. In a previous study, we established a finite element analysis (FEA) model of the acetabular bone defect, which was reconstructed by 3D printed porous Ti6Al4V augments, and evaluated the stress distribution and clinical safety of augments, screws, and bones [17]. Until now, the performance of these 3D printed porous augments in animal models has not been systemically elucidated.

In this study, we established a miniswine model of the acetabular bone defect and implanted the 3D printed porous augments that were anatomically compatible with the bone defect. We further evaluated the bone ingrowth, biomechanics, and matching degree of the 3D printed porous augments in the animals.

2. Materials and Methods

2.1. Establishment and Validation of the Animal Model of the Acetabular Bone Defect. All animal experiments in this study were approved by the Experimental Animal Ethics Committee of the General Hospital of Chinese People's Liberation Army, Beijing, China. Bama miniswine (female, 14–18 months old with a body weight of 25–30 kg) were used to establish and validate the animal model of the acetabular bone defect. The swine were routinely maintained in the Experimental Animal Center of the General Hospital of Chinese People's Liberation Army. These miniswine were divided into three groups, with three animals in each group. Animals in group 1 were subjected to the biomechanical test immediately after augment implantation; swine in group 2 were biomechanically tested 12 weeks after augment implantation; pigs in group 3 were histologically examined 12 weeks after augment implantation. The miniswine were kept and fed in separate cages according to standard animal care protocols [18]. All the surgeries were performed on the right

acetabulum of the miniswine. The anesthetic methods included intramuscular and general anesthesia. Intramuscular anesthetics were a mixture of ketamine hydrochloride and xylazine hydrochloride (1:1 ratio, 15–25 mg/kg). The general anesthetic was 3% pentobarbital sodium (30 mg/kg). The vital signs (heart rate, breathing, and oxygen saturation) of the miniswine were carefully monitored, and intravenous fluid therapy involving glucose and lactated Ringer's solution was used during the operation.

At the first surgical phase of defect model establishment (Figures 1(a)–1(d)), the operation sites were removed of hair, shaved, disinfected, and draped. A straight 10 cm skin incision was made at the hip via the anterolateral approach. Then, the anterosuperior wall of the acetabulum was exposed clearly and a Paprosky IIB acetabular bone defect (an equilateral triangle with sides of about 2 cm) was made as previously reported [19]. The wound site was sutured for closure, and the acetabular bone defect was left untreated for approximately 1 week (waiting for fabrication by the 3D printed Ti6Al4V augment).

2.2. Design and Fabrication of the 3D Printed Porous Ti6Al4V Augment. Computed tomography (CT) scan of the animal pelvis was taken immediately after the establishment of the bone defect model. The pelvis and porous Ti6Al4V augment were three-dimensionally reconstructed on a direct metal laser sintering (DMLS) system (EOSINT M280, Germany) using a computer-aided design (CAD) software package (Mimics Research 20.0, Materialise, Belgium). A medical Ti6Al4V powder (EOS, Germany) with particles sized from 15 μm to 53 μm was used. The porous augments were 3D printed at a scanning rate of 7 m/s and a power of 200 W.

The inner pore parameters were as follows: a cubic-shaped lattice structure had a pore size of 400 μm , a strut size of 200 μm , and a porosity of 60%. The thickness of the porous Ti6Al4V coating was 1 mm, while the rest of the augment was of solid Ti6Al4V. Meanwhile, the position, direction, length, and diameter of screws and Kirschner wires (for temporary intraoperative fixation of the augment) were designed according to the residual bone stock of acetabular defects. The length of the screw ranged between 16 mm and 20 mm. The diameters of screws and K-wires were 4.0 mm and 1.5 mm, respectively. After printing, the 3D printed porous augments were cleaned, polished, sterilized, and then implanted. (Figures 2(a)–2(d) and 2(f)).

2.3. Porosity and Mechanical Evaluation of the 3D Printed Porous Augments. Printed specimens, with a diameter of 10 mm and a height of 20 mm, were used for evaluation of porosity and mechanical properties against the International Organization for Standardization (ISO 13314:2011). The total porosity and open porosity were measured using the gravimetric method and Archimedes' principle, respectively. The pore morphology, including pore size and strut size, was evaluated by using scanning electron microscopy (SEM, Zeiss Supra 55, Germany). The compressive strength of the porous Ti6Al4V augment was determined by employing a computer-controlled mechanical testing machine (Instron-8874, Instron, USA) at a loading speed of 1 mm/min. The

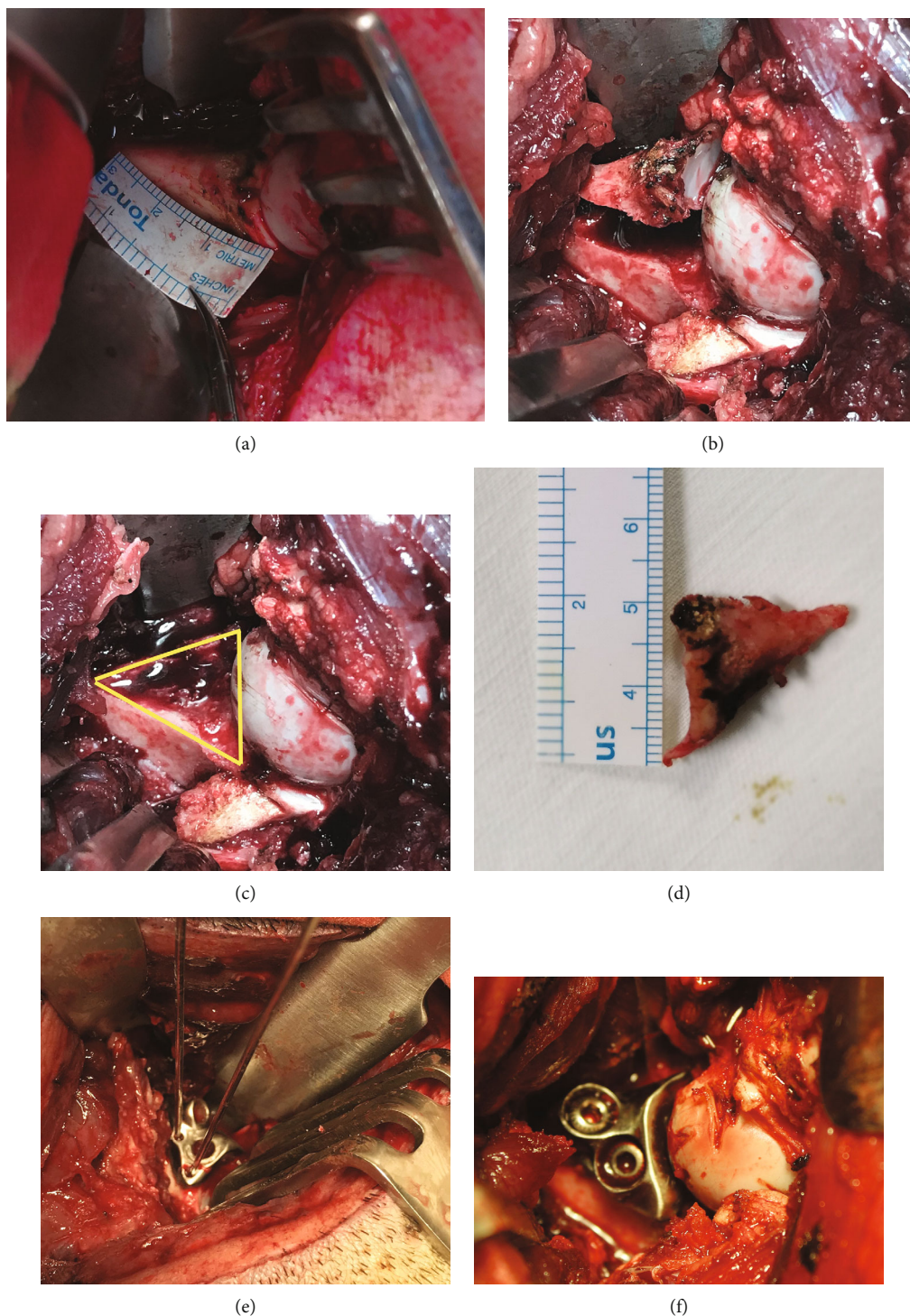


FIGURE 1: Representative pictures showing the establishment of the acetabular bone defect model and implantation of the 3D printed porous Ti6Al4V augment into miniswine. (a) The size of the acetabular bone defect was determined by a ruler. (b) The anterosuperior wall of the acetabulum was exposed clearly. (c) The bone defect model was completely created (the yellow triangle). (d) The size of the osteotomized bone was measured. (e) The 3D printed porous Ti6Al4V augment was temporarily fixed by two K-wires. (f) Two screws were inserted into the augment screw holes.

elastic modulus of the porous Ti6Al4V augment was calculated on the linear region of the stress-strain curve. The final measurements were averaged from five specimens in every group.

2.4. *Implantation of the 3D Printed Porous Ti6Al4V Augment.* At the second surgical phase of the 3D printed porous Ti6Al4V augment implantation (Figures 1(e) and 1(f)), preoperative preparation and exposure were similar to

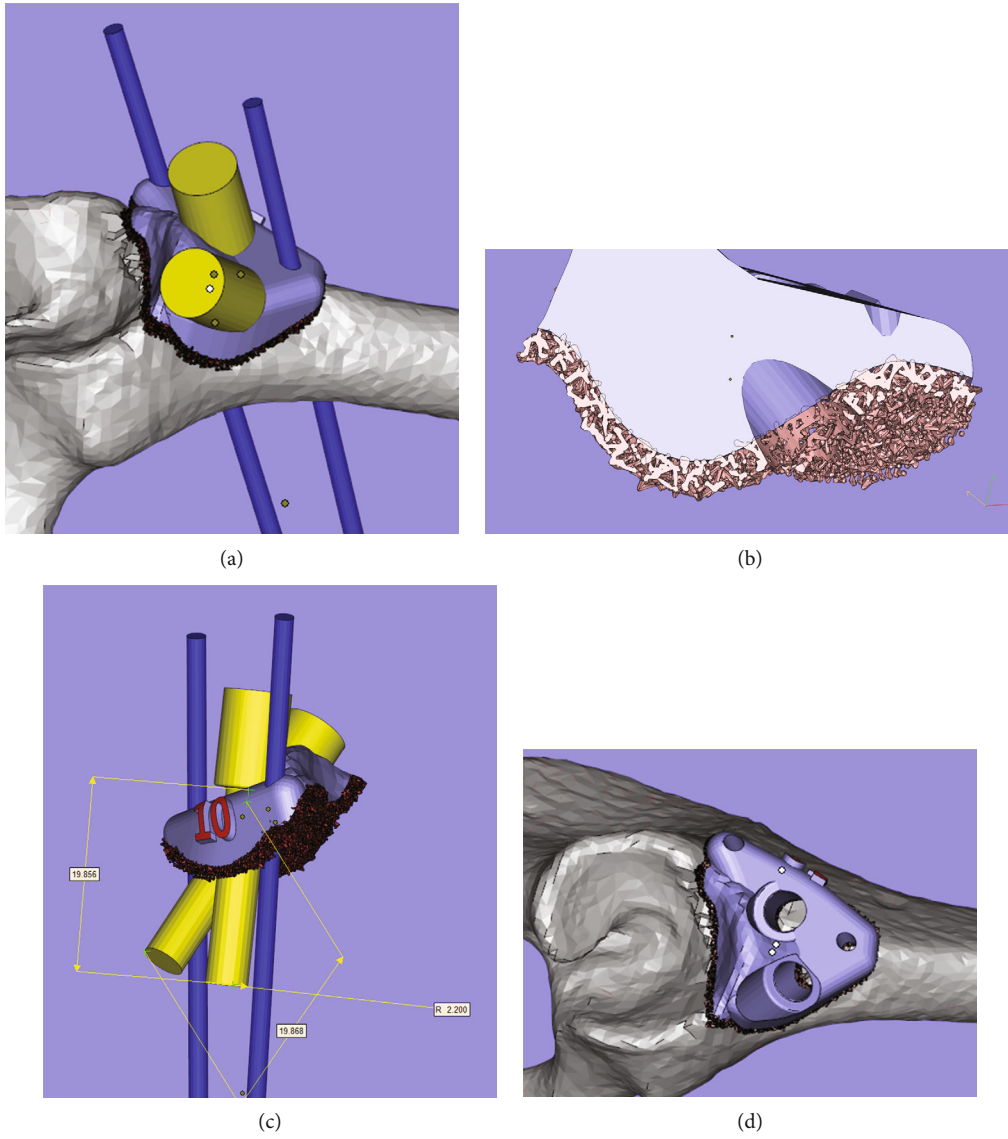


FIGURE 2: Continued.

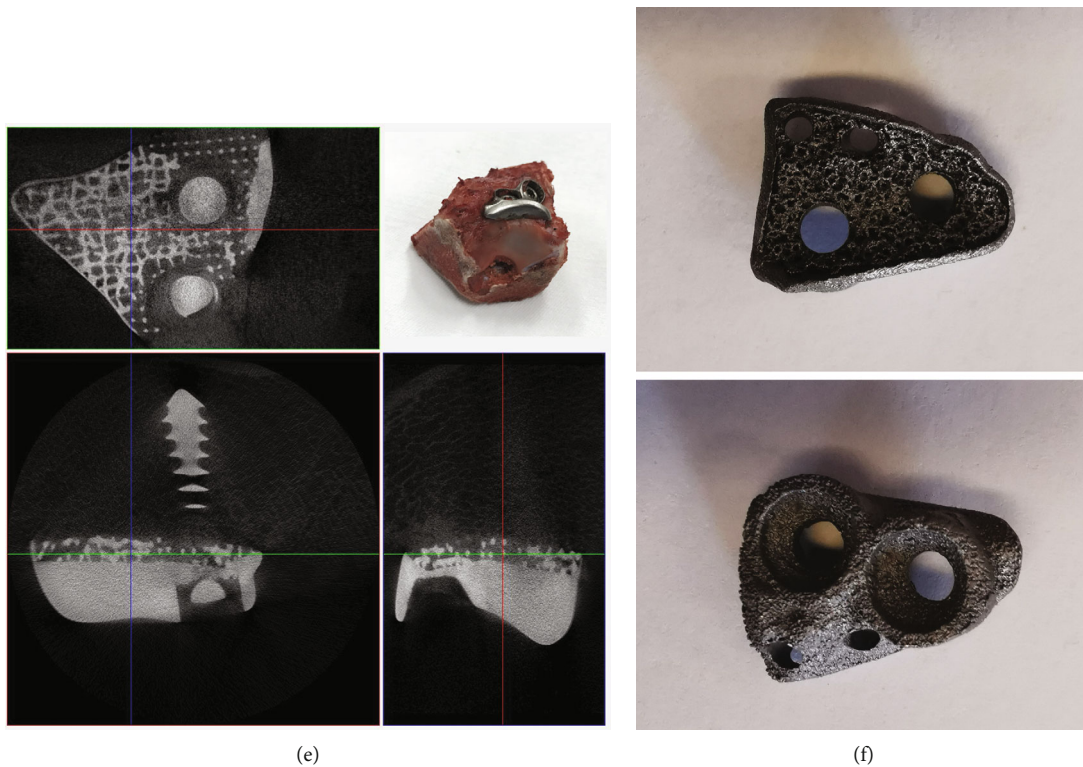


FIGURE 2: The graphical illustration of the design of the 3D printed porous Ti6Al4V augment and the micro-CT imaging of the acetabulum along with the augment taken from miniswine 3 months after implantation. (a) The thickness of the porous Ti6Al4V coating was 1 mm, and the rest of the augment was solid Ti6Al4V. (b) The designed length of screws was 16-20 mm. (c) The designed direction of screws. (d) The final design of the 3D printed porous Ti6Al4V augment fixed on the acetabulum. (e) The micro-CT imaging showing bone formation within the porous augments, and the specimen was taken 12 weeks after surgery (the inset in the upper-right corner). (f) The enlarged photo of the 3D printed porous Ti6Al4V augment.

the first phase. The individual porous augment was placed on the acetabular defect surface, and two 1.5 mm K-wires were used for temporary fixation. The augment matched well with the defect in terms of shape and size as observed by the naked eye. Then, two screws of appropriate length were inserted into the augment screw holes. Immediate stability of the augment was confirmed by shaking tests. The muscle tissues and skin were sutured layer by layer. After surgery, two injections of penicillin G (at 80 wu/time) were administered 48 hours after the implantation and at incision dressing.

All miniswine were subjected to pelvis CT scan immediately after surgery, and the DICOM data were used for the three-dimensional reconstruction of the augment. Then, the matching degree was calculated in terms of the overlapping ratio between the designed augment and the implanted one (Figures 3(a)–3(d)).

2.5. Microcomputed Tomography. To evaluate the ingrowth of the bone tissues around the porous Ti6Al4V augment, specimens, prior to histological examination, were observed under micro-CT (SkyScan 1172, Belgium) under the following conditions: 100 kV acceleration voltage at $75 \mu\text{A}$ (current). All specimens were scanned at a complete 360° rotation, with an exposure time of 1600 ms and a resolution of $13.75 \mu\text{m}$.

2.6. Biomechanical Test (Push-Out Test). The push-out test was conducted on a computer-controlled mechanical testing machine (Instron-E3000, Instron, USA) at a loading speed of 0.5 mm/min. The augment-containing bone specimen with an intact iliac wing from a sacrificed miniswine was embedded into a sensor, and the other side was a metal cone serving as the femoral head. The ultimate shear strength was recorded when the implanted augment started to move after continuous loading. The structure of the mechanical testing platform is shown in Figure 4(a).

2.7. Histological and Histomorphometric Analyses. Three miniswine (group 3) were prepared for histological analysis. To evaluate the bone ingrowth distance over time, fluorochrome (two injections), tetracycline (25 mg/kg) and calcein green (at 25 mg/kg), were administered intramuscularly 14 and 13 days (tetracycline) and 4 and 3 days (calcein green) before sacrificing at 12 weeks after surgery.

Augment-containing bone specimens were then fixed in formalin, dehydrated, and then embedded. Next, they were sectioned with a low-speed cutter (IsoMet™, Buehler, USA) in serial sections of $300 \mu\text{m}$ and ground to a thickness of $50 \mu\text{m}$. The newly formed bone was determined by the distance between the two fluorochrome labels using an epifluorescent microscope (DMi8, Leica, Germany) (Figure 5(a)). The amount of new bone and bone ingrowth to the porous

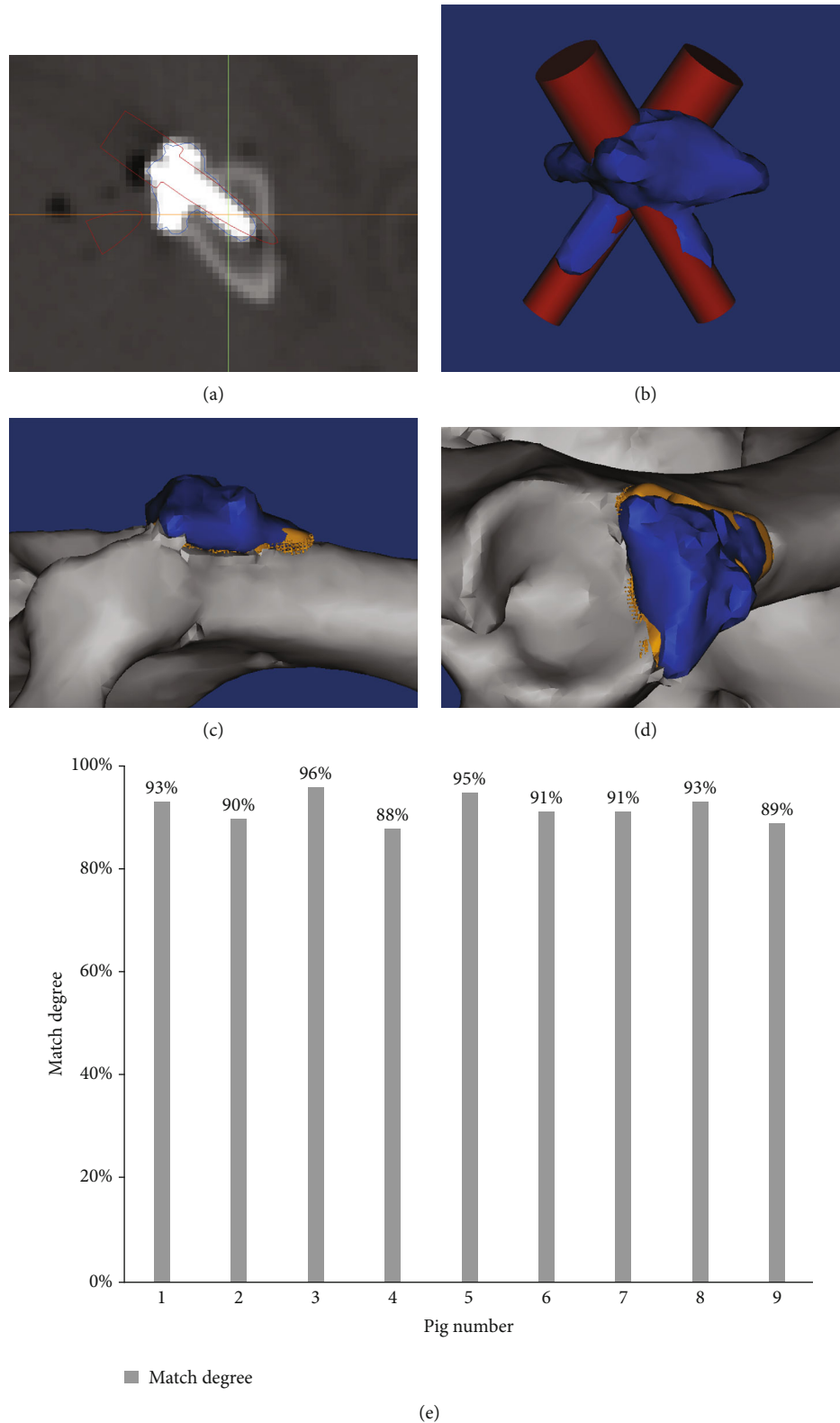


FIGURE 3: The graphical illustration of the calculation of matching degree with the three-dimensional reconstruction of the augment as shown by CT scans, and the values of matching degree in individual swine. (a) Postoperative CT scan identified the screw direction. (b) The overlapping ranges of designed and implanted augments and screws. (c, d) The implanted augment matched with the defect bone surface (blue, implanted augment; golden yellow, designed augment). (e) The matching degrees of implanted augments in individual swine, with the mean \pm SD value being $91.40 \pm 3.01\%$ ($n = 9$).

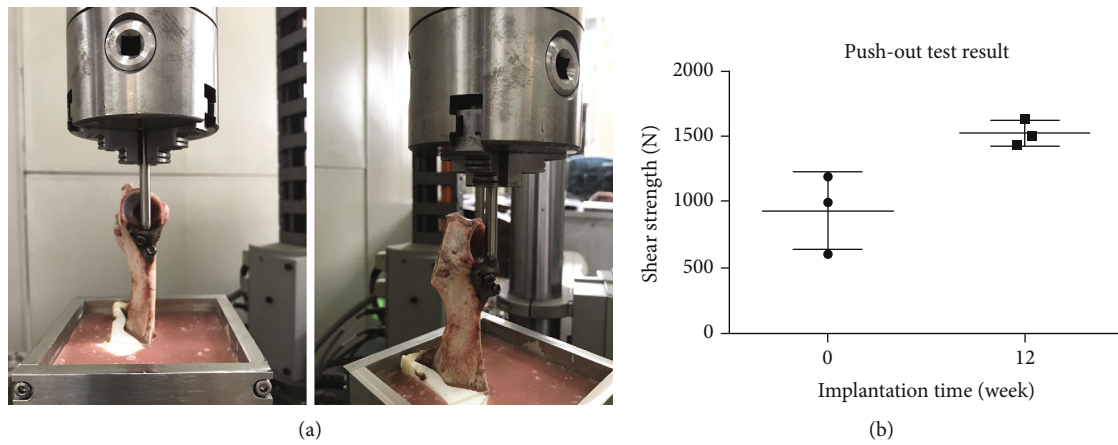


FIGURE 4: Representative pictures showing the platform for the push-out test and the results of the push-out test in 3 swine. (a) The pictures of the mechanical testing platform for the push-out test. (b) The ultimate shear strength immediately (0 weeks) and 12 weeks after surgery. $p < 0.05$ ($n = 3$).

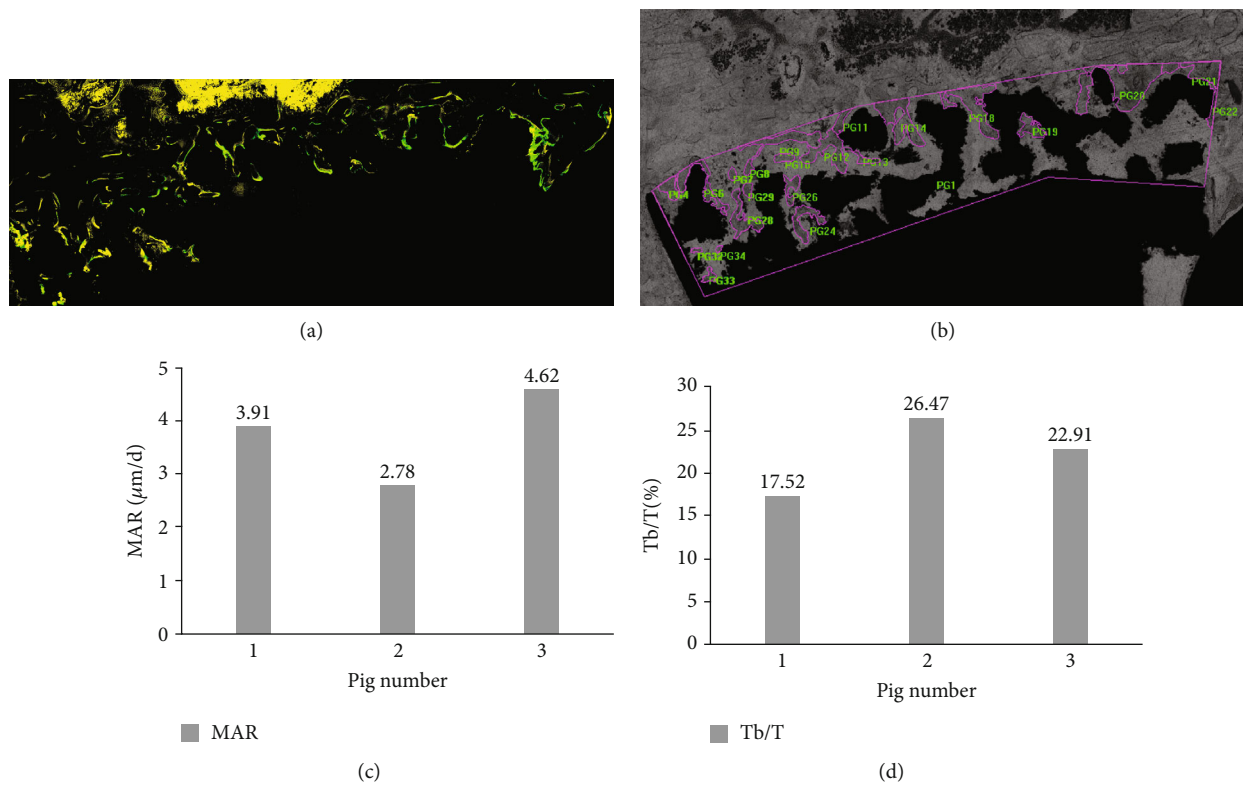


FIGURE 5: Histological and histomorphometric analyses of the implanted augment 12 weeks after implantation. (a) The newly formed bone was determined by the distance between the two fluorochrome labels (tetracycline and calcein green bands) using an epifluorescent microscope. (b) The amount of new bone and bone ingrowth to the interior of the pores was calculated using image processing software, presented as a percentage of the total bone-implant interface area. (c) Bone mineral apposition rate (MAR) was $3.77 \pm 0.93 \mu\text{m/d}$ ($n = 3$; the numbers indicate the values in three individual swine). (d) Percentage bone volume of new bone (Tb/T) 12 weeks after surgery was $22.30 \pm 4.51\%$ ($n = 3$; the numbers indicate the values in three individual swine).

Ti6Al4V coating was calculated, by using an image processing software package (Image-Pro Plus 6.0, Media Cybernetics, USA), as a percentage of the total bone-implant interface area (Figure 5(b)). The bone mineral apposition rate (MAR) was calculated by dividing the distance between the two fluorochrome labels by 10 days (the time interval between the two injections of fluorochrome) and expressed

as mm per day. Tb/T referred to the ratio of the tissue bone area to the total view area of the region of interest, which included the new bone area and material area.

2.8. Statistical Analysis. All the analyses were performed using SPSS for Windows (version 18.0, SPSS Inc., Chicago, Illinois, USA). Comparison of rates was made by the chi-

squared test, while numerical data were compared by using a paired sample *t*-test (normal distribution and homoscedasticity) or a Wilcoxon rank test. A *p* value less than 0.05 was considered statistically significant.

3. Results

3.1. Porosity and Mechanical Characterization. Measurement of porosity on the 3D printed porous Ti6Al4V augments by using the gravimetric method and against Archimedes' principle revealed that total porosity and open porosity of the samples were $55.48 \pm 0.61\%$ and $49.02 \pm 2.22\%$, respectively. The pore size and strut size measured by using SEM were $319.23 \pm 25.05 \mu\text{m}$ and $240.10 \pm 23.50 \mu\text{m}$, respectively. Biomechanically, the stiffness of porous augment was $21464.60 \pm 1091.69 \text{ N/mm}$, compressive strength was $231.10 \pm 11.77 \text{ MPa}$, and elastic modulus was $5.35 \pm 0.23 \text{ GPa}$, respectively.

3.2. Experimental and Photographic Results. We achieved a 100% success rate with the establishment of the acetabular bone defect, as evidenced by successful implantation, no loosening and displacement, and good joint activity in all the animals. However, the failure rate of the 3D printed augment implantation was 18.18% (2 of 11 swine). One swine developed a deep infection after implantation, and the other one had screw loosening and augment detachment from the acetabular bone.

Micro-CT imaging was used to assess the bone ingrowth around the porous augment. As shown in Figure 2(e), bone formation occurred within porous augments. The three-dimensional reconstruction of CT data showed that the individual augment anatomically matched well with the defect, and the degree of matching in these 9 swine was $91.40 \pm 3.01\%$ (Figure 3(e)).

3.3. Push-Out Test Results. Shear strength reflects prosthetic stability after implantation and was detected by push-out tests. The ultimate shear strength immediately and 12 weeks after surgery was $929.46 \pm 295.99 \text{ N}$ and $1521.93 \pm 98.38 \text{ N}$, respectively ($p = 0.0302$) (Figure 4(b)). Since, in the actual situation, the augment and the screws were also under the compressive stress, the shear strength measured in this biomechanical model might be representative of the ultimate shear strength after surgery.

3.4. Histological and Histomorphometric Evaluation of Bone Formation. Tetracycline and calcein green bands are indicative of new bone formation and allow the measurement of the mineral apposition rate during the observation period. The bone mineral apposition rate (μm per day) 12 weeks post operation was $3.77 \pm 0.93 \mu\text{m/d}$ (Figure 5(c)). The percentage bone volume of new bone 12 weeks after surgery was $22.30 \pm 4.51\%$ (Figure 5(d)).

4. Discussion

To better repair severe acetabular bone defects, the present work characterized the performance of the 3D printed porous Ti6Al4V augments in an animal model. The results in miniswine demonstrated that the augments fabricated in

our study had good bone tissue biocompatibility and biomechanical properties. The postoperative CT data showed that the 3D printed augments morphologically well matched with the bone defect and the acetabular components.

The effects of porosity, pore size, and shape on the biological behaviors of porous Ti6Al4V prostheses have been previously investigated [20–23]. Heinel et al. demonstrated that the three-dimensional structures with an interconnected mean porosity of 61.3% and a pore size of $450 \mu\text{m}$ were suitable for tissue ingrowth and vascularization [20]. The 3D printed porous Ti6Al4V scaffold with a total porosity of 58% and a pore size of $500 \pm 50 \mu\text{m}$ possessed mechanical properties similar to human bone and promoted osseointegration and tissue integration in animal experiments [21]. Wieding and Wolf measured the uniaxial compression, bending, and torsion strength of the porous Ti6Al4V scaffold and exhibited that pore size of $400 \mu\text{m}$ was numerically optimal for porous bone scaffold structures to match the elastic properties of human bone [22]. They also showed that the cubic design had the lowest elastic modulus and the fastest new bone formation [22]. Another study investigated the influence of the pore shape on mechanical properties and showed that the cubic scaffold was conducive to osseointegration and tissue integration [23].

Given that the surface of severe acetabular bone defects was not entirely cancellous bone, the defect surface of many revision THA patients would experience partial corticalization due to long-term wear. Therefore, the pore parameters in the current study were a compromise between the mechanical and biological considerations, i.e., cubic-shaped lattice structure, with a pore size of $400 \mu\text{m}$, a strut size of $200 \mu\text{m}$, and a porosity of 60%. After printing by direct metal laser sintering (DMLS), the porous Ti6Al4V augments, with a total porosity of $55.48 \pm 0.61\%$ and a pore size of $319.23 \pm 25.05 \mu\text{m}$, were used in this study. And the compressive strength and elastic modulus of the porous Ti6Al4V augments were $231.10 \pm 11.77 \text{ MPa}$ and $5.35 \pm 0.23 \text{ GPa}$, respectively. These porous parameters of the 3D printed Ti6Al4V augments were favorable for bone tissue integration, and their mechanical properties also fit those of the human cortical bone in terms of elasticity.

The ultimate goal of bone defect repair by porous prostheses is to attain osseointegration between implant and human bone and long-term biological fixation [13, 24, 25]. Thomsen et al. revealed that the bone-implant contact, 6 weeks after surgery, was 29–41% in the femoral and tibial bone defect of rabbits [24]. A long-term sheep experiment by Palmquist et al. demonstrated that the bone-implant contact, 26 weeks after implantation, was up to 57% [25]. Ponader et al. examined the direct contact between the bone and implant surfaces to assess the ingrowth of osseous tissue inside the porous structure (a porosity of 61.3% and a pore size of $450 \mu\text{m}$) and found that the volume of newly formed bone tissue inside implants 14 days, 30 days, and 60 days after implantation was roughly 14.44%, 29.46%, and 46.31%, respectively [13]. The percentage bone volume of new bone in our study 12 weeks after surgery was $22.30 \pm 4.51\%$, and the bone mineral apposition rate was $3.77 \pm 0.93 \mu\text{m/d}$, which was consistent with previously reported findings [13, 24, 25].

The ultimate shear strength and the minimum load that separates bone from the augment are effective indicators of stability of the implanted augment, since they objectively reflect the adhesive strength between the augment and the newly formed bone tissues. The ultimate shear strength in our study immediately and 12 weeks after surgery was 929.46 ± 295.99 N and 1521.93 ± 98.38 N ($p = 0.0302$), respectively. The body weight of the miniswine in our study was 25–30 kg, while the mean shear strength immediately after surgery was 929.46 N (approximately 90 kg body weight), which was three times the body weight of a miniswine. Consequently, the immediate stability between the bone and the augment sufficed to support the daily activity of miniswine. As to the volume of newly formed bone inside the porous augment, the shear strength increased to 1521.93 N 12 weeks after the operation.

These results suggested that the 3D printed porous Ti6Al4V augments fabricated in this study had good bone tissue biocompatibility and biomechanical properties. In addition, our previous study on the finite element analysis also indicated that the periacetabular bone strength was adequate to support the patients' single-legged standing immediately after surgery [17]. Moreover, the postoperative three-dimensional reconstruction of CT data showed that the porous augment anatomically matched well with the acetabular bone defect.

This study had several limitations. First, only one type of acetabular bone defect (Paprosky IIB) was created in the current animal experiments. The Paprosky IIB type bone defect only represents the injury of the dome region of the acetabulum with the biggest shear strength, when compared to other types of acetabular bone defects. Second, the uncontrolled nature of the study prevented us from proving the advantages of the 3D printed porous Ti6Al4V augments over other alternatives. However, the positive results in both the animal models made us believe that the 3D printed porous Ti6Al4V augment is an effective choice for managing severe acetabular bone defects.

In summary, the 3D printed porous Ti6Al4V augment presented good bone tissue biocompatibility and biomechanical properties in our animal model. These augments anatomically well matched with the defect bone. Therefore, the 3D printed porous Ti6Al4V augment possesses great potential as an alternative for individualized treatment of severe acetabular bone defects.

Data Availability

The datasets used and/or analyzed during the current study are available from the corresponding authors on reasonable request.

Ethical Approval

The study was approved by the Medical Ethics Committee of the General Hospital of Chinese People's Liberation Army and performed in accordance with the ethical standards in the 1964 Declaration of Helsinki.

Disclosure

The manuscript submitted does not contain information about medical device(s)/drug(s).

Conflicts of Interest

The authors declare no conflict of interest.

Authors' Contributions

Jun Fu, Yi Xiang, and Ming Ni have contributed equally to this work and are the co-first authors. All authors have read the journal's authorship agreement.

Acknowledgments

We are indebted to Shenzhen Institutes of Advanced Technology (Chinese Academy of Sciences), Orthopaedic Laboratory of Beijing Jishuitan Hospital, and Naton Institute of Medical Technology, for their assistance in the histopathologic preparation, micro-CT scan, and the porous Ti6Al4V augment fabrication in this study. This project was supported by grants from the National Key Research and Development Program of China (Nos. 2020YFC2004900 and 2017YFB1104100) and the Military Medical and Health Achievements Expansion Project (19WKS09).

References

- [1] S. Kurtz, K. Ong, E. Lau, F. Mowat, and M. Halpern, "Projections of primary and revision hip and knee arthroplasty in the United States from 2005 to 2030," *The Journal of Bone and Joint Surgery-American Volume*, vol. 89, no. 4, pp. 780–785, 2007.
- [2] W. Y. Shon, S. S. Santhanam, and J. W. Choi, "Acetabular reconstruction in total hip arthroplasty," *Hip & Pelvis*, vol. 28, no. 1, pp. 1–14, 2016.
- [3] J. M. Cuckler, "Management strategies for acetabular defects in revision total hip arthroplasty," *The Journal of Arthroplasty*, vol. 17, no. 4, pp. 153–156, 2002.
- [4] M. Fernandez-Fairen, A. Murcia, A. Blanco, A. Merono, A. Murcia Jr., and J. Ballester, "Revision of failed total hip arthroplasty acetabular cups to porous tantalum components: a 5-year follow-up study," *The Journal of Arthroplasty*, vol. 25, no. 6, pp. 865–872, 2010.
- [5] S. M. Sporer and W. G. Paprosky, "The use of a trabecular metal acetabular component and trabecular metal augment for severe acetabular defects," *The Journal of Arthroplasty*, vol. 21, no. 6, pp. 83–86, 2006.
- [6] M. R. Whitehouse, B. A. Masri, C. P. Duncan, and D. S. Garbuz, "Continued good results with modular trabecular metal augments for acetabular defects in hip arthroplasty at 7 to 11 years," *Clinical Orthopaedics and Related Research*, vol. 473, no. 2, pp. 521–527, 2015.
- [7] V. Swaminathan and J. L. Gilbert, "Fretting corrosion of CoCrMo and Ti6Al4V interfaces," *Biomaterials*, vol. 33, no. 22, pp. 5487–5503, 2012.
- [8] J. Li, W. Li, Z. Li et al., "In vitro and in vivo evaluations of the fully porous Ti6Al4V acetabular cups fabricated by a sintering technique," *RSC Advances*, vol. 9, no. 12, pp. 6724–6732, 2019.

- [9] B. Zhang, X. Pei, C. Zhou et al., "The biomimetic design and 3D printing of customized mechanical properties porous Ti6Al4V scaffold for load-bearing bone reconstruction," *Materials & Design*, vol. 152, pp. 30–39, 2018.
- [10] S. Kujala, J. Ryhänen, A. Danilov, and J. Tuukkanen, "Effect of porosity on the osteointegration and bone ingrowth of a weight-bearing nickel–titanium bone graft substitute," *Biomaterials*, vol. 24, no. 25, pp. 4691–4697, 2003.
- [11] J. Wang, M. Yang, Y. Zhu, L. Wang, A. P. Tomsia, and C. Mao, "Phage nanofibers induce vascularized osteogenesis in 3D printed bone scaffolds," *Advanced Materials*, vol. 26, no. 29, pp. 4961–4966, 2014.
- [12] S. M. Kalantari, H. Arabi, S. Mirdamadi, and S. A. Mirsalehi, "Biocompatibility and compressive properties of Ti-6Al-4V scaffolds having Mg element," *Journal of the Mechanical Behavior of Biomedical Materials*, vol. 48, pp. 183–191, 2015.
- [13] S. Ponader, C. Von Wilmowsky, M. Widenmayer et al., "In vivo performance of selective electron beam-melted Ti-6Al-4V structures," *Journal of Biomedical Materials Research Part A*, vol. 92, no. 1, pp. 56–62, 2010.
- [14] R. Ramakrishnaiah, A. A. al kheraif, A. Mohammad et al., "Preliminary fabrication and characterization of electron beam melted Ti-6Al-4V customized dental implant," *Saudi Journal of Biological Sciences*, vol. 24, no. 4, pp. 787–796, 2017.
- [15] P. Honigmann, N. Sharma, B. Okolo, U. Popp, B. Msallem, and F. M. Thieringer, "Patient-specific surgical implants made of 3D printed PEEK: material, technology, and scope of surgical application," *BioMed Research International*, vol. 2018, Article ID 4520636, 8 pages, 2018.
- [16] H. Lal and M. K. Patralekh, "3D printing and its applications in orthopaedic trauma: a technological marvel," *Journal of Clinical Orthopaedics and Trauma*, vol. 9, no. 3, pp. 260–268, 2018.
- [17] J. Fu, M. Ni, J. Chen et al., "Reconstruction of severe acetabular bone defect with 3D printed Ti6Al4V augment: a finite element study," *BioMed Research International*, vol. 2018, Article ID 6367203, 8 pages, 2018.
- [18] A. C. Smith and M. M. Swindle, "Preparation of swine for the laboratory," *ILAR Journal*, vol. 47, no. 4, pp. 358–363, 2006.
- [19] W. G. Paprosky, P. G. Perona, and J. M. Lawrence, "Acetabular defect classification and surgical reconstruction in revision arthroplasty: a 6-year follow-up evaluation," *The Journal of Arthroplasty*, vol. 9, no. 1, pp. 33–44, 1994.
- [20] P. Heinel, L. Muller, C. Korner, R. F. Singer, and F. A. Muller, "Cellular Ti-6Al-4V structures with interconnected macro porosity for bone implants fabricated by selective electron beam melting," *Acta Biomaterialia*, vol. 4, no. 5, pp. 1536–1544, 2008.
- [21] P. K. Srivas, K. Kapat, P. Dadhich et al., "Osseointegration assessment of extrusion printed Ti6Al4V scaffold towards accelerated skeletal defect healing via tissue in-growth," *Bio-printing*, vol. 6, pp. 8–17, 2017.
- [22] J. Wieding, A. Wolf, and R. Bader, "Numerical optimization of open-porous bone scaffold structures to match the elastic properties of human cortical bone," *Journal of the Mechanical Behavior of Biomedical Materials*, vol. 37, pp. 56–68, 2014.
- [23] M. Schumacher, U. Deisinger, R. Detsch, and G. Ziegler, "Indirect rapid prototyping of biphasic calcium phosphate scaffolds as bone substitutes: influence of phase composition, macroporosity and pore geometry on mechanical properties," *Journal of Materials Science: Materials in Medicine*, vol. 21, no. 12, pp. 3119–3127, 2010.
- [24] P. Thomsen, J. Malmström, L. Emanuelsson, M. Rene, and A. Snis, "Electron beam-melted, free-form-fabricated titanium alloy implants: material surface characterization and early bone response in rabbits," *Journal of Biomedical Materials Research Part B: Applied Biomaterials*, vol. 90, no. 1, pp. 35–44, 2009.
- [25] A. Palmquist, A. Snis, L. Emanuelsson, M. Browne, and P. Thomsen, "Long-term biocompatibility and osseointegration of electron beam melted, free-form-fabricated solid and porous titanium alloy: experimental studies in sheep," *Journal of Biomaterials Applications*, vol. 27, pp. 1003–1016, 2013.

Research Article

Reconstruction of Bony Defects after Tumor Resection with 3D-Printed Anatomically Conforming Pelvic Prostheses through a Novel Treatment Strategy

Wei Peng ¹, Runlong Zheng,¹ Hongmei Wang,² and Xunwu Huang ¹

¹Department of Orthopedic Surgery, Eighth Medical Center of Chinese PLA General Hospital, Beijing 100091, China

²Department of Oncology, Eighth Medical Center of Chinese PLA General Hospital, Beijing 100091, China

Correspondence should be addressed to Xunwu Huang; kuanguanjie@126.com

Received 5 August 2020; Revised 9 October 2020; Accepted 11 November 2020; Published 1 December 2020

Academic Editor: Xiaojun Duan

Copyright © 2020 Wei Peng et al. This is an open access article distributed under the Creative Commons Attribution License, which permits unrestricted use, distribution, and reproduction in any medium, provided the original work is properly cited.

There has been an increasing interest and enormous applications in three-dimensional (3D) printing technology and its prosthesis, driving many orthopaedic surgeons to solve the difficult problem of bony defects and explore new ways in surgery approach. However, the most urgent problem is without an effective prosthesis and standard treatment strategy. In order to resolve these problems, this study was performed to explore the use of a 3D-printed anatomically conforming pelvic prosthesis for bony defect reconstruction following tumor resection and to describe a detailed treatment flowchart and the selection of a surgical approach. Six patients aged 48-69 years who had undergone pelvic tumor resection underwent reconstruction using 3D-printed anatomically conforming pelvic prostheses according to individualized bony defects between March 2016 and June 2018. According to the Enneking and Dunham classification, two patients with region I+II tumor involvement underwent reconstruction using the pubic tubercle-anterior superior iliac spine approach and the lateral auxiliary approach and one patient with region II+III and three patients with region I+II+III tumor involvement underwent reconstruction using the pubic tubercle-posterior superior iliac spine approach. The diagnoses were chondrosarcoma and massive osteolysis. After a mean follow-up duration of 30.33 ± 9.89 months (range, 18-42), all patients were alive, without evidence of local recurrence or distant metastases. The average blood loss and blood transfusion volumes during surgery were 2500.00 ± 1461.51 ml (range, 1200-5000) and 2220.00 ± 1277.62 ml (range, 800-4080), respectively. During follow-up, the mean visual analogue scale (VAS) score decreased, and the mean Harris hip score increased. There were no signs of hip dislocation, prosthetic loosening, delayed wound healing, or periprosthetic infection. This preliminary study suggests the clinical effectiveness of 3D-printed anatomically conforming pelvic prostheses to reconstruct bony defects and provide anatomical support for pelvic organs. A new surgical approach that can be used to expose and facilitate the installation of 3D-printed prostheses and a new treatment strategy are presented. Further studies with a longer follow-up duration and larger sample size are needed to confirm these encouraging results.

1. Introduction

The pelvis is a very important component of the skeletal system that helps stabilize and protect the organs in the pelvis. As the three-dimensional (3D) geometry of the pelvic bone is complex, reconstruction of pelvic bony defects following the resection of large pelvic bone tumors poses a great challenge to orthopaedic surgeons worldwide. Historically, surgeons have used massive allografts or autografts in their attempts to reconstruct these bony defects [1, 2]. However, the many shortcomings associated with allografts or auto-

grafts, such as malalignment, malrotation, nonunion, rejection, infection, and refracture, significantly limit the application of this technique [3-6].

At present, the functional and anatomical restoration of the pelvis is the most concerning problem associated with reconstruction. With developments in implantation techniques, prosthetic reconstruction after tumor resection has gradually been adopted by many scholars [7-11]. Several kinds of prosthesis can be used for reconstruction, such as a saddle endoprosthesis, [10, 12] an ice cream cone endoprosthesis [8, 13], and a modular hemipelvic endoprosthesis.

Saddle and ice cream cone prostheses require a sufficient amount of preserved iliac bone after tumor resection to support the prosthesis, and because they do not provide anatomical reconstruction, they cannot reconstruct the intact pelvic ring or transfer the biomechanical load of the lower limb, leading to a high occurrence of prosthetic instability or looseness. Meanwhile, due to its emphasis on functional recovery, the modular hemipelvic endoprosthesis cannot protect pelvic organs.

With the development of 3D printing techniques that can be applied to the clinic, 3D-printed prostheses have been used in the reconstruction of bony defects following complex pelvic bone tumor resection [14]. Moreover, 3D-printed pelvic prostheses have been used to accurately repair bony defects and improve pelvic function [15, 16]. However, the current approach to using 3D-printed prostheses for pelvic reconstruction is still lacking; because there is no standard treatment strategy, an entirely anatomically conforming pelvic prosthesis has not been reported, and there is no suitable approach by which the pelvis can be easily exposed.

Here, we report a novel treatment strategy and an anatomically conforming shape pelvic prosthesis for the treatment of bony defects after pelvic tumor resection. Compared with previously reported prostheses [9, 10, 13], the prosthesis described herein has an improved anatomically conforming shape and differs in its functional design. Our study also focuses more on the strategies of reconstruction than previous studies. To our knowledge, this is the first report of an entirely anatomically conforming hemipelvic prosthesis, a standard treatment strategy for pelvic reconstruction.

2. Materials and Methods

2.1. Clinical Data. Between March 2016 and June 2018, six patients with pelvic tumors underwent tumor resection and hemipelvic replacement with a 3D-printed anatomically conforming pelvic prosthesis in Eighth Medical Center of Chinese PLA General Hospital. Inclusion criteria are as follows: (1) pelvic primary low-grade malignant tumors with a good preoperative response to chemotherapy or radiotherapy, with no damage to the external iliac vessels, femoral nerve, sciatic nerve, or main muscles such as the gluteus maximus, and with no tumor metastasis; (2) large osteolytic benign tumors; and (3) pelvic chondrosarcoma, especially around the acetabulum. Exclusion criteria are as follows: (1) metastases from other sites, such as the lung; (2) intolerance to anaesthesia; and (3) malnutrition, a preoperative haemoglobin level below 100 g/l or a plasma albumin level below 30 g/l. There were four male and two female patients with a mean age of 56.00 ± 8.05 years (range, 48-69). All patients underwent preoperative plain radiography of the pelvis, 3D computed tomography (3D-CT) of the pelvis, magnetic resonance imaging (MRI) of the pelvis, and an electrical capacitance tomography (ECT) bone scan (Figures 1 and 2). Needle or incisional biopsy was performed before the operation.

We performed this study after obtaining approval from the Institutional Human Ethical Committee of the 8th

Medical Centre, Chinese PLA General Hospital (no 309202008061535).

2.2. Workflow Chart of the Surgical Plan. The study design consisted of the following preoperative preparation, prosthesis preparation, surgical approach, and follow-up steps (Figure 3), which are described in detail in subsequent subsections. [1] Preoperative preparation included plain radiography of the pelvis, 3D-CT, MRI, an ECT bone scan, and needle biopsy. [2] Preoperative embolization reduces intraoperative bleeding, making tumor resection, osteosynthesis, and implantation of hip prostheses possible. [3] The 3D-printed prostheses were designed and manufactured (through CT data collection and image processing, design of the prosthesis, 3D printing of an osteotomy guide, and an implant simulation experiment). [4] Surgery was performed through the pubic tubercle-posterior superior iliac spine or the pubic tubercle-anterior superior iliac spine approach and/or the lateral auxiliary approach (selected based on the classification of bony defects), comprising osteotomy and implantation. [5] Postoperative management and follow-up were performed.

2.3. Data Collection and Image Processing. A set of whole pelvic CT scans comprising the sacrum, ilium, pubis, and ischium was acquired with a 320-detector row CT scanner (Philips Corporation, Japan). Axial images with a slice thickness of 0.5 mm were obtained. The digital images were saved in digital imaging and communications in medicine format and then uploaded into a medical image control system (Mimics 17.0 Software, Materialise Corporation, Belgium) for 3D reconstruction and editing.

2.4. Design and Manufacture of the 3D-Printed Anatomically Conforming Pelvic Prosthesis. From our experience in the current study, we have developed the following considerations. [1] The shape of an anatomically conforming prosthesis should aptly fill the bony defect, provide the biomechanical load-bearing capacity for the body, and protect the organs in the pelvis. [2] The prosthetic surface should be firmly integrated with the bone, muscle, and tendon structure of the host, which is a key factor for long-term success [17]. (3) The weight and elastic modulus of the prosthesis need to be taken into consideration so that the prosthesis is not bulky and to avoid stress resulting in a shielding fracture. [4] Guidance of the fixation screws should be effective and accurate.

To produce each of the 3D-printed anatomically conforming pelvis prostheses that addressed a bony defect specific to an individual, the mirror image of the hemipelvis on the unaffected side was combined with the bony defect (as derived from the CT images of each patient), and the prosthesis was then manufactured by 3D printing (Chun Li Zheng Da Medical Instruments Corporation, Ltd., Beijing, China, and Ai Kang Yi Cheng Medical Instruments Corporation, Ltd., Beijing, China) using titanium alloy (Ti6Al4V).

Based on the mirror image principle of 3D printing technology, each complete anatomically conforming prosthesis consisted of an ilium, pubis, and ischium, thus protecting

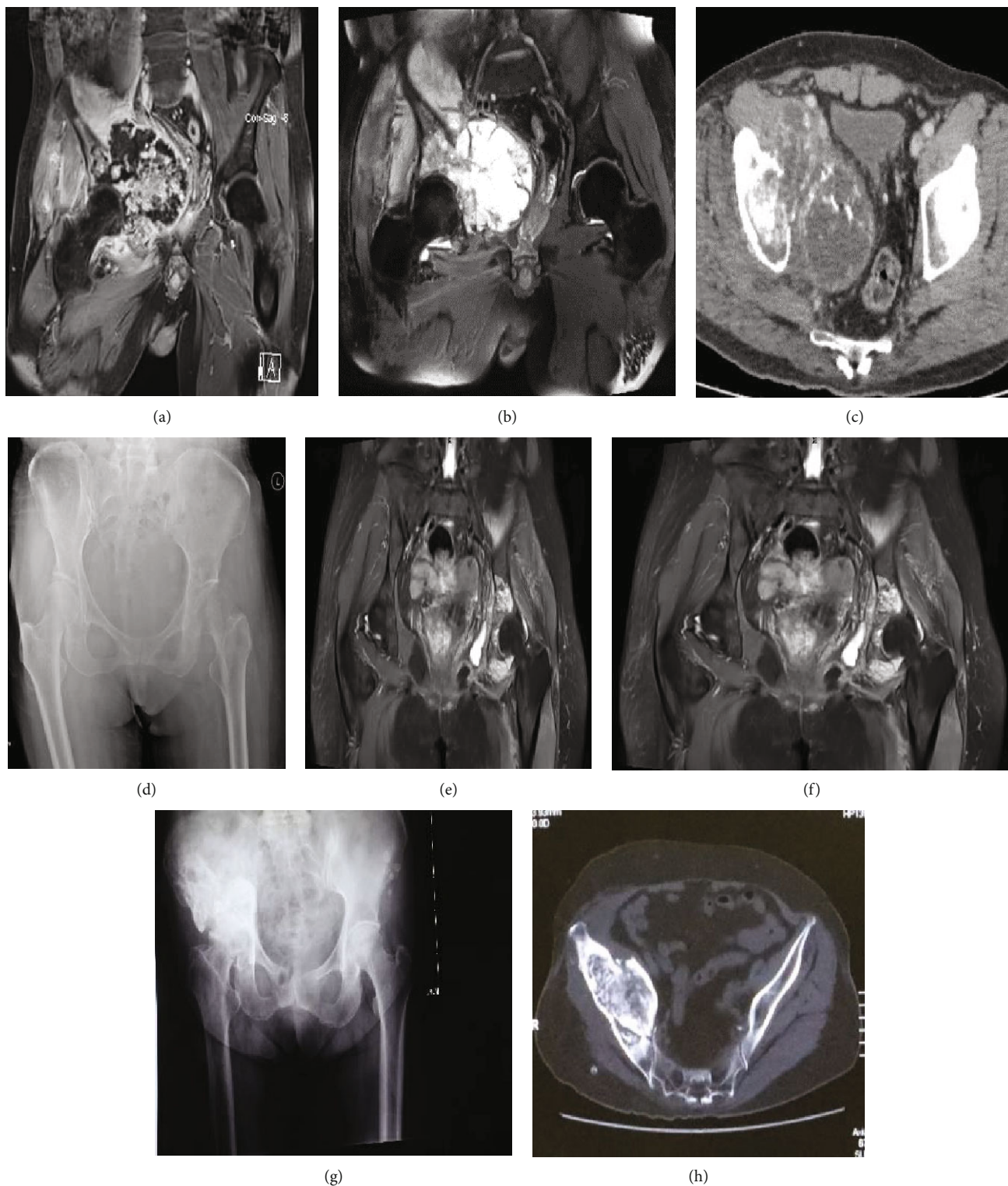


FIGURE 1: Preoperative radiography, MRI, and CT images. (a) Coronal T2-weighted perfusion MRI scan demonstrating tumor involvement in pelvic regions I+II+III. (b) Coronal T2-weighted MRI scan demonstrating tumor involvement in pelvic regions I+II+III. (c) CT image demonstrating tumor involvement in pelvic regions I+II+III. (d) X-ray image demonstrating tumor involvement in pelvic regions II+III. (e) Coronal T2-weighted perfusion MRI scan demonstrating tumor involvement in pelvic regions II+III. (f) Coronal T2-weighted MRI scan demonstrating tumor involvement in pelvic regions II+III. (g) X-ray image demonstrating tumor involvement in pelvic regions I+II. (h) CT image demonstrating tumor involvement in pelvic regions I+II.

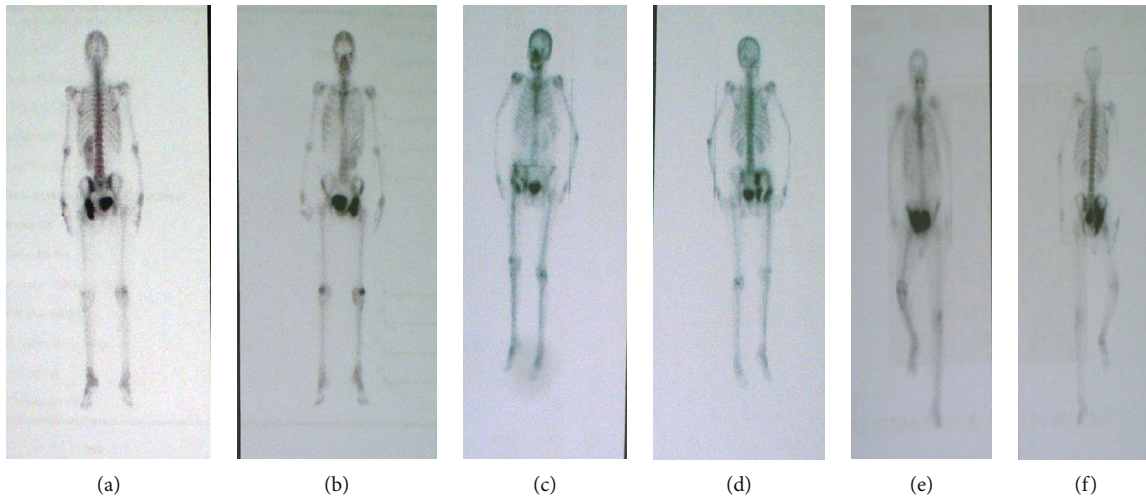


FIGURE 2: Preoperative electrical capacitance tomography (ECT) bone scans. (a, b) ECT image demonstrating tumor involvement in pelvic regions II+III without distant metastases. (c, d) ECT image demonstrating tumor involvement in pelvic regions I+II without distant metastases. (e, f) ECT image demonstrating tumor involvement.

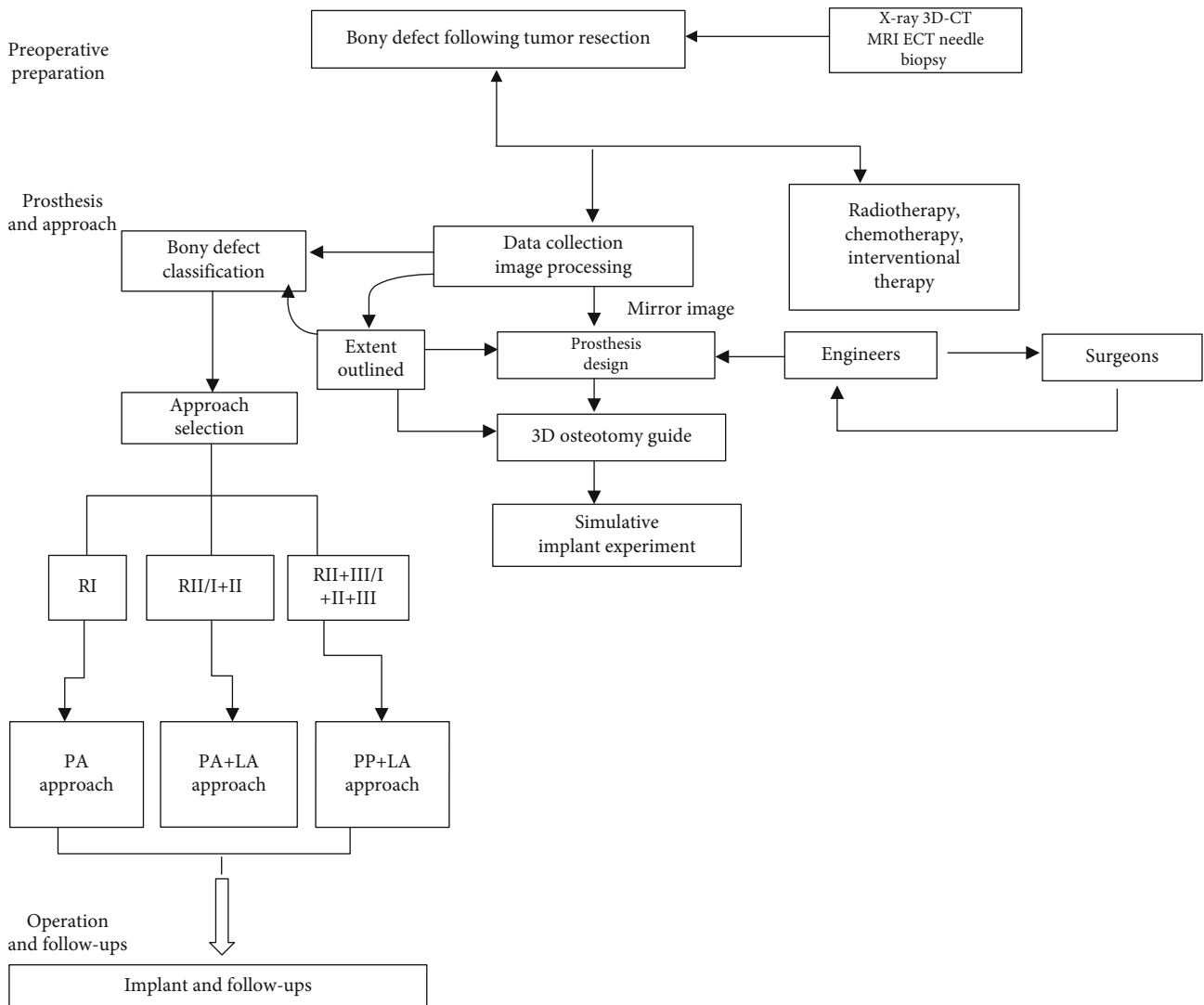


FIGURE 3: Workflow of a novel treatment strategy for treating pelvic bony defects with 3D-printed prostheses.

the organs in the pelvis and reestablishing biomechanical loads to recover pelvic function. Of course, the above components were considered when designing the prosthesis, as well as the extent of the bone defect after osteotomy. The obturator foramen was designed as an open ring without the inferior pubic ramus, to facilitate installation and avoid damaging the neurovascular bundle that passes through the obturator foramen. In addition, the ischial tuberosity was designed as a polished surface, providing support and comfort. With no inferior ischial branch, the obturator foramen was designed in an open-loop state that was easy to implant and reduced the risk of injury to vital structures. The anteversion and abduction angles of the acetabulum exactly matched the patient's anatomy. There were three fixed holes at the bottom of the acetabulum to facilitate implantation of the total hip joint. To increase the initial postoperative stability of the reconstruction, the fixed system of the prosthesis included locking screw holes and universal pores.

To reduce the weight of the prosthesis and promote osteointegration, the main structure of the prosthesis body was designed with large holes in a honeycomb-like configuration. The pore diameter of the prosthesis interface with bone ranged from 400 to 450 μm and exhibited a coverage rate of 70% and a thickness of 1.5 mm. A solid structure with a certain strength was designed on the mechanical support portion.

Before surgery, the prosthesis was generated as a whole or part specific for fitting the resected bone or bony defect (Figure 4). Data collection and image processing took three days, while 3D printing prosthesis fabrication, postprocessing cost one week.

2.5. 3D-Printed Osteotomy Guide and Implant Simulation Experiment. A 3D-printed 1:1 plastic model of the pelvic prosthesis, which was produced using the same data and 3D printing technique as the osteotomy guide, was used for preoperative planning and as a reference during the operation. A precise and limited cutting depth of the saw blade was set to prevent the saw from damaging the organs in the pelvis. After a simulation of the osteotomy procedure, a similar simulation experiment was performed for the 3D-printed pelvic prosthesis to determine whether the 3D-printed prosthesis matched perfectly with the residual hemipelvic model (Figure 5).

2.6. Surgical Approaches

2.6.1. Preoperative Preparation. Routine enemas were performed twice 12 hours before the operation. After general anaesthesia induction, the patient was placed in a lateral or floating position.

2.6.2. Pubic Tubercle-Posterior Superior Iliac Spine (PP) Approach. For the pubic tubercle-posterior superior iliac spine approach, an incision 60 cm in length was made to expose the tumor focus (Figure 6). Starting from approximately 1 cm above the pubic tubercle, the incision passed through the anterior superior iliac spine and ended at the posterior superior iliac spine. The skin and subcutaneous tissue were incised successively. The gluteus maximus muscle

and the external oblique muscle of the abdomen were exposed. As the lateral femoral cutaneous nerve was sometimes encountered at the lateral edge of the incision, care was taken to avoid unnecessary nerve injury. The external oblique muscle was separated from the superficial inguinal canal to the anterior superior iliac spine. The spermatic cord in males or round ligament in females was separated carefully and pulled apart with a rubber band. The anterior sheath of the rectus abdominis muscle was cut to expose the inferior portion of the rectus abdominis muscle. The iliacus muscle was separated from the medial iliac wing. The retropubic space was reached when the rectus abdominis muscle was separated from the pubic symphysis via a transverse incision. After opening the posterior wall of the inguinal canal (which is formed by the internal oblique and transverse abdominal muscles), the inferior epigastric artery was ligated. Then, the fibers of the transverse and internal oblique muscles were separated from the lateral half of the inguinal ligament. The peritoneum was retracted with gauze to expose the femoral artery, femoral nerve, and iliopsoas tendon. After protecting the neurovascular bundle, the medial wall of the acetabulum and the superior pubic ramus were exposed. The gluteus maximus, gluteus medius, and gluteus minimus muscles were peeled from the iliac spine; then, these muscles were carefully retracted inferiorly along with muscles from the anterior compartment of the thigh to expose. The inferior gluteal artery and nerve were avoided to prevent damage. After removing the joint capsule, the femoral neck was sawed from the greater trochanter to a location 1.5 cm above the lesser trochanter. Then, the femoral head was removed.

2.6.3. Lateral Auxiliary (LA) Approach. After exposure of the ilium and pubis as well as part of the ischium, a supplementary incision was performed. For this supplementary posterolateral approach, a longitudinal incision was made with a length of 20 cm from the greater trochanter along the femoral shaft. The tensor fascia lata and gluteus maximus muscles were bluntly separated along the muscle fibers, and then, the sciatic nerve was protected. After removing the attached muscle group from the sciatic tubercle, the whole hemipelvis was freed.

2.6.4. Surgical Approach Selection. The tumors were classified as follows according to the location of the tumor or bony defect in different areas of the pelvis, using the Enneking and Dunham classification [18]: the ilium (region I), acetabulum (region II), and pubis and ischium (region III). Then, based on our experience, the appropriate surgical approach, as described below, was identified and implemented (Table 1). The novel surgical approach, with the goal of resection, was defined by considering the classification of and the extent to which the tumor invaded the pelvis.

- (1) Region I resection and reconstruction (using the PA approach): for patients with iliac tumors, the operation was performed using the following approach: one incision from the pubic tubercle to the anterior superior iliac spine
- (2) Region II/I+II resection and reconstruction (using the PA approach plus the lateral auxiliary approach):

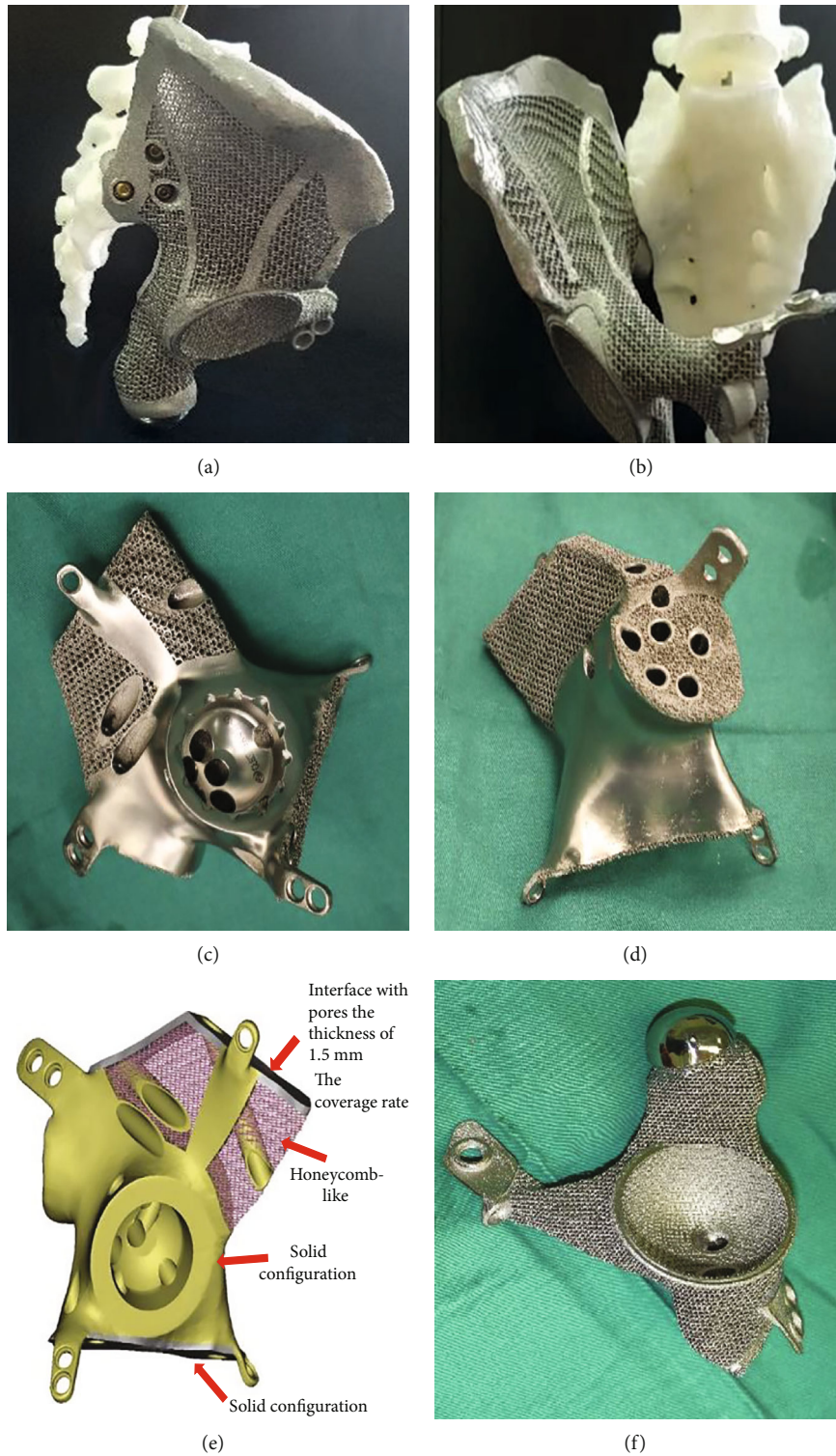
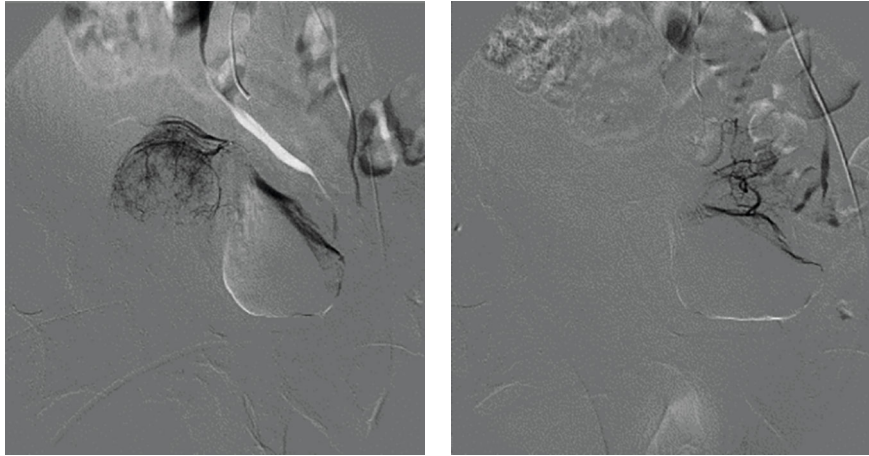
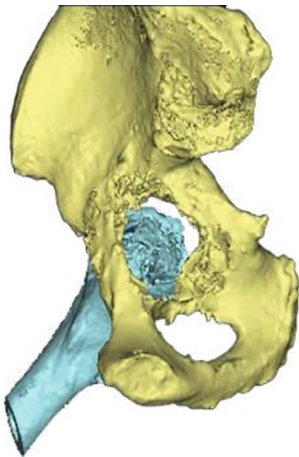


FIGURE 4: The 3D-printed pelvic prosthesis. (a) Lateral view of a prosthesis designed for the hemipelvis. (b) Anterior view of a prosthesis designed for the hemipelvis. (c) Anterior view of a prosthesis designed for pelvic regions I+II. (d) Posterior view of a prosthesis designed for pelvic regions I+II. (e) Illustration of the prosthesis design fabricated by the electron beam melting technique with a porosity of 70% and a pore size of 400 to 450 μm . (f) Anterior view of the prosthesis designed for pelvic regions II+III.

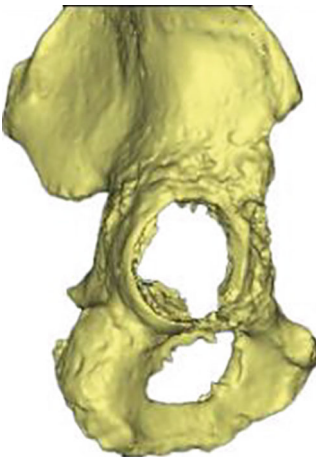


(a)

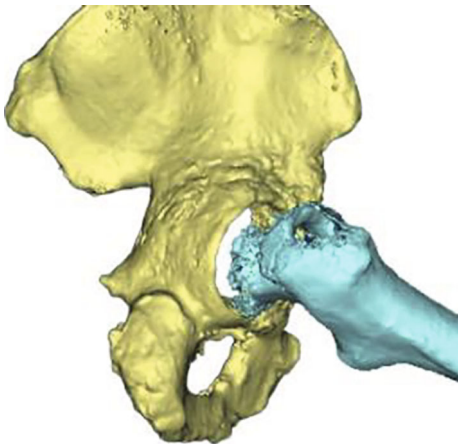
(b)



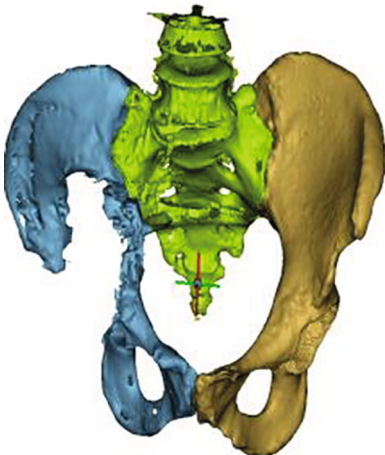
(c)



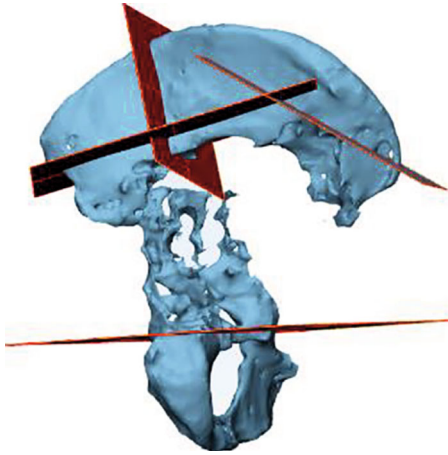
(d)



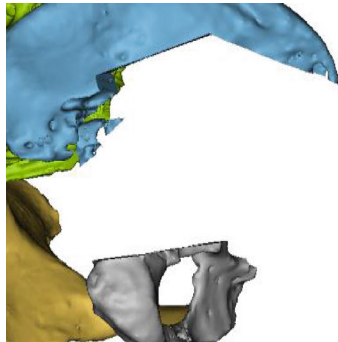
(e)



(f)



(g)



(h)

FIGURE 5: Continued.



FIGURE 5: Preoperative planning. (a, b) Embolization was performed to prevent severe hemorrhage. (c–e) 3D-CT image of a tumor in region II. (f–i) The designed osteotomy guide with cutting platforms or slits that matched the planned resection planes. (j–m) Implant trial. (n–p) Drill guide on the implant for drilling the saw paths.

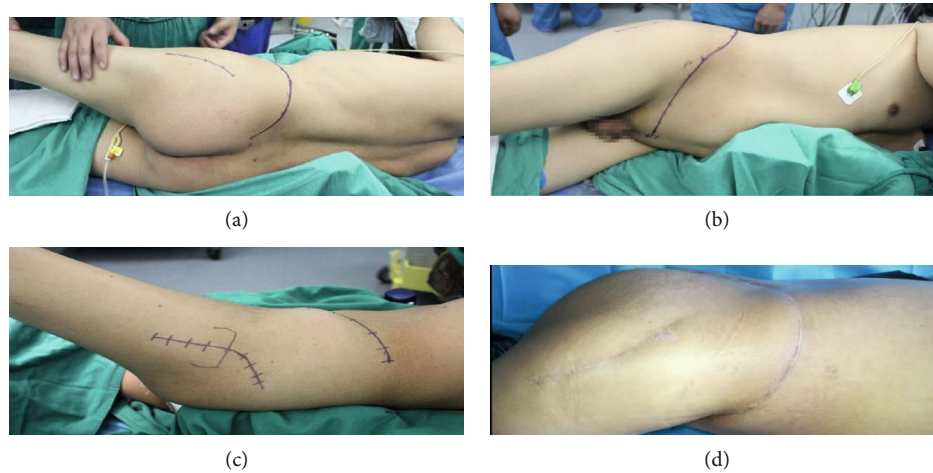


FIGURE 6: Skin incisions. (a) Posterior view of the pubic tubercle-posterior superior iliac spine approach and the lateral auxiliary approach. (b) Anterior view of the pubic tubercle-posterior superior iliac spine approach and the lateral auxiliary approach. (c) Lateral view of the anterior half of the novel approach and the lateral auxiliary approach. (d) Postoperative wound healing at the one-year follow-up.

TABLE 1: Definition of the surgical classification and management strategy proposed for each type of resection.

| Categorization pelvic involvement | R I | R II/I+II | R II+III/I+II+III |
|-----------------------------------|-------------------------------|---------------------------------|---|
| Tumor location | Ilium | Acetabulum/ilium and acetabulum | Acetabulum, pubis, and ischium/hemipelvis |
| Incision | | | |
| Start point | Pubic tubercle | Pubic tubercle | Pubic tubercle |
| End point | Anterior superior iliac spine | Anterior superior iliac spine | Posterior superior iliac spine |
| Lateral auxiliary incision | No | Yes | Yes |
| Prosthesis component | Ilium | Acetabulum/ilium and acetabulum | Acetabulum, pubis and ischium/hemipelvis |

for patients with acetabular tumors, the operation was performed using the following approach: one incision from the pubic tubercle to the anterior superior iliac spine as well as the lateral auxiliary incision

- (3) Region II+III/I+II+III resection and reconstruction (using the PP approach + the lateral auxiliary approach)

2.6.5. Osteotomy and Prosthesis Implantation. To increase the accuracy of osteotomy and shorten the operative time, a 3D-printed osteotomy guide was developed. The basic principle of the osteotomy guide was designed following the extent of the affected hemipelvis according to the preoperative CT and MRI patient data. The entire process of designing the 3D-printed osteotomy guide was achieved with a preoperatively designed location and 3D-printed cutting guides. The 3D-printing osteotomy guide was fixed at the corresponding region of the bone surface to perform the osteotomy. Under the assistance of the osteotomy guide, the ilium, pubis, and/or ischium was resected. After osteotomy, the 3D-printed anatomically conforming pelvic prosthesis that had been adapted precisely to the bony defect of the pelvis was firmly fixed with cancellous screws and locking screws after drilling via a drill guide. The pubic part of the prosthesis was fixed to the residual part of the pubis or the opposite

pubic ramus. The iliac part of the prosthesis was fixed to the iliac crest, the sacroiliac joint, or the residual part of the sacroiliac joint with screws. A polyethylene elevated-rim acetabular liner or a restricted acetabular was cemented to the acetabular rim of the hemipelvic prosthesis for fixation. A cementless femoral stem and metal head were implanted after reaming of the femoral medullary cavity (Figures 7). The surgical field was flushed with a medical pulse irrigator (Beijing Wanjie Medical Device Corporation, Ltd., Beijing, China) to reduce the risk of infection.

2.7. Postoperative Management and Main Outcome Measures. During the postoperative period, two silicone drainage tubes were maintained until the drainage volume was less than 50 ml in 24 hours, and second-generation cephalosporin was administered intravenously for seven days. Anticoagulation agents were administered subcutaneously for prophylaxis against deep vein thrombosis for four weeks. Initiation of mobilization was advised when the drainage tubes were removed postoperatively and if there was no pain, no symptoms of instability, and no perioperative complications. All patients underwent postoperative pelvic plain radiography to assess implant orientation and implant failure, such as loosening or fracture, every three months during the first year postoperatively and every six months thereafter. Functional outcome was evaluated by the Harris hip score

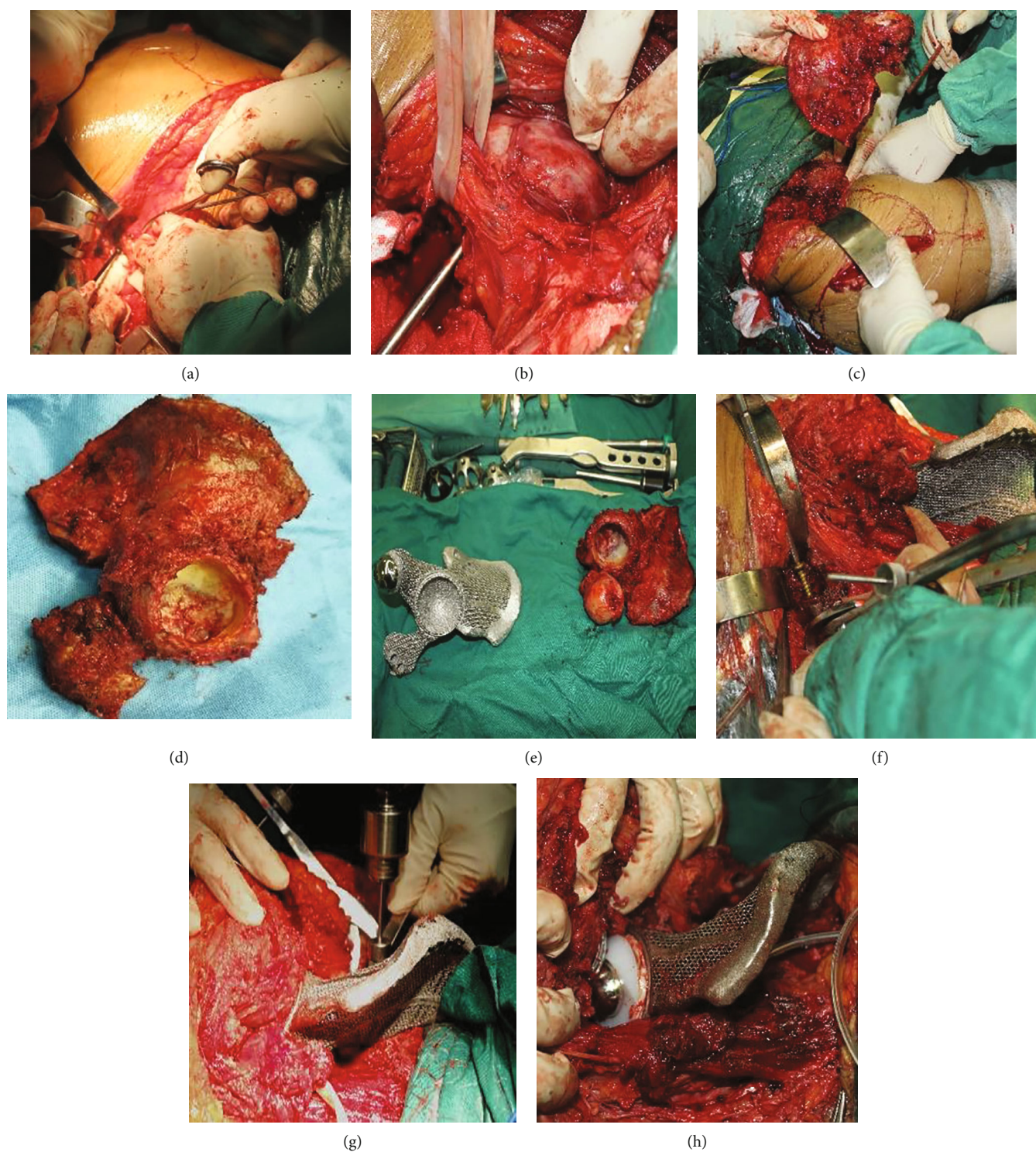


FIGURE 7: Surgical steps of resection and implantation. (a) An incision was made. (b) The neurovascular bundle was protected. (c) The hemipelvis was removed. (d) The intact hemipelvis. (e) Comparison of the intact hemipelvis and the 3D-printed hemipelvic prosthesis. (f) Implantation of the 3D-printed hemipelvic prosthesis. (g) Fixation of the prosthesis with a drill. (h) Implantation of the total hip prosthesis.

every month during the first three months of follow-up and every three months thereafter. Preoperative and postoperative pain at rest was assessed using a visual analogue scale (VAS) and the Musculoskeletal Tumor Society (MSTS) score for evaluating patient activity.

2.8. *Statistical Analysis.* Results of VAS score, Harris hip score, follow-up duration, MSTS-93 score, intraoperative blood loss, volume of blood transfused, postoperative drainage volume and operation time were expressed as means \pm SD and were analyzed with SPSS Statistics software, version

23.0 (IBM, Armonk, New York, USA). Statistical significance for the results of VAS score and Harris hip score was determined by paired *t*-test. $p < 0.05$ was considered statistically significant.

3. Results

3.1. Patient Data. Data pertaining to clinical characteristics were recorded—specifically, age, sex, symptoms, duration in months, Enneking and Dunham classification, and diagnosis. Clinical data are summarized in Table 2. The chief complaints were persistent pain in the inguinal area and a fixed local mass in the stomach. X-ray showed osteolytic bone destruction, CT scan showed incomplete bony shell and unclear boundary around the tumor, and soft tissue mass protruded from the bony shell and showed inhomogeneous density. MRI scan showed that the tumor had heterogeneous intensity on T1 and T2 images in five cases, MRI signal intensity of the bone marrow disappeared and had a long T1 and long T2 signal intensity changes in one case, and the radionuclide concentration of tumor foci could be seen on ECT images. According to radiology, Region I and II involvement was found in two patients, region II and III involvement in one patient, and regions I, II, and III involvement in three patients.

3.2. Surgical Outcome. All operations were completed successfully. The five patients with chondrosarcoma, characterized by a large soft tissue mass, underwent wide excision, and the other patient with massive osteolysis underwent marginal excision. Two patients underwent implantation of the 3D-printed prosthesis via the PA approach in addition to the LA approach; the other four patients underwent implantation of the 3D prosthesis via the PP approach in addition to the LA approach. The mean intraoperative blood loss was 2500.00 ± 1461.51 ml (range, 1200-5000), the average volume of blood transfused during surgery was 2220.00 ± 1277.62 ml (range, 800-4080), and the mean postoperative drainage volume was 937.50 ± 474.44 ml (range, 395-1730). The mean operation time was 247.50 ± 103.52 min (range, 135-420 min). Pathological evidence of the intraoperative specimen confirmed the diagnosis from the preoperative biopsy (Figure 8). All cases were studied by pathology correlated with radiology. Among the six patients, five were diagnosed with chondrosarcoma, and the other was diagnosed with massive osteolysis.

3.3. Follow-Up Data. After a mean follow-up duration of 30.33 ± 9.89 months (range, 18-42), all patients were alive and without evidence of local recurrence or distant metastases. Hip dislocation, aseptic loosening, bone resorption, periprosthetic fractures (Figure 9), wound infection, and delayed wound healing were not observed in these patients during the short-term follow-up.

The mean preoperative VAS score was 7.167 ± 1.47 (range, 5-9) one week before operation, and the mean postoperative VAS score was 2.83 ± 1.47 (range, 1-5) at the last follow-up ($t = 4.914$, $p = 0.004$). The mean preoperative Harris hip score was 32.33 ± 11.11 (range, 20-50) one week

before operation, and the mean postoperative Harris hip score was 58.17 ± 13.92 (range, 40-78) at the last follow-up ($t = -7.289$, $p = 0.001$). The MSTs score was 19.83 ± 4.26 (range, 15-26) at the last follow-up. The patients were able to walk with crutches after an average of 76.17 ± 10.30 days (range, 62-91) (Table 3, Figure 10).

4. Discussion

We establish a novel strategy on reconstruction of bony defects after tumor resection with 3D-printed anatomically conforming pelvic prostheses. With the use of this technology, it will enhance accuracy in preoperative planning and the improvement in outcomes. Herein, we discuss our experience with a 3D-printed prosthesis and address the following: first, how to plan the treatment strategy; second, how to design the prosthesis; and third, how to select the surgical approach.

4.1. Planning for the Treatment Strategy. We created a flowchart to illustrate hypothetical management strategies. Based on the results of our study and the flowchart of the study design presented in Figure 3, we propose a similar process for the selection of treatment strategy. With an effective clinical flowchart, it would be beneficial to select surgical indications, simplify the corresponding treatment process, and observe postoperative follow-up. We preliminarily identified multiple possible contributing factors for an effective treatment strategy, including preoperative preparation, tumor classification, and postoperative management. Radiology of data collection played an important role in preoperative preparation.

Good outcomes begin with meticulous planning of the therapy procedure. To ensure surgical accuracy, it is necessary to collect imaging data, such as X-ray, 2D-CT, 3D-CT, MRI, or ECT bone scan data, during the preoperative planning stage. Preoperative lung CT and whole-body isotope bone scans were used to determine the presence of lung and systemic metastases. Invasion of the ureteropelvic segment and important nerve tissues were assessed by preoperative angiography and electromyography. We carried out simulation and guided osteotomy according to the imaging data collected before operation. Application of a 3D-printed osteotomy guide achieves limited exposure and high accuracy and facilitates the desired osteotomy procedure, [19, 20] aiding in precise prosthesis implantation. By using an osteotomy guide, secondary damage to adjacent vessels and nerves can be avoided [21, 22].

It is another concern on how to reduce intraoperative bleeding in preoperative planning. Resection of pelvic tumors causes severe blood loss, even postoperative death [23]. Preoperative tumor vessel embolization can reduce intraoperative bleeding. Blood loss was a major concern in this study, and the estimated average amount of bleeding was approximately 2500 ml, the success of which was attributed not only to the selection of surgical approach and technique but also to the use of preoperative arterial embolization [24]. Selection of the occluding material and the interval between embolization and surgery are keys to the success of embolization [25]. In this study, gel foam was used as an occluding

TABLE 2: Demographics of patients who received a 3D-printed anatomically conforming pelvic prosthesis.

| Case | Age | Sex | Classification* | Diagnosis | Symptoms | Duration in months |
|------|-----|-----|-----------------|--------------------|---------------|--------------------|
| 1 | 48 | F | Region I+II | Massive osteolysis | Pain | 24 |
| 2 | 57 | M | Region I+II+III | Chondrosarcoma | Pain and mass | 5 |
| 3 | 69 | M | Region II+III | Chondrosarcoma | Pain and mass | 6 |
| 4 | 52 | M | Region I+II | Chondrosarcoma | Pain and mass | 8 |
| 5 | 49 | M | Region I+II+III | Chondrosarcoma | Pain and mass | 8 |
| 6 | 61 | F | Region I+II+III | Chondrosarcoma | Pain and mass | 10 |

*According to the Enneking and Dunham classification [18].

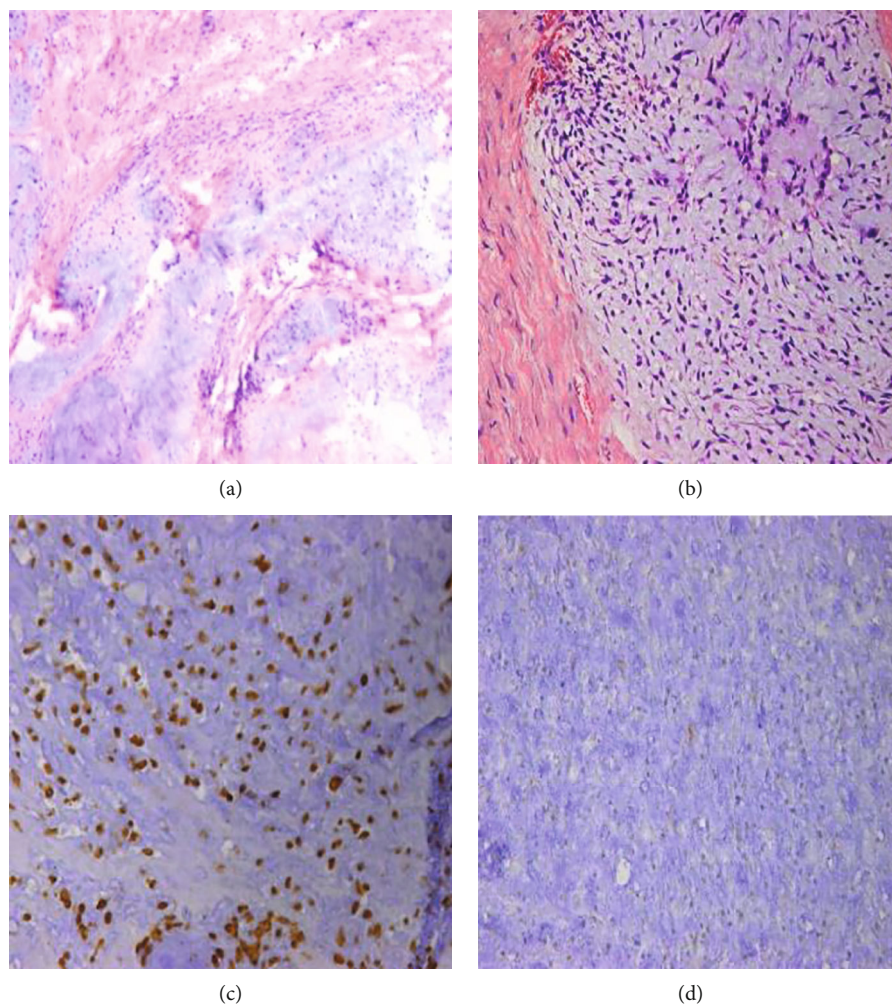


FIGURE 8: Immunohistochemical pathological evidence from the intraoperative specimen confirms the preoperative diagnosis of chondrosarcoma in a 57-year-old patient. (a) HE $\times 40$. (b) HE $\times 100$. (c) Vimentin $\times 100$. (d) S-100 $\times 100$.

material 1-6 days before operation, which was effective and safe.

In the preoperative planning process, it is very important to select suitable patients with appropriate indications and exclude inappropriate patients with contraindications. A sensitive response to preoperative neoadjuvant chemotherapy and radiotherapy is very important in the treatment of pelvic malignancies, as these types of therapy shrink the tumor volume and clear the tumor boundary [26].

Dislocation is the most common complication in the early postoperative stage. No dislocation or loosening was observed in our patients, which may be associated with the strict postoperative management as shown in our flowchart. This finding could also be attributed to acetabular component positioning [27], soft tissue laxity around the joint [28], and nerve injury. [29] Based on previous experience obtained from the current study, an elevated-rim acetabular liner, a locked hip prosthesis, braces, neutral orthopaedic

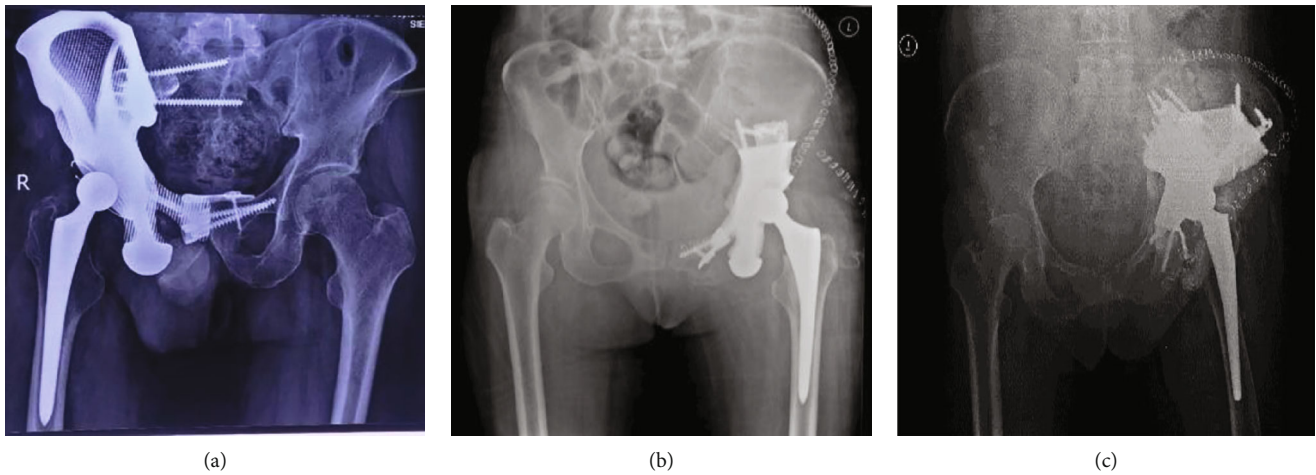


FIGURE 9: Postoperative X-ray images. (a) Prosthesis for regions I+II+III. (b) Prosthesis for regions II+III. (c) Prosthesis for regions I+II.

TABLE 3: Data related to the operation and follow-up of patients undergoing reconstruction following tumor resection.

| Variable | Value |
|---|---|
| Operation time, mean (min) | 247.50 ± 103.52 (range 135-420) |
| Intra-operative blood loss, mean (ml) | 2500.00 ± 1461.51 (range 1200-5000) |
| Intra-operative blood transfused, mean (ml) | 2220.00 ± 1277.62 (range 800-4080) |
| Post-operative drainage volume, mean (ml) | 937.50 ± 474.44 (range 395-1730) |
| Follow-up duration | 30.33 ± 9.89 months (range 18-42) |
| VAS (pre vs. post) | 7.167 ± 1.47 (range 5-9) vs. 2.83 ± 1.47 (range 1-5) |
| MSTS-93 score, mean | 19.83 ± 4.26 (range 15-26) |
| Harris score (pre vs. post) | 32.33 ± 11.11 (range 20-50) vs. 58.17 ± 13.92 (range 40-78) |
| Average time to walking | 76.17 ± 10.30 (range 62-91) |



FIGURE 10: The patient could sit and stand without assistance at the one-year follow-up.

shoes, and low branch traction were applied in order to help prevent dislocation. The occurrence of hip dislocation was reduced after scar tissue was formed around the hip joint. Previous studies have shown a high risk of infection in patients after undergoing pelvic reconstruction [30]. A medical pulse irrigator and sufficient drainage were applied to reduce the incidence of infection, and no cases of infection occurred in our study during the follow-up period.

4.2. Designing the Prosthesis. To obtain satisfactory functional results with reconstruction, restoration of the anatomical integrity of the pelvic ring should be taken into account when designing the prosthesis. Moreover, the selection of the type and extent of pelvic resection informs prosthesis design, including the components, shape, width, and length of the prosthesis. In the present study, the prosthesis was fixed to the remaining ilium (or the sacrum), pubic rami (same side or the other side), and ischial rami by screws through reserved holes, which allowed immediate stability and continuity of the pelvic ring. Besides considering the integrity of the pelvic ring, we design the ischial tubercle of the prosthesis into a polished surface, which can improve the comfort when sitting.

The porous surface structure of the prosthesis was designed to reduce the incidence of prosthetic loosening, enhance bone ingrowth, minimize stress shielding, and reduce its weight using electron beam melting technology [17]. Previous studies have reported that this porous structure acts as an osteoconductive scaffold for bone ingrowth and applies a stimulus for bone formation [31]. It has been suggested that porous structures with pore diameters ranging from 400 to 800 μm and high porosity (75%) are the most effective in promoting prosthesis osteointegration [32, 33]. Poblath et al. reported that a prosthesis designed in a honeycomb-like configuration could minimize stress shielding while ensuring resistance against mechanical failure and increased bone formation [34]. According to these findings, the surface of our 3D-printed prosthesis was designed with a pore diameter of 400 μm and a porosity of 75%. We hypothesized that compared with a smooth surface, this porous structure would enable the well-vascularized soft tissue to better reattach to the prosthesis. In practice, the high postoperative Harris hip score in our study confirmed this hypothesis. Furthermore, we demonstrated the achievement of good radiographic fusion and hip function without any cases of prosthetic loosening or fracture on X-ray at the last follow-up.

Through 3D image processing, safe and dangerous areas of screw fixation can be strictly depicted before surgery to improve safety [35]. A predesigned 3D printing screw hole has been successfully used to drill holes with an accurate orientation and length and to guide screws into the correct position during surgery. The use of preoperative 3D image processing is a safe, effective, and accurate means to avoid the need for repeat detection of the bone defect, increasing the operative time and reducing the incidence of secondary damage. In our study, cement was used to seal the cap of the screws to prevent screw withdrawal. In future research, we plan to use locking screws and holes. Currently, preoperative utilization of the 3D 1:1 prosthesis model aid in our understanding of the operation process, shortens the operative time, and reduces the occurrence of complications. Moreover, 3D-printed osteotomy guides have been widely applied in bone tumor resection due to their accuracy [36]. A previous study demonstrated that the maximum error of the 3D-printed osteotomy guide was significantly lower than that of a free-hand osteotomy guide [22]. Under the assistance of a 3D-printed osteotomy guide, intraoperative injury to adjacent blood vessels and nerves can be avoided [21, 22].

4.3. Selecting a Surgical Approach. Optimal outcomes are associated with the correct selection of surgical approaches and techniques. Tumor classification is vital, as there is not a single surgical approach that permits safe resection and implantation. The selected approach should also be aimed at avoiding the dissection of important muscle groups, thus reducing the risk of injury to neurovascular bundles. Therefore, the effective surgical approach should be selected according to the tumor classification.

In this novel approach, it is necessary to remove the attachment point of the muscle on the iliac crest and peel away the iliac muscle as well as to avoid serious injury, lateral femoral cutaneous nerve damage, bladder injury, bleeding, extended wound closure time, infection, and other complica-

tions. Various surgical approaches (ilioinguinal/modified Stoppa) have been previously reported [37]. Compared with the ilioinguinal approach and the modified Stoppa approach, the novel approach has the following advantages: [1] the muscles are peeled away from the bone as a sleeve together, avoiding damage to external rotation muscles and neurovascular bundles and reducing the risk of infection and [2] due to the satisfactory exposure, it is easy to perform tumor resection and reconstruct the pelvic bony defect with less bleeding.

The volume of blood loss and operative time in this study were partially due to the choice of surgical approach. A long surgical time and a massive blood loss volume might increase the incidence of postoperative infection [9, 21, 33]. Compared with the approach and the modified Stoppa, our novel approach is superior in terms of reducing the operative time and blood loss volume, according to our preliminary evidence. Further studies with larger sample sizes are needed to confirm this hypothesis. In our patients, the average volume of blood loss and the average amount of blood transfused during surgery were lower than many previous reports in which other approaches were used [38–40]. We attribute this reduced bleeding to the selection of the approach. As a qualitative comparison of the operative effectiveness of our approach, the surgical time in our patients was approximately 4 hours, while Gómez-Palomo et al. reported a surgical time of 6 hours using the ilioinguinal approach for internal hemipelvectomy and reconstruction assisted by 3D printing technology in a patient with pelvic sarcoma [41].

4.4. Strengths and Weaknesses. To our knowledge, this study is the first to report reconstruction of the hemipelvis using a fully integrated, anatomically conforming hemipelvic prosthesis, or to propose a novel surgical approach for pelvic tumor resection. We also present the treatment strategy. However, this study had some limitations. [1] A comparison group was not included because there were not enough patients in the study, but that the sample size limited the power and also a comparison group was not included. [2] The relatively short follow-up duration did not account for determining late complications in all the patients. [3] There were several drawbacks to the study design. Specifically, large holes in the prosthesis should be utilized according to the anatomical origins of muscles to guarantee accurate fixation and reconstruction of important muscles/tendons, such as the quadriceps femoris and iliac muscles. [4] The stability of the contralateral sacroiliac joint could be affected by the rigid fixation method and osseointegration, a biomechanical performance analysis was not performed in this study, and the prosthesis design should be improved in future studies. [5] The extensive costs associated with 3D printing, the high requirements for the techniques and team members, and the long manufacturing period are also limitations for the extensive application of this approach.

5. Conclusions

This is the report of a detailed design for a 3D-printed anatomically conforming hemipelvic prosthesis and a novel treatment strategy in treating the pelvic tumor. In our study,

the giant pelvic tumors were resected with large bony defects remaining in need of reconstruction. Reconstruction was achieved with a highly matched, 3D-printed prosthesis with an anatomically conforming design and with surgical techniques that included the novel approach and other supplementary steps to reduce injury. Despite these favorable outcomes, additional studies with long-term follow-up durations are required. Further research will be of value for patients with complex pelvic tumors.

Data Availability

The dataset supporting the conclusions of this study is available, and we agree to share the dataset.

Conflicts of Interest

There are no conflicts of interest to declare.

References

- [1] L. Karalashvili, A. Kakabadze, M. Uhryn, H. Vyshnevskaya, K. Ediberidze, and Z. Kakabadze, "Bone grafts for reconstruction of bone defects (review)," *Georgian Medical News*, vol. 282, pp. 44–49, 2018.
- [2] P. Anract, D. Biau, A. Babinet, and B. Tomeno, "Pelvic reconstructions after bone tumor resection," *Bulletin du Cancer*, vol. 101, no. 2, pp. 184–194, 2014.
- [3] M. Campanacci and R. Capanna, "Pelvic resections: the Rizzoli Institute experience," *The Orthopedic Clinics of North America*, vol. 22, no. 1, pp. 65–86, 1991.
- [4] M. I. O'Connor and F. H. Sim, "Salvage of the limb in the treatment of malignant pelvic tumors," *The Journal of Bone & Joint Surgery*, vol. 71, no. 4, pp. 481–494, 1989.
- [5] T. Ozaki, A. Hillmann, D. Bettin, P. Wuisman, and W. Winkelmann, "High complication rates with pelvic allografts: Experience of 22 sarcoma resections," *Acta Orthopaedica Scandinavica*, vol. 67, no. 4, pp. 333–338, 2009.
- [6] R. B. Stephenson, H. Kaufer, and F. M. Hankin, "Partial pelvic resection as an alternative to hindquarter amputation for skeletal neoplasms," *Clinical Orthopaedics and Related Research*, vol. 242, pp. 201–211, 1989.
- [7] H. Liang, T. Ji, Y. Zhang, Y. Wang, and W. Guo, "Reconstruction with 3D-printed pelvic endoprostheses after resection of a pelvic tumour," *The Bone & Joint Journal*, vol. 99-B, no. 2, pp. 267–275, 2017.
- [8] S. P. Issa, D. Biau, A. Babinet, V. Dumaine, M. Le Hanneur, and P. Anract, "Pelvic reconstructions following periacetabular bone tumour resections using a cementless ice-cream cone prosthesis with dual mobility cup," *International Orthopaedics*, vol. 42, no. 8, pp. 1987–1997, 2018.
- [9] B. Wang, X. Xie, J. Yin et al., "Reconstruction with modular hemipelvic endoprosthesis after pelvic tumor resection: a report of 50 consecutive cases," *PLoS One*, vol. 10, no. 5, 2015.
- [10] J. A. Jansen, M. A. J. van de Sande, and P. D. S. Dijkstra, "Poor Long-term Clinical Results of Saddle Prosthesis After Resection of Periacetabular Tumors," *Clinical Orthopaedics and Related Research*, vol. 471, no. 1, pp. 324–331, 2013.
- [11] D. Donati, G. D'Apote, M. Boschi, L. Cevolani, and M. G. Benedetti, "Clinical and functional outcomes of the saddle prosthesis," *Journal of Orthopaedics and Traumatology*, vol. 13, no. 2, pp. 79–88, 2012.
- [12] M. Danişman, M. U. Mermerkaya, Ş. Bekmez, M. Ayvaz, B. Atila, and A. M. Tokgözoğlu, "Reconstruction of periacetabular tumours with saddle prosthesis or custom-made prosthesis, functional results and complications," *HIP International*, vol. 26, no. 2, pp. e14–e18, 2018.
- [13] N. E. Fisher, J. T. Patton, R. J. Grimer et al., "Ice-cream cone reconstruction of the pelvis: a new type of pelvic replacement," *The Journal of Bone and Joint Surgery. British volume*, vol. 93-B, no. 5, pp. 684–688, 2011.
- [14] Q. Han, K. Zhang, Y. Zhang et al., "Individual resection and reconstruction of pelvic tumor with three-dimensional printed customized hemi-pelvic prosthesis: a case report," *Medicine (Baltimore)*, vol. 98, no. 36, 2019.
- [15] X. Chen, L. Xu, Y. Wang, Y. Hao, and L. Wang, "Image-guided installation of 3D-printed patient-specific implant and its application in pelvic tumor resection and reconstruction surgery," *Computer Methods and Programs in Biomedicine*, vol. 125, pp. 66–78, 2016.
- [16] H. Fan, J. Fu, X. Li et al., "Implantation of customized 3-D printed titanium prosthesis in limb salvage surgery: a case series and review of the literature," *World Journal of Surgical Oncology*, vol. 13, no. 1, 2015.
- [17] F. A. Shah, A. Snis, A. Matic, P. Thomsen, and A. Palmquist, "3D printed Ti6Al4V implant surface promotes bone maturation and retains a higher density of less aged osteocytes at the bone-implant interface," *Acta Biomaterialia*, vol. 30, pp. 357–367, 2016.
- [18] W. F. Enneking and W. K. Dunham, "Resection and reconstruction for primary neoplasms involving the innominate bone," *The Journal of Bone and Joint Surgery. American Volume*, vol. 60, no. 6, pp. 731–746, 1978.
- [19] K. C. Wong, S. M. Kumta, N. V. Geel, and J. Demol, "One-step reconstruction with a 3D-printed, biomechanically evaluated custom implant after complex pelvic tumor resection," *Computer Aided Surgery*, vol. 20, no. 1, pp. 14–23, 2015.
- [20] J. Wang, L. Min, M. Lu et al., "Three-dimensional-printed custom-made hemipelvic endoprosthesis for primary malignancies involving acetabulum: the design solution and surgical techniques," *Journal of Orthopaedic Surgery and Research*, vol. 14, no. 1, p. 389, 2019.
- [21] L. Ma, Y. Zhou, Y. Zhu et al., "3D-printed guiding templates for improved osteosarcoma resection," *Scientific Reports*, vol. 6, no. 1, 2016.
- [22] T. Jentzsch, L. Vlachopoulos, P. Fünstahl, D. A. Müller, and B. Fuchs, "Tumor resection at the pelvis using three-dimensional planning and patient-specific instruments: a case series," *World Journal of Surgical Oncology*, vol. 14, no. 1, p. 249, 2016.
- [23] A. K. Freeman, C. J. Thorne, C. L. Gaston et al., "Hypotensive epidural anesthesia reduces blood loss in pelvic and sacral bone tumor resections," *Clinical Orthopaedics and Related Research*, vol. 475, no. 3, pp. 634–640, 2017.
- [24] S. Bading, E. Mössinger, S. Baus, and L. Bastian, "Surgical treatment of osseous metastases of the pelvis," *Der Unfallchirurg*, vol. 107, no. 5, pp. 420–428, 2004.
- [25] H. P. Jander and N. A. Russinovich, "Transcatheter gelfoam embolization in abdominal, retroperitoneal, and pelvic hemorrhage," *Radiology*, vol. 136, no. 2, pp. 337–344, 1980.
- [26] A. A. Salunke, J. Shah, V. Warikoo et al., "Surgical management of pelvic bone sarcoma with internal hemipelvectomy: oncologic and functional outcomes," *J Clin Orthop Trauma*, vol. 8, no. 3, pp. 249–253, 2017.

- [27] F. E. Rowan, B. Benjamin, J. R. Pietrak, and F. S. Haddad, "Prevention of dislocation after total hip arthroplasty," *The Journal of Arthroplasty*, vol. 33, no. 5, pp. 1316–1324, 2018.
- [28] M. Takao, Y. Otake, N. Fukuda, Y. Sato, M. Armand, and N. Sugano, "The posterior capsular ligamentous complex contributes to hip joint stability in distraction," *The Journal of Arthroplasty*, vol. 33, no. 3, pp. 919–924, 2018.
- [29] Y. Higuchi, Y. Hasegawa, and N. Ishiguro, "Leg lengthening of more than 5 cm is a risk factor for sciatic nerve injury after total hip arthroplasty for adult hip dislocation," *Nagoya Journal of Medical Science*, vol. 77, no. 3, pp. 455–463, 2015.
- [30] S. Miwa, T. Shirai, N. Yamamoto et al., "Risk factors for surgical site infection after malignant bone tumor resection and reconstruction," *BMC Cancer*, vol. 19, no. 1, p. 33, 2019.
- [31] H. D. Kim, S. Amirthalingam, S. L. Kim, S. S. Lee, J. Rangasamy, and N. S. Hwang, "Biomimetic Materials and Fabrication Approaches for Bone Tissue Engineering," *Advanced Healthcare Materials*, vol. 6, no. 23, 2017.
- [32] J. Markhoff, J. Wieding, V. Weissmann, J. Pasold, A. Jonitz-Heincke, and R. Bader, "Influence of different three-dimensional open porous titanium scaffold designs on human osteoblasts behavior in static and dynamic cell investigations," *Materials (Basel)*, vol. 8, no. 8, pp. 5490–5507, 2015.
- [33] R. Wei, W. Guo, T. Ji, Y. Zhang, and H. Liang, "One-step reconstruction with a 3D-printed, custom-made prosthesis after total en bloc sacrectomy: a technical note," *European Spine Journal*, vol. 26, no. 7, pp. 1902–1909, 2017.
- [34] A. M. Pobloth, S. Checa, H. Razi et al., "Mechanobiologically optimized 3D titanium-mesh scaffolds enhance bone regeneration in critical segmental defects in sheep," *Sci Transl Med*, vol. 10, no. 423, p. eaam8828, 2018.
- [35] K. C. Wong and S. M. Kumta, "Computer-assisted tumor surgery in malignant bone tumors," *Clinical Orthopaedics and Related Research*, vol. 471, no. 3, pp. 750–761, 2013.
- [36] V. Y. Ng, J. H. DeClaire, K. R. Berend, B. C. Gulick, and A. V. Lombardi, "Improved accuracy of alignment with patient-specific positioning guides compared with manual instrumentation in TKA," *Clinical Orthopaedics and Related Research*, vol. 470, no. 1, pp. 99–107, 2012.
- [37] M. P. Mott, R. E. Meehan, and H. Zhu, "Ilioinguinal approach to manage benign pelvic and acetabular tumors," *American Journal of Orthopedics (Belle Mead, N.J.)*, vol. 30, no. 7, pp. 554–559, 2001.
- [38] K. R. Dai, M. N. Yan, Z. A. Zhu, and Y. H. Sun, "Computer-aided custom-made hemipelvic prosthesis used in extensive pelvic lesions," *The Journal of Arthroplasty*, vol. 22, no. 7, pp. 981–986, 2007.
- [39] B. Wang, Y. Hao, F. Pu, W. Jiang, and Z. Shao, "Computer-aided designed, three dimensional-printed hemipelvic prosthesis for peri-acetabular malignant bone tumour," *International Orthopaedics*, vol. 42, no. 3, pp. 687–694, 2018.
- [40] W. Sun, J. Li, Q. Li, G. Li, and Z. Cai, "Clinical effectiveness of hemipelvic reconstruction using computer-aided custom-made prostheses after resection of malignant pelvic tumors," *The Journal of Arthroplasty*, vol. 26, no. 8, pp. 1508–1513, 2011.
- [41] J. M. Gómez-Palomo, F. J. Estades-Rubio, S. Meschian-Coretti, E. Montañez-Heredia, and F. J. De Santos-de la Fuente, "Internal hemipelvectomy and reconstruction assisted by 3D printing technology using premade intraoperative cutting and placement guides in a patient with pelvic sarcoma: a case report," *JBJS Case Connect.*, vol. 9, no. 4, 2019.

Research Article

3D Printed Personalized Guide Plate in the Femoral Head Core Decompression

Liangliang Cheng , Xing Qiu, Lei Yang, Chi Xiao, Baoyi Liu, Chukwuemeka Samuel Okoye, and Dewei Zhao 

Department of Orthopaedics, Affiliated Zhongshan Hospital of Dalian University, No. 6 Jiefang St, Dalian, Liaoning Province 116001, China

Correspondence should be addressed to Dewei Zhao; zhaodewei2016@163.com

Received 6 August 2020; Revised 27 September 2020; Accepted 7 November 2020; Published 19 November 2020

Academic Editor: Xiaojun Duan

Copyright © 2020 Liangliang Cheng et al. This is an open access article distributed under the Creative Commons Attribution License, which permits unrestricted use, distribution, and reproduction in any medium, provided the original work is properly cited.

Objective. To investigate the feasibility of using 3D printed personalized guide plates in core decompression procedures for the treatment of osteonecrosis of the femoral head (ONFH). **Methods.** The clinical data of 8 patients undergoing femoral head core decompression from January to December 2019 were analyzed retrospectively. Three-dimensional (3D) images of the patients were reconstructed from the CT scan data taken preoperatively. From the data obtained, puncture position, drill hole, and depth were evaluated, and individualized 3D puncture guide plates were designed using Mimics 21.0 software. During the operation, the needle went through the hole of the guide plate, the depth of the drill was controlled, and the obtained bone tissues were sent for pathological evaluation. Intraoperative X-ray and postoperative pathological results were used to evaluate the success of the puncture. **Results.** The individualized guide plates used for core decompression on the 8 patients were well fitted with the anatomic structure of the puncture site, and the direction and depth of the needle insertion were consistent with the preoperative design. The operation time was about 15-22 mins. The position of the decompression tunnel was the same as the designed plate. The postoperative pathology showed necrotic bone tissue. There were no postoperative complications such as infection, bleeding, and fracture. **Conclusion.** The 3D printed individualized guide plate can simplify core decompression and would make this procedure more accurate, safe, and quick, in addition to obtaining necrotic tissues for pathological examination.

1. Introduction

Osteonecrosis of the femoral head (ONFH) is a destructive bone condition most commonly affecting young and middle-aged patients. ONFH often progresses to femoral head collapse, which in some patients may require total hip arthroplasty (THA) [1–4]. Core decompression is one choice of treatment for early-stage ONFH. Depending on the specific condition, multiple-tunnel decompression or single-tunnel decompression may be adopted. At present, the location of the needle is mainly determined by C-arm fluoroscopy during surgical operation. For young patients with small necrotic areas, repeated fluoroscopy is needed to make the needle reach the ideal position. In recent years, 3D printed techniques have emerged in the field of medicine due to their high precision, fast construction speed, and on-demand manufacture [5, 6].

Orthopedics, oncology, radiotherapy, and other disciplines use 3D printed personalized guide plates to assist surgery [5–7]. However, the use of this technology in the core decompression procedure has been rarely reported. Recently, the orthopedics department of Affiliated Zhongshan Hospital of Dalian University applied the use of a 3D printed personalized guide plate in core decompression for the treatment of early-stage ONFH and achieved good clinical results.

1.1. Clinical Data. From January to December 2019, the clinical data of eight patients with early-stage ONFH who required core decompression were analyzed retrospectively. The patients included 4 males and 4 females, with ages ranging from 22 to 48 years. Their clinical symptoms included hip pain and limited hip movement. All cases were diagnosed as ONFH (ARCO II) by X-ray and MRI. The study

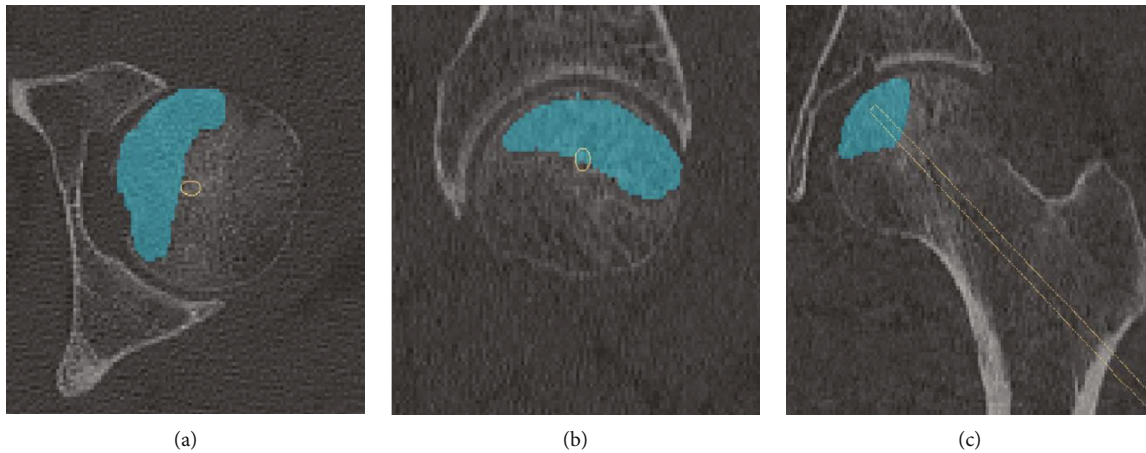


FIGURE 1: The blue area is the necrotic area of the femoral head, and the yellow line is the location of the decompression pathway: (a) horizontal, (b) sagittal, and (c) coronal.

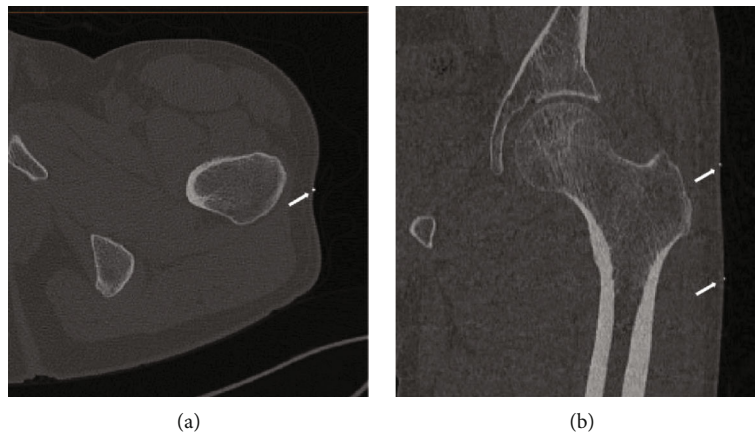


FIGURE 2: The little white dots indicated by the white arrow are the metal lines: (a) horizontal and (b) coronal.

was approved by the Ethics Committee of Affiliated Zhongshan Hospital of Dalian University. All patients signed the informed consent form.

1.2. Three-Dimensional Model of ONFH. CT scan data were collected before the operation, and three metal wires were used to mark the hip joint before the data were collected. When taking the CT scan, patients were asked to keep their toes close together and their legs straight. After completion of the scan, the CT data was exported to the medical processing software, Mimics 21.0 (Materialise, Belgium). The images were segmented according to the gray value difference amongst the femoral head, skin soft tissue, and the metal wire. The targeted region was segmented with a different threshold, and the 3D virtual model was reconstructed. The three-dimensional model was optimized, and the osteonecrotic lesion was delineated as the region of interest. The location and shape of the lesion and the relationship between the lesion and the metal lines were highlighted. (Figures 1 and 2).

1.3. Planning of the Decompression Tunnel and Design of Personalized Guide Plates. The center point of the lesion was used as the target point of the decompression tunnel, and

the decompression tunnel was planned from the lower part of the greater trochanter of the femur to the center of the necrotic area. After the decompression tunnel was determined, the distance from the skin needlepoint to the decompression target point was measured by the software, and the guide plate was constructed using the software “expansion” function. Taking the decompression tunnel as the center, 5-6 decompression tunnels were designed parallel to it for multitunnel fine needle core decompression. Finally, the redundant parts were removed by the Boolean operation, and the guide plate was customized. The surface of the guide plate in contact with the skin was marked with a trace line on the skin surface of the patient, to easily locate the accurate surface during surgery.

1.4. 3D Printing of the Personalized Guide Plate Model. From Mimics 21.0 software, the guide plate model was exported as a STL file into the 3D printing machine (Stratasys F170) for rapid production of the guide plate. After printing the plate, metal excesses were pruned, the plate was checked on the patient to ensure proper fitting, and the plate surface trace metal line and the trace line marked on the body surface were inspected for consistency. If the comparisons align correctly, the guide plate is sterilized and sealed at low temperature.

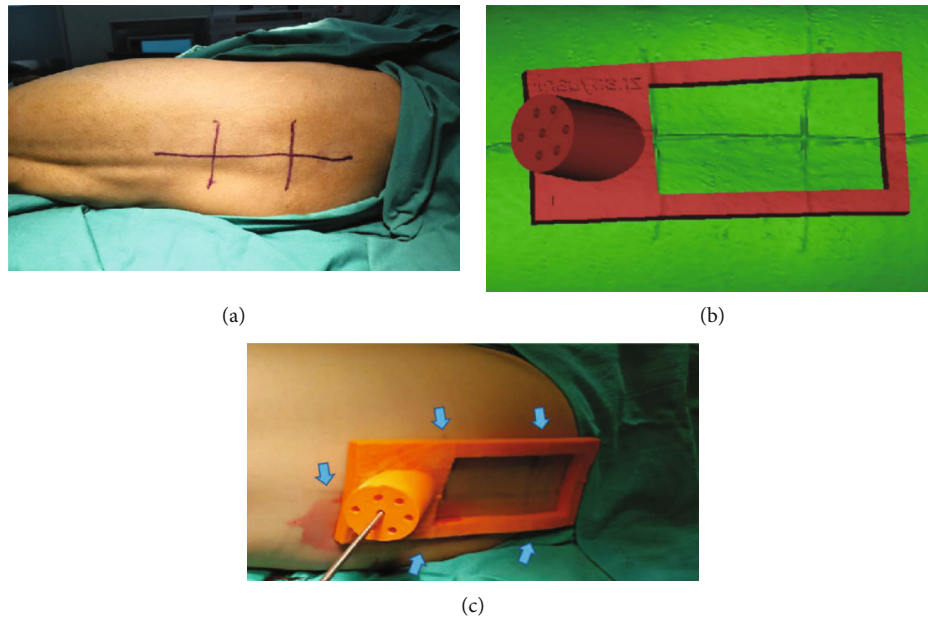


FIGURE 3: (a) A marker line for the location of the metal line on the body surface; (b) a personalized guide plate designed by the software; (c) the use of a 3D printed personalized guide plate (the blue arrow indicates the location of the marker line).

1.5. The Application of the Individualized Guide Plate in Core Decompression. After anesthesia, the patient was placed in a horizontal position, and the lower limbs were extended with the toes close to each other, to mimic the same body positioning during CT scan. The marked line on the guide plate is fitted on to the trace line marked on the body surface. Kirschner wire was passed through the guide tunnel in the guide plate, and the needle was slowly penetrated through the predetermined depth. Fluoroscopy was used to confirm the positioning; then, the guide plate was removed. A 1 cm longitudinal incision was made at the insertion of the Kirschner wire, and trephine was drilled along the Kirschner wire. The Kirschner wire was then pulled out, and necrotic bone was taken out for pathological examination (Figures 3–6).

2. Results

The individualized guide plate of the 8 patients fitted properly. The position, direction, and depth of the inserted needle were consistent with the preoperative design. All core decompression operations were completed once, and X-ray fluoroscopy of C-arm confirmed that all the Kirschner wires reached the target point and that the necrotic bone tissues were successfully removed. The operation time was 15–22 mins. There were no postoperative complications such as infection, bleeding, and fracture. The histopathologic diagnosis was necrotic bone tissue.

3. Discussion

In clinical practice, the treatment of early-stage ONFH is relatively difficult. Core decompression is an effective method to treat early-stage ONFH [8–11]; however, differing results are obtained. Core decompression reduces the pressure in the femoral head through the decompression tunnel,

improves the femoral head blood circulation, and at the same time removes the necrotic bone from the focus area, leaving out the healthy bone tissue. Therefore, the location of the decompression tunnel is very important. If the target point of the decompression tunnel can reach the central area of the necrotic focus, it will be more accurate and more effective to remove the necrotic bone. At present, clinicians use intraoperative X-ray fluoroscopy repeatedly to adjust the location of the needle to reach the target point. Repeated punctures can disrupt normal bone tissue and blood circulation within the femoral head and may exacerbate osteonecrosis [12, 13]. Precise puncture decompression is very necessary. At present, navigation technology is used to assist core decompression, which can make the location of puncture decompression more accurate and flexible, but it is necessary to install a positioning device and adjust navigation during the operation which increases the patient limb injury and prolongs the surgical time, and navigation equipment is expensive and so may decrease its usage in the clinics [14].

As 3D printing technology matures [15], existing techniques can be used to design a 1 : 1 model with a prototype based on the patient's CT data. Complete preoperative planning can be made, and a drill approach can be simulated with a computer. Finally, a personalized 3D printed decompression guide plate is made using 3D printing technology, which improves the accuracy and efficiency of core decompression.

There are many kinds of 3D printed personalized guide plates used during orthopedic operations [4–6]. They are applied to the bone surface, but not to the surface of the skin, because of the mobility of the skin and soft tissue. The position of the guide plate changes when the body position is changed or pulled apart. Therefore, ensuring the proper positioning of the guide plate is the key to this kind of operation. In this study, before CT scan, 3–4 metal wires were fixed to the thin lateral soft tissue of the greater trochanter of

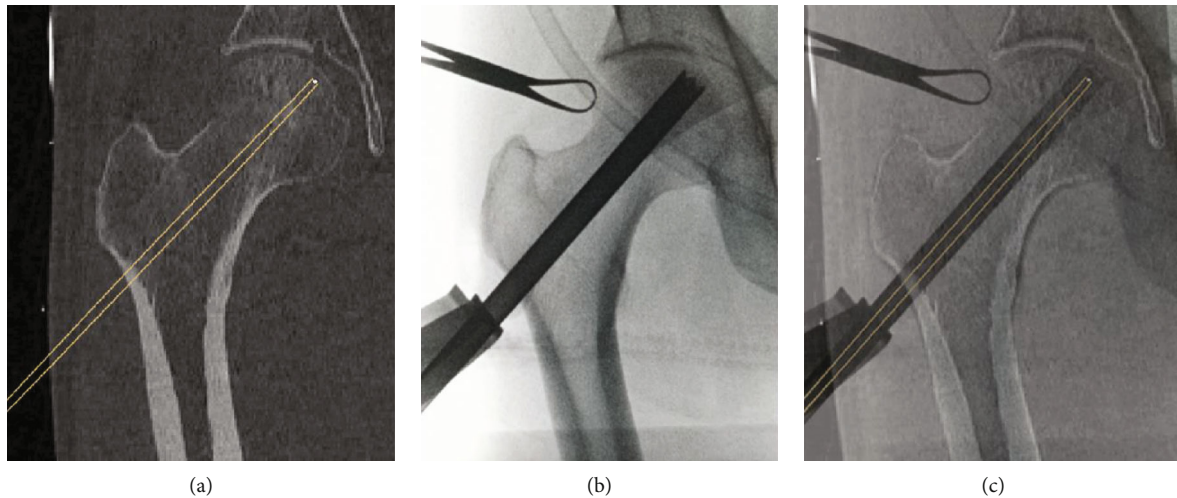


FIGURE 4: The preoperative design and intraoperative X-ray film of the decompression tunnel in coronal view (anteroposterior view): (a) the location of the decompression tunnel designed in the software; (b) the X-ray film of the decompression tunnel during the operation; (c) the overlapping of (a, b), which shows the consistency of the intraoperative and preoperative design.

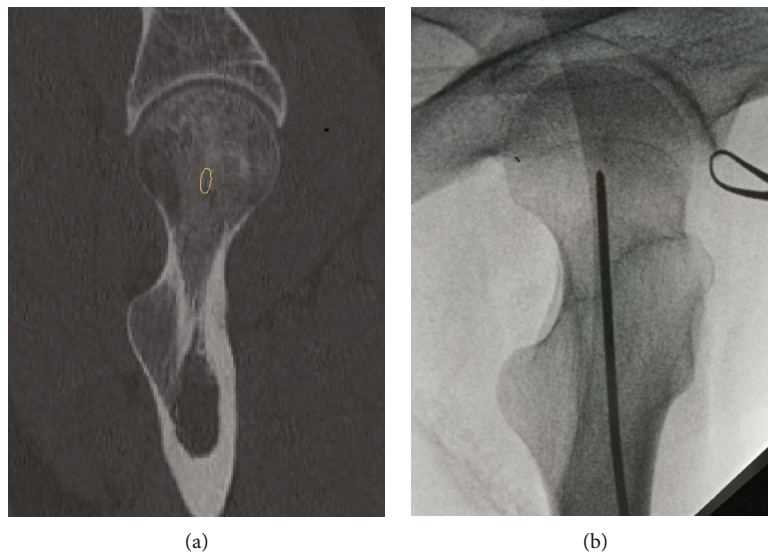


FIGURE 5: The preoperative design and intraoperative X-ray film of the decompression tunnel in sagittal view (lateral view): (a) the location of the decompression tunnel designed with the software; (b) the X-ray film of the decompression tunnel during the operation.

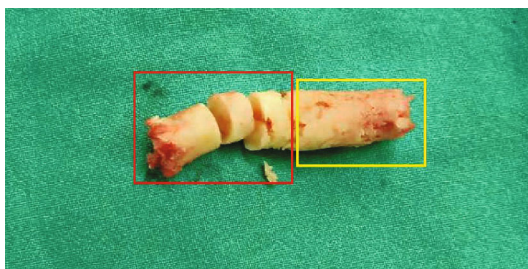


FIGURE 6: The bone tissue was removed through core decompression. The red frame area is necrotic bone tissue, and the yellow frame area is healthy cancellous bone tissue.

the femur as a body surface marker, and the range was as wide as possible; it is important to keep the patient's position during preoperative CT examination consistent with that

during intraoperative core decompression, in order to ensure that the appearance and tension of the patient's skin and soft tissue are as consistent as possible. The insertion point at the lateral femur was designed to be 1 cm below the greater trochanter where the cortical bone is thickening. The insertion point of Kirschner's needle can easily penetrate the cortical bone in this position, thus reducing the deviation of the insertion point caused by sliding of Kirschner's needle. During surgery, the guide plate is gently attached to the trace line marked on the skin surface in a gentle manner to avoid deformation of the skin and soft tissue, which may lead to change of position of the puncture tunnel. Finally, the Kirschner wire with a sharp tip is used for the operation, to ensure that there is no resistance when penetrating the skin and soft tissue and also to avoid error caused by the deformation of Kirschner's needle. For fat patients, because of the

thicker skin and soft tissue, we often design several parallel puncture tunnels on the guide plate that can be used during the surgery if there is a need for adjustment. Strict design and standard operation can ensure the accuracy of a 3D printed personalized guide plate on the skin surface. All cases completed in our clinics were carried out according to the preoperation plan; the results were verified by intraoperative X-ray fluoroscopy and postoperative histopathology.

Although modern medicine already has computer navigation, robot, and other directional equipment [15], for assisting core decompression surgery and for accurate drill of the core decompression, most hospitals and patients cannot afford the high cost of the directional equipment. Thus, orthopedic surgeons still rely on hand punctures and X-rays to repeatedly adjust the position. When the patient has small necrosis focus areas or a necrosis focus positioned in a special location, inaccurate multiple drills by the surgeon may ensure. As a new technology, 3D printing personalized guide plate positioning has the advantages of low price, accurate positioning during surgery, and no damage to healthy tissue, which improves surgical efficiency, making the use of 3D printing effective, and this technology overcomes the deficiencies of the traditional surgical methods.

To sum up, digital design and 3D printing technology are convenient for the femoral head core decompression procedure. They offer accuracy, safety, affordability, and suitability for all levels of medical institutions and is thus worthy to be promoted for use in clinical practice.

Data Availability

The readers can access the data supporting the conclusions of this study.

Conflicts of Interest

All the authors have no conflict of interest.

Acknowledgments

This work was supported by the Dalian Science and Technology Innovation Fund Project (no.2020JJ27SN077), the Dalian Science and Technology Innovation Fund Project (no.2018J11CY030), and the Health Industry research Project (no.201402016).

References

- [1] M. A. Mont, H. S. Salem, N. S. Piuze, S. B. Goodman, and L. C. Jones, "Nontraumatic osteonecrosis of the femoral head: where do we stand today?: A 5-year update," *The Journal of Bone and Joint Surgery. American Volume*, vol. 102, no. 12, pp. 1084–1099, 2020.
- [2] H. R. Choi, M. E. Steinberg, and E. Y. Cheng, "Osteonecrosis of the femoral head: diagnosis and classification systems," *Current Reviews in Musculoskeletal Medicine*, vol. 8, no. 3, pp. 210–220, 2015.
- [3] C. G. Zalavras and J. R. Lieberman, "Osteonecrosis of the femoral head: evaluation and treatment," *The Journal of the American Academy of Orthopaedic Surgeons*, vol. 22, no. 7, pp. 455–464, 2014.
- [4] S. Banerjee, K. Issa, R. Pivec, B. H. Kapadia, H. S. Khanuja, and M. A. Mont, "Osteonecrosis of the hip: treatment options and outcomes," *The Orthopedic Clinics of North America*, vol. 44, no. 4, pp. 463–476, 2013.
- [5] C. Wang, L. Zhang, T. Qin et al., "3D printing in adult cardiovascular surgery and interventions: a systematic review," *Journal of Thoracic Disease*, vol. 12, no. 6, pp. 3227–3237, 2020.
- [6] T. Bartel, A. Rivard, A. Jimenez, C. A. Mestres, and S. Müller, "Medical three-dimensional printing opens up new opportunities in cardiology and cardiac surgery," *European Heart Journal*, vol. 39, no. 15, pp. 1246–1254, 2018.
- [7] W. C. H. Parr, J. L. Burnard, P. J. Wilson, and R. J. Mobbs, "3D printed anatomical (bio)models in spine surgery: clinical benefits and value to health care providers," *Journal of Spine Surgery*, vol. 5, no. 4, pp. 549–560, 2019.
- [8] T. P. Pierce, J. J. Jauregui, R. K. Elmallah, C. J. Lavernia, M. A. Mont, and J. Nace, "A current review of core decompression in the treatment of osteonecrosis of the femoral head," *Current Reviews in Musculoskeletal Medicine*, vol. 8, no. 3, pp. 228–232, 2015.
- [9] P. Hernigou and F. Beaujean, "Treatment of osteonecrosis with autologous bone marrow grafting," *Clinical Orthopaedics and Related Research*, vol. 405, pp. 14–23, 2002.
- [10] M. T. Houdek, C. C. Wyles, J. R. Martin, and R. J. Sierra, "Stem cell treatment for avascular necrosis of the femoral head: current perspectives," *Stem Cells and Cloning: Advances and Applications*, vol. 7, pp. 65–70, 2014.
- [11] E. Larson, L. C. Jones, S. B. Goodman, K. H. Koo, and Q. Cui, "Early-stage osteonecrosis of the femoral head: where are we and where are we going in year 2018?," *International Orthopaedics*, vol. 42, no. 7, pp. 1723–1728, 2018.
- [12] L. Lin, Y. Jiao, X. G. Luo et al., "Modified technique of advanced core decompression for treatment of femoral head osteonecrosis," *World Journal of Clinical Cases*, vol. 8, no. 13, pp. 2749–2757, 2020.
- [13] A. K. Aggarwal, K. Poornalingam, A. Jain, and M. Prakash, "Combining platelet-rich plasma instillation with core decompression improves functional outcome and delays progression in early-stage avascular necrosis of femoral head: a 4.5- to 6-year prospective randomized comparative study," *The Journal of Arthroplasty*, 2020.
- [14] J. Beckmann, J. Goetz, H. Baethis, T. Kalteis, J. Grifka, and L. Perlick, "Precision of computer-assisted core decompression drilling of the femoral head," *Archives of Orthopaedic and Trauma Surgery*, vol. 126, no. 6, pp. 374–379, 2006.
- [15] F. Wang, J. Zhu, X. Peng, and J. Su, "The application of 3D printed surgical guides in resection and reconstruction of malignant bone tumor," *Oncology Letters*, vol. 14, no. 4, pp. 4581–4584, 2017.

Research Article

3D-Printed Patient-Specific Instrumentation Technique Vs. Conventional Technique in Medial Open Wedge High Tibial Osteotomy: A Prospective Comparative Study

Yunhe Mao ¹, Yang Xiong,¹ Qi Li,¹ Gang Chen,¹ Weili Fu,¹ Xin Tang,¹ Luxi Yang,² and Jian Li ¹

¹Department of Sports Medicine, West China Hospital, Sichuan University, No. 37, Guoxue Alley, Chengdu, China

²Sichuan International Expo Group, Chengdu, China

Correspondence should be addressed to Jian Li; hxlijian.china@163.com

Received 7 August 2020; Revised 8 October 2020; Accepted 6 November 2020; Published 17 November 2020

Academic Editor: Xiaojun Duan

Copyright © 2020 Yunhe Mao et al. This is an open access article distributed under the Creative Commons Attribution License, which permits unrestricted use, distribution, and reproduction in any medium, provided the original work is properly cited.

Purpose. The purpose of this study was to compare the accuracy and clinical outcomes of the medial open wedge high tibial osteotomy (MOWHTO) using a three-dimensional (3D-) printed patient-specific instrumentation (PSI) with that of conventional surgical techniques. **Methods.** A prospective comparative study which included 18 patients who underwent MOWHTO using 3D-printed PSI technique (3D-printed group) and 19 patients with conventional technique was conducted from Jan 2019 to Dec 2019. After the preoperative planning, 3D-printed PSI (cutting guide model) was used in MOWHTO for 3D-printed group, while freehand osteotomies were adopted in the conventional group. The accuracy of MOWHTO for each method was compared using the radiological index obtained preoperatively and postoperatively, including mechanical femorotibial angle (mFTA) and medial mechanical proximal tibial angle (mMPTA), and correction error. Regular clinical outcomes were also compared between the 2 groups. **Results.** The correction errors in the 3D-printed group were significantly lower than the conventional group (mFTA, $0.2^\circ \pm 0.6^\circ$ vs. $1.2^\circ \pm 1.4^\circ$, $P = 0.004$) (mMPTA, $0.1^\circ \pm 0.4^\circ$ vs. $2.2^\circ \pm 1.8^\circ$, $P < 0.00001$). There was a significantly shorter duration ($P < 0.00001$) and lower radiation exposures ($P < 0.00001$) for the osteotomy procedure in the 3D-printed group than in the conventional group. There were significantly higher subjective IKDC scores ($P = 0.009$) and Lysholm scores ($P = 0.03$) in the 3D-printed group at the 3-month follow-up, but not significantly different at other time points. Fewer complications occurred in the 3D-printed group. **Conclusions.** With the assistance of the 3D-printed patient-specific cutting guide model, a safe and feasible MOWHTO can be conducted with superior accuracy than the conventional technique.

1. Introduction

Medial open wedge high tibial osteotomy (MOWHTO) is a well-established surgical procedure in dealing with early or mild stage of knee osteoarthritis (OA), and this native knee-preserving surgery could ensure long-lasting clinical success (>10 years) in the overall treatments of knee OA [1, 2]. MOWHTO is typically applied for the correction of varus malalignment of the lower extremities in isolated medial compartment arthritis of the knee [3–5]. If accurately performed, MOWHTO has the potential to delay

or even possibly prevent the development of end-stage OA, by shifting the weight-bearing axis toward the lateral compartment [3, 6]; the loading is redistributed, and knee function is thereby restored and could avert total knee arthroplasty (TKA).

Nevertheless, the downsides of this procedure remain notable. Except for the high rates of knotty local complications, including increased tibial slope, hinge fractures, infections, and delayed union [7, 8], the main obstacle lies in the accuracy of performing osteotomy [9]. A successful MOWHTO requires the angular correction to be achieved

accurately in both the sagittal and coronal planes, making it fairly challenging to determine the accurate osteotomy opening distance with the current conventional techniques [4, 10]. The systematic review by Van den Bempt et al. [4] revealed that the accuracy of conventional MOWHTO was below 75% in 8 out of 14 cohorts. Small errors in osteotomy positioning can lead to severe local complications such as lateral cortex fractures [11], and minor inaccuracy of angular correction in the coronal plane hinders the long-term success of this operation and even accelerates the progression of OA [12]. For the small tolerance for errors and the complexity for mastery, conventional MOWHTO gradually comes to be an unfavorable alternative [13].

However, the newly developed ancillary technology in the modality of 3D-printed patient-specific instrumentation (PSI) may be a solution to the accuracy requirements of HTO planning and execution [13]. This technique was initially carried out in maxillofacial surgery [14]; however, its practicability was more adequately embodied in the later orthopedic studies [5, 15–17]. The feasibility and proof-of-concept study by Victor and Premanathan [17] reported PSI for 14 cases of osteotomy around the knee yielded satisfactory outcomes, suggesting it to be a prospective solution. In the study by Van Genechten et al. [5], similar competent postoperative overall results were achieved by MOWHTO with the assistance of the 3D-printed PSI. Moreover, with a safer and faster osteotomy, it allows orthopedists to perform more concomitant surgeries at one time, such as meniscectomy and anterior cruciate ligament reconstruction (ACLR) [18–20]. Nevertheless, despite all these desirable superiorities, there was an evident scarcity of prospective comparative studies with robust evidences to prove the clinical advantages of PSI over conventional techniques in MOWHTO.

This study is thus designed to identify the safety, feasibility, and reliability of 3D-printed PSI for MOWHTO and to determine whether this novel technique could achieve better clinical outcomes and accuracy, when compared with conventional MOWHTO, in terms of correcting the varus malalignments in patients with isolated medial compartment OA. The null hypothesis was that MOWHTO with PSI technique could offer better clinical outcomes, fewer complications, and more accurate realignment over the traditional MOWHTO.

2. Methods

2.1. Patients. 18 MOWHTO surgeries with 3D-printed PSI technique and 19 conventional MOWHTO were conducted between Jan 2019 and Dec 2019 at Sports Medicine Center, Western China Hospital, Sichuan University. The study was approved by the Health Sciences Research Ethics Board at Sichuan University and at the local research ethics board at each institution (ID: 2018534).

Patients were considered for inclusion if they meet the following criteria: (1) age between 35 and 60 years old; (2) isolated medial compartment OA, Kellgren-Lawrence grade \leq III; (3) radiological evidences for varus malalignment (varus $> 6^\circ$, mechanical medial proximal tibial angle, mMPTA $< 85^\circ$); (4) ROM: flexion $\geq 120^\circ$, loss of extension $\leq 10^\circ$; and (5) outer bridge grade for cartilage injury $< IV$

(defect area $< 2.5 \text{ cm}^2$). Patients were thoroughly informed about the pre- and postoperative radiology protocol, the planning procedure, and the PSI surgical technique. On a voluntary basis, for the patients who agreed to take HTO at our medical center, either with novel PSI or conventional technique, preoperative hip-to-ankle double-limb weight-bearing X-ray view of the knee (anteroposterior (AP), lateral view), whole lower limb CT scan of both sides, and MRI of the affected knee were taken. The same imaging protocol was repeated 3 months and 12 months after surgery to evaluate the angular correction in both sagittal and coronal planes, the accuracy of hardware positioning, the condition of the cartilage, and the healing of the osteotomy.

All included patients in both groups had completed the prementioned radiology protocol and clinical assessments. The demographic characteristics of the included patients were shown in Table 1.

2.2. Preoperative Planning. With reference to the methodology and parameters provided by Chieh-Szu et al. [21, 22], under the guidance of a radiology engineer (B.J.), by using the DICOM (digital imaging and communication in medicine) data, continuum-based tibial and fibular models from the CT image (slice thickness: 1.5 mm; image resolution: 512×512 pixels) were reconstructed as the intact model. A computerized osteotomy simulation software (OsteoMaster) was adopted to create the 3D bone anatomy virtual models of the lower limbs (Figure 1).

After the optimal sagittal and coronal correction angles, depth, width, height, slope, and position of the osteotomy were determined, the PSI cutting guide model was then built accordingly using additive layer manufacturing (3D printing) for the accurate osteotomy in the material of hydroxyapatite. Every osteotomy case was planned by a single investigator (Y.X.) who was highly trained in working with 3D medical software programs according to the protocol previously mentioned (Figure 1).

2.3. Surgical Procedures. Surgeries were performed by a single senior surgeon (J.L.). Firstly, intra-articular procedures were performed, arthroscopy was taken at each patient in the exploration for concomitant diseases, and articular debridement, free body removal, meniscectomy, or ACLR were conducted if necessary.

For the PSI technique, a 10-cm vertical medial tibia skin incision was made 2 cm below the tibial articular surface; then, the pes anserinus tendon was explored and loosen to allow greater surgical exposure; the tibial insertion of the superficial layer of the fibular collateral ligament (FCL) was then released, and osseous landmarks were made for the PSI cutting guide model positioning, fixed by saw pins. Then, the two-planar osteotomy was performed by a swing saw through the cutting grooves of the guide model, the wedge shape gap was widened length by length with steel rulers and fixed at the predetermined angle via a metal bar stabilizer, then a distractor was used to maintain this interspace, and the PSI guide model was removed. Finally, a properly curved HTO plate was attached to the medial surface of the tibia as closely as possible, and the locking plate was tightly

TABLE 1: Demographic characteristics of the two groups.

| | 3D-printed PSI (mean \pm SD) | Conventional (mean \pm SD) | <i>P</i> value |
|---|--------------------------------|------------------------------|----------------|
| Age, years | 44.2 \pm 11.7 | 41.8 \pm 10.2 | n.s |
| Sex (male : female) | 4 : 14 | 5 : 14 | n.s |
| Right : left | 11 : 7 | 13 : 6 | n.s |
| BMI | 25.6 \pm 3.68 | 25.1 \pm 3.91 | n.s |
| ROM (°) | 126 \pm 11.2 | 121 \pm 10.3 | n.s |
| mFTA (°) | 172.2 \pm 1.7 | 172.0 \pm 1.9 | n.s |
| mMPTA (°) | 86.3° \pm 2.28° | 83.4° \pm 2.15° | n.s |
| mLDFA (°) | 88.9 \pm 1.86 | 89.4 \pm 1.57 | n.s |
| OA Kellgren–Lawrence grading (I : II : III) | 2 : 8 : 8 | 4 : 5 : 10 | — |
| Planned wedge opening (mm) | 8.9 \pm 1.1 | 8.5 \pm 1.5 | n.s |
| Meniscus injury (<i>n</i>) | 7 | 8 | n.s |
| ACL injury (<i>n</i>) | 2 | 3 | n.s |

Abbreviations: 3D: three-dimensional; PSI: patient-specific instrumentation; SD: standard deviation; n.s: not significant; BMI: body mass index; ROM: range of motion; mFTA: mechanical femorotibial angle; mMPTA: mechanical medial proximal tibial angle; mLDFA: mechanical lateral distal femoral angle; OA: osteoarthritis; ACL: anterior cruciate ligament.

fixed by screws. Autogenous or allogenic bones were implanted if the lateral border of the osteotomy opening was larger than 10 mm (Figure 2).

As for conventional MOWHTO, under the guidance of intraoperative C-arm fluoroscope, the osteotomy sites were determined visually by the free hand of the senior surgeon (J.L.); the same two-plane osteotomy procedures were performed accordingly. The correction angle, hardware positioning, and accuracy were determined recurrently by the C-arm fluoroscope, and the exposures of radiography were recorded. The same criteria were applied for bone grafting.

2.4. Radiological and Arthroscopic Assessment. Radiological measurements were performed for both groups after surgery in the prementioned protocol (preoperatively, postoperatively, 3 months, and 12 months after surgery) by a single observer (YH.M.). All angles mentioned above were measured on the double-limb full-length standing position X-ray plain film (anteroposterior view), which is the benchmark of the measurement of the mechanical leg axis [23]. In the coronal plane, the mechanical femorotibial angle (mFTA, or weight-bearing line), the mechanical medial proximal tibial angle (mMPTA), and the mechanical lateral distal femoral angle (mLDFA) were measured. Correction errors for the mFTA and the mMPTA accounting for accuracy in the coronal plane were also calculated. Special attention was paid to correct the positioning of both legs/feet on the full-length standing X-ray views before angle measurements were undertaken. OA severity was scored according to the Kellgren–Lawrence scale. And upon the request of the internal fixation removal by patients, a concomitant arthroscopy was performed to assess the condition of intra-articular structures (cartilage, meniscus, ligaments, etc.)

2.5. Clinical and Functional Assessment. Commonly accepted patient-reported outcome measures including the International Knee Documentation Committee (IKDC) score and

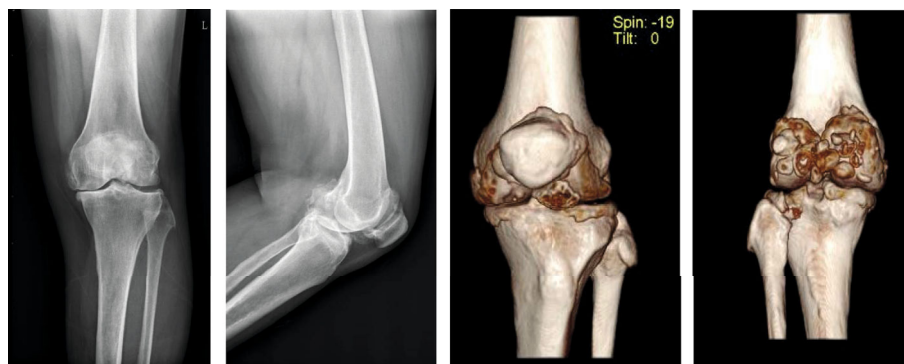
Lysholm score were used to assess the patients' subjective knee function. The subjective IKDC score is an 18-item, region-specific, patient-reported questionnaire containing the domains of symptoms, function, and sports activities [24]. The IKDC has been proven to be a valid and reliable instrument for patients who have knee injury and disability [25].

Intraoperative and postoperative adverse events up to 1 year were carefully documented for the assessment of technique safety. Common complications [8] including hinge fractures, delayed union/nonunion, infection, and deep vein thrombosis were strictly observed and duly managed. Visual analogue scale (VAS) was used to assess the preoperative pain and postoperative pain (24 hours, 48 hours, 1 month, 3 months, 6 months, and 12 months). The surgical duration for osteotomy, days of hospitalization, and dose of radiation (C-arm) were also recorded in every case. Standard follow-up with the senior surgeon (J.L.) was provided at 1 month, 3 months, 6 months, and 12 months postoperatively.

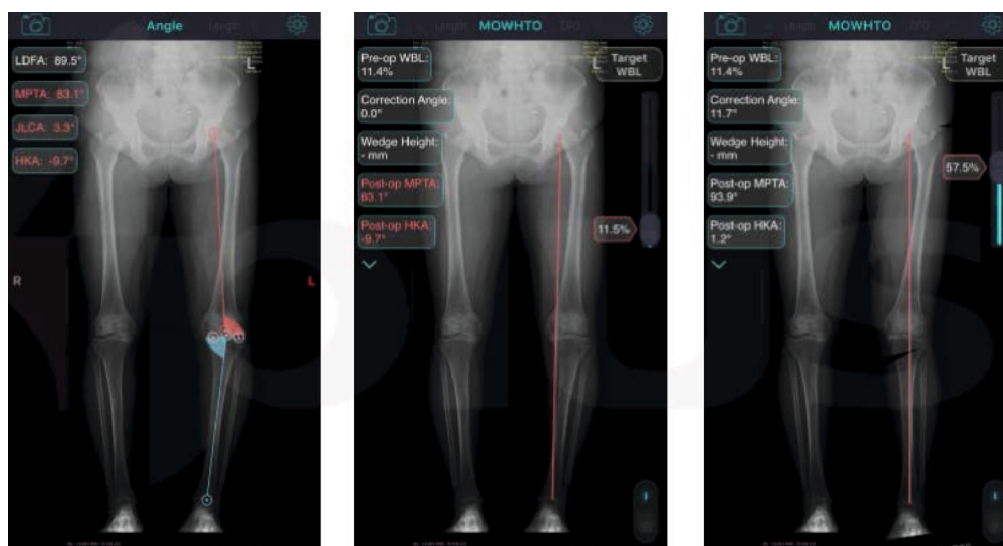
2.6. Statistical Analysis. All statistical tests were performed in Software Package for Social Sciences (SPSS) Statistics version 25.0. Categorical data were compared with Fisher exact tests. Continuous data were tested for normality and compared with either Student *t*-tests or Mann–Whitney tests depending on normality. A bivariate Spearman rank correlation was conducted to evaluate the relation between the mMPTA and mFTA in terms of effective correction. *P* values <0.05 were considered statistically significant.

3. Results

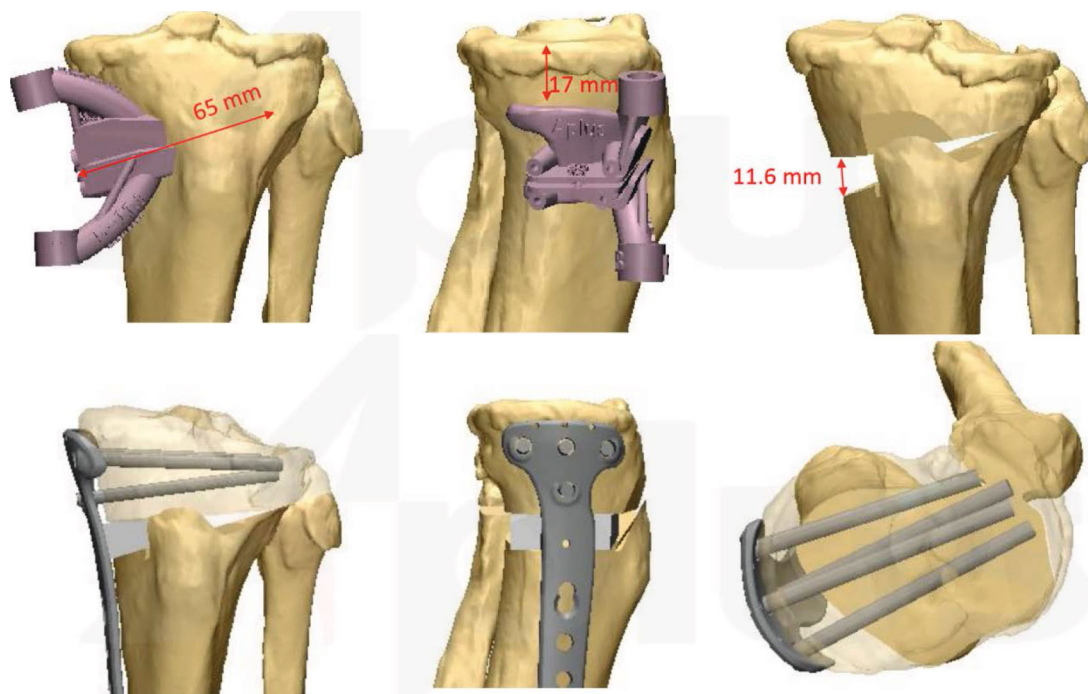
3.1. Radiological and Arthroscopic Outcomes. The postoperative full-length double-limb weight-bearing X-ray was regularly taken in all patients for the assessment of postoperative mFTA, mMPTA, and mLDFA. There were 3 patients in the 3D-printed PSI group and 4 patients in the



(a)



(b)



(c)

FIGURE 1: Continued.

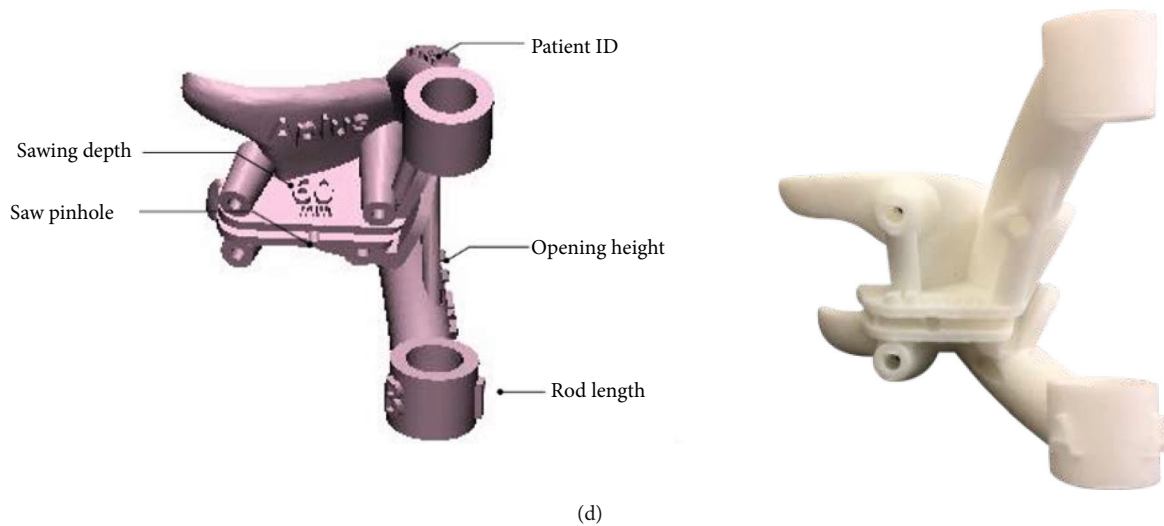


FIGURE 1: Female, 43 ys, suffered from left knee varus deformity, osteoarthritis (medial compartment, K-L III), and synovial chondromatosis (a). Preoperatively planned optimal mFTA and mMPTA were measured (b), osteotomy was simulated (c), and PSI was printed (d).

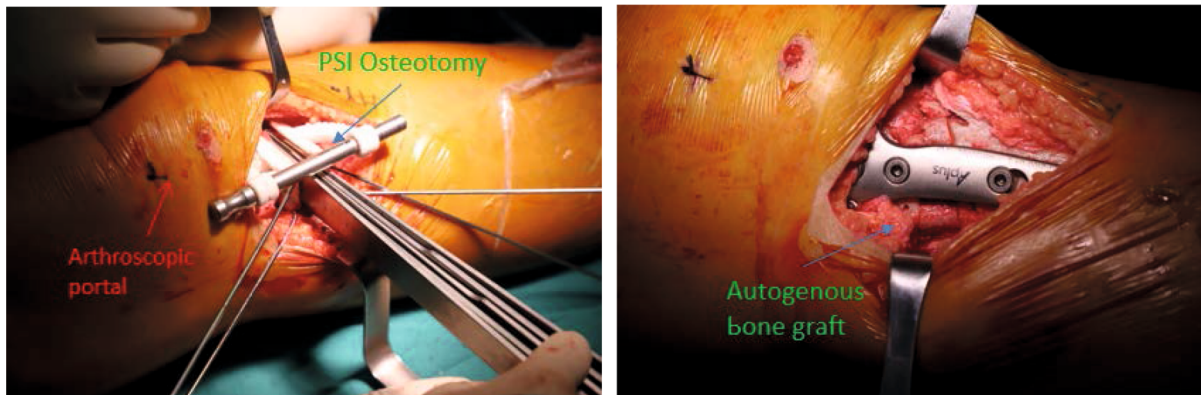


FIGURE 2: In operation, firstly, arthroscopic debridement of the synovial chondromatosis was conducted. Then, a two-planar osteotomy was performed, the wedge shape gap was widened and fixed at the predetermined angle via a metal bar stabilizer, and the locking plate was tightly fixed by screws. Autogenous bone grafting was implanted.

conventional group requested for the removal of the internal fixation; all plates and screws were successfully removed, and concomitant arthroscopies were conducted. In 1 patient of the 3D-printed PSI group, arthroscopic results showed the cartilage degeneration recovered from the preoperative Outerbridge grade III to the postoperative Outerbridge grade I (Figure 3).

3.2. *mFTA*. The mFTA was corrected from a preoperative mean angle of $172.2^\circ \pm 1.7^\circ$ to a postoperative mean angle of $180.7^\circ \pm 0.7^\circ$ in the 3D-printed PSI group and from a preoperative mean angle of $173.3^\circ \pm 1.7^\circ$ to a postoperative mean angle of $179.7^\circ \pm 1.8^\circ$ in the conventional group. The PSI group preoperative planning for mFTA is to be corrected to $180.5^\circ \pm 0.91^\circ$. The postoperative results showed there was a larger absolute mFTA in the 3D group than the conventional group ($P = 0.02$). The mFTA correction in the 3D-printed PSI group was $8.5^\circ \pm 1.9^\circ$, which is significantly higher than the conventional group with a correction of

$6.4^\circ \pm 1.90^\circ$ ($P = 0.0008$) (Table 2). When compared to the target mFTA in the preoperational planning, the 3D-printed PSI group had a significantly smaller correction error than the conventional group (0.2 ± 0.6 vs. 1.2 ± 1.4 , $P = 0.004$) (Figure 4).

3.3. *mMPTA*. The mMPTA was corrected from a preoperative mean angle of $86.3^\circ \pm 2.28^\circ$ to a postoperative mean angle of $91.2^\circ \pm 0.65^\circ$ in the 3D-printed PSI group and from a preoperative mean angle of $83.4^\circ \pm 2.15^\circ$ to a postoperative mean angle of $89.3^\circ \pm 2.13^\circ$ in the conventional group. The PSI group preoperative planning for mMPTA is to be corrected to $91.3^\circ \pm 0.87^\circ$. The postoperative results showed there was a larger absolute mMPTA in the 3D group than the conventional group ($P = 0.0002$). The mMPTA correction in the 3D-printed PSI group was $7.5^\circ \pm 2.16^\circ$, which is significantly higher than the conventional group with a correction of $5.9^\circ \pm 2.22^\circ$ ($P = 0.03$). When compared with the preoperative target mMPTA, there was a significantly smaller

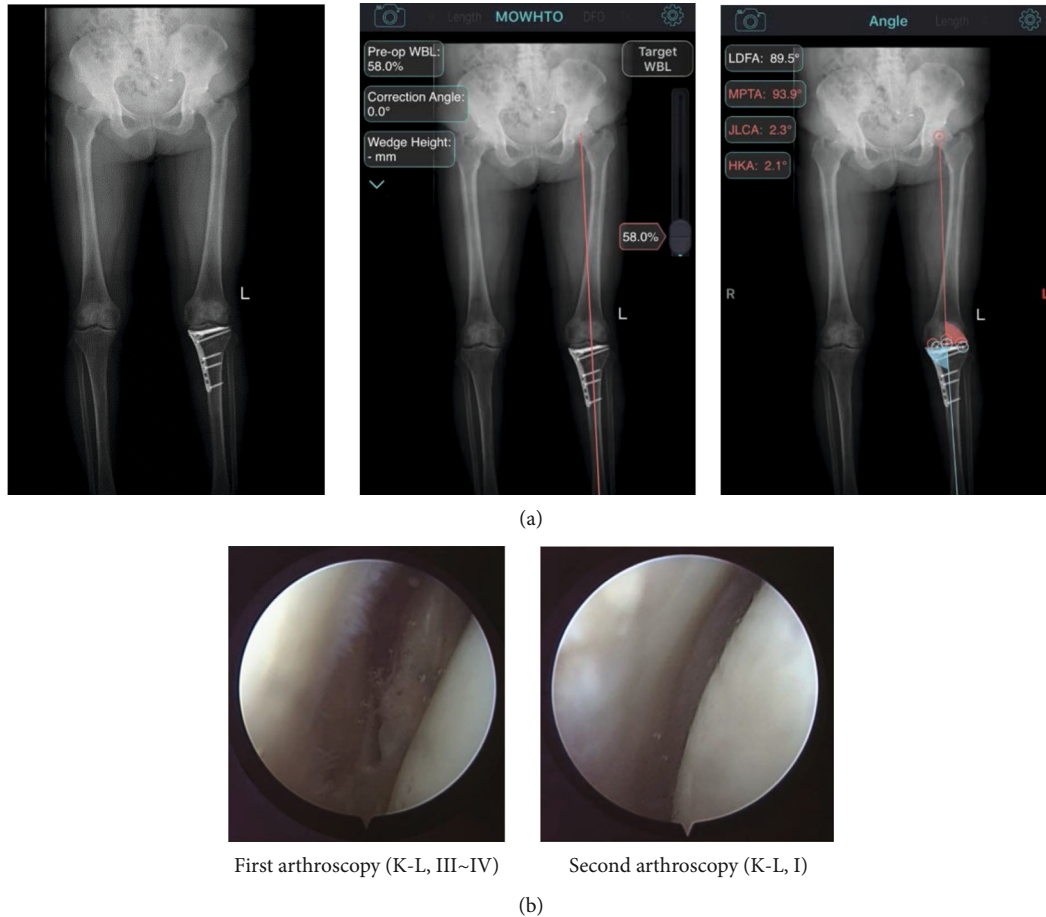


FIGURE 3: Full-length double-limb weight-bearing X-rays were taken for the assessment of the postoperative mFTA and mMPTA in the prementioned case, which were totally consistent with the target angles (a). The second arthroscopic look showed the cartilage degeneration recovered 18 months after surgery (b).

TABLE 2: Preoperative, target, and postoperative mFTA measured at double-limb full-length standing position X-ray.

| | 3D-printed PSI (<i>n</i> = 18) | Conventional (<i>n</i> = 19) | <i>P</i> value |
|------------------|------------------------------------|----------------------------------|-------------------|
| mFTA (°) | | | |
| Correction angle | 8.5 ± 1.9 | 6.4 ± 1.9 | <i>P</i> = 0.0008 |
| Correction error | 0.2 ± 0.6 | 1.2 ± 1.4 | <i>P</i> = 0.004 |

mFTA: mechanical femorotibial angle; 3D: three-dimensional; PSI: patient-specific instrumentation; $P_{pre} = 0.05$; $P_{target} = 0.15$; $P_{post} = 0.02$.

correction error in the PSI group than in the conventional group (0.1 ± 0.4 vs. 2.2 ± 1.8 , $P < 0.00001$) (Table 3) (Figure 5).

3.4. mL DFA. All patients in both groups did not meet the surgical indications for DFO. As for the preoperative and postoperative mL DFA in 3D-printed PSI group, the mean angles were $88.9^\circ \pm 1.86^\circ$ and $89.0^\circ \pm 1.82^\circ$, respectively; there was no significant change observed in this group. No significant changes were observed in the conventional group in terms of preoperative and postoperative mL DFA; the

mean angles were $89.4^\circ \pm 1.57$ and $88.8^\circ \pm 1.85$, respectively (Table 4).

3.5. Patient-Reported Outcomes and Clinical Outcomes. In every case, a successful surgical procedure was conducted, and no intraoperative complications were observed, while the exposures of intraoperative C-arm fluoroscopy in the PSI group (1.3 ± 0.12) were significantly smaller than the conventional group (4.1 ± 0.57) ($P < 0.00001$). Moreover, there was a significantly shorter time for the osteotomy procedure in the PSI group (37.8 ± 7.14) than in the conventional group (54.6 ± 11.72) ($P < 0.00001$), and this allowed more concomitant treatments. No significant differences were found in the VAS scores postoperatively at each time point (Figure 6); neither was found in hospitalization days. There were 2 patients in the conventional group caught up with lateral hinge fracture at the 1-month follow-up, delayed weight-bearing and moderate rehabilitation protocols were made for them. There were 3 patients in the conventional group and one patient in the PSI group detected to have intermuscular venous thrombosis by ultrasound postoperatively (color Doppler ultrasound examinations of the lower extremity were performed 3 days after surgery regularly); no special anticoagulant therapy was applied, and those

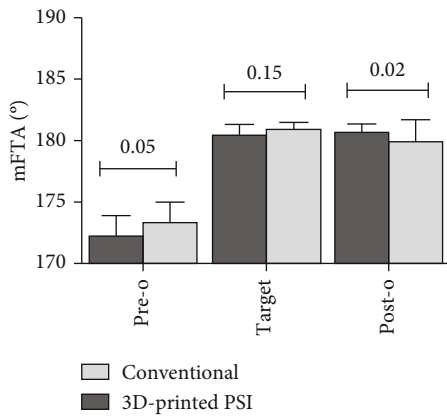


FIGURE 4: Preoperative, target, and postoperative mFTA measured at double-limb full-length standing position X-ray. mFTA: mechanical femorotibial angle; 3D: three-dimensional; PSI: patient-specific instrumentation; $P_{pre} = 0.05$; $P_{target} = 0.15$; $P_{post} = 0.02$.

TABLE 3: Preoperative, target, and postoperative mMPTA measured at double-limb full-length standing position X-ray.

| | 3D-printed PSI (n = 18) | Conventional (n = 19) | P value |
|------------------|-------------------------|-----------------------|---------------|
| mMPTA (°) | | | |
| Correction angle | 7.5 ± 2.2 | 5.9 ± 2.2 | $P = 0.03$ |
| Correction error | 0.1 ± 0.4 | 2.2 ± 1.8 | $P < 0.00001$ |

mMPTA: mechanical medial proximal tibial angle; 3D: three-dimensional; PSI: patient-specific instrumentation; $P_{pre} = 0.79$; $P_{target} = 0.45$; $P_{post} = 0.0002$.

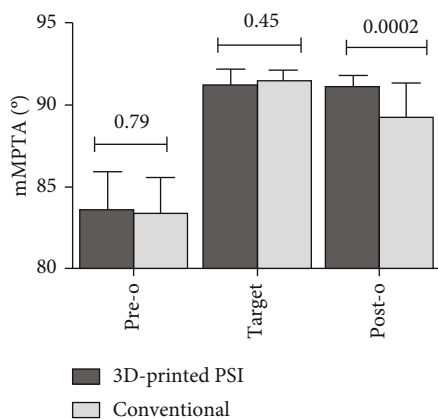


FIGURE 5: Preoperative, target, and postoperative mMPTA measured at double-limb full-length standing position X-ray. mMPTA: mechanical medial proximal tibial angle; 3D: three-dimensional; PSI: patient-specific instrumentation; $P_{pre} = 0.79$; $P_{target} = 0.45$; $P_{post} = 0.0002$.

patients were asymptomatic at each follow-up. Minor local infection signs were found in one PSI patient at the osteotomy site, which was probably caused by allogenic bone graft;

TABLE 4: mL DFA.

| | 3D-printed PSI (n = 18) | Conventional (n = 19) |
|---------------|-------------------------|-----------------------|
| mL DFA (°) | | |
| Preoperative | 88.9 ± 1.86 | 89.4 ± 1.57 |
| Postoperative | 89.0 ± 1.82 | 88.8 ± 1.85 |
| P value | n.s | n.s |

Abbreviations: mFTA: mechanical femorotibial angle; mMPTA: medial mechanical proximal tibial angle; mL DFA: mechanical lateral distal femoral angle; n.s: not significant; 3D: three-dimensional; PSI: patient-specific instrumentation.

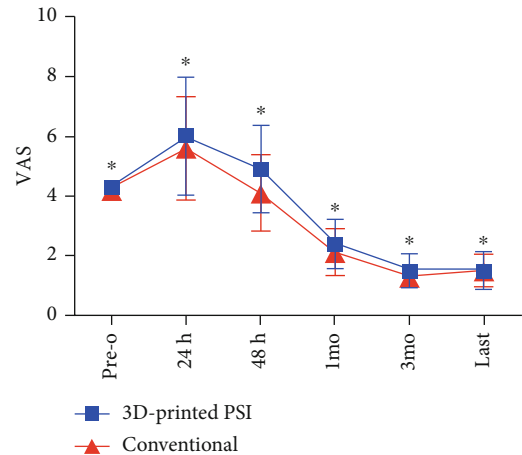


FIGURE 6: VAS at preoperative, 24 h, 48 h, 1 month, 3 months, and last follow-up after the operation. VAS: visual analogue scale (VAS; with 0, no pain, to 100, the worst imaginable pain); 3D: three-dimensional; PSI: patient-specific instrumentation; * $P > 0.05$; Pre-o: preoperative.

the infection was controlled by antibiotics and immobilization. One patient in the conventional group had a postoperative intra-articular infection, debridement under arthroscopy was conducted, adequate drainage and antibiotic therapy were also applied, and the patient fully recovered afterwards (Table 5).

As for patient-reported functional measurements, there were significantly higher scores observed in the 3D-printed PSI group than the conventional group in terms of both subjective IKDC score (76.6 ± 7.9 vs. 69.1 ± 9.6, $P = 0.009$) and Lysholm score (76.4 ± 8.9 vs. 70.4 ± 7.8, $P = 0.03$) at the 3-month follow-up. No significant differences regarding both the IKDC scores and Lysholm scores were noticed between the two groups at other times of follow-up (Figures 7 and 8).

4. Discussion

The goal of MOWHTO is to change the abnormal load of the medial knee compartment in patients with varus deformity and prevent the further development of osteoarthritis [26–28]. By correcting the alignment, MOWHTO evenly distributed the excessive load from the lower medial compartment to the whole articular surface [12, 28]. The general aim was to bring the weight-bearing axis to 62.5% of

TABLE 5: Clinical outcomes.

| | 3D-printed PSI | Conventional | P value |
|--|----------------|--------------|---------------|
| Feasibility | | | |
| Operation time of osteotomy (min) | 37.8 ± 7.14 | 54.6 ± 11.72 | $P < 0.00001$ |
| Radiation exposures (n) | 1.3 ± 0.12 | 4.1 ± 0.57 | $P < 0.00001$ |
| Hospitalization (d) | 5.6 ± 1.28 | 6.2 ± 1.34 | n.s |
| Bone graft | 2.1 ± 0.33 | 2.2 ± 0.37 | n.s |
| Complications (n) | | | |
| Displaced (>2 mm) lateral hinge fracture | 0 | 0 | — |
| Undisplaced (<2 mm) lateral hinge fracture | 0 | 2 | — |
| Deep vein thrombosis | 1 | 3 | — |
| Infection | 1 | 1 | — |
| Hardware failure | 0 | 0 | — |

Abbreviations: VAS: visual analogue score; n.s: not significant; 3D: three-dimensional; PSI: patient-specific instrumentation.

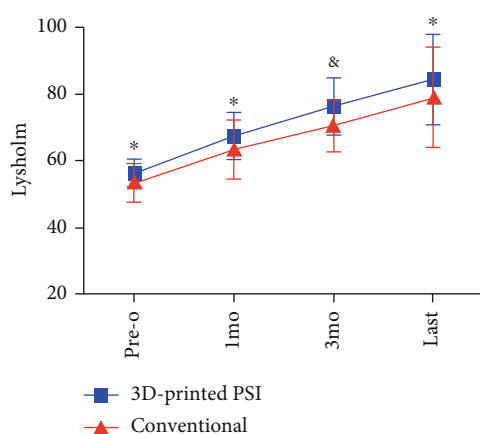


FIGURE 7: Preoperative and postoperative Lysholm scores at 1 month, 3 months, and last follow-up. 3D: three-dimensional; PSI: patient-specific instrumentation; pre-o: preoperative; mo: month.

* $P_{\text{pre-o,1mo,last}} > 0.05$. & $P_{3\text{mo}} = 0.03$.

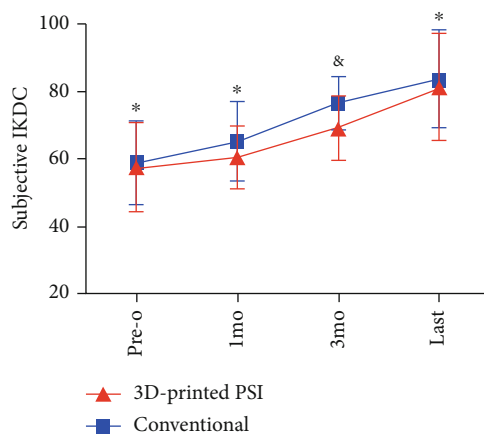


FIGURE 8: Preoperative and postoperative subjective IKDC scores at 1 month, 3 months, and last follow-up. 3D: three-dimensional; PSI: patient-specific instrumentation; pre-o: preoperative; mo: month.

* $P_{\text{pre-o,1mo,last}} > 0.05$. & $P_{3\text{mo}} = 0.009$.

the proximal tibia width [29], but more recent biomechanical and clinical studies advocate a less aggressive overcorrection [6, 30, 31]. In this study, a 55%~60% proximal tibial width as the target weight-bearing axis was chosen. On the purpose of preserving a native knee joint, MOWHTO is an effective procedure of postponing the requirement of partial or total knee arthroplasty [7, 32] and creates the probability of cartilage recovery. The precision of the osteotomy is one of the cornerstones for successful OWHTO surgery. Conventional HTO planning and execution is commonly performed on two-dimensional radiographs [33] (X-rays, C-arm), and in face of deformities on both sagittal and coronal planes, the traditional technique seems to be incompetent and prone to error [34]. Moreover, the hip-knee-ankle angle (HKA), which is used to plan HTO, was reported to be inconsistent preoperatively, intraoperatively, and postoperatively in most cases [35, 36]; this is due to the variation in both knee rotation and flexion under different circumstances. In the era of precision medicine, the lack of consistency in conventional MOWHTO is probably the biggest barrier for this technique to become widely accepted [17].

The most important finding of this study is that this novel 3D-printed PSI technique is capable of delivering a higher level of accuracy in angular correction than conventional techniques. By the hand of an experienced surgeon, though the postoperative mFTAs of the conventional HTO also achieved the “acceptable range” (valgus from 3° to 6°) mentioned by Hernigou et al. [37]; nevertheless, there was a significantly shorter operation duration in the PSI group than the conventional technique. In addition to the improvement of accuracy and surgical duration, the PSI technique is a safer approach with higher feasibility for fewer complications and adverse events occurred in the 3D-printed PSI group, and there was a lower dosage of radiation brought by intraoperative C-arm scanning. These merits not only allow more concomitant treatment procedures (debridement, meniscectomy, ACLR, etc.) but also ensure enhanced recovery after surgery. To our knowledge, only a few studies have been reporting feasibility and accuracy outcomes about the clinical use of PSI in

osteotomy around the knee [5, 15, 17, 19, 20, 22]. In the study by Van Genechten et al. [5], the two planar MOWHTOs were performed in a relatively conventional manner (freehand), while a PSI 3D-printed wedge and cast were adopted instead of the HTO plate. Interestingly, they also got excellent correction outcomes; this precision was achieved by the patient-specific wedge model fixation rather than the osteotomy procedure itself. As such, the accuracy of the precised MOWHTO can be achieved in more than one way with the assistance of the PSI 3D-printed technique. In earlier laboratory studies, the finite element analysis (FEA) model by Chieh-Szu et al. [21] indicated there was a significant reduction of compressive load on the tibial plateau in their PSI osteotomy knees when compared with conventional ones (78.8 MPa vs. 91.9 MPa, under 600-N force); it revealed the PSI technique was capable of improving the structural stability, and this novel approach may have the potential to reduce the incidence of hardware dislocation and hinge fractures. In all, although the techniques of PSI and execution of related HTOs varied greatly, the outcomes turned favourable for PSI 3D-printed technique in all existing studies. However, the accuracy and clinical advantage of PSI over the conventional surgical methodology in MOWHTO still needs to be proven in large comparative studies with long-term follow-up.

Moreover, the effective treatment for knee OA is not merely about the correction of malalignment; further attention should be paid to the intra-articular illness. A visual assessment under arthroscopy can provide a more effective diagnosis of cartilage degeneration. In addition, treatment for the concomitant disease of OA (such as loose body, synovitis, meniscus injury, and ACLR) can also be practiced arthroscopically. A comprehensive surgical treatment merits further focus; we should not be limited to isolated osteotomy. Besides, to obtain robust immediate postoperative stability and biomechanics, autogenous bone grafting was recommended in cases with the wedge opening higher than 10 mm, and a crossing screw may also be considered; thus, enhanced recovery after surgery can be achieved.

5. Conclusion

With the assistance of 3D-printed PSI, a safe and feasible MOWHTO can be conducted with superior accuracy than the conventional techniques. The combination of precise 3D osteotomy cutting guide model contributed to a more accurate translation from planning to surgery, and a shorter operation duration created the opportunities for more concomitant treatments.

Data Availability

The results in this study are available from the corresponding author on reasonable request.

Conflicts of Interest

There are no conflicts of interest.

Authors' Contributions

Yunhe Mao and Yan Xiong are co-first authors. Jian Li is the corresponding author.

Acknowledgments

This study was supported by the 1.3.5 project for disciplines of excellence, West China Hospital, Sichuan University.

References

- [1] M. Darees, S. Putman, T. Brosset, T. Roumazielle, G. Pasquier, and H. Migaud, "Opening-wedge high tibial osteotomy performed with locking plate fixation (TomoFix) and early weight-bearing but without filling the defect. A concise follow-up note of 48 cases at 10 years' follow-up," *Orthopaedics & Traumatology, Surgery & Research*, vol. 104, no. 4, pp. 477–480, 2018.
- [2] M. E. Hantes, P. Natsaridis, A. A. Koutalos, Y. Ono, N. Doxariotis, and K. N. Malizos, "Satisfactory functional and radiological outcomes can be expected in young patients under 45 years old after open wedge high tibial osteotomy in a long-term follow-up," *Knee Surgery, Sports Traumatology, Arthroscopy*, vol. 26, no. 11, pp. 3199–3205, 2018.
- [3] R. R. Bannuru, M. C. Osani, E. E. Vaysbrot et al., "OARS guidelines for the non-surgical management of knee, hip, and polyarticular osteoarthritis," *Osteoarthritis and Cartilage*, vol. 27, no. 11, pp. 1578–1589, 2019.
- [4] M. Van den Bempt, W. Van Genechten, T. Claes, and S. Claes, "How accurately does high tibial osteotomy correct the mechanical axis of an arthritic varus knee? A systematic review," *The Knee*, vol. 23, no. 6, pp. 925–935, 2016.
- [5] W. van Genechten, W. van Tilborg, M. Van den Bempt, A. Van Haver, and P. Verdonk, "Feasibility and 3D Planning of a Novel Patient-Specific Instrumentation Technique in Medial Opening-Wedge High Tibial Osteotomy," *The Journal of Knee Surgery*, 2020.
- [6] J. L. Martay, A. J. Palmer, N. K. Bangerter et al., "A preliminary modeling investigation into the safe correction zone for high tibial osteotomy," *The Knee*, vol. 25, no. 2, pp. 286–295, 2018.
- [7] J. F. Konopka, A. H. Gomoll, T. S. Thornhill, J. N. Katz, and E. Losina, "The cost-effectiveness of surgical treatment of medial unicompartmental knee osteoarthritis in younger patients," *The Journal of Bone and Joint Surgery. American Volume*, vol. 97, no. 10, pp. 807–817, 2015.
- [8] R. Martin, T. B. Birmingham, K. Willits, R. Litchfield, M. E. Lebel, and J. R. Giffin, "Adverse event rates and classifications in medial opening wedge high tibial osteotomy," *The American Journal of Sports Medicine*, vol. 42, no. 5, pp. 1118–1126, 2014.
- [9] D. W. Elson, "The surgical accuracy of knee osteotomy," *The Knee*, vol. 24, no. 2, pp. 167–169, 2017.
- [10] Z. P. Wu, P. Zhang, J. Z. Bai et al., "Comparison of navigated and conventional high tibial osteotomy for the treatment of osteoarthritic knees with varus deformity: a meta-analysis," *International Journal of Surgery*, vol. 55, pp. 211–219, 2018.
- [11] S. B. Han, D. H. Lee, G. M. Shetty, D. J. Chae, J. G. Song, and K. W. Nha, "A "safe zone" in medial open-wedge high tibia osteotomy to prevent lateral cortex fracture," *Knee Surg Sports Traumatol Arthrosc*, vol. 21, no. 1, pp. 90–95, 2013.

- [12] T. R. Sprenger and J. F. Doerzbacher, "Tibial osteotomy for the treatment of varus gonarthrosis. Survival and failure analysis to twenty-two years," *The Journal of Bone and Joint Surgery. American Volume*, vol. 85, no. 3, pp. 469–474, 2003.
- [13] G. G. Jones, M. Jaere, S. Clarke, and J. Cobb, "3D printing and high tibial osteotomy," *EFORT Open Rev*, vol. 3, no. 5, pp. 254–259, 2018.
- [14] D. P. Sarment, K. Al-Shammari, and C. E. Kazor, "Stereolithographic surgical templates for placement of dental implants in complex cases," *The International Journal of Periodontics & Restorative Dentistry*, vol. 23, no. 3, pp. 287–295, 2003.
- [15] H. J. Kim, J. Park, J. Y. Shin, I. H. Park, K. H. Park, and H. S. Kyung, "More accurate correction can be obtained using a three-dimensional printed model in open-wedge high tibial osteotomy," *Knee Surgery, Sports Traumatology, Arthroscopy*, vol. 26, no. 11, pp. 3452–3458, 2018.
- [16] S. Lu, Y. Z. Zhang, Z. Wang et al., "Accuracy and efficacy of thoracic pedicle screws in scoliosis with patient-specific drill template," *Medical & Biological Engineering & Computing*, vol. 50, no. 7, pp. 751–758, 2012.
- [17] J. Victor and A. Premanathan, "Virtual 3D planning and patient specific surgical guides for osteotomies around the knee," *Bone Joint J*, vol. 95-b, 11_Supple_A, pp. 153–158, 2013.
- [18] M. Donnez, M. Ollivier, M. Munier et al., "Are three-dimensional patient-specific cutting guides for open wedge high tibial osteotomy accurate? An in vitro study," *Journal of Orthopaedic Surgery and Research*, vol. 13, no. 1, p. 171, 2018.
- [19] M. Munier, M. Donnez, M. Ollivier et al., "Can three-dimensional patient-specific cutting guides be used to achieve optimal correction for high tibial osteotomy? Pilot study," *Orthopaedics & Traumatology, Surgery & Research*, vol. 103, no. 2, pp. 245–250, 2017.
- [20] R. Pérez-Mañanes, J. Burró, J. Manaute, F. Rodriguez, and J. Martín, "3D Surgical Printing Cutting Guides for Open-Wedge High Tibial Osteotomy: Do It Yourself," *The Journal of Knee Surgery*, vol. 29, no. 8, pp. 690–695, 2016.
- [21] J. Chieh-Szu Yang, C. F. Chen, and O. K. Lee, "Benefits of opposite screw insertion technique in medial open-wedge high tibial osteotomy: a virtual biomechanical study," *J Orthop Translat*, vol. 20, pp. 31–36, 2020.
- [22] J. C.-S. Yang, C.-F. Chen, C.-A. Luo et al., "Clinical Experience Using a 3D-Printed Patient-Specific Instrument for Medial Opening Wedge High Tibial Osteotomy," *BioMed Research International*, vol. 2018, Article ID 9246529, 9 pages, 2018.
- [23] L. Sharma, J. Song, D. T. Felson, S. Cahue, E. Shamiyeh, and D. D. Dunlop, "The role of knee alignment in disease progression and functional decline in knee osteoarthritis," *JAMA*, vol. 286, no. 2, pp. 188–195, 2001.
- [24] J. J. Irrgang, A. F. Anderson, A. L. Boland et al., "Development and Validation of the International Knee Documentation Committee Subjective Knee Form," *The American Journal of Sports Medicine*, vol. 29, no. 5, pp. 600–613, 2017.
- [25] L. D. Higgins, M. K. Taylor, D. Park et al., "Reliability and validity of the international knee documentation committee (IKDC) subjective knee form," *Joint, Bone, Spine*, vol. 74, no. 6, pp. 594–599, 2007.
- [26] G. Bauer, J. Insall, and T. Koshino, "Tibial osteotomy in gonarthrosis (osteo-arthritis of the knee)," *The Journal of Bone and Joint Surgery. American Volume*, vol. 51, no. 8, pp. 1545–1563, 1969.
- [27] J. N. Insall, D. M. Joseph, and C. Msika, "High tibial osteotomy for varus gonarthrosis. A long-term follow-up study," *The Journal of Bone and Joint Surgery. American Volume*, vol. 66, no. 7, pp. 1040–1048, 1984.
- [28] K. Yasuda, T. Majima, T. Tsuchida, and K. Kaneda, "A ten- to 15-year follow-up observation of high tibial osteotomy in medial compartment osteoarthritis," *Clin Orthop Relat Res*, no. 282, pp. 186–195, 1992.
- [29] T. H. O. M. A. S. W. DUGDALE, F. R. A. N. K. R. NOYES, and D. A. V. I. D. STYER, "Preoperative Planning for High Tibial osteotomy. The effect of lateral tibiofemoral separation and tibiofemoral length," *Clinical Orthopaedics and Related Research*, no. 274, pp. 248–264, 1992.
- [30] J. C. Stanley, K. G. Robinson, B. M. Devitt et al., "Computer assisted alignment of opening wedge high tibial osteotomy provides limited improvement of radiographic outcomes compared to fluoroscopic alignment," *The Knee*, vol. 23, no. 2, pp. 289–294, 2016.
- [31] G. J. van de Pol, N. Verdonshot, and A. van Kampen, "The value of the intra-operative clinical mechanical axis measurement in open-wedge valgus high tibial osteotomies," *The Knee*, vol. 19, no. 6, pp. 933–938, 2012.
- [32] W. B. Smith II, J. Steinberg, S. Scholtes, and I. R. Mcnamara, "Medial compartment knee osteoarthritis: age-stratified cost-effectiveness of total knee arthroplasty, unicompartamental knee arthroplasty, and high tibial osteotomy," *Knee Surgery, Sports Traumatology, Arthroscopy*, vol. 25, no. 3, pp. 924–933, 2017.
- [33] J. Brinkman, P. Lobenhoffer, J. Agneskirchner, A. Staubli, A. Wymenga, and R. van Heerwaarden, "Osteotomies around the knee: patient selection, stability of fixation and bone healing in high tibial osteotomies," *The Journal of Bone and Joint Surgery. British Volume*, vol. 90, no. 12, pp. 1548–1557, 2008.
- [34] H. Kawakami, N. Sugano, K. Yonenobu et al., "Effects of rotation on measurement of lower limb alignment for knee osteotomy," *Journal of Orthopaedic Research*, vol. 22, no. 6, pp. 1248–1253, 2004.
- [35] T. Koshino, M. Takeyama, L. S. Jiang, T. Yoshida, and T. Saito, "Underestimation of varus angulation in knees with flexion deformity," *The Knee*, vol. 9, no. 4, pp. 275–279, 2002.
- [36] K. E. Swanson, G. W. Stocks, P. D. Warren, M. R. Hazel, and H. F. Janssen, "Does axial limb rotation affect the alignment measurements in deformed limbs?," *Clin Orthop Relat Res*, vol. 371, no. 371, pp. 246–252, 2000.
- [37] P. Hernigou, D. Medevielle, J. Debeyre, and D. Goutallier, "Proximal tibial osteotomy for osteoarthritis with varus deformity. A ten to thirteen-year follow-up study," *The Journal of Bone and Joint Surgery. American Volume*, vol. 69, no. 3, pp. 332–354, 1987.

Research Article

Influence of the Postcuring Process on Dimensional Accuracy and Seating of 3D-Printed Polymeric Fixed Prostheses

Jaewon Kim¹ and Du-Hyeong Lee² 

¹Department of Periodontics and Endodontics, School of Dental Medicine, University at Buffalo, New York, USA

²Department of Prosthodontics, School of Dentistry, Institute for Translational Research in Dentistry, Kyungpook National University, Daegu 41940, Republic of Korea

Correspondence should be addressed to Du-Hyeong Lee; dewylee@knu.ac.kr

Received 17 June 2020; Revised 17 September 2020; Accepted 9 November 2020; Published 16 November 2020

Academic Editor: Xiaojun Duan

Copyright © 2020 Jaewon Kim and Du-Hyeong Lee. This is an open access article distributed under the Creative Commons Attribution License, which permits unrestricted use, distribution, and reproduction in any medium, provided the original work is properly cited.

The postcuring process is essential for 3-dimensional (3D) printing of photopolymer-based dental prostheses. However, the deformation of prostheses resulting from the postcuring process has not been fully investigated. The purpose of this study was to evaluate the effects of different postcuring methods on the fit and dimensional accuracy of 3D-printed full-arch polymeric fixed prostheses. A study stone model with four prosthetic implant abutments was prepared. A full-arch fixed dental prosthesis was designed, and the design was transferred to dental computer-aided manufacturing (CAM) software in which supports were designed to the surface of the prosthesis design for 3D printing. Using a biocompatible photopolymer and a stereolithography apparatus 3D printer, polymeric prostheses were produced ($N = 21$). In postcuring, the printed prostheses were polymerized in three different ways: the prosthesis alone, the prosthesis with supports, or the prosthesis on a stone model. Geometric accuracy of 3D-printed prostheses, marginal gap, internal gap, and intermolar distance was evaluated using microscopy and digital techniques. Kruskal-Wallis and Mann-Whitney U tests with Bonferroni correction were used for the comparison of results among groups ($\alpha = 0.05$). In general, the mean marginal and internal gaps of cured prostheses were the smallest when the printed prostheses were cured with seating on the stone model ($P < 0.05$). With regard to the adaptation accuracy, the presence of supports during the postcuring process did not make a significant difference. Error in the intermolar distance was significantly smaller in the model seating condition than in the other conditions ($P < 0.001$). Seating 3D-printed prosthesis on the stone model reduces adverse deformation in the postcuring process, thereby enabling the fabrication of prostheses with favorable adaptation.

1. Introduction

Interim fixed dental prostheses are usually made in clinics with autopolymerizing acrylic resins [1, 2]. This conventional manual methodology is still the mainstream approach in fabricating fixed prosthodontics but is labor-intensive and uncomfortable for patients because the direct fabrication of prostheses is performed inside the patient's mouth, and heating occurs during polymerization. Because of these drawbacks, digital scanning and computer-aided design/computer-aided manufacturing (CAD/CAM) technologies are increasingly being used to fabricate interim polymeric prostheses [3, 4]. The oral anatomic shape is

virtually registered using an optical scanner, and the scan data are imported into dedicated dental CAD software, in which the cementation space of the prosthetic crown is set and a final prosthesis is designed [5]. The design is then transferred to CAM software where the 3D image is divided into 2D cross-sectional images and processed to the polymeric prosthesis using additive manufacturing technologies [6]. The final fabrication process is the postcuring treatment of the printed prosthesis [6].

The 3D printing technologies have diversified treatment procedures and have become an alternative to manual and subtractive methods in medical and dental fields [7–10]. There are several different ways to print polymeric

prostheses, such as stereolithography apparatus (SLA), digital light processing, fused deposition modeling, and polymer jetting [11, 12]. The SLA printing method uses liquid photopolymer, and objects are built layer-by-layer using site-specific polymerization by an ultraviolet laser [13]. For the production of interim dental prostheses via SLA printing, several photocurable resins are available and approved for long-term intraoral use [6, 14]. Commonly used acrylic resins could be cytotoxic to the human body in the uncured state [15], but the biocompatibility significantly improves after postcuring and cleaning in the 3D-printed objects [6, 16]. The quality of 3D-printed objects significantly varies depending on operational parameters, fabrication workflow, materials, and devices [16, 17]. The contemporary 3D-printed polymers for interim dental applications exhibit low anisotropy and appropriate properties required for the end product [6, 14]. The mechanical and physicochemical properties of photopolymers available on the market are reported to be comparable to those of conventional autopolymerizing acrylic resins [6, 8].

The postcuring process increases the degree of polymerization of the printed object, which affects the final mechanical properties and the amount of the object's residual monomer [6, 14, 16]. However, postcuring can also cause dimensional deformation in the general structure and warping in any thin areas of an object because of the inherent change of the chemical bonds during polymerization [18]. Although the postcuring process is essential for the photopolymer-based 3D printing of dental prostheses, whether or not different postcuring methods affect the geometric accuracy of the prosthesis has not been fully investigated. The purpose of this study was to evaluate the effects of different postcuring conditions on the geometric accuracy of fabrication of full-arch polymeric fixed prostheses that were created using SLA 3D printing. The adaptation of prostheses on abutments and dimensional deformation were assessed by means of a marginal gap, internal gap, and intermolar distance. The null hypothesis was that the differences in the postcuring methods for printed polymeric prostheses would not affect the accuracy of their fabrication.

2. Materials and Methods

2.1. Fabrication of the Study Model and Full-Arch Polymeric Prostheses. The overall study procedure is described in Figure 1. The edentulous study stone model was prepared, with four prosthetic implant abutments (FreeForm ST; Osstem, Seoul, Korea) that were connected to implants (USII; Osstem) placed in the canine and second premolar areas. A virtual model was created by digitizing the surface of the stone model using a laboratory-based scanner (IDC S1; Amann Girrbach, Koblach, Austria) and was transferred to a dental design software program (R2CAD; MegaGen, Daegu, Korea), which designed a 12-unit implant-supported fixed dental prosthesis (Figure 2). The design file was transferred to a CAM software program for 3D printing (Raydent Studio; Ray, Hwaseong-si, Korea), in which supports were installed on the occlusal surface of the prosthesis design (Figure 3). Subsequently, interim acrylic prostheses

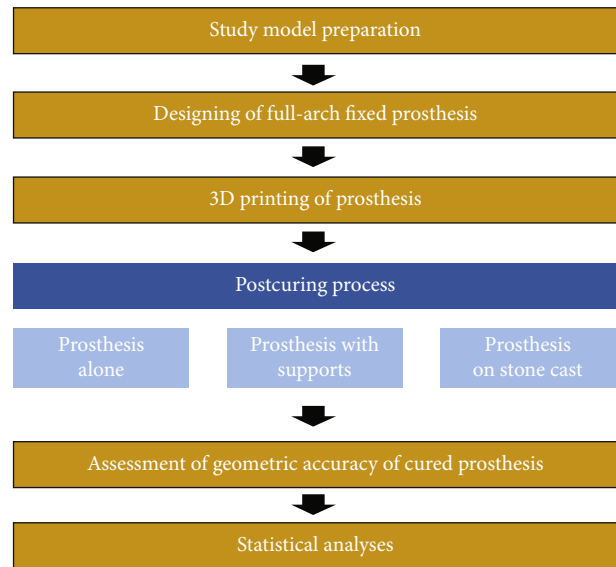


FIGURE 1: Workflow of this study.

were produced by printing a biocompatible photopolymer (Raydent C&B; Ray) in a SLA 3D printer (Meg-Printer II; MegaGen) with a layering thickness of $50\ \mu\text{m}$ and with a wavelength of $405\ \text{nm}$ (Table 1). The printed prostheses were then rinsed thoroughly under running water and spray dried at room temperature according to the manufacturer's instructions.

2.2. Postcuring Process of 3D-Printed Prostheses. In the postcuring procedure, the printed prostheses were polymerized in an ultraviolet curing unit of the 3D printer for 15 minutes with a wavelength of $395\ \text{nm}$ and radiation power at $60\ \text{mW}/\text{cm}^2$. Three different methods were used for the postcuring procedure ($n = 7$ in each group; $N = 21$) (Figure 4): prosthesis alone (P group), prosthesis with supports (PS group), and prosthesis on the stone model (PM group). In the P group, supports were removed from the printed prosthesis using a cutter, and postcuring was performed. In the PS group, the prosthesis was cured without removing the supports. In the PM group, supports were removed, and the printed prosthesis was seated on the prosthetic abutments of a stone model, and then, the postcuring was performed. For random sampling, the printed prostheses were allocated to each group consecutively in the order of fabrication. All 3D printing and postcuring processes were performed by a single operator (D.H.L.).

2.3. Evaluation of Fabrication Accuracy of Prostheses. The geometric accuracy of 3D-printed prostheses was evaluated using a vertical marginal gap, internal gap, and intermolar distance. For the marginal gap assessment, the cured prosthesis was passively fitted on the stone model, and the model with prosthesis was positioned perpendicular to the table of the stereomicroscope (EGVM-452M; EG Tech, Seoul, Korea) using utility wax. The midbuccal and lingual margin areas in all abutments were then imaged three times at a magnification of $60\times$ with the stereomicroscope, and each value was

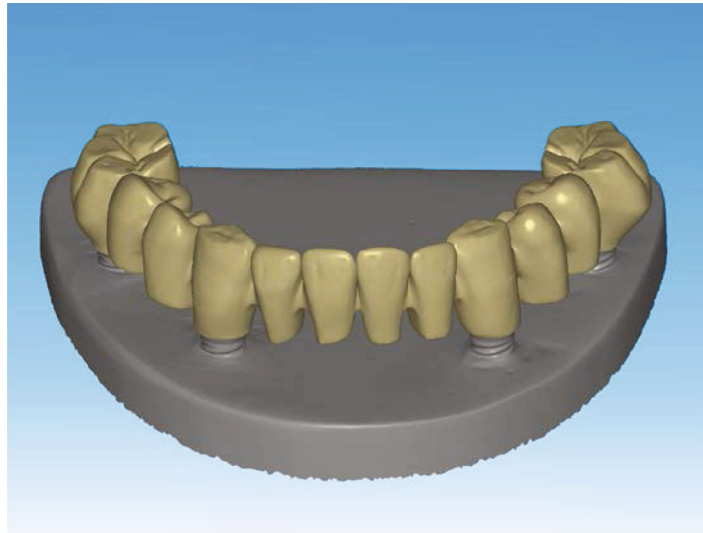


FIGURE 2: Design of implant-supported full-arch fixed dental prosthesis.

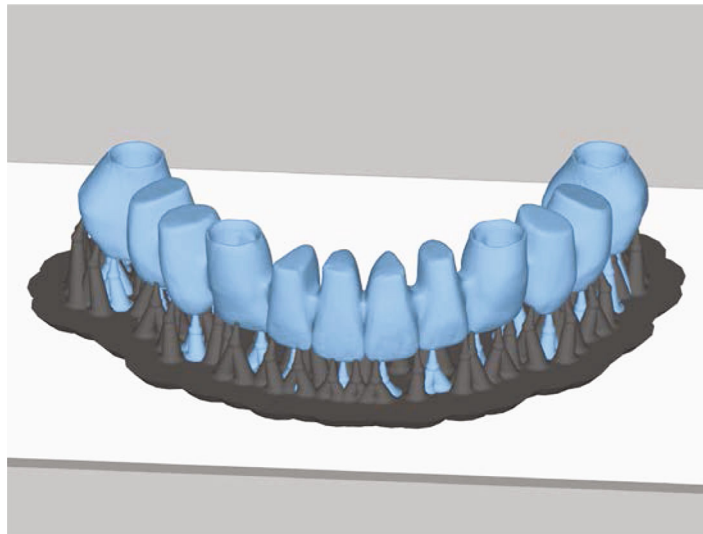


FIGURE 3: Insertion of support structures into the prosthesis design for the 3D printing procedure.

TABLE 1: Composition of photopolymer used*.

| Component | CAS No. | % |
|--|-------------|---------|
| α, α' -[[1-Methylethylidene)di-4,1-phenylene]bis[ω -[(2-methyl-1-oxo-2-propenyl)oxy]poly(oxy-1,2-ethanediyl) | 41637-38-1 | 20~35 |
| 7,7,9(or 7,9,9)-Trimethyl-4,13-dioxo-3,14-dioxa-5,12-diazahexadecane-1,16-diyl 2-methyl-2-propenoate | 72869-86-4 | 20~28 |
| 2-Methyl-2-propenoic acid 1,2-ethanediylbis(oxy-2,1-ethanediyl) ester | 109-16-0 | 20~25 |
| Phenylbis(2,4,6-trimethylbenzoyl)phosphine oxide | 162881-26-7 | 1~10 |
| Rutile (TiO ₂) | 1317-80-2 | 0.1 ~ 5 |

*Manufacturer's information.

determined by averaging three measurements. The measurement value was defined as the vertical marginal discrepancy that was vertical marginal misfit measured parallel to the path of draw of the prosthesis [19]. For the internal gap assessment, a triple-scan technique was used, with three digital scans taken using a structured light scanner (Breuck-

mann SmartScan; AICON 3D Systems GmbH, Braunschweig, Germany) [5]. The first scan was of the cured prosthesis alone, the second was of the study model, and the third was of the prosthesis on the study model. The data of the three scans were delivered to an image analysis software program (Geomagic DesignX; 3D Systems, Rock Hill, SC,

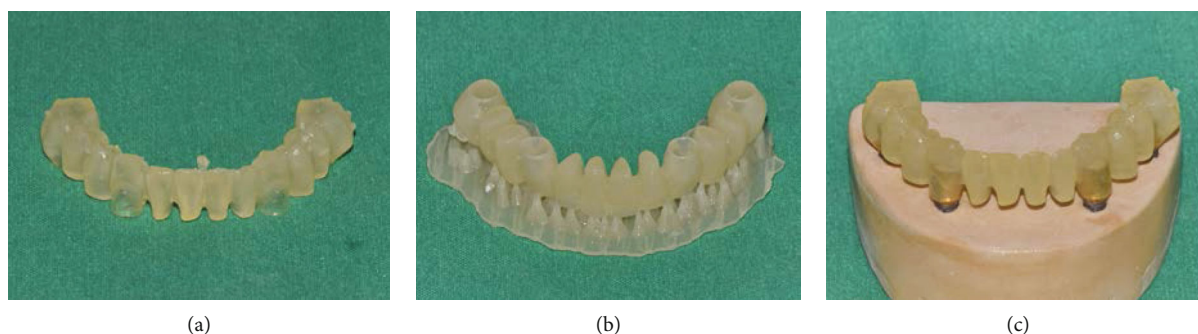


FIGURE 4: Postcuring methods: (a) prosthesis alone, (b) prosthesis with supports, and (c) prosthesis on the stone model.

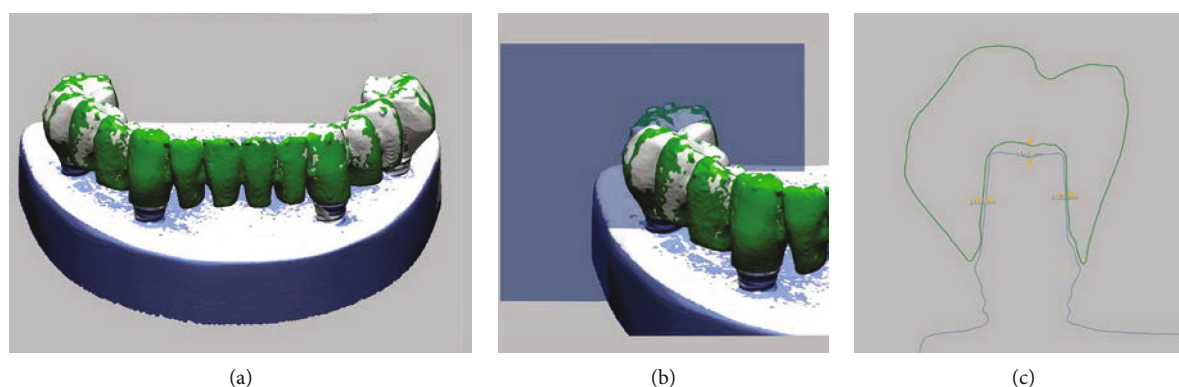


FIGURE 5: The triple scan technique for assessing the internal gap of the 3D-printed prosthesis: (a) image matching of scans, (b) measurement plane formation, and (c) cross-sectional image in the abutment area.

USA), where the three scan images were merged using an area-designated best-fit image matching (Figure 5(a)) [20]. The image alignment to the closest fit with the corresponding images was enabled using an iterative closest point (ICP) algorithm [21]. The cross-sectional line images were buccolingually obtained at the midpoint of the abutment (Figure 5(b)), and the internal gap, the perpendicular distances from the external surface of the abutment to the internal surface of the prosthesis, was measured at the center points of the buccal, lingual, and occlusal aspects (Figure 5(c)). For the intermolar distance assessment, a virtual cross-sectional plane passing through two central fossae of the first molars on both sides was created, and the distance between the most external points of the buccal surfaces of the left and right first molars was measured and compared with that of the prosthesis design image using the image analysis software program. All measurements for evaluating the accuracy of 3D-printed prostheses were carried out by a single examiner blinded to the research objective.

2.4. Statistical Analysis. All outcome variable data were reported as mean \pm standard deviation. The Kruskal-Wallis test was used for the comparison of the results among groups that used different postcuring methods using the IBM Statistical Package for the Social Sciences (SPSS) v25.0 for Windows (IBM Corp., Chicago, IL, USA). The statistical significance level was set at 0.05. The Mann-Whitney U test

with Bonferroni correction was used for post hoc analyses ($\alpha = 0.017$).

3. Results

Table 2 presents the results of fit and dimensional discrepancy of the 3D-printed acrylic prostheses at each measurement point. In general, the PM group showed the lowest mean discrepancy, followed by the PS and P groups. The PS and P groups showed no significant difference in any measurement outcome. The highest discrepancy was found in the measurements of the occlusal area, especially in the P group. Figure 6 shows images of the marginal gap in the different postcuring groups. The PM group exhibited significantly smaller marginal gaps than the other groups. Figure 7 shows the outlines of the molars of 3D-printed prostheses and the design image in the cross-sectional view. Again, the discrepancy of intermolar distance was the smallest in the PM group.

4. Discussion

This study was designed to find a postcuring method that minimizes the adverse dimensional change for 3D-printed polymeric prostheses. The results showed that the adaptation and dimension of cured prostheses were most accurate when the printed prostheses were cured with seating on the stone model. Thus, the null hypothesis that the differences in the postcuring methods for printed polymeric prostheses would

TABLE 2: Discrepancy values (mean \pm standard deviation; μm) of 3D-printed polymeric fixed prostheses fabricated by different postcuring methods.

| Area | Prosthesis alone | Postcuring methods | | <i>P</i> |
|-----------------|-------------------------------|-------------------------------|-------------------------------|----------|
| | | Prosthesis with supports | Prosthesis on the stone model | |
| Margin, buccal | 274.4 \pm 64.4 ^a | 233.0 \pm 40.3 ^a | 91.8 \pm 27.4 ^b | 0.008 |
| Axial, buccal | 122.1 \pm 51.6 | 125.4 \pm 47.8 | 94.7 \pm 64.5 | 0.468 |
| Occlusal | 332.8 \pm 70.7 ^a | 311.7 \pm 58.2 ^a | 126.3 \pm 27.3 ^b | 0.009 |
| Axial, lingual | 138.6 \pm 46.7 ^a | 134.3 \pm 28.4 ^a | 64.4 \pm 22.2 ^b | 0.019 |
| Margin, lingual | 256.4 \pm 46.2 ^a | 196.8 \pm 38.7 ^a | 89.0 \pm 26.7 ^b | 0.004 |
| Intermolar | 115.4 \pm 25.3 ^a | 105.9 \pm 12.9 ^a | 39.2 \pm 17.7 ^b | 0.008 |

Different superscript lowercase letters indicate significant differences within a row ($\alpha = 0.05$).

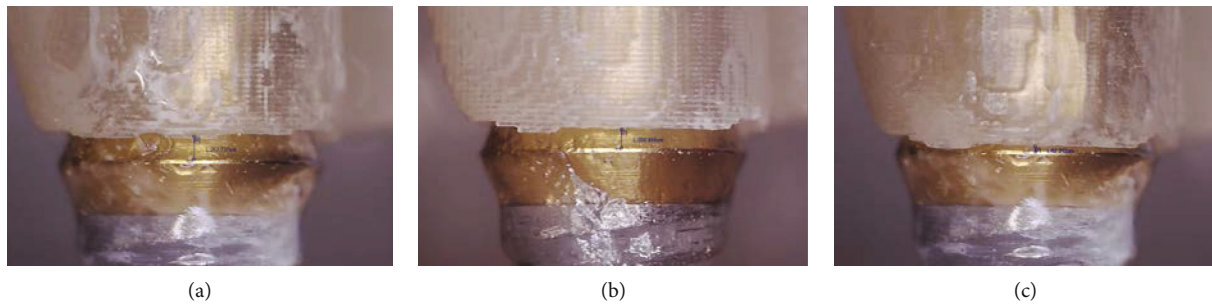


FIGURE 6: Microscopic image for marginal gap measurement: (a) prosthesis alone, (b) prosthesis with supports, and (c) prosthesis on the stone model.



FIGURE 7: Evaluation of discrepancy of the intermolar distance between 3D-printed and design image of prosthesis.

not affect the accuracy of their fabrication was rejected. The mean marginal gap of prostheses in the PM group was lower than 120 μm , which was in a clinically acceptable range. The error in the intermolar distance was significantly smaller in the PM group than the other groups of postcuring without the model. Leaving the supports did not significantly decrease the dimensional error that happened in the postcuring process.

During the printing process, each layer is briefly exposed to curing light and partially solidified. This incomplete poly-

merization is needed to allow fusion between layers [22]. After the printing process, postcuring is performed to achieve the maximum strength and full density of the material [23]. Chemically, the polymerization of resin material is the increase of the conversion degree, which is a chemical structure change from carbon double bonds (C=C) to carbon single (C-C) bonds [24]. The change in chemical structure inevitably involves a dimensional change of the object [23, 25]. Accordingly, the amount of deformation in postcuring could be affected by the change in the conversion

degree. The findings of the present study showed that deformation during postcuring could be minimized when the 3D-printed prosthesis was seated on the abutments of the stone model, leading to markedly low misfit and dimensional error. This might happen because the underlying abutments played the role of mechanical guides that blocked unwanted deformation. Therefore, it is recommended that 3D-printed prostheses are placed on the abutments of the model during the postcuring process. This method may help fabricate prostheses that are closely fitted to abutments in the mouth, in addition to less cement leakage, less need for occlusal adjustment, and better performance of the prosthesis in the long term [26].

The novelty of this study is that it is the first to investigate the impact of postcuring methods on dimensional accuracy in the 3D printing of full-arch polymeric fixed prostheses. Although the design of this study was controlled, there are several limitations derived from its *in vitro* nature. Comprehensive clinical studies including tooth-supported and implant-supported conditions are necessary, and the clinical marginal and internal fit of prostheses needs to be assessed to confirm the findings of the present study. In addition, the deformation phenomenon that occurs during the postcuring process should be evaluated using different 3D printing methods, such as digital light processing, fused deposition modeling, and polymer jetting. Photopolymers are composed of oligomers, monomers, and photoinitiators, and the curing of photopolymers is affected by wavelength, power of light, and radiation time. Thus, further studies on materials and curing setting are needed to optimize the postcuring process.

5. Conclusions

Within the limitations of this study, the postcuring process affects the fit and dimensional accuracy of 3D-printed polymeric prostheses. Seating of the prosthesis on the stone model is recommended to minimize the deformity of the prosthesis during the postcuring process.

Data Availability

The data used to support the findings of this study are included within the article.

Conflicts of Interest

The authors declare that there is no conflict of interest regarding the publication of this paper.

Authors' Contributions

J Kim contributed to the conceptualization of this study, data curation, formal analysis, investigation, and original drafting. DH Lee was involved in the methodology, formal analysis, investigation, review, editing, and supervision of this study.

Acknowledgments

The authors thank Yong-Do Choi for help with the laboratory work.

References

- [1] D. R. Burns, D. A. Beck, and S. K. Nelson, "A review of selected dental literature on contemporary provisional fixed prosthodontic treatment: report of the Committee on Research in Fixed Prosthodontics of the Academy of Fixed Prosthodontics," *Journal of Prosthetic Dentistry*, vol. 90, no. 5, pp. 474–497, 2003.
- [2] D. G. Gratton and S. A. Aquilino, "Interim restorations," *Dental Clinics of North America*, vol. 48, no. 2, pp. 487–497, 2004.
- [3] F. Mangano and G. Veronesi, "Digital versus analog procedures for the prosthetic restoration of single implants: a randomized controlled trial with 1 year of follow-up," *BioMed Research International*, vol. 2018, Article ID 5325032, 20 pages, 2018.
- [4] N. Alharbi, S. Alharbi, V. Cuijpers, R. B. Osman, and D. Wismeijer, "Three-dimensional evaluation of marginal and internal fit of 3D-printed interim restorations fabricated on different finish line designs," *Journal of Prosthodontic Research*, vol. 62, no. 2, pp. 218–226, 2018.
- [5] M. Kim, J. Kim, H. N. Mai et al., "Comparative clinical study of the marginal discrepancy of fixed dental prosthesis fabricated by the milling-sintering method using a presintered alloy," *The Journal of Advanced of Prosthodontics*, vol. 11, no. 5, pp. 280–285, 2019.
- [6] M. Revilla-León, M. J. Meyers, A. Zandinejad, and M. Özcan, "A review on chemical composition, mechanical properties, and manufacturing work flow of additively manufactured current polymers for interim dental restorations," *Journal of Esthetic and Restorative Dentistry*, vol. 31, no. 1, pp. 51–57, 2019.
- [7] X. J. Duan, H. Q. Fan, F. Y. Wang, P. He, and L. Yang, "Application of 3D-printed customized guides in subtalar joint arthrodesis," *Orthopaedic Surgery*, vol. 11, no. 3, pp. 405–413, 2019.
- [8] A. Tahayeri, M. Morgan, A. P. Fugolin et al., "3D printed versus conventionally cured provisional crown and bridge dental materials," *Dental Materials*, vol. 34, no. 2, pp. 192–200, 2018.
- [9] H. N. Mai, K. B. Lee, and D. H. Lee, "Fit of interim crowns fabricated using photopolymer-jetting 3D printing," *Journal of Prosthetic Dentistry*, vol. 118, no. 2, pp. 208–215, 2017.
- [10] C. Polzin, S. Spath, and H. Seitz, "Characterization and evaluation of a PMMA-based 3D printing process," *Rapid Prototyping Journal*, vol. 19, no. 1, pp. 37–43, 2013.
- [11] M. Revilla-León, M. J. Meyer, A. Zandinejad, and M. Özcan, "Additive manufacturing technologies for processing zirconia in dental applications," *International journal of computerized dentistry*, vol. 23, no. 1, pp. 27–37, 2020.
- [12] R. van Noort, "The future of dental devices is digital," *Dental Materials*, vol. 28, no. 1, pp. 3–12, 2012.
- [13] J. W. Stansbury and M. J. Idacavage, "3D printing with polymers: challenges among expanding options and opportunities," *Dental Materials*, vol. 32, no. 1, pp. 54–64, 2016.
- [14] J. Jockusch and M. Özcan, "Additive manufacturing of dental polymers: an overview on processes, materials and applications," *Dental Materials Journal*, vol. 39, no. 3, pp. 345–354, 2020.
- [15] A. Bagheri and J. Jin, "Photopolymerization in 3D printing," *ACS Applied Polymer Materials*, vol. 1, no. 4, pp. 593–611, 2019.
- [16] F. Alifui-Segbaya, "Biomedical photopolymers in 3D printing," *Rapid Prototyping Journal*, vol. 26, no. 2, pp. 437–444, 2019.

- [17] N. Alharbi, R. Osman, and D. Wismeijer, "Effects of build direction on the mechanical properties of 3D-printed complete coverage interim dental restorations," *Journal of Prosthetic Dentistry*, vol. 115, no. 6, pp. 760–767, 2016.
- [18] J. R. Dizon, A. Espera, Q. Chen, and R. Advincula, "Mechanical characterization of 3D-printed polymers," *Additive Manufacturing*, vol. 20, pp. 44–67, 2017.
- [19] J. R. Holmes, S. C. Bayne, G. A. Holland, and W. D. Sulik, "Considerations in measurement of marginal fit," *Journal of Prosthetic Dentistry*, vol. 62, no. 4, pp. 405–408, 1989.
- [20] S. Holst, M. Karl, M. Wichmann, and R. E. Matta, "A new triple-scan protocol for 3D fit assessment of dental restorations," *Quintessence International*, vol. 42, no. 8, pp. 651–657, 2011.
- [21] A. Almukhtar, X. Ju, B. Khambay, J. McDonald, and A. Ayoub, "Comparison of the accuracy of voxel based registration and surface based registration for 3D assessment of surgical change following orthognathic surgery," *PLoS One*, vol. 9, no. 4, article e93402, 2014.
- [22] J. Crivello and E. Reichmanis, "Photopolymer materials and processes for advanced technologies," *Chemistry of Materials*, vol. 26, pp. 533–548, 2013.
- [23] K. Yoshida and E. H. Greener, "Effect of photoinitiator on degree of conversion of unfilled light-cured resin," *Journal of Dentistry*, vol. 22, no. 5, pp. 296–299, 1994.
- [24] D. H. Lee, H. N. Mai, J. C. Yang, and T. Y. Kwon, "The effect of 4,4'-bis(N,N-diethylamino) benzophenone on the degree of conversion in liquid photopolymer for dental 3D printing," *The Journal of Advanced of Prosthodontics*, vol. 7, no. 5, pp. 386–391, 2015.
- [25] M. Balkenhol, M. Knapp, P. Feger, U. Heun, and B. Wöstmann, "Correlation between polymerization shrinkage and marginal fit of temporary crowns," *Dental Materials*, vol. 24, no. 11, pp. 1575–1584, 2008.
- [26] D. Ehrenberg, G. I. Weiner, and S. Weiner, "Long-term effects of storage and thermal cycling on the marginal adaptation of provisional resin crowns: a pilot study," *Journal of Prosthetic Dentistry*, vol. 95, no. 3, pp. 230–236, 2006.

Corrigendum

Corrigendum to “Prime-Boost Vaccination Using Chemokine-Fused gp120 DNA and HIV Envelope Peptides Activates Both Immediate and Long-Term Memory Cellular Responses in Rhesus Macaques”

Hong Qin,^{1,2} Pramod N. Nehete ,³ Hong He ,^{2,4} Bharti Nehete,³ Stephanie Buchl,³ Soung-chul Cha,^{1,2} Jagannadha K. Sastry,^{2,3,4} and Larry W. Kwak^{1,2}

¹Department of Lymphoma and Myeloma, M. D. Anderson Cancer Center, The University of Texas, Houston, TX 77030, USA

²Center for Cancer Immunology Research, M. D. Anderson Cancer Center, The University of Texas, Houston, TX 77030, USA

³Department of Veterinary Sciences, M. D. Anderson Cancer Center, The University of Texas, Bastrop, TX 78602, USA

⁴Department of Immunology, M. D. Anderson Cancer Center, The University of Texas, Houston, TX 77030, USA

Correspondence should be addressed to Jagannadha K. Sastry; jsastry@mdanderson.org

Received 18 June 2020; Accepted 22 June 2020; Published 31 October 2020

Copyright © 2020 Hong Qin et al. This is an open access article distributed under the Creative Commons Attribution License, which permits unrestricted use, distribution, and reproduction in any medium, provided the original work is properly cited.

In the article titled “Prime-Boost Vaccination Using Chemokine-Fused gp120 DNA and HIV Envelope Peptides Activates Both Immediate and Long-Term Memory Cellular Responses in Rhesus Macaques” [1] (published when the journal was titled *Journal of Biomedicine and Biotechnology*), as raised on PubPeer, there is duplication of panels in Figure 2 [2].

Figure 2(e) is the same as Figure 2(i).

Figure 2(f) is the same as Figure 2(i), though Figure 2(f) has a blue block in the top right of the dot plot. Figure 2(g) is the same as Figure 2(k).

Figures 2(e)–2(g) were directly above Figures 2(i)–2(k) in the figure. Dr. Jagannadha Sastry reexamined the original data with the third author Hong He who conducted the assay and data analysis and found that this error was introduced when copying data from FlowJo to PowerPoint. The authors provided a corrected figure redone by Dr. He, as shown below:

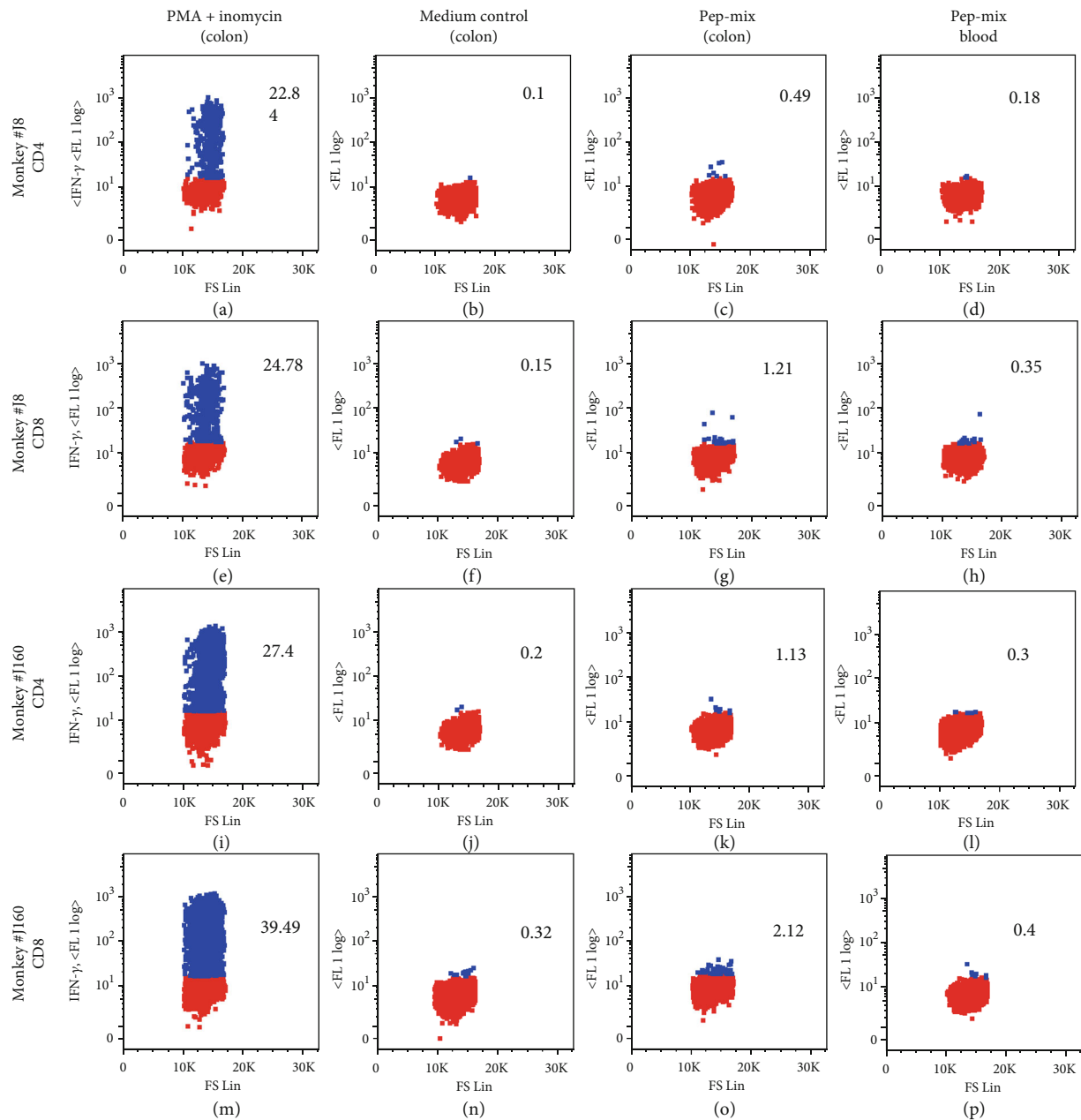


FIGURE 2: The immunization strategy elicited mucosal long-term memory T cell immune responses. Production of IFN- γ by CD3⁺CD4⁺ or CD3⁺CD8⁺ memory T cells isolated from the colon was analyzed in the vaccinated macaques one year after final peptide-cocktail boost. Lamina propria lymphocytes (LPL) from colon biopsy samples were stimulated with peptide-mix or mitogens for 6 h. Both untreated (control) and stimulated cells were stained for surface markers, followed by fixation, permeabilization, and intracellular staining of IFN- γ . Live cells were identified by gating on Aqua-negative cells. The cells gated on CD3⁺CD4⁺ and CD3⁺CD8⁺ were further separated as the memory population according to the expression of CD95 (data not shown). The percentage values indicate the population of IFN- γ -producing CD3⁺ CD95⁺CD4⁺ or CD3⁺ CD95⁺CD8⁺ lymphocytes.

References

- [1] H. Qin, P. N. Nehete, H. He et al., "Prime-boost vaccination using chemokine-fused gp120 DNA and HIV envelope peptides activates both immediate and long-term memory cellular responses in rhesus macaques," *BioMed Research International*, vol. 2010, Article ID 860160, 7 pages, 2010.
- [2] *PubPeer* June 2014. <https://pubpeer.com/publications/A7B8ED57E20508332BC1D533D2741D>.

Corrigendum

Corrigendum to “Combined Industrial Wastewater Treatment in Anaerobic Bioreactor Post-Treated in Constructed Wetland”

Bibi Saima Zeb ¹, **Qaisar Mahmood** ¹, **Saima Jadoon** ², **Arshid Pervez**,¹
Muhammad Irshad ¹, **Muhammad Bilal**,¹ and **Zulfiqar Ahmad Bhatti**¹

¹Department of Environmental Sciences, COMSATS Institute of Information Technology, Abbottabad 22060, Pakistan

²Department of Natural Resources Engineering and Management, University of Kurdistan, Erbil, Iraq

Correspondence should be addressed to Qaisar Mahmood; mahmoodzju@gmail.com

Received 29 April 2020; Accepted 21 May 2020; Published 29 September 2020

Copyright © 2020 Bibi Saima Zeb et al. This is an open access article distributed under the Creative Commons Attribution License, which permits unrestricted use, distribution, and reproduction in any medium, provided the original work is properly cited.

In the article titled “Combined Industrial Wastewater Treatment in Anaerobic Bioreactor Post-treated in Constructed Wetland” [1], there were typographical errors and errors in the figures. These have been corrected in the revised version shown below:

- (1) The abstract was revised for typographical errors
- (2) Language corrections were made in the text
- (3) The objectives of the study were clearly mentioned
- (4) All acronyms were spelled out when used for the first time
- (5) Corrections were made to the captions of Figures 1 to 10, to aid clear understanding of the plots
- (6) Table 2 was deleted as its values were repeated in Table 3 and hence section 3.1 was also deleted
- (7) A separate Discussion section was added
- (8) An additional article was cited as reference 42 [2] and the previous references 42-49 became references 43-50

The corrected article is as follows.

Abstract

Constructed Wetland (CW), containing monoculture of *Arundo donax* L., was investigated for the post-treatment of effluent from Anaerobic Bioreactor (ABR) treating combined

industrial wastewater. Different dilutions of combined industrial wastewater (20, 40, 60, and 80% v/v) and original wastewater were fed into the ABR as pretreatment. ABR effluent was post-treated by the laboratory scale CW. The removal efficiencies of Chemical Oxygen Demand (COD), Biochemical Oxygen Demand (BOD), Total Suspended Solids (TSS), nitrates and ammonia were 80%, 78-82%, 91.7%, 88-92% and 100%, respectively, for original industrial wastewater treated in ABR. ABR was found efficient in the removal of the metals Ni, Pb and Cd with removal efficiencies in the order of Cd (2.7%) > Ni (79%) > Pb (85%). Post-treatment of the ABR-treated effluent was carried out in lab scale CW planted with *A. donax* L. CW was effective in removal of COD and various heavy metals present in ABR effluents. Post-treatment in CW resulted in reducing the metal concentrations of Ni, Pb and Cd to 1.95 mg/L, 0 mg/L and 0.004 mg/L, respectively, which were within the limits of permissible water quality standards for industrial effluents. The treatment strategy was effective and sustainable to treat combined industrial wastewater.

1. Introduction

Pakistan's current population of 180 million is expected to grow to about 221 million by the year end 2025 [1]. In Pakistan and other developing countries, water pollution is a major threat to the livelihood of people [2]. Heavy metal contamination of aquatic and terrestrial ecosystems is a major environmental problem. Each pollution problem calls

for specific optimal and cost-effective solutions; if one technology proves less effective or ineffective, another takes its place. It is indispensable to treat industrial wastewaters for their subsequent use for irrigation, drinking and other purposes. In addition, due to an increased scarcity of clean water, there is a need for appropriate management of available water resources [3]. Factors like profound demographic changes, economic changes and the global energy crisis are compelling the implementation of low-cost natural treatment systems for domestic and industrial wastewaters [1].

In recent years, wastewater treatment strategies have shifted to one of the most promising methods, i.e. biological anaerobic treatment with the adoption of high rate anaerobic systems like up-flow anaerobic sludge blanket (UASB) reactor and other related treatment systems. The outstanding characteristics of high-rate Anaerobic Bioreactors (ABR) include anaerobic microorganisms capable of aggregation, low operational and maintenance costs, energy recovery in the form of biogas, low energy consumption and low production of digested sludge [4-7]. In developing countries like India, Brazil and Colombia, where financial resources are generally scarce due to high energy costs, the process is familiar as one of the most feasible methods for wastewater treatment. Despite several modifications, the quality of ABR-treated effluent hardly ever meets the discharge standards [6, 8]. Lettinga and co-researchers applied ABR process for municipal wastewater treatment since the early 1980s [9-13] and reported that about 70% chemical oxygen demand (COD) removal can be achieved under warm climates [6, 14, 15]. Since its inception, wider hype has been gained by this process [16, 17]. ABR-treated effluents can be employed for irrigation of various crops. However, such type of effluent may be high in COD, biological oxygen demand (BOD) and coliforms [18]. Thus, additional post-treatment strategy is mandatory for ABR-treated effluents if further use is desired [19-21].

CW wastewater treatment systems are engineered structures specifically designed for treating wastewater by optimizing the physical, chemical and biological processes that occur in natural wetland ecosystems [1, 18, 22-24]. CW is known as green technology, which uses plants for the removal of contaminants from a specified area, and the process is known as phytoremediation [25]. CW is a low cost or economical on-site wastewater treatment technology which is not only effective but also aesthetically pleasing. Since 1980, the utilization of the CW for the treatment of variety of wastewater has quickly become widespread. The amount of nutrients removed by plants and stored in their tissues is highly relative, which depends on the plant type, biomass and nutrient concentration in tissues [26].

The plant species, media like sand and gravel of specific ratio and size and containers are the foundation materials for CW. There are two major types of CW: subsurface flowing water (SSF) CW and free water surface (FWS) flowing CW. A variety of macrophytes are used in CW and the most common are floating macrophytes (i.e. *Lemna* spp or *Eichhornia crassipes*), submerged macrophytes (i.e. *Elodea canadensis*) and rooted emergent macrophytes (i.e. *Phragmites australis* and *Typha angustifolia*). The plants roots create a

conducive environment for microbial growth and in winter the plant litter acts as an insulator. CW is an attached-growth biological reactor, which tender higher pollutant removal efficiency through physical, chemical and biological mechanisms. The common removal mechanisms associated with wetlands include sedimentation, coagulation, adsorption, filtration, biological uptake and microbial transformation [3, 24, 27].

CW technology is well-known at present, but it is not well documented for treating specific industrial effluents [28-30] and it can be used for polishing effluents of anaerobic bioreactors. A variety of post-treatment configurations based on various combinations with ABR have been studied; ABR followed by final polishing units (FPU) or polishing pond (PP) is a common process used in India, Colombia and Brazil due to its simplicity in operation [6, 31-33]. The implementation of low-cost, simple mitigation measures is required for the timely control and sustainable management of pollution problems in developing countries. The objective of this study was to evaluate the performance of ABR for the treatment of combined industrial wastewater followed by post-treatment in CW planted with *A. donax*.

2. Materials and Methods

2.1. Collection of Wastewater and Treatment. The industrial wastewater was collected from a combined drain at Hattar Industrial Estate (HIE), Hattar, Pakistan as grab samples. A number of industries are operating in HIE, like steel reolling, paper recycling, ghee, food, beverages and cement. The physicochemical parameters like pH, turbidity and electric conductivity (EC) were determined onsite using portable pH, EC and turbidity analyzer, while the rest were analyzed in the laboratory within 24 h. As a treatment strategy and to avoid toxic effects of the pollutants, various dilutions (with distilled water) of wastewater included 20, 40, 60 and 80% (v/v) to feed into ABR, after which original wastewater was also treated in ABR and then CW.

2.2. ABR Experimental Set-up. This research work was carried out in the Bioremediation Laboratory of COMSATS Institute of Information Technology, Abbottabad, Pakistan. In this study, ABR was used as primary treatment step. A lab scale ABR was operated in up-flow mode with biomass retention as shown in Figure 1. The reactor is made of Perspex with a working volume of 5 L. The influent was pumped into ABR using a peristaltic pump from the influent vessel to the reactor (Figure 1). The flow rate was adjusted according to results of a startup study. A recycling pump was used to mix the influent (substrate) and sludge (biocatalyst) and to decrease possible substrate inhibition. The ratio of recycle flow to the influent flow was set at about 2.5-3. Bioreactor start up was carried out by feeding synthetic wastewater and nutrient solution at various Organic Loading Rate (OLR) and COD by using organic compounds at a fixed Hydraulic Retention Time (HRT) but increasing OLR, and at a fixed OLR but decreasing HRT. The ABR reactor in the Department of Environmental Sciences, COMSATS, Abbottabad was used for various types of

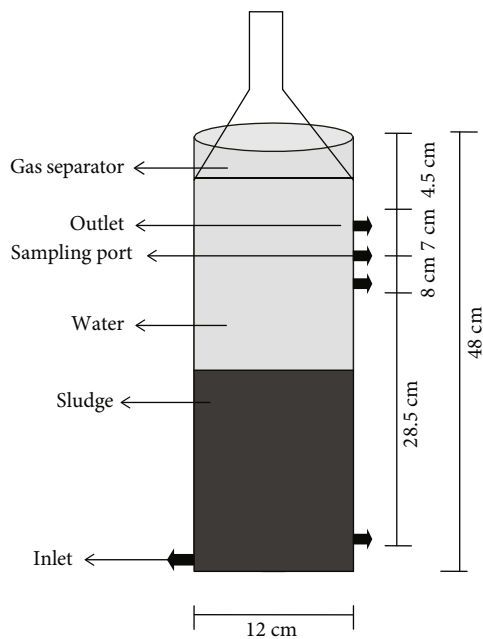


FIGURE 1: Schematic diagram of a lab scale anaerobic bioreactor with its dimensions.

the wastewater treatments in the past. Different wastewaters like domestic, industrial, municipal wastewater were treated through this ABR.

Inoculum was collected from the anaerobic methanogenic reactor in COMSATS Institute of Information and Technology Abbottabad, operating in the same laboratory. Its total solids (TS) and volatile solids (VS) were 115.6 g/L and 33.61 g/L, respectively, with VS/TS ratio of 0.25. The ABR reactor was fed with synthetic wastewater in order to enrich the sludge and for acclimatization of bacteria to the new substrates.

The reactor was fed on a daily basis with freshly prepared synthetic influent containing NaHCO_3 (as a source of inorganic carbon for the growth of bacteria), MgCl_2 , KH_2PO_4 , (1 g/L each), $(\text{NH}_4)_2\text{SO}_4$ (0.24 g/L) and trace element solution (1 ml/L). The trace element solution contained $\text{Na}_2\text{-EDTA}$ (5 g/L), NaOH (11 g/L), $\text{CaCl}_2 \cdot 2\text{H}_2\text{O}$ (11 g/L), $\text{FeCl}_2 \cdot 4\text{H}_2\text{O}$ (3.58 g/L), $\text{MnCl}_2 \cdot 2\text{H}_2\text{O}$ (2.5 g/L), ZnCl_2 (1.06 g/L), $\text{CoCl}_2 \cdot 6\text{H}_2\text{O}$ (0.5 g/L), $(\text{NH}_4)_6\text{Mo}_7\text{O}_{24} \cdot 4\text{H}_2\text{O}$ (0.5 g/L) and $\text{CuCl}_2 \cdot 2\text{H}_2\text{O}$ (0.14 g/L). Sucrose is used as source of COD, the starting COD feeding to the ABR reactor was 200 mg/L and, then increased up to 3000 mg/L. The influent was flushed with argon gas for five minutes to create anoxic conditions. The ABR reactor was operated at 20°C, operating at a different HRT (hydraulic retention time) and Organic Loading Rates in order to analyze the process performance.

2.3. Experimental Set-up. The lab scale experimental CW consisted of two independent rectangular basins (length: 120 cm, width: 90 cm, depth: 40 cm). The basins were filled with gravel, sand and soil from bottom to top with one layer of each as shown in Figure 2. Each basin had a 10% slope and was equipped with a nozzle outlet to discharge the treated

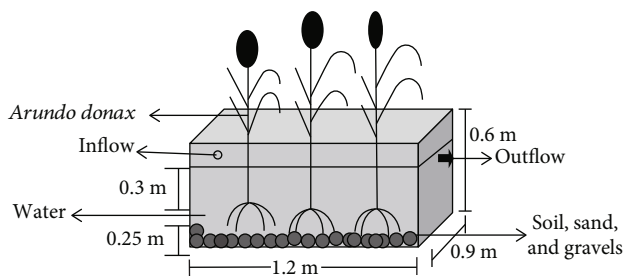


FIGURE 2: Schematic diagram of a laboratory scale CW for the treatment of combined industrial wastewater.

TABLE 1: Dimensions and operating conditions of experimental CW.

| Dimensions of CW | |
|-------------------------------|------------------------------------|
| Length | 1.2 m |
| Width | 0.9 m |
| Total height | 0.6 m |
| Total container volume | 0.432 m ³ |
| Water depth | 0.3 m |
| Substrate depth | 0.25 m |
| Plant name | <i>Arundo donax</i> L (Giant reed) |
| No. of rhizome/m ² | 3 |
| Operational conditions | |
| OLR | 538 kg/ha/d |
| HRT | 3 days |
| Hydraulic load rate (HLR) | 862 m ³ /ha/d |

effluent. The CW was planted with *A. donax* (6 shoots/m²) taken from the botanical garden of the institute.

An unplanted bed served as a control. Treated effluents were collected directly from the lab scale experimental plant. The operational conditions of the experimental set up of CW are shown in Table 1. All plants, sand and gravel were properly washed before planting into CW system.

Pollutant removal rates (%) were calculated according to the following equation:

$$R (\%) = [1 - (C_f/C_i)] \times 100 \quad (1)$$

Where: R is the removal rate, C_i is the concentration (mg/L) of the considered parameter in the untreated WW (influent), C_f is the concentration (mg/L) of the considered parameter in the treatment bed effluent.

2.4. Analytical Procedures. Raw and treated samples were analyzed for their BOD, COD, EC, pH, turbidity etc., according to the standard methods [34]. For COD determination closed reflux, colorimetric method included digestion at 150°C for 2 h in COD vials followed by spectrophotometer reading at 530 nm [34]. The pH was measured using a digital pH meter (HANNA, HI 991003 Sensor) while total dissolved solids (TDS) and conductivity were determined by HANNA, HI9835 Microprocessor. Heavy metals were analyzed through atomic absorption spectrophotometer. At least three readings were taken for each parameter each time and then the mean value was calculated.

TABLE 2: The performance of ABR in treating combined industrial effluents.

| Parameters | Influent/raw wastewater | | | | | ABR effluent | | | | | % removal | | | | Original WW |
|-------------------------|-------------------------|-------|-------|-------|-------------|--------------|-------|-------|-------|-------------|-----------|------|------|-------|-------------|
| | 20% | 40% | 60% | 80% | Original WW | 20% | 40% | 60% | 80% | Original WW | 20% | 40% | 60% | 80% | |
| pH | 8.1 | 8.48 | 8.6 | 8.76 | 10.2 | 7.89 | 8.31 | 8.52 | 8.66 | 8.41 | — | — | — | — | — |
| Conductivity (μ s) | 627 | 646 | 645 | 676 | 702 | 654 | 616 | 645 | 687 | 702 | — | — | — | — | — |
| TDS | 378 | 330 | 344 | 394 | 411 | 339 | 324 | 334 | 357 | 365 | 10 | 2 | 3 | 9 | 11 |
| VS | 712 | 812 | 780 | 1333 | 1400 | 83 | 85 | 93 | 215 | 115 | 88 | 89.5 | 88 | 83.8 | 91.7 |
| TS | 600 | 520 | 1050 | 1160 | 1960 | 45 | 86.3 | 163.9 | 97.2 | 305 | 92 | 83.5 | 86 | 90 | 84 |
| COD | 70 | 189 | 284 | 379 | 474 | 42 | 54 | 121 | 159 | 297 | 40 | 47.8 | 57.3 | 58.04 | 37.34 |
| BOD | 23.3 | 25.4 | 50.9 | 77 | 84.8 | 18.5 | 4.16 | 5.1 | 10.2 | 18.5 | 82 | 80 | 80 | 81 | 78 |
| Nitrates | 24 | 59 | 83 | 98 | 145 | 1.8 | 6.1 | 9.23 | 8.9 | 16 | 92.5 | 89.6 | 88.8 | 90.9 | 88.9 |
| Ammonia | 17 | 23 | 45 | 57 | 82 | 2.1 | 2.1 | 4.5 | 8 | 10 | 87.6 | 90.8 | 90 | 85.9 | 87.8 |
| Lead | 0.131 | 0.653 | 1.335 | 1.851 | 2.337 | 0.558 | 0.653 | 1.222 | 2.109 | 2.703 | 64 | 27.8 | 8.46 | 7.4 | 2.7 |
| Nickle | .117 | .225 | .315 | .271 | .403 | 0.079 | 0.015 | 0.035 | 0.074 | 1.014 | 92.1 | 93.4 | 87 | 79 | 79 |
| Cadmium | .026 | .026 | .021 | .009 | .048 | 0.009 | 0.009 | 0.007 | 0.001 | 0.007 | 65.4 | 65.4 | 66.7 | 88.9 | 85.4 |

2.5. *Statistical Analysis.* Collected data were analyzed by descriptive statistics and arithmetic averages of percent removal were calculated using Microsoft Excel XP version 2010 and Origin Lab 8.

3. Results and Discussion

3.1. *Pretreatment of Combined Industrial Wastewater in ABR.* The ABR was fed with combined industrial wastewater for treatment at retention time of 12 h. The treated effluent characteristics and percent removal efficiency are showed in Table 2.

The results describe the performance of the ABR for the treatment of combined industrial wastewater, as the concentrations of COD before pretreatment were 70, 189, 284, 379 and 474 mg/L, respectively, for 20, 40, 60 and 80% dilutions, and original wastewater. After pre-treatment with ABR, the COD was reduced to 42, 54, 121, 159, 297 mg/L with 40.0, 40.8, 57.3, 58.0, 37.3% removal efficiency, respectively. The results in Figure 3 show the maximum COD removal efficiency for the 80% dilution of the wastewater through ABR. The ABR also reduced the BOD concentrations of the dilutions in 78 to 82%, as shown in Figure 3. The BOD concentration reduced from 23.3, 25.4, 50.9, 77.0 and 84.8 mg/L to 18.5, 4.16, 5.1, 10.2 and 18.5, respectively. It was observed from the results that ABR showed excellent removal efficiency for BOD.

Total solids were tremendously removed by 84% with the corresponding concentration of 1960 mg/L for original wastewater. The concentration of $\text{NO}_3\text{-N}$ was reduced from 24, 59, 83, 98, 145 to 1.8, 6.1, 9.23, 8.9, and 16 mg/L for 20, 40, 60, 80% dilutions and original wastewater. ABR showed 88 to 92% removal efficiency for the $\text{NO}_3\text{-Nitrogen}$ as shown in Figure 4.

Similarly, the removal efficiency of $\text{NH}_4\text{-N}$ was 87.6, 90.8, 90, 85.9 and 87.8% for the four different dilutions 20, 40, 60, 80% and original wastewater, respectively, as shown in Figure 4. The concentrations of $\text{NH}_4\text{-N}$ of 17, 23, 45, 57

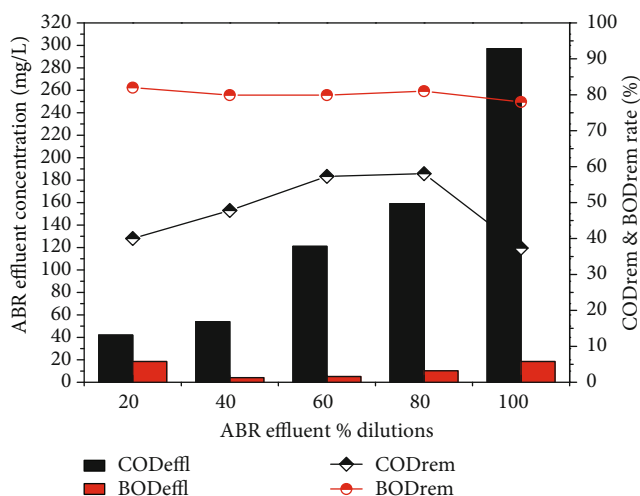


FIGURE 3: CODeffl and BODeffl concentration (mg/L), CODrem and BODrem efficiency (%) of a lab scale ABR reactor for combined industrial wastewater.

and 82 mg/L were reduced to 2.1, 2.1, 4.5, 8 and 10 mg/L. On the other hand, Pb, Ni and Cd removal by reactor was 2.7%, 79% and 85.4% for real industrial wastewater. Heavy metal removal was found in the order $\text{Cd} > \text{Ni} > \text{Pb}$ as shown in Figure 5.

3.2. *Post Treatment of ABR Effluent with CW.* The pre-treated effluent was then further treated by CW for 30 days for each dilution. The results for FWS CW effluent are shown in Figures 6–10 with pollutant removal efficiency.

The results of treatment in CW showed efficient removal efficiency for COD, BOD, TS, nitrates, ammonia and metals like Pb, Ni and Cd. The residual concentrations of COD and BOD were 64.3, 66.7, 67, 76.4, 82.4 and 78.4, 76, 80.3, 80.3 and 78.4 mg/L, respectively, for the corresponding dilutions of 20, 40, 60, 80% and original WW as shown in

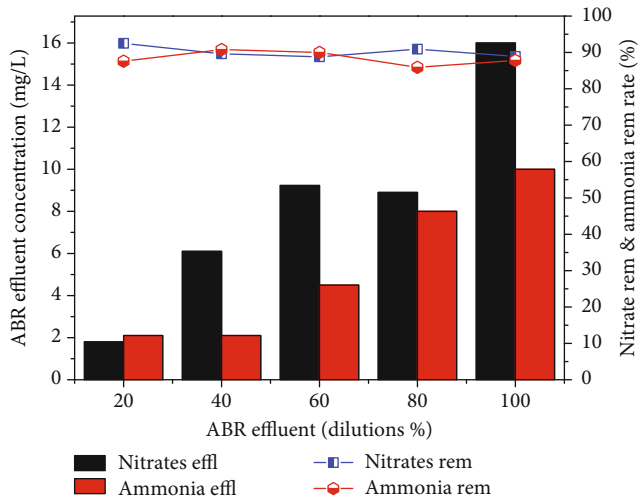


FIGURE 4: Nitrates Removal efficiency of pretreatment of combined industrial wastewater with ABR.

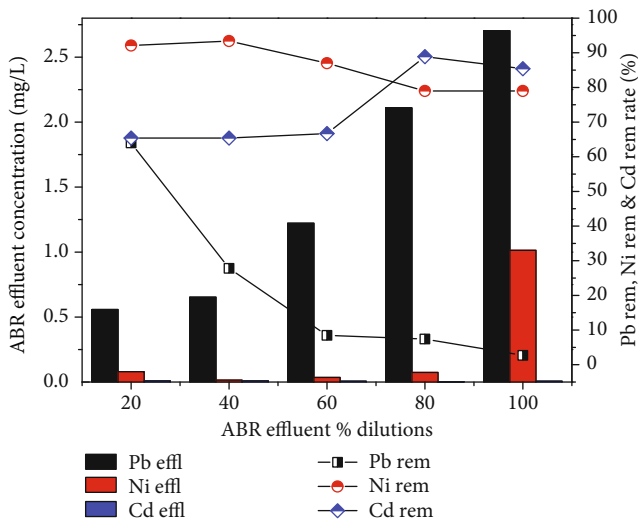


FIGURE 5: Removal efficiency of Pb, Ni and Cd by ABR.

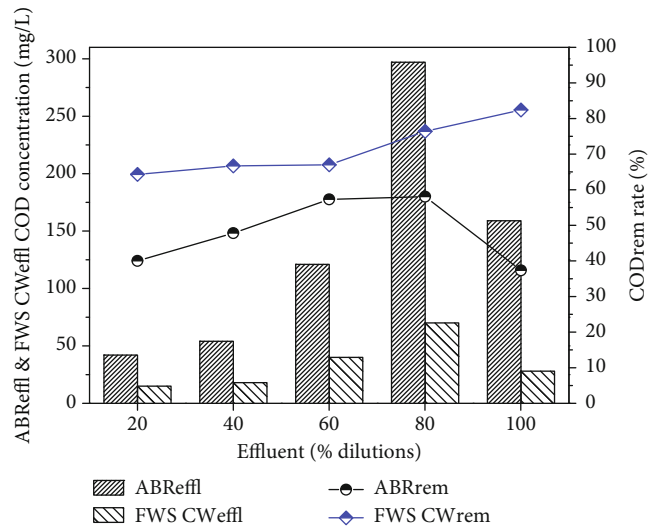


FIGURE 6: Comparison of ABR and CW for COD removal.

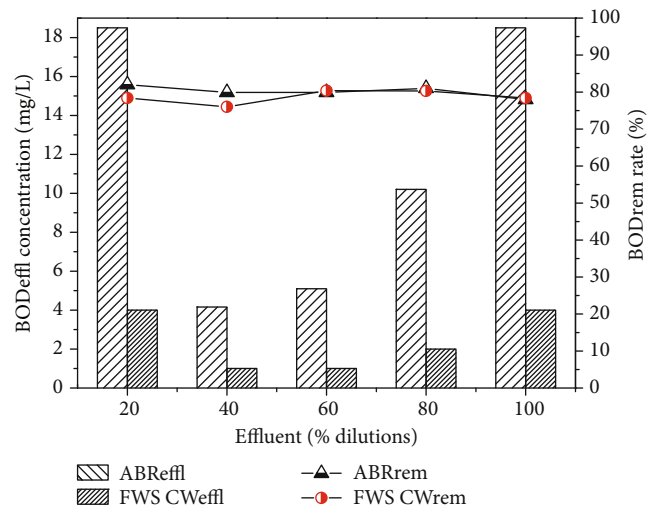


FIGURE 7: Comparison of ABR and CW for BOD removal.

Figures 6 and 7. The CW showed the highest COD removal efficiency of 82.4% for original WW, but at the same dilution the BOD was reduced to 78.4%. Nitrates and ammonia removal efficiency was found to be 95, 82, 86, 72, 75% for the respective concentrations of 1.8, 6.1, 9.23, 8.9 and 16 mg/L of the corresponding four different dilutions and original pre-treated effluent. Ammonia removal was not satisfactory compared to other parameters and the highest removal efficiency was 70.1% by CW.

3.3. Discussion. Previous workers observed that the treatment of complex industrial wastewater reduced the efficiency of the ABR [35], as also observed in the present study. However, ABR showed promising results regarding treatment of BOD in the present work. During anaerobic digestion of organic matter, biochemical reactions take place which are affected by heavy metal presence [35]. It is clear from the results that soluble heavy metals rapidly decreased at the initial concen-

trations. It depends on which chemical form the heavy metal exists in. The most common and important form of heavy metals are precipitation (as sulfides, carbonates and hydroxides), sorption on to solid form (inhibitory effect of heavy metals on anaerobic sludge) [36]. Ni could be bound in all forms. So it was clear that high initial concentrations were tolerated by the ABR sludge and thus showed the satisfactory removal of heavy metals.

However, the residual concentration of organic (BOD and COD) and heavy metals in the anaerobic reactor effluent usually exceeds the maximum permissible level prescribed by the effluent discharge standards of most developing countries [20, 37-38]. From this standpoint, post-treatment of anaerobic effluent is necessary to reduce these contaminants to the required level [39].

CW normally improves the dissolved oxygen (DO) in wetland. The introduction of excess organic matter may result in depletion of oxygen from an aquatic system.

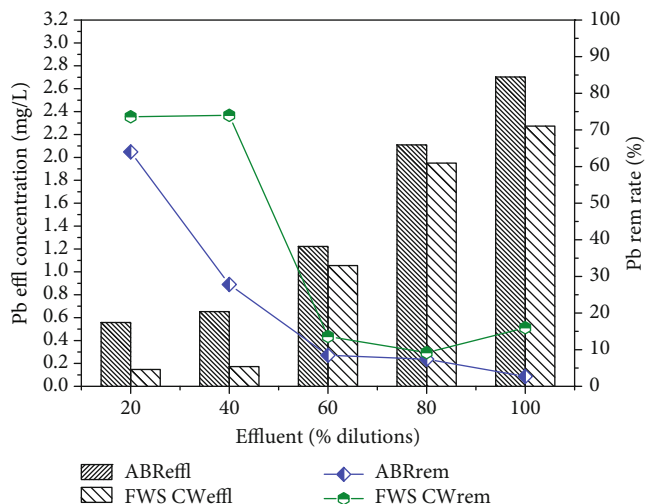


FIGURE 8: Comparison of % removal efficiency of Pb in ABR and FWS CW.

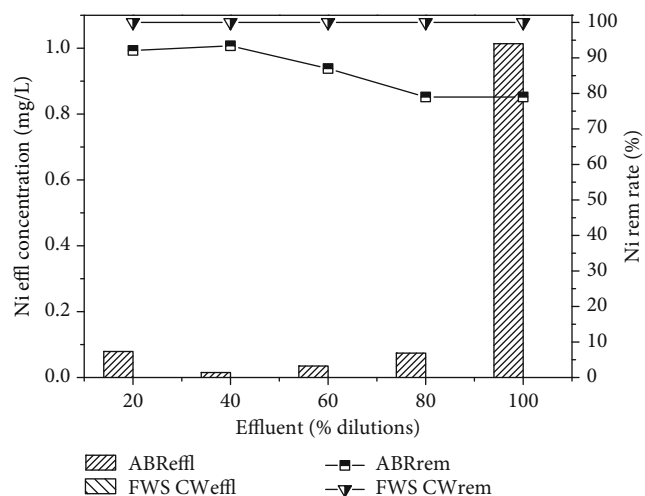


FIGURE 9: Comparison of percent removal efficiency of Ni in ABR and FWS SCW.

Prolonged exposure to low dissolved oxygen levels (<5.0–6.0 mg/L) may not directly kill an organism, but will increase its susceptibility to other environmental stresses. Exposure to <30% saturation (<2.0 mg/L oxygen) for one to four days kills most of the biota in a system. If oxygen-requiring organisms perish, the remaining organisms will be air-breathing insects and anaerobic (not requiring oxygen) bacteria [40]. If all oxygen is depleted, aerobic (oxygen-consuming) decomposition ceases. So, treating pollutants in wetlands may help to increase DO, which is consumed by the other aerobes. In this experiment during the post-treatment by CW the DO increased to 8.8 mg/L.

Industrial wastewater was previously treated in two-stage constructed wetland [41] planted with *Typha latifolia* and *Phragmites australis*. For tannery wastewater, CW may be an interesting treatment option. Two-stage series of horizontal subsurface flow CW with *Phragmites australis* (UP series) and *Typha latifolia* (UT series) provided high removal of

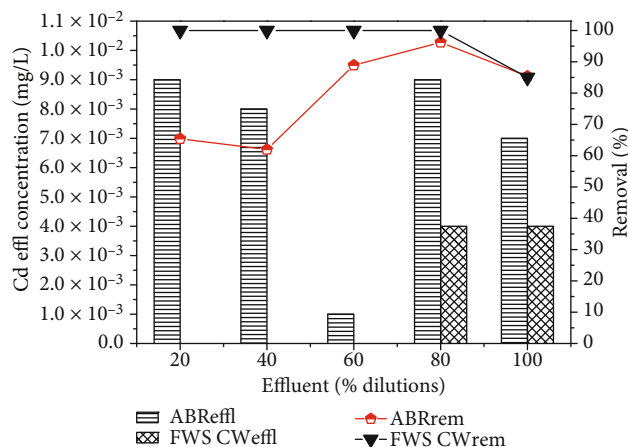


FIGURE 10: Comparison of % removal efficiency of Cd in ABR and FWS CW.

organics from tannery wastewater, up to 88% of BOD₍₅₎ (from an inlet of 420 to 1000 mg/L) and 92% of COD (from an inlet of 808 to 24vx49 mg/L) and of other contaminants, such as nitrogen, operating at hydraulic retention times of 2, 5 and 7 days. Overall mass removals of up to 1294 kg COD/ha/d and 529 kg BOD₍₅₎/ha/d were achieved for a loading ranging from 242 to 1925 kg COD/ha/d and from 126 to 900 kg BOD₍₅₎/ha/d. Plants were resilient to the conditions imposed, however *P. australis* exceeded *T. latifolia* in terms of propagation [41].

In the present study, *A. donax* was used in the CW for post-treatment, which showed an efficient performance for the further removal of pollutants from the ABR pre-treated effluent. The results confirmed that effluent showed traces of heavy metals Ni and Cd with the corresponding ABR treated wastewater at almost all the levels of dilutions of 20, 40, 60, 80% and original wastewater. CW showed the maximum removal efficiency for Ni and Cd as depicted in Figures 9 and 10, respectively. CW post-treatment of Pb was not satisfactory in reduction of its concentration. Using the San Joaquin Marsh constructed wetlands, the removal efficiencies for four heavy metal elements Cd, Cu, Pb and Zn were evaluated. It was found that the effluent metal concentrations were not substantially lower than the influent. The removal efficiencies of 23.9%, 10.6%, and 17.6% were found for Cd, Cu, and Zn, respectively. No significant reduction was observed for concentrations of Pb [43].

The removal of metals and metalloids from contaminated waters was investigated in constructed wetlands. Metal removal rates in wetlands depend on the type of element (Hg > Mn > Fe ¼ Cd > Pb ¼ Cr > Zn ¼ Cu > Al > Ni > As), their ionic forms, substrate conditions, season, and plant species. Standardized procedures and data are lacking for efficiently comparing properties of plants and substrates. The study depicted the relative treatment efficiency index (RTEI) to quantify treatment impacts on metal removal in constructed wetlands [44].

Various mechanisms, including sedimentation, filtration, chemical precipitation, adsorption, microbial interactions

and uptake by vegetation have been attributed with the removal of metals within CW. Specifically, the major processes that are responsible for metal removal in CW are binding to sediments and soils, precipitation as insoluble salts and uptake by plants and bacteria [45]. In CW, substrate interactions remove most metals from contaminated water [46]. The anoxic condition of wetland soil helps create an environment for immobilization of heavy metals in the highly reduced sulfite or metallic form [47]. Wetland plants adsorb and accumulate metals in tissues, which can play important role in CW pollutant treatment efficiency [48]. Phytoremediation, using vegetation to remove, detoxify, or stabilize heavy metal pollutants, is an accepted tool for cleaning polluted soils and waters [49]. Research has also shown that metal storage in sediment is influenced by vegetation. Concentrations of metals were significantly higher in the vegetated sediments than in the non-vegetated sediments [50].

4. Conclusion

This paper presented the evaluation results on removal efficiencies for COD, BOD, nitrates, TS, and heavy metals (Cd, Ni, Pb) in ABR and post-treated by a lab scale *Arundo donax* based CW. It was clearly observed that post-treatment accomplished efficient removal of the COD, BOD, TS, Ni, and Cd. The efficiency of both the treatment systems was not very satisfactory for Pb removal. Because of the positive effects of vegetation on metal removal efficiency, CWs containing *A. donax* is recommended for HIE combined wastewater treatment.

References

1. Q. Mahmood, A. Pervez, B.S. Zeb, H. Zaffar, H. Yaqoob, M. Waseem, Zahidullah, S. Afsheen, "Natural treatment systems as sustainable ecotechnologies for the developing countries", *Biomed Research International*, vol. 2013, pp. 1-9. 2013
2. B.S. Zeb, Q. Mahmood, A. Pervez, "Characteristics and performance of anaerobic wastewater treatment (a review)", *Journal of Chemical Society of Pakistan*, vol. 35, pp. 217-232. 2013.
3. A.K. Mungray, Z.V.P. Murthy, J.T. Ashwin, "Post treatment of up- flow anaerobic sludge blanket based sewage treatment plant effluents" A review, *Desalination and Water Treatment*, vol. 22, pp. 220-237.2010
4. A.C. Van Haandel, G. Lettinga, "Anaerobic Sewage Treatment, A Practical Guide for Regions with a Hot Climate" John Wiley and Sons, New York. 1994.
5. C.Y. Gomec, "High- rate anaerobic treatment of domestic wastewater at ambient operating temperatures A review on benefits and drawbacks", *Journal of Environmental Science and Health*, vol. 45, pp. 1169- 84. 2010.
6. A.A. Khan, R.Z. Gaur, V.K. Tyagi, A. Khurshed, B. Lew, A.A. Kazmi, I. Mehrotra, "Sustainable Options of Post Treatment of ABR Effluent Treating Sewage: A Review", *Resource Conservation and Recycling*, vol. 55, pp. 1232-1251. 2011a.
7. J.Y. Ji, Y.J. Xing, Z.T. Ma, M. Zhang, P. Zheng, "Acute toxicity of pharmaceutical wastewaters containing antibiotics to anaerobic digestion treatment" *Chemosphere*, vol. 91, pp. 1094-1098.2013.
8. B. Lew, M. Belavski, S. Admon, S. Tarre, M. Green, "Temperature effect on ABR reactor operation for domestic wastewater treatment in temperate climate regions", *Water Science and Technology*, vol. 48, pp. 25-30.2003.
9. G. Lettinga, A.F.M. van Velsen, S.W. Hobma, W. D. Zecuw, A. Klapwijk, "Use of the Upflow Sludge Blanket (USB) Reactor Concept for Biological Wastewater Treatment, Especially for Anaerobic Treatment", *Biotechnology and Bioengineering*, vol. 22, pp. 699-734. 1980.
10. G. Lettinga, A. de Man, A.R.M. van der Last, W. Wiegant, K. van Knippenberg, J. Frijns, J.C.L. van Buuren, "Anaerobic Treatment of Domestic Sewage and Wastewater", *Water Science and Technology*, vol. 27, pp. 67-73. 1993.
11. L. Seghezze, R.G. Guerra, S.M. González, A.P. Trupiano, M.E. Figueroa, C.M. Cuevas, G. Zeeman, G. Lettinga, "Removal Efficiency and Methanogenic Activity Profiles in a Pilot-scale ABR Reactor Treating Settled Sewage at Moderate Temperatures", *Water Science and Technology*, vol. 45, pp. 243-248.2002.
12. M. von Sperling, C.A.L. Chernicharo, "Biological Wastewater Treatment in Warm Climate Regions", IWA Publishing London, UK. 2005.
13. G. Lettinga, "Towards feasible and sustainable environmental protection for all", *Aquatic Ecosystem and Health Management*, vol. 11, pp. 116-24.2008.
14. A. Schellinkhout, C.J. Collazos, "Full- scale Application of the ABR Technology for Sewage Treatment", *Water Science and Technology*, vol. 25, pp. 159-166. 1992
15. J.T. Souza, E. Foresti, "Domestic Sewage Treatment in an Up- flow Anaerobic Sludge Blanket Sequential Batch System," *Water Science and Technology*, vol. 133, pp. 73-84. 1996.
16. A. A Khan, "Post treatment of ABR effluent: Aeration and Variant of ASP", *PhD Thesis*. IIT Roorkee India. 2012.
17. A.A. Khan, R.Z. Gaur, B. Lew, I. Mehrotra, A.A. Kazmi, "Effect of Aeration on the Quality of Effluent of ABR Reactor Treating Sewage", *Journal of Environmental Engineering-ASCE*, vol. 137, no 6, pp. 464-472. 2011c.
18. M. A. El-Khateeb, A. Z. El-Bahrawy, "Extensive Post Treatment Using Constructed Wetland", *Life Science Journal*, vol. 10, pp. 560-568. 2013.
19. W. Verstraete, P. Vandevivere, "New and broader applications of anaerobic digestion", *Critical Review of Environmental Science and Technology*, vol. 29, pp. 151-173, 1999.
20. N. Sato, T. Okubo, T. Onodera, A. Ohashi, H. Harada, "Prospects for a self - sustainable sewage treatment system: A case study on full - scale ABR system in India's Yamuna River Basin", *Journal of Environmental Management*, vol. 80, pp. 198-207. 2006.
21. A. K. Mungray, P. Kumar, "Anionic surfactants in treated sewage and sludge: Risk assessment to aquatic and terrestrial environments", *Bioresource Technology*, vol. 99, pp. 2919-2929. 2008.

22. M. A. El-Khateeb, F. A. El-Gohary, "Combining ABR Technology and Wetland for Domestic Wastewater Reclamation and Reuse, *Water Supply*, vol. 3, pp. 201-208. 2003.
23. B. Hegazy, M. A. El-Khateeb, A. El-adly Amira, M. M. Kamel, "Low-cost Wastewater Treatment Technology", *Journal of Applied Science*, vol. 7, pp. 815-819. 2007.
24. M. A. El-Khateeb, A. Z. Al - Herrawy, M. M. Kamel, F.A. ElGohary, "Use of wetlands as post treatments of anaerobically treated effluent", *Desalination*, vol. 245, pp. 50-59. 2009.
25. V. Mudgal, N. Madaan, A. Mudgal, "Heavy metals in plants, phytoremediation: Plants used to remediate heavy metal pollution" *Agriculture and Biology Journal of North America*, vol. 1, pp. 40- 46. 2010.
26. N. Korboulewsky, R. Wang, V. Baldy, "Purification processes involved in sludge treatment by a vertical flow wetland system: focus on the role of the substrate and plants on N and P removal", *Bioresource Technology*, vol. 105, pp. 9-14. 2012.
27. C. Wendland, J. Behrendt, T.A. Elmitwalli, I. Al Baz, G. Akcin, O. Alp, R. Otterpohl, "ABR reactor followed by constructed wetland and UV radiation as an appropriate technology for municipal wastewater treatment in Mediterranean countries", in *Proceedings of the 7th specialized conference on small water and wastewater systems in Mexico*, 2006.
28. P. Worall K. J. Peberdy, M. C. Millett, "Constructed wetland and natural conservation", *Water Science and Technology*, vol. 3, pp. 205-213. 1997.
29. C. M. Kao, M. J. Wu, "Control of non-point source pollution by a natural wetland", *Water Science and Technology*, vol. 43, pp. 169- 74. 2001.
30. J. García, P. Aguirre, R. Mujeriego, Y. Huang, L. Ortiz, J. Bayona, "Initial contaminant removal performance factors in horizontal flow reed beds used for treating urban wastewater", *Water Research*, vol. 38, pp. 1669-1678. 2004.
31. M. von Sperling, C. A. M. Mascarenhas, 2005, "Performance of very shallow ponds treating effluents from ABR reactors", *Water Science and Technology*, vol. 51(12), 83-90.
32. M. von Sperling, R. K. X. Bastos, M. T. Kato, "Removal of E. coli and helminth eggs in UASB: Polishing pond systems in Brazil", *Water Science and Technology*, vol. 51, pp. 91-97. 2005.
33. C.A.L Chernicharo, "Post Treatment Options for the Anaerobic Treatment of Domestic Wastewater, A review", *Environmental Science and Biotechnology*, vol. 5, pp. 73- 92. 2006.
34. American Public Health Association Inc. (APHA), 2005. Standard Methods for the Examination of Water and Wastewater, 21st ed. New York, USA.
35. A. Mudhoo, R. M. Pravish, M. Romeela, "Effects of Microwave Heating on Biogas Production, Chemical Oxygen Demand and Volatile Solids Solubilization of Food Residues. World Academy of Science", *Engineering and Technology*, vol. 69, pp. 805-810. 2012.
36. M. Sarioglu, A. Serdar, B. Turgay, "Inhibition effects of heavy metals (copper, nickel, zinc, lead) on anaerobic sludge" *Desalination and Water Treatment*, vol. 23, pp. 55-60. 2010.
37. K. J. Prakash, V. K. Tyagi, AA Kazmi, K Arvind, "Post treatment of ABR reactor effluent by coagulation and flocculation process" *Environmental Progress*, vol. 26, pp. 164-168 .2007.
38. I. Machdar, Y. Sekiguchi, A. Sumino, A. Ohashi, H. Harada, "Combination of a ABR reactor and a curtain type DHS reactor as a cost-effective sewage treatment system for developing countries", *Water Science and Technology*, vol. 42, pp. 83-88.2000.
39. T. V. Kumar, A. A. Khan, A. A. Kazmi, I. Mehrotra, A. K. Chopra, "Slow sand filtration of ABR reactor effluent: A promising post treatment technique", *Desalination*, vol. 249, pp. 571-576.2009.
40. A. M. Gower, "Water quality in catchment ecosystems", John Wiley & Sons, New York. 1980.
41. C. S. C. Calheiros, A. F. Duque, A. Moura, I. S. Henriques, A. Correia, A. Rangel, P. M. L. Castro, "Substrate effect on bacterial communities from constructed wetlands planted with *Typha latifolia* treating industrial wastewater" *Ecological Engineering*, vol. 35, pp. 744-753.2009.
42. J. T. de Sousa, A. C. van Haandel, A. A. Guimaraes, "Post-treatment of anaerobic effluents in constructed wetland systems", *Water Science and Technology*, vol. 44, pp. 213- 9. 2001.
43. S. Hafeznezami, J.-L. Kim, J. Redman, "Evaluating Removal Efficiency of Heavy Metals in Constructed Wetlands", *Journal of Environmental Engineering*, vol. 138, pp. 475-482.2012.
44. L. Marchand, M. Mench, D. L. Jacob, M. L. Otte, "Metal and metalloid removal in constructed wetlands, with emphasis on the importance of plants and standardized measurements: A review", *Environmental Pollution*, vol. 158, pp. 3447-3461.2010.
45. R. H Kadlec, S. D. Wallace, "Treatment wetlands", 2nd ed. CRC Press/Taylor &Francis Group Boca Raton, FL. 2008.
46. D. J. Walker, S. Hurl, "The reduction of heavy metals in a storm water wetland", *Ecological Engineering*, vol. 18, pp. 407-414. 2002.
47. R. P. Gambrell, "Trace and toxic metals in wetlands, A review", *Journal of Environmental Quality*, vol. 23, pp. 883-891. 1994.
48. H. Brix, "Functions of macrophytes in constructed wetlands", *Water Science and Technology* 29: 71-78. 1994.
49. S. Cheng, W. Grosse, F. Karrenbrock, M. Thoennesen, "Efficiency of constructed wetlands in decontamination of water polluted by heavy metals", *Ecological Engineering* vol. 18, pp. 317-325, 2002.
50. J. H. Choi, S. S. Park, P. R. Jaffé, "The effect of emergent macrophytes on the dynamics of sulfur species and trace metals in wetland sediments", *Environmental Pollution*, vol. 140, pp. 286-293. 2006.

Conflicts of Interest

The authors have neither any conflict of interest nor financial gain from the present manuscript.

References

- [1] B. S. Zeb, Q. Mahmood, S. Jadoon et al., "Combined Industrial Wastewater Treatment in Anaerobic Bioreactor Posttreated in Constructed Wetland," *BioMed Research International*, vol. 2013, Article ID 957853, 8 pages, 2013.
- [2] J. T. de Sousa, A. C. van Haandel, and A. A. V. Guimarães, "Post-treatment of anaerobic effluents in constructed wetland systems," *Water Science and Technology*, vol. 44, no. 4, pp. 213–219, 2001.

Research Article

Acetabular Bone Defect in Total Hip Arthroplasty for Crowe II or III Developmental Dysplasia of the Hip: A Finite Element Study

Yinqiao Du , Jun Fu, Jingyang Sun, Guoqiang Zhang, Jiying Chen, Ming Ni ,
and Yonggang Zhou 

Department of Orthopaedics, Chinese People's Liberation Army General Hospital, 28 Fuxing Road, Haidian District, Beijing, China 100853

Correspondence should be addressed to Ming Ni; niming301@163.com and Yonggang Zhou; ygzhou301@163.com

Received 9 May 2020; Accepted 8 August 2020; Published 25 August 2020

Guest Editor: Liu Yang

Copyright © 2020 Yinqiao Du et al. This is an open access article distributed under the Creative Commons Attribution License, which permits unrestricted use, distribution, and reproduction in any medium, provided the original work is properly cited.

Background. The purpose of this study was to establish the finite element analysis (FEA) model of acetabular bone defect in Crowe type II or III developmental dysplasia of the hip (DDH), which could evaluate the stability of the acetabular cup with different types of bone defects, different diameters of femoral ceramic heads, and the use of screws and analyze the stress distribution of screws. **Methods.** The FEA model was based on the CT scan of a female patient without any acetabular bone defect. The model of acetabular bone defect in total hip arthroplasty for Crowe II or III DDH was made by the increasing superolateral bone defect area of the acetabular cup. Point A was located in the most medial part of the acetabular bone defect. A 52 mm PINNACLE cup with POROCOAT Porous coating was implanted, and two screws (the lengths were 25 mm and 40 mm) were implanted to fix the acetabular cup. The stability of the acetabular cup and the von Mises stress of point A and screws were analyzed by a single-legged stance loading applied in 1948 N (normal working). The different diameters of the femoral ceramic head (28 mm, 32 mm, and 36 mm) were also analyzed. **Results.** The von Mises stress of point A was gradually increased with the increasing uncoverage values. When the uncoverage values exceeded 24.5%, the von Mises stress of point A without screws increased significantly, leading to instability of the cup. Screws could effectively reduce the von Mises stress of point A with uncoverage values of more than 24.5%. However, the peak von Mises stress in the screws with the uncoverage values that exceeded 24.5% was considerably increased. The diameter of the femoral ceramic head had no significant effect on the von Mises stress and the stability of the acetabular cup. **Conclusions.** We recommend that uncoverage values of less than 24.5% with or without screw is safe for patients with Crowe II or III DDH.

1. Introduction

Total hip arthroplasty (THA) is one of the most successful surgeries in the 20th century; a gradually increasing amount of patients with developmental dysplasia of the hip (DDH) received THA to release pain and improve function [1–3]. Despite their surgical complexity, DDH patients had also notably low rates of revision and obtained durable clinical results [2, 4–7]. During THA surgery, an obvious superolateral bone defect has been reported to be frequently observed above the surface of the acetabular cup at the level of the true acetabulum, especially in patients with Crowe II or III DDH [7, 8].

It has been recommended that the acetabular cup uncoverage should not exceed 30% of its overall surface [9]. If the uncoverage was more than 30%, a structural bone grafting may be needed [10–12]. However, all of these decisions were made which depended on the intraoperative judgment of surgeons. There is no previous publication reporting the specific value of uncoverage in THA of DDH patients.

The aim of this current study was to establish a finite element analysis (FEA) model of acetabular bone defect in THA for Crowe II or III DDH, in which the acetabular cup was positioned at the anatomical center of rotation of the hip without grafting. Then, the stability of the acetabular cup with different types of bone defects, different diameters

of femoral ceramic heads, the use of screws, and the stress distribution of screws were analyzed.

2. Materials and Methods

The FEA model was based on the geometry of a human pelvis, obtained from the CT scan of a female patient (body-weight: 50 kg) without any acetabular bone defect, who signed an informed consent for this study. The three-dimensional model of the pelvis was restored using Mimics Research 20.0 (Materialise, Belgium). The STL date of the pelvis was used to conduct the reverse engineering reconstruction using Geomagic 2012 (Geomagic, America), which includes segmentation, smoothing, polishing, denoising, and other image processing of the model. Then, this solid model was generated into IGES three-dimensional image. We followed the methods of Fu et al. [13].

According to the actual size of the patient's acetabulum and femur, acetabular and femoral prostheses were assembled using Solidworks 2014 (Dassault, France). The acetabular cup was a 52 mm PINNACLE cup with POROCOAT Porous coating (DePuy, America); cup inclination of 40 degrees and anteversion of 20 degrees were preset using a coordinate system linked with the pelvis. The ceramic liner (DePuy, America) and size 9 LCU femoral prosthesis (Link, Germany) with 28 mm/32 mm/36 mm femoral ceramic head of different diameters (Link, Germany) were implanted. When the diameter of the femoral ceramic head was 36 mm, two screws (the lengths were 25 mm and 40 mm, and the diameter was 6.5 mm) were implanted to fix the acetabular cup.

The solid model was imported into Ansys Workbench 16.2 (Ansys, America), and Boolean operation was performed. Mesh generation was made after setting up all the material properties and interfaces. The mesh size was set as 1 mm using an automatic mesh technique, as validated in a previous study [14]. Element type was chosen as Solid 187. The material properties used in the model are presented in Table 1. The friction coefficient between the cup and the bone was 0.8. And the friction coefficient between the ceramic liner and the femoral ceramic head was 0.06 [15].

The model of acetabular bone defect in THA for Crowe II or III DDH was made as shown in Figures 1(a) and 1(b). Figure 1(a) shows the sector defect, which was identified by extending the arc (defined as arc eAf) formed by the bone-prosthesis border within superolateral bone defect to the edge which was defined by arc eCf, and the arc AC was the longest distance from the sector defect [7, 16]. The straight line ef went through the hip center of rotation (HCOR). The surface area of the defect gradually increased by the length of the arc AC, and the angle α denoted the central angle of the uncovered portion above the cup as shown in Figure 1(b).

A resultant equivalent load (single-legged stance loading) was applied without taking account of muscles around the hip joint. The peak force measurements for the unilateral hip joint were reported in the majority of literature showing 1948 N for normal working [17, 18]. Fixed constraint boundary conditions were assumed at the sacroiliac joint and pubic

TABLE 1: Mechanical properties of materials used in FEA mode.

| Components | Materials | Elastic modulus (MPa) | Poisson's ratio |
|----------------------|-----------------|-----------------------|-----------------|
| Cortical bone | Cortical bone | 17300 | 0.265 |
| Cancellous bone | Cancellous bone | 400 | 0.2 |
| Screws | | | |
| Acetabular component | Titanium alloy | 110600 | 0.326 |
| Femoral prosthesis | | | |
| Ceramic liner | Ceramics | 350000 | 0.22 |
| Femoral ceramic head | | | |

symphysis (Figure 1(c)). The femur was constrained in all directions at the middiaphysis, and the simulated vertical reaction load was applied from the bottom of the femur at 1948 N (Figure 1(d)). Figure 1 shows the general layout used for these FEA models and the details of components, interfaces, load, and constraint boundary. The main analysis was the effect of bone defect, femoral ceramic head, and screw on the stability of the acetabular cup.

3. Results

3.1. The Effect of Different Bone Defects and Femoral Ceramic Head on the Stability of the Acetabular Cup. According to the result of FEA, the diameter of the femoral ceramic head had no significant effect on the von Mises stress of point A and the stability of the acetabular cup. The von Mises stress of point A was gradually increased with the increasing length of the arc AC (uncoverage). When the length of the arc AC exceeded 20 mm (uncoverage > 24.5%, angle α > 44.0°), the von Mises stress of point A improved significantly, leading to prosthesis instability (Figure 2).

3.2. The Effect of Screws on the Stability of the Acetabular Cup. When the diameter of the femoral ceramic head was set on 36 mm and two screws were inserted into the acetabular cup, the von Mises stress of point A with two screws was 12.44 MPa (without screw: 32.98 MPa) on the condition that the length of arc AC was 24 mm (uncoverage: 29.4%, angle α : 52.8°) and the acetabular cup with two screws had no sign of instability (Figure 3).

3.3. Stress Distribution of the Screw for Fixing an Acetabular Cup. The peak von Mises stress of the two screws was located in the upper 1/3 of the two screws, which was 18.83 MPa (0 mm), 19.06 MPa (4 mm), 19.71 MPa (8 mm), 21.29 MPa (12 mm), 23.42 MPa (16 mm), 62.12 MPa (20 mm), and 62.09 MPa (24 mm), respectively. As the length of the arc AC increased, the peak von Mises was gradually moved down along the screw (Figure 4).

4. Discussion

This current study of a three-dimensional FEA model of acetabular bone defect in THA for Crowe II or III DDH was constructed from CT scan date and used to analyze the effect of bone defect, femoral ceramic head, and screws on the

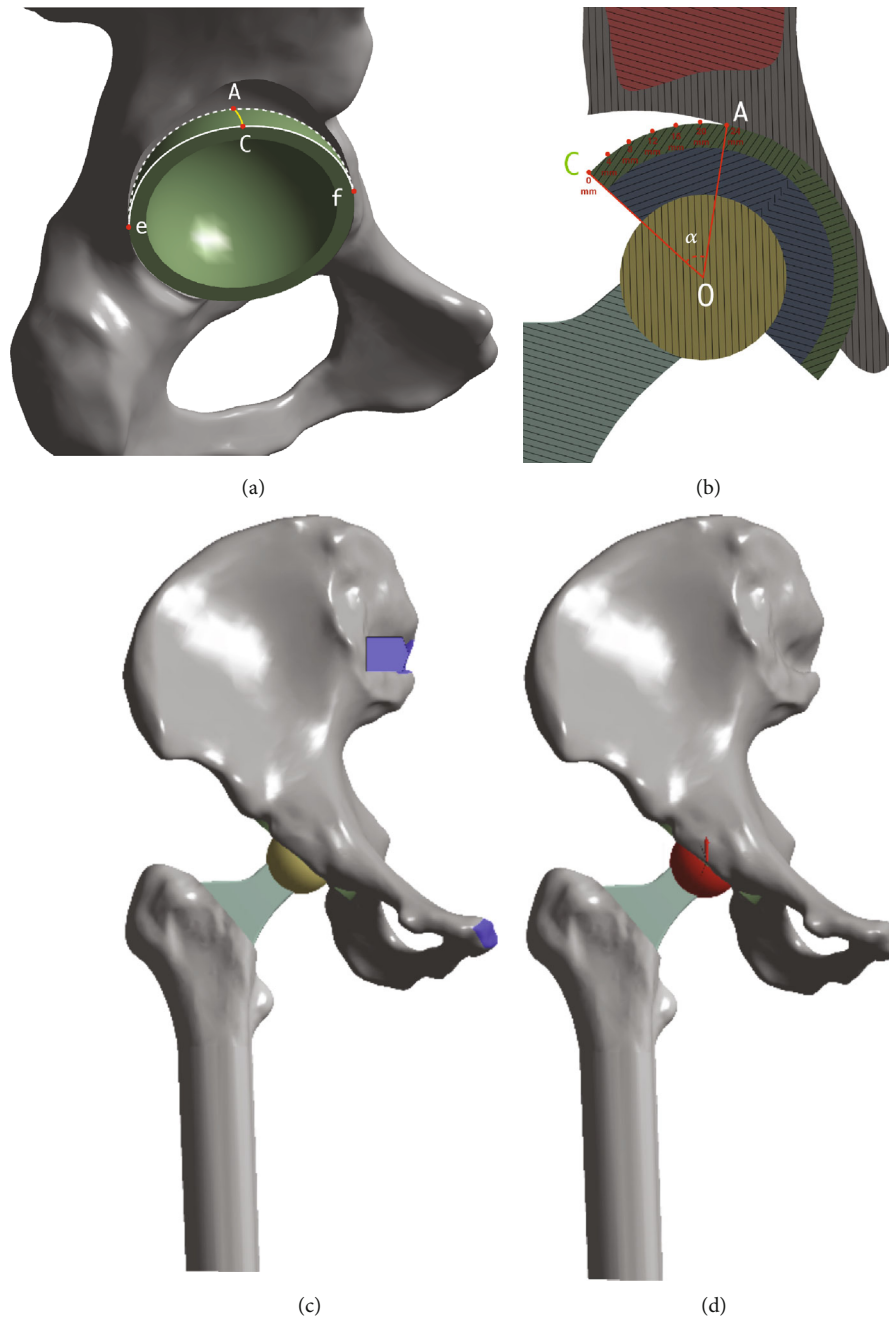


FIGURE 1: (a) The model of acetabular bone defect in total hip arthroplasty for Crowe II or III DDH. (b) The uncoverage area gradually increased by the length of the arc AC, and the angle α denoted the central angle of the uncovered portion above the cup. Angle α was formed by the crossing of line OA and OC. (c) Fixed constraint boundary conditions were assumed at the sacroiliac joint and pubic symphysis. (d) Simulated vertical reaction load was applied from the bottom of the femur.

stability of the acetabular cup. The results showed that the diameter of the femoral ceramic head had no significant effect on the von Mises stress and the stability of the acetabular cup; the acetabular cup primary stability can be achieved with uncoverage values of less than 24.5% (angle α : 44°) without a screw. Screws could effectively reduce the von Mises stress of point A with uncoverage values of more than 24.5%. However, the peak von Mises stress in the screws considerably increased.

In Crowe II or III DDH, the superolateral acetabular deficiency prevents placement of a standard cup to inadequate coverage [16]. Special techniques including high hip center and bone graft may be necessary to address inadequate osseous coverage of the acetabular cup. There is no standard high hip center technique to guide the process of acetabular reconstruction, which leads to the variable clinical outcomes resulting from the high hip center technique. In addition, it remains unclear to what extent the high hip center technique

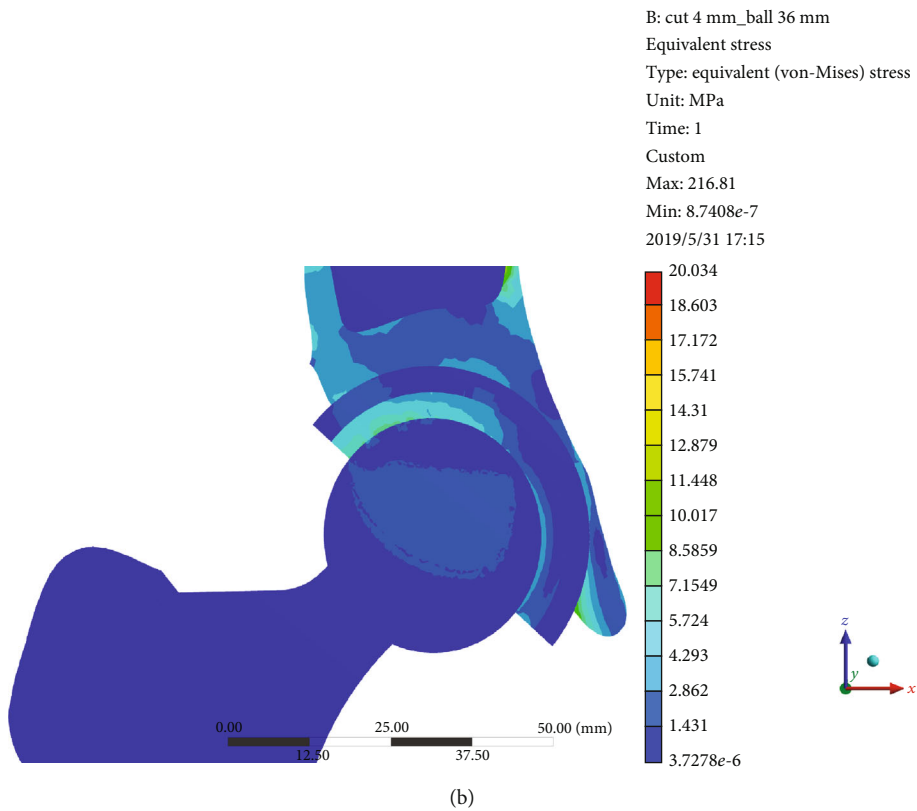
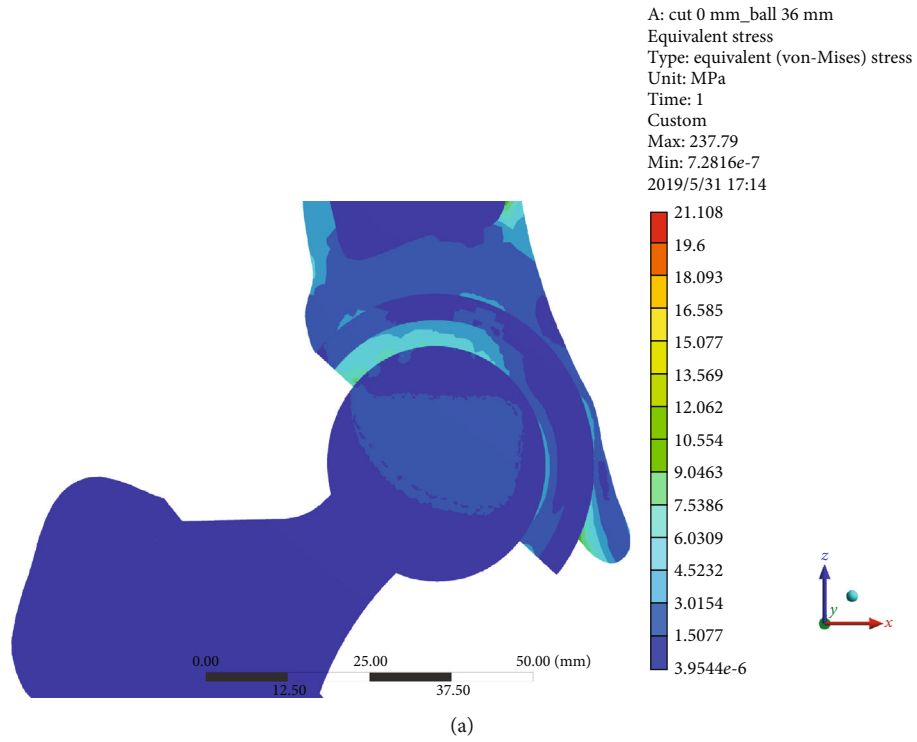


FIGURE 2: Continued.

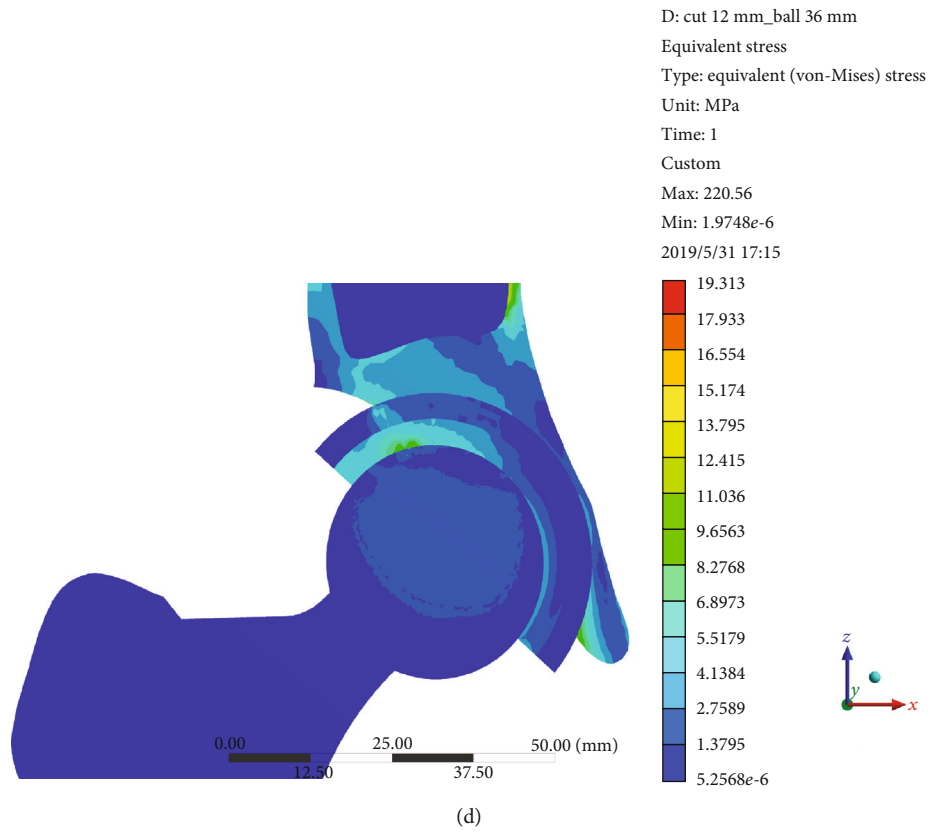
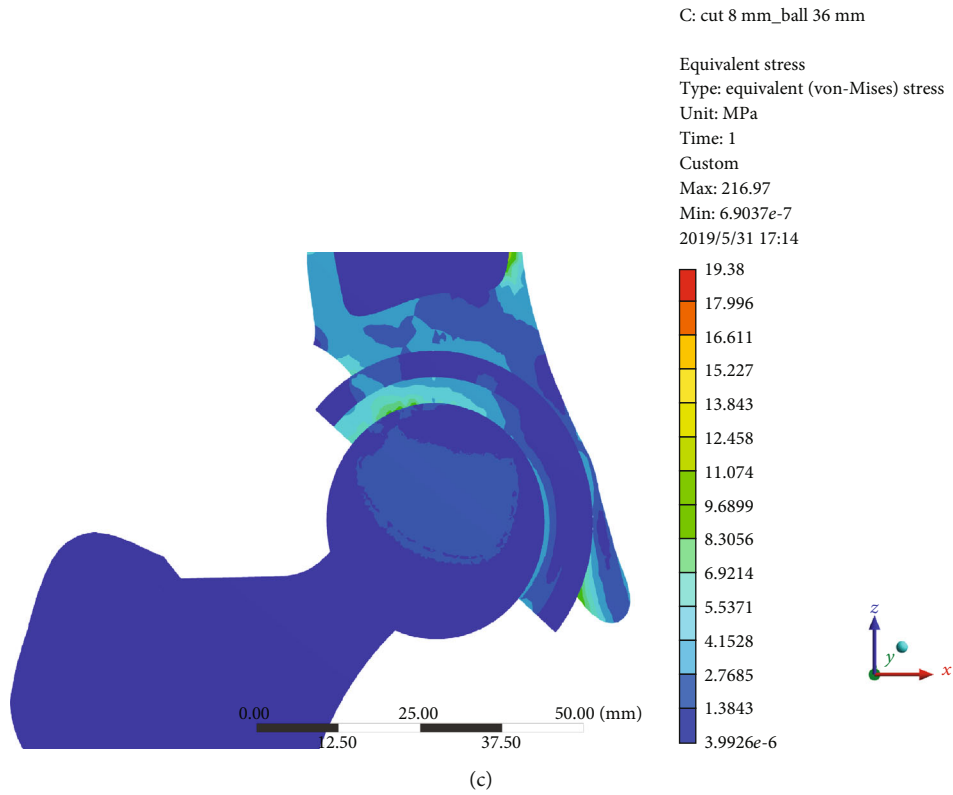


FIGURE 2: Continued.

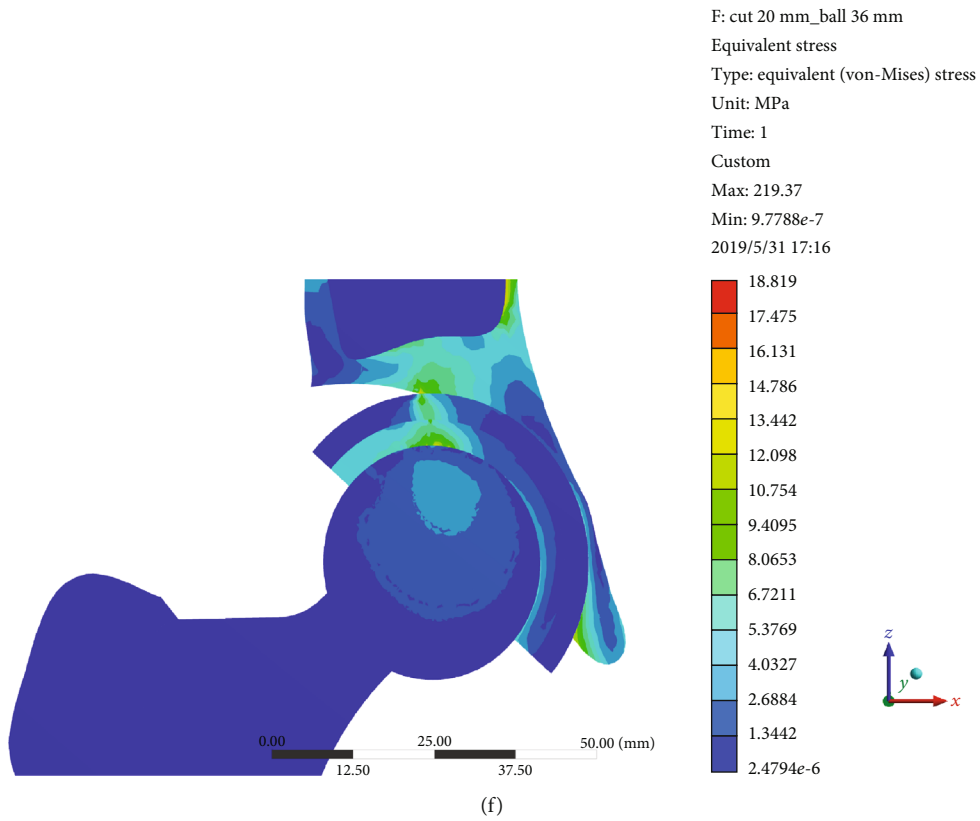
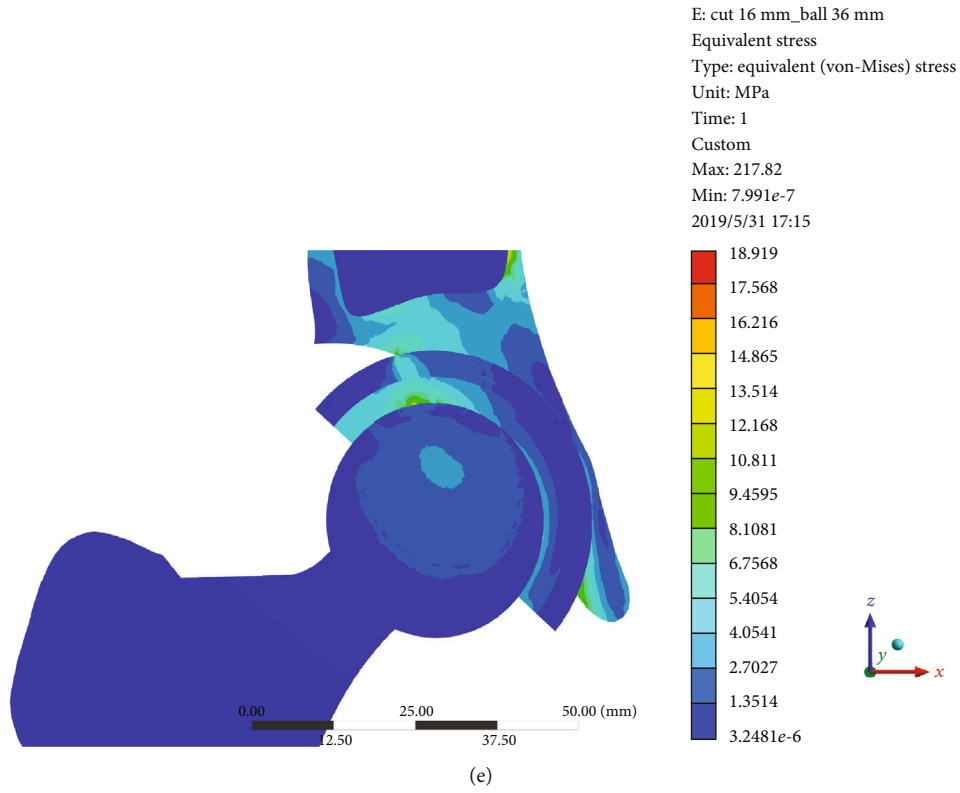


FIGURE 2: Continued.

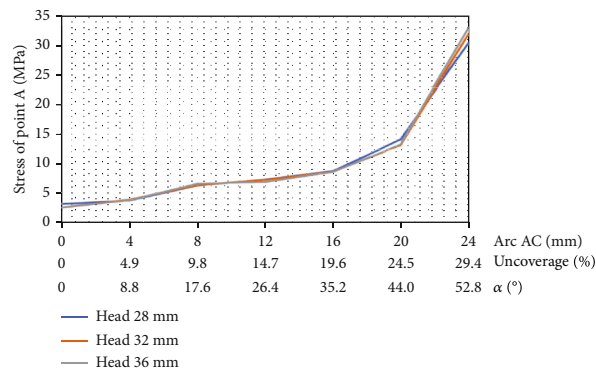
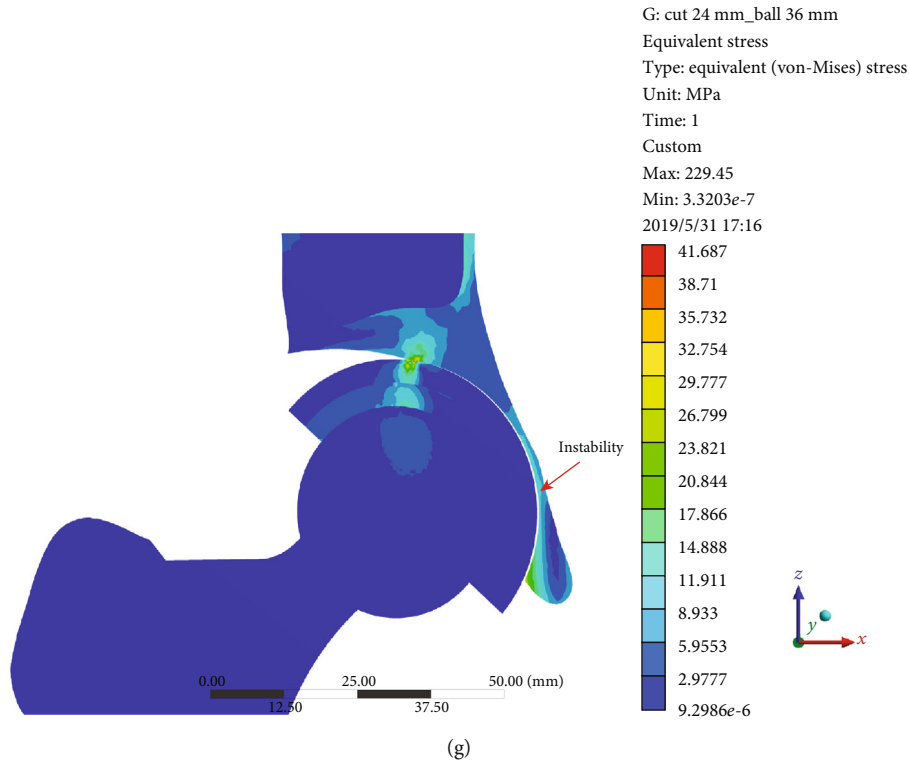


FIGURE 2: The von Mises stress of point A without screw. (a) The length of arc AC was 0 mm with a 36 mm femoral ceramic head. (b) 4 mm. (c) 8 mm. (d) 12 mm. (e) 16 mm. (f) 20 mm. (g) 24 mm. (h) Relationship between the von Mises stress of point A (MPa) and the length of arc AC with different diameters of the femoral ceramic head.

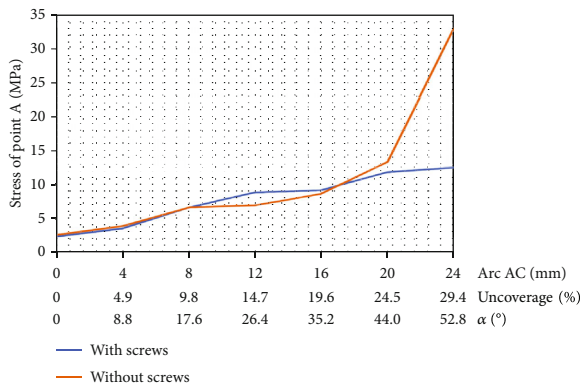


FIGURE 3: Relationship between the von Mises stress of point A (MPa) and the length of arc AC with and without screw.

restores the normal hip biomechanics [19]. Structural bone grafting with the acetabular cup at the level of the true acetabulum was another alternative to reconstruct the defect in DDH patients [20–22]. However, when coverage of the cup by the autograft did not exceed 50%, there will be a high risk of failure in the acetabular cup. And the absorption and collapse of structural bone grafting were also other causes for the failure of structural bone grafting. Therefore, the optimal acetabular cup position is at the level of the true acetabulum that restored the HCOR, the limb-length discrepancy (LLD), and muscle tension around the hip.

Xu et al. [7] measured the three-dimensional coverage postoperatively in 35 patients (45 hips) with Crowe II or III DDH, in which the acetabular cup was positioned at the anatomical center of rotation of the hip. Their research results

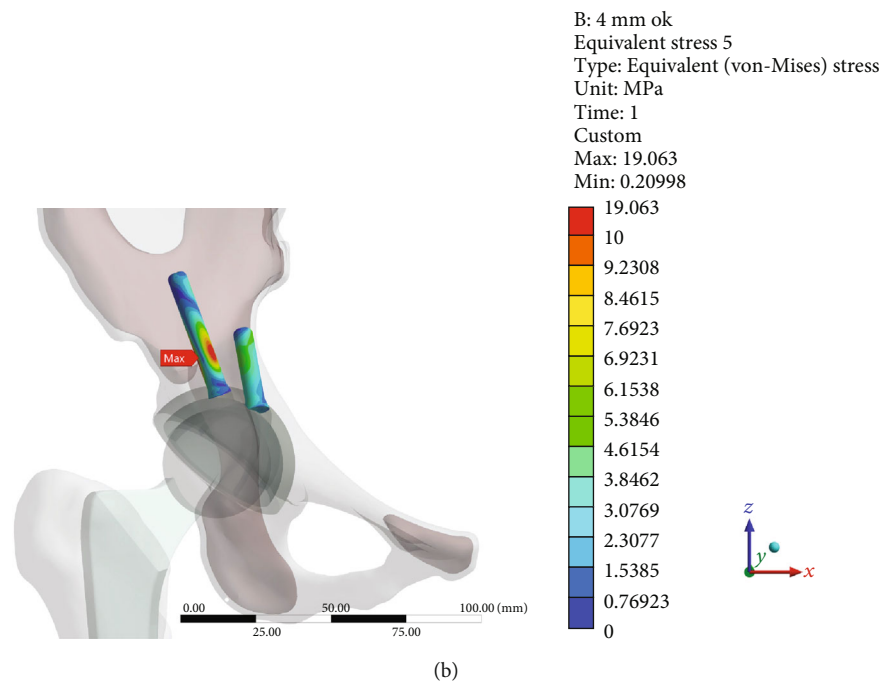
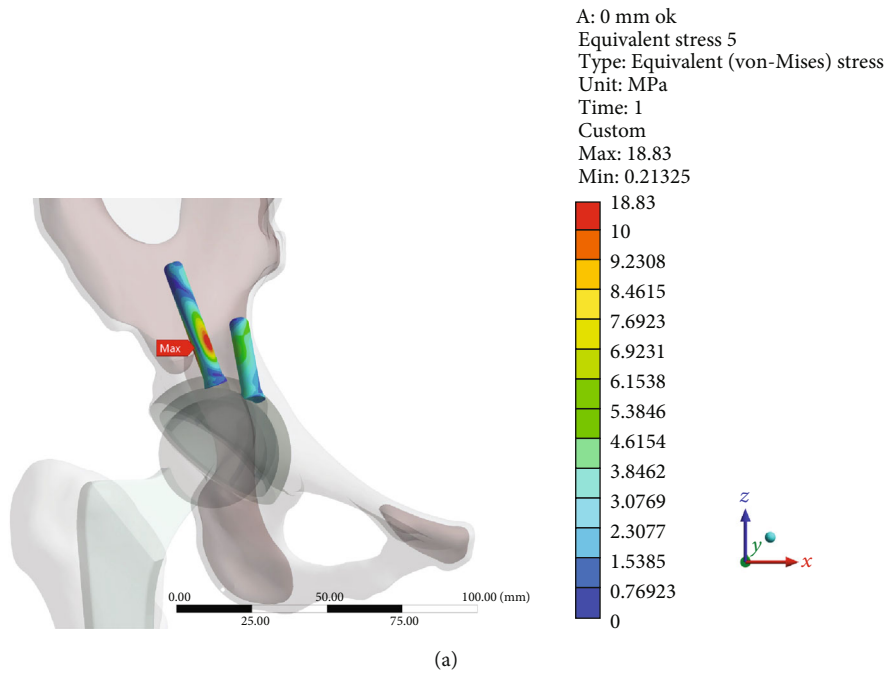


FIGURE 4: Continued.

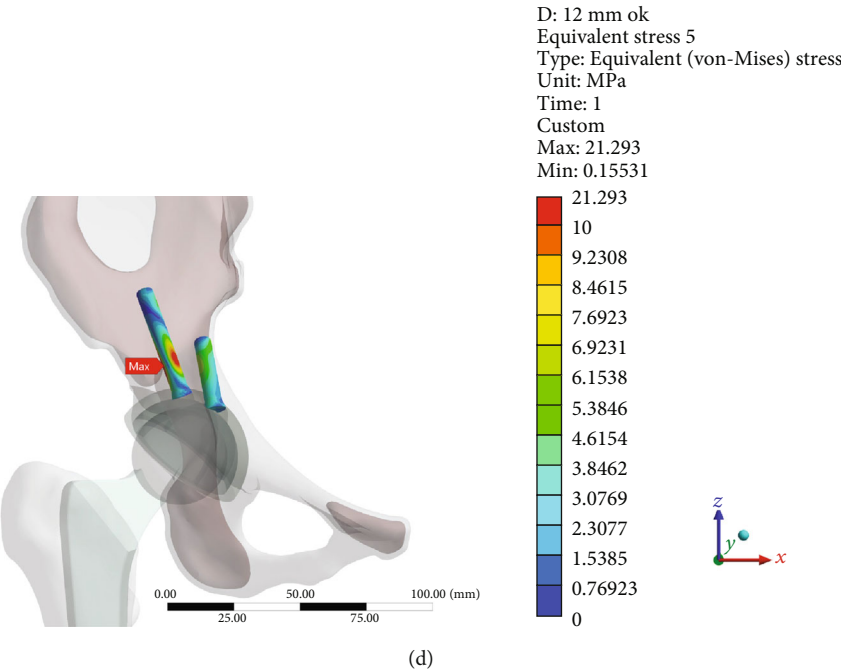
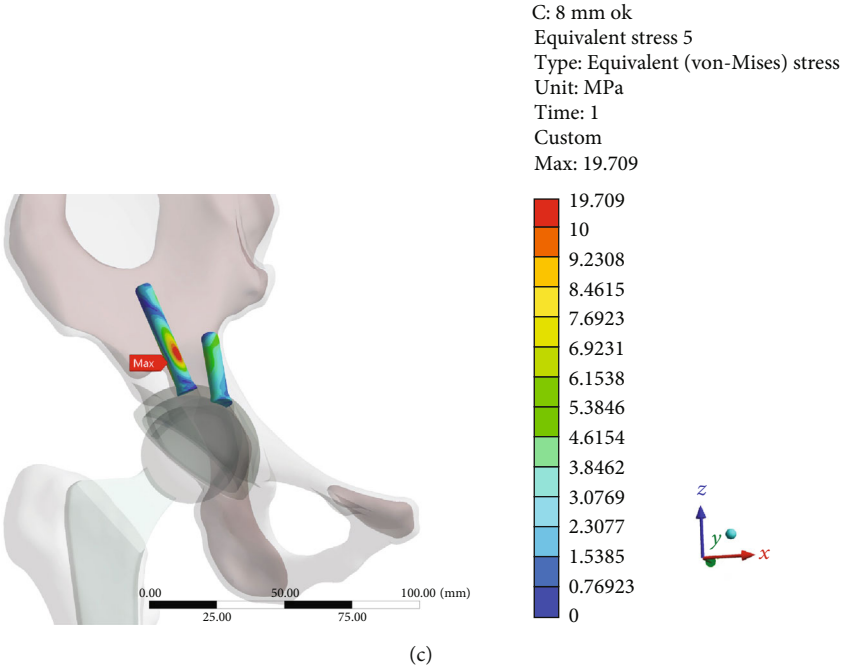
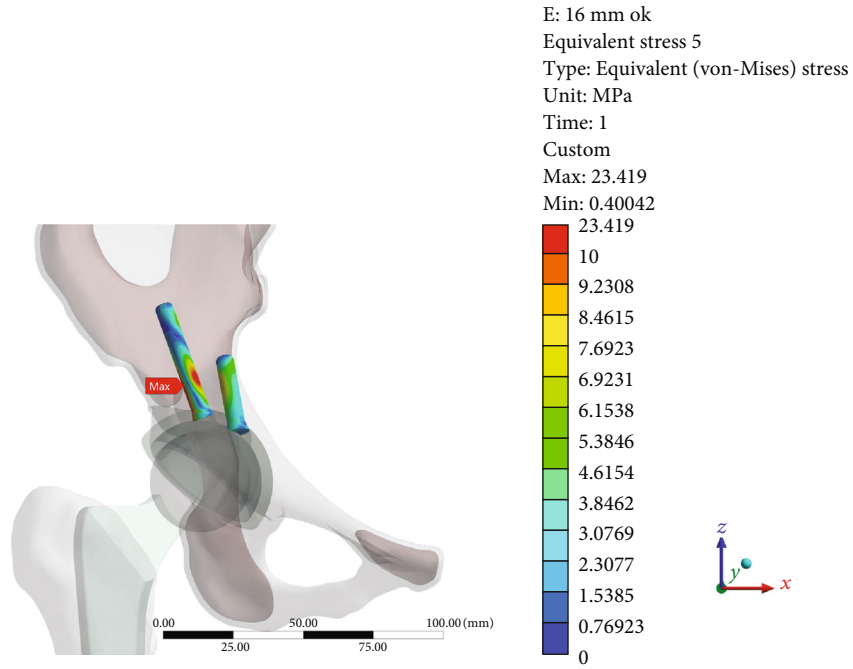
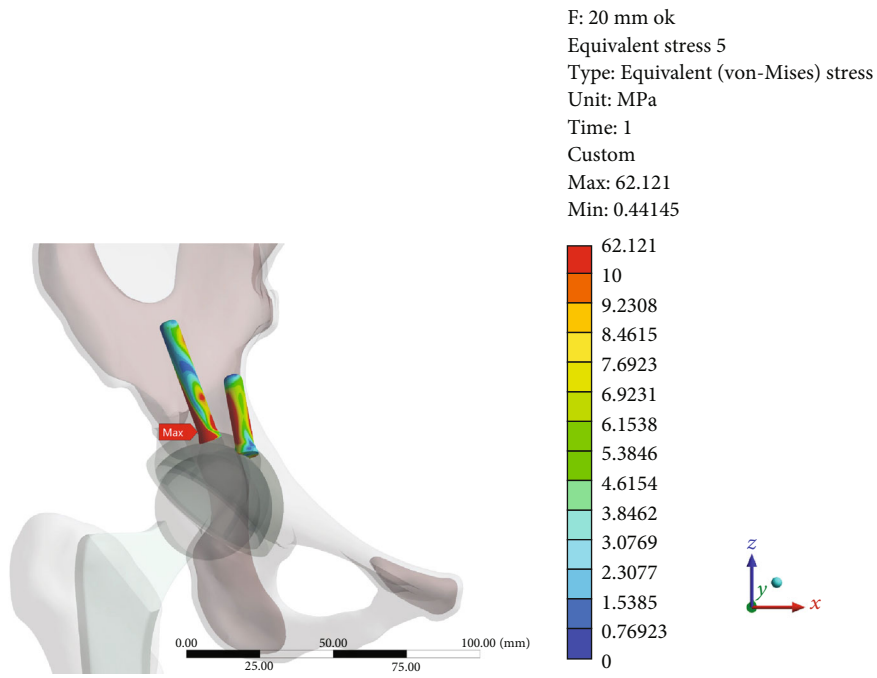


FIGURE 4: Continued.



(e)



(f)

FIGURE 4: Continued.

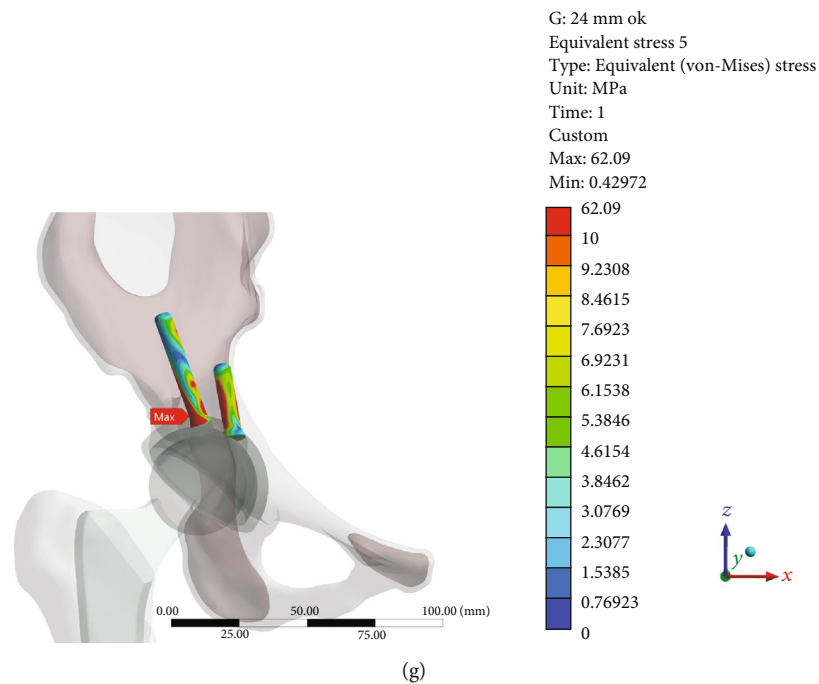


FIGURE 4: The stress distribution of the screw for fixing an acetabular cup: (a) 0 mm; (b) 4 mm; (c) 8 mm; (d) 12 mm; (e) 16 mm; (f) 20 mm; (g) 24 mm.

showed that the postoperative three-dimensional coverage was 85.74% and the height of the uncovered (the length of the arc AC in our study) is a useful parameter to determine the three-dimensional coverage during surgery.

Tikhilov et al. [12] utilized a mathematical computer model based on the FEA and the mechanical experiment to estimate the critical values of uncoverage enabling safe primary fixation of the acetabular cup in arthroplasty patients with DDH. According to their results, cup prosthesis primary stability can be achieved with uncoverage values of less than 15-25% without screw fixation and can reach approximately 35% with two-screw fixation. In our study, a possibility of mounting an acetabular cup with uncoverage within 24.5% (the length of arc AC: 20 mm, angle α : 44°) was demonstrated. This study was consistent with most previous studies that the minimal acetabular cup uncoverage should not exceed 30% of its surface [9–11, 23].

Tikhilov et al. suggested that if extreme uncoverage values of greater than 35% of the acetabular cup were observed, screw fixation did not improve reliable primary stabilization [12]. In our study, the von Mises stress of point A with two screws was considerably decreased on the condition that the length of arc AC was 20 mm (uncoverage: 24.5%, angle α : 44°) compared with that without screw. The use of screws can effectively reduce the stress of point A and improve reliable primary stabilization of the cup. However, the peak von Mises stress in the screws for fixing the acetabular cup with the length of arc AC exceeding 20 mm (uncoverage $> 24.5\%$, angle $\alpha > 44.0^\circ$) was considerably increased.

There are some limitations. This study investigated an ideal model and simulated acetabular bone defect in THA for Crowe II or III DDH which does not necessarily mimic

actual THA surgical environments and the real-life stresses. Additionally, the angle α may not be accurate on the X-ray given complex acetabular bone defects for Crowe II or III DDH. The intraoperative measuring or CT scan may better guide patients with early weight-bearing exercises. We believe our mode may provide a surgical guidance to surgeons while performing THA for patients with Crowe II or III DDH.

5. Conclusions

We recommend that uncoverage values of less than 24.5% (angle $\alpha < 44^\circ$) with or without a screw are safe for patients with Crowe II or III DDH, in which the acetabular cup was positioned on the anatomical center of rotation of the hip. The use of screws can effectively improve the reliable primary stabilization of the cup when the uncoverage values are more than 24.5%.

Data Availability

The data used to support the findings of this study are included within the article.

Conflicts of Interest

The authors declare that they have no conflicts of interest.

Authors' Contributions

Yinqiao Du and Jun Fu have contributed equally to this work.

Acknowledgments

This work received support from the National Key Research and Development Program of China (No. 2017YFB1104104).

References

- [1] C. D. Watts, J. R. Martin, K. A. Fehring, and W. L. Griffin, "Inferomedial hip center decreases failure rates in cementless total hip arthroplasty for Crowe II and III hip dysplasia," *The Journal of Arthroplasty*, vol. 33, no. 7, pp. 2177–2181, 2018.
- [2] O. F. Hitz, X. Flecher, S. Parratte, M. Ollivier, and J.-N. Argenson, "Minimum 10-year outcome of one-stage total hip arthroplasty without subtrochanteric osteotomy using a cementless custom stem for Crowe III and IV hip dislocation," *The Journal of Arthroplasty*, vol. 33, no. 7, pp. 2197–2202, 2018.
- [3] M. Kim and T. Kadowaki, "High long-term survival of bulk femoral head autograft for acetabular reconstruction in cementless THA for developmental hip dysplasia," *Clinical Orthopaedics and Related Research*, vol. 468, no. 6, pp. 1611–1620, 2010.
- [4] J. Shen, J. Sun, H. Ma, Y. Du, T. Li, and Y. Zhou, "High hip center technique in total hip arthroplasty for Crowe type II–III developmental dysplasia: results of midterm follow-up," *Orthopaedic surgery*, 2020.
- [5] M. Montalti, F. Castagnini, F. Giardina, E. Tassinari, F. Biondi, and A. Toni, "Cementless total hip arthroplasty in Crowe III and IV dysplasia: high hip center and modular necks," *The Journal of Arthroplasty*, vol. 33, no. 6, pp. 1813–1819, 2018.
- [6] L. J. Seo, J. Gabor, D. Novikov, J. E. Feng, R. Schwarzkopf, and J. M. Vigdorichik, "Outcomes in 385 developmental dysplastic hips requiring total hip arthroplasty," *Archives of Orthopaedic and Trauma Surgery*, vol. 139, no. 5, pp. 723–728, 2019.
- [7] J. Xu, X. Qu, H. Li, Y. Mao, D. Yu, and Z. Zhu, "Three-dimensional host bone coverage in total hip arthroplasty for Crowe types II and III developmental dysplasia of the hip," *The Journal of Arthroplasty*, vol. 32, no. 4, pp. 1374–1380, 2017.
- [8] C. Wang, H. Xiao, W. Yang et al., "Accuracy and practicability of a patient-specific guide using acetabular superolateral rim during THA in Crowe II/III DDH patients: a retrospective study," *Journal of orthopaedic surgery and research.*, vol. 14, no. 1, p. 19, 2019.
- [9] M. J. Anderson and W. H. Harris, "Total hip arthroplasty with insertion of the acetabular component without cement in hips with total congenital dislocation or marked congenital dysplasia," *The Journal of Bone and Joint Surgery American*, vol. 81, no. 3, pp. 347–354, 1999.
- [10] B. Atilla, H. Ali, M. C. Aksoy, O. Caglar, A. M. Tokgozoglu, and M. Alpaslan, "Position of the acetabular component determines the fate of femoral head autografts in total hip replacement for acetabular dysplasia," *The Journal of Bone and Joint Surgery British*, vol. 89-B, no. 7, pp. 874–878, 2007.
- [11] T. M. Thillemann, A. B. Pedersen, S. P. Johnsen, and K. Søballe, "Implant survival after primary total hip arthroplasty due to childhood hip disorders: results from the Danish Hip Arthroplasty Registry," *Acta Orthopaedica*, vol. 79, no. 6, pp. 769–776, 2009.
- [12] R. Tikhilov, I. Shubnyakov, S. Burns et al., "Experimental study of the installation acetabular component with uncoverage in arthroplasty patients with severe developmental hip dysplasia," *International Orthopaedics*, vol. 40, no. 8, pp. 1595–1599, 2016.
- [13] J. Fu, M. Ni, J. Chen et al., "Reconstruction of severe acetabular bone defect with 3D printed Ti6Al4V augment: a finite element study," *BioMed Research International*, vol. 2018, Article ID 6367203, 8 pages, 2018.
- [14] A. Dutt, "Effect of mesh size on finite element analysis of beam," *International Journal of Mechanical Engineering*, vol. 2, no. 12, pp. 8–10, 2015.
- [15] L. Ma and W. M. Rainforth, "The effect of lubrication on the friction and wear of Biolox®delta," *Acta Biomaterialia*, vol. 8, no. 6, pp. 2348–2359, 2012.
- [16] Y. Nie, F. Pei, B. Shen, P. Kang, and Z. Li, "Implication of acetabular width on the anteroposterior pelvic radiograph of patients with developmental dysplasia of the hip," *The Journal of Arthroplasty*, vol. 30, no. 3, pp. 489–494, 2015.
- [17] G. Bergmann, G. Deuretzbacher, M. Heller et al., "Hip contact forces and gait patterns from routine activities," *Journal of Biomechanics*, vol. 34, no. 7, pp. 859–871, 2001.
- [18] P. Christen, K. Ito, F. Galis, and B. van Rietbergen, "Determination of hip-joint loading patterns of living and extinct mammals using an inverse Wolff's law approach," *Biomechanics and Modeling in Mechanobiology*, vol. 14, no. 2, pp. 427–432, 2015.
- [19] M. W. Pagnano, A. D. Hanssen, D. G. Lewallen, and W. J. Shaughnessy, "The effect of superior placement of the acetabular component on the rate of loosening after total hip arthroplasty," *The Journal of Bone & Joint Surgery*, vol. 78, no. 7, pp. 1004–1014, 1996.
- [20] D. Delimar, A. Aljinovic, and G. Bicanic, "Failure of bulk bone grafts after total hip arthroplasty for hip dysplasia," *Archives of Orthopaedic and Trauma Surgery*, vol. 134, no. 8, pp. 1167–1173, 2014.
- [21] S. Kobayashi, N. Saito, M. Nawata, H. Horiuchi, R. Iorio, and K. Takaoka, "Total hip arthroplasty with bulk femoral head autograft for acetabular reconstruction in DDH," *The Journal of Bone and Joint Surgery American Volume*, vol. 86, Supplement 1, pp. 11–17, 2004.
- [22] P. Bobak, B. M. Wroblewski, P. D. Siney, P. A. Fleming, and R. Hall, "Charnley low-friction arthroplasty with an autograft of the femoral head for developmental dysplasia of the hip," *The Journal of Bone And Joint Surgery British*, vol. 82-B, no. 4, pp. 508–511, 2000.
- [23] L. Wang, A. R. Thoreson, R. T. Trousdale, B. F. Morrey, K. Dai, and K. N. An, "Two-dimensional and three-dimensional cup coverage in total hip arthroplasty with developmental dysplasia of the hip," *Journal of Biomechanics*, vol. 46, no. 10, pp. 1746–1751, 2013.